UC Berkeley
UC Berkeley Electronic Theses and Dissertations

Title

Investigation of the Structure and Function Relationship in Bioelectricity using M13 Virus Model System

Permalink

https://escholarship.org/uc/item/73b0k91r

Author

Kim, Han

Publication Date

2024

Peer reviewed|Thesis/dissertation

eScholarship.org Powered by the California Digital Library
University of California

Investigation of the Structure and Function Relationship in Bioelectricity using M13 Virus Model System

By

Han Kim

A dissertation submitted in partial satisfaction of the

requirements for the degree of

Doctor of Philosophy

in

Applied Science and Technology

in the

Graduate Division

of the

University of California, Berkeley

Committee in charge:

Professor Seung-Wuk Lee, Chair

Professor Lydia Sohn

Professor Grace Gu

Spring 2024

Investigation of the Structure and Function Relationship in Bioelectricity using M13 Virus Model System

Copyright © 2024

by

Han Kim

Abstract

Investigation of the Structure and Function Relationship in Bioelectricity using M13 Virus Model System

by

Han Kim

Doctor of Philosophy in Applied Science and Technology

University of California, Berkeley

Professor Seung-Wuk Lee, Chair

Bioelectricity is generated by a wide spectrum of living organisms, ranging from single-celled entities to intricate multicellular organisms. These organisms have evolved intricate mechanisms to regulate and manage electrical activity. The understanding and controlling of bioelectricity hold the potential to yield diverse bioelectrical applications. However, comprehending bioelectrical systems using conventional organic/inorganic materials remains challenging because these materials lack the inherent complexity and adaptability that make replication difficult, limiting their capacity for modification and customization. Biological systems are highly complex, comprising various components such as nucleic acids, proteins, and tissues that display high specificity and selectivity in their interactions and processes. This complexity and heterogeneity hinder the accurate replication or mimicry of biological processes at the molecular level. Viruses, being submicroscopic infectious entities, serve as powerful tools for advancing our understanding of fundamental biological systems. Using the M13 phage as a model system due to its simple structure, versatile, biocompatible, and massively replicable characteristics, the structure-function relationship of bioelectricity is studied. This thesis explores the responsive electrical properties of viruses to external stimuli such as friction, mechanical stress, heat, and chemical environments. It examines how genetic modifications of viruses alter their structural and electrical properties, introducing practical virus-based bioelectrical applications. By using the M13 phage as a model system for investigating bioelectricity, this research aims to offer valuable insights into the design and development of innovative bioelectrical applications, bridging the gap between conventional materials and biological systems.

Acknowledgements

First and foremost, I would like to express my appreciation to my advisor, Professor Seung-Wuk Lee, for providing me with the opportunity to join his group at the University of California, Berkeley. This experience has marked a significant shift in my confidence within my academic career, as I have acquired skills in critical thinking, problem-solving, goal-setting, and developed a heightened passion to pursue the next steps in my career. Additionally, I consider myself fortunate to have Professors Lydia Sohn and Grace Gu on my thesis committee. I have been in contact with them since my qualifying exam committee in 2020, and their guidance has been instrumental in shaping my research, culminating in the completion of this thesis.

I am truly grateful to have had the pleasure of working with the members, particularly the phage specialists, in the Lee Lab. I want to extend my thanks to Dr. Seungwook Ji for his friendship and guidance. As we entered the Lee Lab after a one-year gap, I spent the most time with him, and we supported each other in achieving our goals. I am grateful to him for helping me settle in the United States and for providing emotional support even outside of the campus. I also want to express my appreciation to Drs. Inseok Chae, Ju Hun Lee, Byung Yang Lee, and Ju-Hyuck Lee. They helped me learn everything I needed to study the phage electricity. Working on projects together with them was a meaningful experience, allowing me to learn their expertise and positive attitude. Special thanks go to Drs. Butaek Lim, Malav Desai, and Hwa Hui Shin. Their support with biological knowledge was instrumental in helping me solidify and complete my projects related to phage engineering. Lastly, I am grateful to Kento Okada for his contributions to the computational studies. Together, we put our heads together and accomplished something meaningful from scratch. I extend my best wishes for his doctoral studies at Cornell University.

I would not be where I am today without the unconditional love and support I received from my parents, Hagdong Kim and Kyungran Park, and my sister, Joori Kim. No matter what choices I made, they always supported, encouraged, and respected me. Thanks to them, I have come this far and learned about life and love. As their son and younger brother, I express my infinite gratitude.

I would like to dedicate my Ph.D. achievements to my wife, Dr. Youngju Choi. Without her love, I would have broken down. I have been able to sustain myself because of her, and I am grateful for her endless support. At the same time, I will never forget her hardships and sacrifices. It is a great honor to get a Ph.D. with her and to embark on this journey of life together.

Table of Contents

Abstract 1
Acknowledgements i
Table of contents ii
List of figures vi
List of tables xviii
Chapter 1 Introduction 1
1.1 Advances in bioelectricity 1
1.2 Electrical properties of materials 2
1.2.1 Triboelectricity 3
1.2.2 Dielectric 5
1.2.3 Piezoelectricity 6
1.2.4 Pyroelectricity 8
1.2.5 Ferroelectricity 10
1.3 Bioelectricity in amino acids 11
1.3.1 Glycine 12
1.3.2 Other amino acids 16
1.4 Bioelectricity in peptides 24
1.5 Bioelectricity in proteins 30
1.6 Bioelectricity in tissues 33
1.7 Virus model system 42
1.7.1 Virus-based nanomaterials 42
1.7.2 M13 bacteriophage model system 43
1.7.2.1 Structural features of the M13 phage 43
1.7.2.2 Biocompatibility and mass production 45
1.7.2.3 Self-assembled nanostructures 46
1.7.2.4 M13 phage-based piezoelectric energy generation 47
1.8 Challenges in the structure-function relationship in biomaterials 48
1.9 Thesis outline 49
Chapter 2 Triboelectricity in M13 phage 51
2.1 Introduction 51
2.2 The structure of genetically engineered M13 phages 52
2.3 Characterization of the triboelectricity in M13 phage 53
2.3.1 Triboelectric effect using Kelvin probe force microscopy 53

2.3.2 Diffusion of the triboelectric charges 55
2.3.3 Triboelectric charge characterization 56
2.4 Molecular mechanisms of the triboelectricity in M13 phage 58
2.4.1 Relative triboelectric charging behaviors of phage films 58
2.4.2 Computational analysis – Extended semiempirical tight-binding calculations 62
2.4.3 Triboelectric series 64
2.5 Characterization of phage-based triboelectric devices 65
2.6 Conclusion 72
2.7 Methods 72
2.7.1 Genetic engineering of M13 phage 72
2.7.2 Surface charge estimation 72
2.7.3 Fabrication of the monolayer M13 phage films 73
2.7.4 Phage quantification 73
2.7.5 Triboelectric characterization using Kelvin probe force microscopy 73
2.7.6 Fabrication of the multilayer M13 phage films 74
2.7.7 Calculation of the energy levels of M13 phage 74
2.7.8 Device fabrication and output characterization 74
Chapter 3 Piezoelectricity in M13 phage 76
3.1 Introduction 76
3.2 Piezoelectric structure of M13 phage 77
3.3 Molecular mechanism of the piezoelectricity in M13 phage 78
3.3.1 Dipole moment of genetically engineered M13 phages 78
3.3.2 Directional dependency of the dipole moment of M13 phage 82
3.4 Surface charge to piezoelectric response studies using scanning probe microscopy 92
3.4.1 Dielectric constant characterization 92
3.4.2 Surface charge density characterization 94
3.5 Vertical and horizontal piezoelectric output characterization 99
3.6 Shear piezoelectric output characterization 100
3.7 Characterization of phage-based piezoelectric devices 104
3.8 Conclusion 108
3.9 Methods 109
3.9.1 Computations of the dipole moment of the M13 phage 109
3.9.2 Gel electrophoresis 110
3.9.3 Isoelectric point 110
3.9.4 Zeta potential 110

3.9.5 Dielectric constant measurements 110
3.9.6 Surface charge density measurements 111
3.9.7 Fabrication of the vertically standing phage films 111
3.9.8 Fabrication of the horizontally aligned phage films 111
3.9.9 Characterization of the piezoelectric coefficient of M13 phage films 112
3.9.10 Characterization of phage-based piezoelectric devices 112
Chapter 4 Pyroelectricity in M13 phage 113
4.1 Introduction 113
4.2 Pyroelectric structure of M13 phage 114
4.2.1 Microscopic pyroelectric structure of M13 phage 114
4.2.2 Macroscopic pyroelectric structure of M13 phage film 116
4.2.3 Pyroelectric characterization of the vertically standing phage films 116
4.3 Pyroelectric potential studies using Kelvin probe force microscopy (KPFM) 120
4.3.1 Pyroelectric potential characterization 120
4.3.2 Pyroelectric coefficient calculation 124
4.4 Molecular mechanism of the pyroelectricity in M13 phage 125
4.4.1 Molecular dynamics simulations 125
4.4.2 Circular dichroism spectroscopy 128
4.5 Pyroelectric signal measurement using near-infrared (NIR) heat 132
4.5.1 Infrared heating mechanism 132
4.5.2 Pyroelectric output characterization 134
4.6 Pyroelectric responses to molecular interactions 138
4.6.1 Introduction 138
4.6.2 Hydrophilic molecular interactions 140
4.6.3 Aromatic molecular interactions 141
4.6.4 Mechanisms of the molecular interactions 143
4.7 Conclusion 144
4.8 Methods 145
4.8.1 Single phage length measurements 145
4.8.2 Mechanical property characterization of phage films 145
4.8.3 Fourier-transform infrared (FT-IT) spectroscopy 146
4.8.4 Pyroelectric characterization using Kelvin probe force microscopy 146
4.8.5 Molecular dynamics simulations 146
4.8.6 Structural analysis using circular dichroism spectroscopy 146
4.8.7 Structural analysis using dynamic light scattering 147

4.8.8 Pyroelectric characterization upon near-infrared heating 147
4.8.9 Optimization of the temperature variations of infrared heating 147
Chapter 5 Conclusion and future perspectives 149
5.1 Concluding remarks 149
5.2 Future perspectives 150
5.2.1 Enhancing the performance of phage-based triboelectric devices 151
5.2.2 Optimizing the piezoelectric effect of phage-based piezoelectric devices 151
5.2.3 Investigating the responsivity and novel phage-based pyroelectrical applications 152
5.2.4 Exploring the ferroelectricity in M13 phage 152
References 154
Appendix 194
A.1 Calculation of the coordinates of positive and negative charges 194
A.2 Deformation of a M13 phage model 196
A.3 Temperature controller in Kelvin probe force microscopy measurements 198
A.4 Information of graphic figures 206

List of figures

Figure 1-1. Hierarchical relationship among various subgroups of materials 22

Figure 1-2. (a) Working principle of the triboelectric effect. The triboelectric effect is a phenomenon related to the generation of electric charge through the contact and separation of materials. It involves the transfer of electrons between two materials, resulting in one material acquiring a positive charge while the other acquires a negative charge. (b) Triboelectric series of conventional materials. The triboelectric series is a list that ranks materials based on their tendency to gain or lose electrons when in contact with other materials. The materials at the left of the series have a lower affinity for electrons, while those at the right have a higher affinity. 24

Figure 1-3. Dielectric properties in materials. When an electric field is applied to a dielectric, the electric charges within the material do not move freely as there are not loosely bound or free electrons available for drifting. Instead, they undergo a slight shift from their average equilibrium positions, leading to dielectric polarization..... 25

Figure 1-4. Working principle of the piezoelectric effect. When mechanical stress is applied to a piezoelectric material, it causes a deformation in the crystal lattice. This deformation leads to a displacement of positive and negative charges within the material, creating an internal electric dipole moment. The movement of charges results in the separation of positive and negative charges, breaking its electrical equilibrium. 27

Figure 1-5. Schematic representation of a piezoelectric tensor. A piezoelectric tensor described the relationship between mechanical stress and electrical polarization in a material. 27

Figure 1-6. Working principle of the pyroelectric effect. Pyroelectric materials exhibit a change in their electric polarization in response to variations in temperature. Pyroelectric materials exhibit a spontaneous electric polarization due to the arrangement of charges within the crystal lattice. When the temperature of the pyroelectric material changes, it affects the thermal motion of atoms and ions within the crystal lattice. The temperature change causes a shift in the positions of these charged particles, leading to a change in the distribution of electric dipoles within the material. The redistribution of electric dipoles results in a net electric polarization in the material. This change in polarization leads to the generation of an electric field within the material, breaking its electrical equilibrium. 28

Figure 1-7. Working principle of the ferroelectric effect. The ferroelectric effect is a phenomenon observed in specific materials that display inherent polarization, which can be reversed by applying an external electric field. The material generates spontaneous electric polarization as a result of the alignment of electric dipoles within its crystal lattice. When an external electric field is introduced to a ferroelectric material, it impacts the orientation of the electric dipoles. This external electric field applies torque to the dipoles, prompting them to reorient in alignment with the applied field. As the dipoles undergo this reorientation, the polarization of the material undergoes a change in response to the applied electric field. The material can exhibit a significant polarization even with a relatively small, applied field due

to the cooperative behavior of the electric dipoles. A notable characteristic of ferroelectric materials is their capacity to preserve polarization even after removing the external electric field. If the direction of the external electric field is reversed, the dipoles respond by reorienting themselves, causing the material's polarization to switch in the opposite direction. 30

Figure 1-8. The chemical structure of an amino acid includes electron lone pairs on the nitrogen in the amino group on the oxygens in the carboxyl group, leading to the presence of partial dipole moments. 31

Figure 1-9. The formation of a dipole moment in glycine. 34

Figure 1-10. a, α-glycine exhibit zero spontaneous polarization due to its centrosymmetric structure. The polarization of glycine molecules counteract each other, resulting in zero polarization. b, The dipole moments in glycine molecules create a spontaneous polarization along the y-axis, contributing to an increased longitudinal 22 piezoelectric coefficient. c, The γ-glycine unit cell exhibit a spontaneous polarization along the z-axis due to the collective alignment of dipole moments, which is directly linked to the longitudinal 33 piezoelectric coefficient. 34

Figure 1-11. Schematic images of positively charged amino acids (arginine and histidine) and negatively charged amino acids (glutamate and aspartate) depict dipole moments. In positively charged amino acids, these dipole moments are formed from the carboxyl group toward the amino group, whereas in negatively charged amino acids, they are oriented in the opposite direction. 40

Figure 1-12. The triboelectric series of amino acids indicates that positively charged amino acids, classified as positive triboelectric materials, typically donate electrons due to their low work functions. Conversely, negatively charged amino acids, categorized as negative triboelectric materials, tend to accept electrons due to their high work functions 40

Figure 1-13. The hierarchical structures of diphenylalanine (FF) peptide assembly involve six FF monomers forming a repeating unit in a hexagonally symmetric structure. This structure exhibits a spontaneous polarization of 1.3 D perpendicular to the plane. The repeating units are stacked through hydrogen bonds and π-π stacking, resulting in self-assembled FF peptide tubular structures. 47

Figure 1-14. The hierarchical structures of Pro-Phe-Phe (PFF) and Hyp-Phe-Phe (OFF) peptides. (a) The chemical structures of the tripeptides PFF and OFF. (b) OFF peptides form through intermolecular hydrogen bonds, creating an extended helical-like structure. The net dipole moment of the molecule aligns along the helical axis, with molecular and crystal dipole moments of 6.7 and 1.9 D, respectively. (c) OFF peptides assemble in parallel structures using aromatic zipper structures. (d) OFF peptides self-assemble into fibrillar structures. 48

Figure 1-15. The hierarchical structures of collagen. (a) The chemical structure of the collagen motif: Gly-Pro-Hyp. (b) The chemical structure of the collagen chain, specifically Type I (PDB code: 1CAG). (c) The structure of tropocollagen, which consists of triple helices with a length of 300 nm and a diameter of 1.5 nm. (d) The structure of collagen fibrils, which

are stabilized through crosslinks between collagen molecules and exhibit staggered spacing with gap and overlap regions. (e) The highly oriented structure of collagen fibers in connective tissues. 52

Figure 1-16. The hierarchical structures of bone. (a) Schematic image of bone. (b) The basic structural unit of bone, known as the osteon, is composed of concentric layers of bone matrix called lamellae. (c) Collagen fibers are the primary structural component of bone, composed of collagen fibrils. (d) Collagen fibrils are bundles of collagen molecules (tropocollagens) arranged in a staggered, overlapping pattern. (e) Hydroxyapatite, a mineral in bone, has crystals deposited between the collagen molecules in a hexagonal centrosymmetric structure. (f) Tropocollagen is the basic unit of collagen in tissues, forming a triple helix structure consisting of three polypeptide chains. 58

Figure 1-17. The hierarchical structure of a tendon includes collagen fibers as the primary structural component, aligned parallel to each other. Individual collagen fibers group together to form primary fiber bundles, which are surrounded by a thin layer of connective tissue called endotenon. Primary bundles then group to form secondary fiber bundles, surrounded by a thicker layer of connective tissue called peritenon. Tertiary fiber bundles, formed by grouping secondary bundles, are surrounded by a layer of loose connective tissue containing blood vessels and nerves, known as epitenon 59

Figure 1-18. The hierarchical structure of aorta. It consists of an innermost layer lined by a single layer of endothelial cells. The tunica intima, a thin connective tissue layer, maintains the artery wall's integrity and regulates substance passage between blood and surrounding tissues. The tunica media, the thickest layer, is separated from the tunica intima by an elastic lamina and is composed of collagen fibers, elastin fibers, and smooth muscle cells. The outermost layer, the tunica adventitia, provides structural support to the artery and mainly consists of collagen fibers 60

Figure 1-19. The structure of the M13 phage. (a) M13 phage has a filamentous shape measuring 880 nm in length and 6.6 nm in diameter. (b) and (c) It is composed of 2700 copies of pVIII proteins with five-fold rotational and two-fold screw symmetry, exhibiting a non-centrosymmetric structure. pVIII protein consists of 50 residues and forms a dipole moment from the N-terminal to C-terminal direction. 63

Figure 1-20. Schematic of the M13 phage depicting the arrangement of coat proteins. The surface structure of these coat proteins can be modified through genetic engineering technique. This allows for the customization of the molecular configurations of the phage surface to align with specific characteristics, enabling the presentation of the corresponding peptide motif on the coat proteins of the phage. 64

Figure 1-21. M13 phages can be efficiently produced in large quantities through bacterial infection, providing a cost-effective means of generating a significant number of phages. The life cycle of the M13 phage involves rapid replication, allowing for quick and scalable production of the phage. 65

Figure 2-1. Schematic of the M13 phage structure and surface charges. (a) The M13 phage possess a filamentous structure, measuring 880 nm in length and 6.6 nm in diameter, and is

encased by 2700 copies of pVIII major coat proteins. (b) Side view of the pVIII protein of 4E-phage highlighted with the surface exposed area (light blue color) and the engineered peptides (yellow color). (c) Primary structure of the major coat protein for the 4E-phage. The engineered four glutamates (4E) are underlined. Amino acids displayed on the surface are indicated in blue. Reprinted with permission. Copyright 2021, American Chemical Society. 71

Figure 2-2. Characterization of the triboelectrification of the M13 phage using a Ti/Pt-coated AFM tip. Reprinted with permission. Copyright 2021, American Chemical Society. 73

Figure 2-3. Characterization of triboelectrification of the M13 phage. (a) AFM height profile image of a monolayer phage film, where mechanical force was applied within the red dotted box, and the triboelectric charges were observed in the black dotted box. (b) Time-lapse KPFM images capturing the evolution of triboelectric charges on the surface of the M13 phage within the region outlined by the dotted box in (a). Reprinted with permission. Copyright 2021, American Chemical Society. 74

Figure 2-4. Time-dependent triboelectric potential profiles of the phage surface along the dashed line in Figure 2-3b. The contact area is indicated by the dotted line, measured as 0 μm. Reprinted with permission. Copyright 2021, American Chemical Society..... 75

Figure 2-5. Time-dependent electric discharging and diffusion behavior in the 1E- to 4E-phages. Experimentally measured data is represented by filled markers, while calculated data is indicated by open markers. Reprinted with permission. Copyright 2021, American Chemical Society. 76

Figure 2-6. Intrinsic triboelectric potentials for the 1E- to 4E-phages were computed. The mean values from seven replicates are specified. Reprinted with permission. Copyright 2021, American Chemical Society. 77

Figure 2-7. Working principle of a Tribo-PhD. Reprinted with permission. Copyright 2021, American Chemical Society. 79

Figure 2-8. Triboelectric voltage observed during the contact and separation of the 1E-phage (bottom substrate) with the 1E- to 4E-phages (top substrate). Reprinted with permission. Copyright 2021, American Chemical Society. 79

Figure 2-9. Generation of Relative triboelectric voltage among different phage types. ΔN represents the disparity in glutamate numbers between the engineered phages at the top and bottom. Reprinted with permission. Copyright 2021, American Chemical Society. 80

Figure 2-10. The relative triboelectric charging characteristics of each phage in relation to other phage types (1E-4E-phages). Scale bar represents 5 seconds. Reprinted with permission. Copyright 2021, American Chemical Society..... 81

Figure 2-11. Extended semiempirical tight-binding calculations reveal the LUMO level of the pVIII coat protein in the 1E- to 4E-phages. Reprinted with permission. Copyright 2021, American Chemical Society. 82

Figure 2-12. The extended semiempirical tight-binding calculation results to show the LUMO level of the N-terminus peptides of the pVIII coat protein. The LUMO levels for AEGDP,

AEEGDP, AEEEGDP, and AEEEEDP are -7.14, -7.24, -7.32, and -7.44 eV, respectively. Reprinted with permission. Copyright 2021, American Chemical Society. 83

Figure 2-13. The relative triboelectrification of the 4E-phage in relation to traditional triboelectric materials such as nylon, polyethylene terephthalate (PET), polyimide (PI), polytetrafluoroethylene (PTFE), and perfluoroalkoxy (PFA). Reprinted with permission. Copyright 2021, American Chemical Society. 84

Figure 2-14. Schematic figure of a large-scaled Tribo-PhD. Reprinted with permission. Copyright 2021, American Chemical Society. 85

Figure 2-15. Output voltage and current of the Tribo-PhD. Reprinted with permission. Copyright 2021, American Chemical Society. 86

Figure 2-16. Switching polarity test on the Tribo-PhD. Output voltage (a) and (b) and current (c) and (d) were measured by connecting the probes in the opposite orientation to the Tribo-PhD, demonstrating the reverse polarity changes. Reprinted with permission. Copyright 2021, American Chemical Society. 86

Figure 2-17. Contrasting the impact of piezoelectricity and triboelectricity on the output voltages of a Tribo-PhD. (a) Output voltage of Tribo-PhD resulting from both piezoelectric and triboelectric sources. (b-c) Enlarged output voltage signals extracted from the black- and red-dashed boxes in Figure 2-16a. Reprinted with permission. Copyright 2021, American Chemical Society. 87

Figure 2-18. Output voltage and current observed across various external resistances, ranging from 10 k Ω to 1 GΩ, in the Tribo-PhD. Reprinted with permission. Copyright 2021, American Chemical Society. 87

Figure 2-19. Analysis of power density based on resistance reveals that the highest power density is attainable at 100 MΩ. Reprinted with permission. Copyright 2021, American Chemical Society. 88

Figure 2-20. Evaluation of the durability of the Tribo-PhD through a 10,000-cycle test. The mechanical durability assessment, conducted under a compressive force of 7.5 N and a frequency of 1.0 Hz, demonstrates outstanding stability and resilience in the Tribo-PhD. Reprinted with permission. Copyright 2021, American Chemical Society. 88

Figure 2-21. Triboelectric characterization of the Tribo-PhD in relation to humidity and temperature. (a) With an increase in humidity from 40 to 80 %, both voltage and current decreased from 76 to 52 V and from 5.1 to 2.9 μA, respectively. (b) With a temperature rise from 20 to 90 °C, the voltage and current decreased from 76 to 58 V and 5.1 to 2.9 μA, respectively. Reprinted with permission. Copyright 2021, American Chemical Society. 89

Figure 2-22. Charging characteristics of the Tribo-PhD device across various capacitors. Reprinted with permission. Copyright 2021, American Chemical Society. 89

Figure 2-23. Photographs of 30 LEDs connected to the Tribo-PhD. The images show the LEDs when the room light was switched on (left) and off (right). Reprinted with permission. Copyright 2021, American Chemical Society. 90

Figure 2-24. (a) Diagram illustrating the connections between the OLEDs and the Tribo-PhD. 8 OLEDs were linked in series to the Tribo-PhD. (b) Images capturing the operation of the OLEDs. All 8 OLEDs emitted light when manual compressive force was applied. The photos show the OLEDs in both illuminated (left) and non-illuminated (right) conditions with the room light on and off, respectively. Reprinted with permission. Copyright 2021, American Chemical Society. 90

Figure 3-1. Schematic diagram of the M13 phage and its piezoelectric properties. (a-b) The M13 phage has a non-centrosymmetric structure due to its five-fold rotational and two-fold screw symmetry of pVIII proteins. (c) Schematic representation of a pVIII protein. The formation of the net dipole moment from the N-terminal to the C-terminal is ascribed to the surface charge dipole moment and core dipole moment, which arise from the surface charges and the α-helical protein structure, respectively. 97

Figure 3-2. (a-c) The polarization of the phage reacts to diverse mechanical stresses, resulting in the manifestation of a directional piezoelectric effect. 99

Figure 3-3. Schematic representation of a piezoelectric tensor. 99

Figure 3-4. (a) and (b) The M13 phage structure with five-fold rotational and two-fold screw symmetry. (c) The structure of the M13 phage does not fit into the traditional crystallographic framework. 100

Figure 3-5. The calculated dipole moment of a 1 repeating unit (RU) of the M13 phage. ... 100

Figure 3-6. (a) The shift between the center of positive and negative charges within a pVIII protein. (b) and (c) The displacement of the charge center expands with the integration of negatively charged residues on the protein surface, leading to an elevation in the dipole moment. 101

Figure 3-7. (a-c) The change in the dipole moment of 1 RU in normal longitudinal, normal transverse, and shear orientations. 103

Figure 3-8. (a) The model of an unstrained 1 RU of the M13 phage. (b-d) The structural modifications in normal piezoelectric modes. (e-g) The structural adjustments in shear piezoelectric modes. 104

Figure 3-9. (a) Atomic configurations within the peptide bond. (b) Variations in atomic distance for the unstrained, vertical (normal longitudinal d33), horizontal (normal longitudinal d11), and shear d15 piezoelectric modes. The minimal changes in atomic distance suggest that the pVIII protein retains its structural integrity under mechanical stresses. 104

Figure 3-10. (a) Dihedral angles within the peptide bond. (b) Dihedral angle for the unstrained, vertical (normal longitudinal d_{33}), horizontal (normal longitudinal d_{11}), and shear d_{15} piezoelectric modes. The minimal changes in dihedral angle suggest that the pVIII protein retains its structural integrity under mechanical stresses. 105

Figure 3-11. The calculated piezoelectric coefficients for different piezoelectric modes for (a) normal longitudinal, (b) normal transverse, and (c) shear piezoelectric modes. 106

Figure 3-12. Diagram illustrating the setup of the EFM system used for dielectric constant characterization 112

Figure 3-13. (a) EFM image of the horizontally aligned WT-phage film. (b-c) Profiles indicating height and deflection along the dashed line in (a) for the horizontally aligned WT-phage film. (d) Dielectric constant of the WT-phage calculated from (b) and (c). (e) Dielectric constants computed for WT- and engineered phages. 113

Figure 3-14. Schematic of the EFM system used for surface charge density characterization. 114

Figure 3-15. (a) The frequency images of WT- and engineered phages. (b) Frequency profiles of the WT- and engineered phages from (a). 115

Figure 3-16. Calculated surface charge densities of the WT- and engineered-phages. Error bars indicate one standard deviation. 115

Figure 3-17. Isoelectric point calculations for WT- and engineered-phages. 116

Figure 3-18. Gel electrophoresis measurements for WT- and engineered-phages. 116

Figure 3-19. Zeta potential measurements for WT- and engineered-phages. 117

Figure 3-20. Comparison of PFM amplitude versus applied voltage for WT- and engineered phages along the normal longitudinal d33 piezoelectric mode. 118

Figure 3-21. Comparison of PFM amplitude versus applied voltage for WT- and 4E-phages along the normal longitudinal d11 piezoelectric mode. 119

Figure 3-22. Schematic representation of Piezo-PhD in shear orientation. 120

Figure 3-23. Output voltage and current measurement of Piezo-PhDs in different piezoelectric modes. Shear piezoelectric output was measured at tilted angle of 60°. 121

Figure 3-24. Shear output voltage measurements of Piezo-PhDs. (a) Shear output voltage of Piezo-PhDs at different tilted angles. (b) Calculated shear output voltage from (a). (c) Comparison of piezoelectric output voltage among vertical, shear, and horizontal modes. . 122

Figure 3-25. Shear output current measurements of Piezo-PhDs. (a) Shear output current of Piezo-PhDs at different tilted angles. (b) Calculated shear output current from (a). (c) Comparison of piezoelectric output current among vertical, shear, and horizontal modes. 123

Figure 3-26. (a) and (b) Schematic of piezoelectric output characterization measurement setup. (c) Photograph of a Piezo-PhD. 124

Figure 3-27. Working principle of a Piezo-PhD. Upon applying mechanical force to the piezoelectric device based on phages, the polarization of the phages undergoes a shift. Consequently, electrons migrate through the external conductive wire to establish electrical equilibrium. 124

Figure 3-28. Application of mechanical force to the Piezo-PhD and the resultant generation of voltage and current. 125

Figure 3-29. Polarity switching test on the Piezo-PhD. Output voltage (a) and (b) and current (c) and (d) were recorded by connecting the probes in the opposite orientation to the Piezo-PhD, presenting the reverse polarity changes. 126

Figure 3-30. Output voltage and power density observed across various external resistances, ranging from 120 kΩ to 1 GΩ, in the Piezo-PhD. 126

Figure 3-31. Charging characteristics of the Piezo-PhD device across various capacitors. .. 127

Figure 3-32. Photographs of 22 light-emitting diodes illuminating by the operation of the Piezo-PhD. 127

Figure 4-1. (a) Schematic diagram of the M13 phage and its pyroelectric properties. (b) and (c) The M13 phage has a non-centrosymmetric structure due to its five-fold and two-fold screw symmetry of pVIII proteins. Additionally, the M13 phage has a spontaneous polarization due to the intrinsic dipole moment of the pVIII protein. Reprinted with permission. Copyright 2023, Advanced Materials. 134

Figure 4-2. The α-helical protein structures of the pVIII protein impart it with inherent polarization. When the secondary structure transitions from an α-helix to a random coil, the spontaneous polarization diminishes. Reprinted with permission. Copyright 2023, Advanced Materials. 134

Figure 4-3. Schematic diagram of a vertically standing M13 phage film. Through the implementation of specific binding between the pIII proteins and the substrate using 6H-Ni-NTA, the phage film demonstrates a unidirectional arrangement of spontaneous polarization (P_s). Reprinted with permission. Copyright 2023, Advanced Materials. 135

Figure 4-4. AFM topographic image of a vertically standing phage film. The height of the phage film aligns closely with the length of an individual phage, as illustrated by the red dotted lines. Reprinted with permission. Copyright 2023, Advanced Materials. 136

Figure 4-5. Individual phage length profiles for both wild-type and engineered phages. All phages exhibited a length of approximately 980 nm with minimal variations. Reprinted with permission. Copyright 2023, Advanced Materials. 136

Figure 4-6. KPFM surface potential images of a vertically standing phage film. The surface potential of the phage film demonstrates a consistent electric potential throughout its surface, as highlighted by the red dotted lines. Reprinted with permission. Copyright 2023, Advanced Materials. 137

Figure 4-7. Surface roughness characterization of vertically standing phage films. The variation of the roughness for different phage types was negligible. Reprinted with permission. Copyright 2023, Advanced Materials. 137

Figure 4-8. Young's modulus characterization of vertically standing phage films. The variation of the Young's modulus for different phage types was negligible. Reprinted with permission. Copyright 2023, Advanced Materials. 138

Figure 4-9. AFM height profile images and FT-IR spectra of vertically standing phage films. AFM height images and profiles of vertically standing phage were created using phage concentrations of (a) and (d) 1 mg mL^{-1}, (b) and (e) 15 mg mL^{-1}, and (c) and (f) 30 mg mL^{-1}.

Schematic representations of the phages illustrate their potential orientations within the films. (g) FT-IR spectra of the vertically standing phage film on gold substrates, corresponding to the concentrations indicated in AFM images (a-f). (h) FT-IR spectra of the 1E-, 2E-, 3E-, 4E-, and WT-phage films prepared using a phage concentration of 30 mg mL^{-1}. Reprinted with permission. Copyright 2023, Advanced Materials. 138

Figure 4-10. Surface potential representation of a vertically standing phage film without the application of heat using KPFM. The associated profiles of pyroelectric potential, temperature, and temperature variation rate for the phage film are graphed. Reprinted with permission. Copyright 2023, Advanced Materials. 140

Figure 4-11. KPFM image of a 4E-phage film while subjected to heat. The accompanying profiles illustrate the pyroelectric potential, temperature, and temperature variation rate of the phage film. Reprinted with permission. Copyright 2023, Advanced Materials. 141

Figure 4-12. Pyroelectric assessment of M13 phage with randomly organized structures. (a) Illustration of the pyroelectric characterization using KPFM. By applying a 4E phage solution on Ni-NTA coated Au films, we generated randomly oriented phage films with minimal net polarization. (b) KPFM images of a randomly oriented phage film, showing the surface potential of the 4E phage film (a) without heat application and (b) under heat application at a temperature variation rate of 1.14 ℃ min^{-1}. (c) The pyroelectric potential of the phage film depicted in (b). The corresponding profiles of pyroelectric potential, temperature, and temperature variation rate for the phage film are illustrated. The pyroelectric potential is negligible due to the randomly aligned polarization of the phage film. Reprinted with permission. Copyright 2023, Advanced Materials. 142

Figure 4-13. Pyroelectric potentials of various phage films under heat exposure with a temperature variation rate of 1.08 ℃ min^{-1}. Reprinted with permission. Copyright 2023, Advanced Materials. 142

Figure 4-14. Pyroelectric potentials exhibited by different types of phage films in response to diverse temperature fluctuations. Reprinted with permission. Copyright 2023, Advanced Materials. 143

Figure 4-15. Temperature-dependent polarization change in the M13 phage. (a) MD simulated structures of a pVIII protein at 300 K and 350 K. The unfolding of the α-helical structure of the pVIII protein leads to a reduction in the polarization of the M13 phage. (b) MD results depicting the temperature-dependent dipole moment of an individual pVIII protein. Reprinted with permission. Copyright 2023, Advanced Materials. 145

Figure 4-16. Assessment of the quantity of hydrogen bonds existing within the loops of the pVIII protein. With the rise in temperature, the number of hydrogen bonds steadily diminished, attributed to the structural transformation from α-helices to random coils. Reprinted with permission. Copyright 2023, Advanced Materials..... 146

Figure 4-17. Determination of the dipole moment of the M13 phage at temperatures of 300 K and 350 K. Dipole moments were computed in supramolecular structures with escalating repeating units. The dipole moment exhibited a consistent decrease with increasing

temperature. 0 repeating unit signifies a single pVIII protein. Reprinted with permission. Copyright 2023, Advanced Materials. 146

Figure 4-18. Variation in the spacing between the loops of the pVIII protein based on temperature. The change in the polarization of the M13 phage is attributed to the modification in the secondary structure of the major coat proteins, rather than a thermal expansion effect in these proteins. Reprinted with permission. Copyright 2023, Advanced Materials. 147

Figure 4-19. Circular dichroism spectra of the WT-phage exhibiting a temperature-dependent structural transition from an α-helix to a random coil configuration during heating. Reprinted with permission. Copyright 2023, Advanced Materials. 148

Figure 4-20. Temperature-dependent CD spectra of the wild-type M13 phage illustrating the shift from an α-helix to a random coil configuration during heating. Additionally, CD spectra for various genetically engineered phages are depicted: (a) 1E phage, (b) 2E phage, (c) 3E phage, (d) 4E phage, and (e) YEEE phage. The CD spectra reveal the structural transformation from an α-helix to a random coil for each type of phage. Reprinted with permission. Copyright 2023, Advanced Materials. 149

Figure 4-21. CD spectra of the M13 phage. (a) Changes in the CD signal during the heating process. (b-d) CD spectra at specific wavelength regions (193, 208, and 222 nm), revealing a decrease in the α-helical structural feature of the pVIII protein. (e) The CD signal during the cooling phase. (f-h) CD spectra at typical wavelength regions (193, 208, and 222 nm), illustrating a restoration of the α-helical structural characteristic of the pVIII protein to its initial state. These findings indicate a reversible structural transformation. Reprinted with permission. Copyright 2023, Advanced Materials. 150

Figure 4-22. DLS analysis during the heating and cooling sequences. The DLS results indicate the absence of phage aggregation during both the heating and cooling phases. DLS characterization of the M13 phage was conducted in a Tris buffer (12.5 mM Tris and 37.5 mM NaCl) at (a) 20 ℃, (b) 25 ℃, and (c) 30 ℃. Despite minimal adjustments in particle size throughout the heating and cooling procedures, alterations were observed in the CD signal at 222 nm. Reprinted with permission. Copyright 2023, Advanced Materials. 151

Figure 4-23. Pyroelectric characterization of a Pyro-PhD. Schematic diagram depicting the generation of pyroelectric potential. Schematic illustration outlining the pyroelectric characterization of a vertically standing Pyro-PhD through NIR laser thermal stimulation. Reprinted with permission. Copyright 2023, Advanced Materials..... 152

Figure 4-24. UV-vis spectra of M13 phages. The absorbance at the wavelength of 808 nm is minimal. Reprinted with permission. Copyright 2023, Advanced Materials. 153

Figure 4-25. Temperature fluctuation generated by a NIR laser (808 nm) with a square function. Reprinted with permission. Copyright 2023, Advanced Materials. 154

Figure 4-26. (a) Temperature profile under laser irradiation. (b) Temperature variation rate under laser irradiation. Reprinted with permission. Copyright 2023, Advanced Materials. . 154

Figure 4-27. (a) Output voltage of the Pyro-PhD. (b) Output current of the Pyro-PhD. Reprinted with permission. Copyright 2023, Advanced Materials.....155

Figure 4-28. (a) Output voltage of the Pyro-PhD under different NIR intensities. (b) Output current of the Pyro-PhD under varying NIR intensities. Reprinted with permission. Copyright 2023, Advanced Materials. 155

Figure 4-29. Temperature variation rates of the Pyro-PhD under varying levels of NIR intensity irradiation. Reprinted with permission. Copyright 2023, Advanced Materials. 156

Figure 4-30. Pyroelectric analysis of a randomly aligned Pyro-PhD during infrared heating. (a) Diagram illustrating the pyroelectric characterization of a randomly aligned Pyro-PhD under NIR laser thermal stimulation. (b) Temperature fluctuations induced by a NIR laser with a square function. (c) and (d) Temperature and temperature variation rate during laser application. (e) and (f) Output voltage and current of the Pyro-PhD. Reprinted with permission. Copyright 2023, Advanced Materials. 156

Figure 4-31. Durability test of the Pyro-PhD for 3000 cycles. Reprinted with permission. Copyright 2023, Advanced Materials. 157

Figure 4-32. Configuration for molecular sensing experiments employing Pyro-PhDs. A Pyro-PhD is enclosed within a cage, and the introduction of target VOCs is regulated using MFCs.....158

Figure 4-33. Pyroelectric response of YEEE Pyro-PhD under different levels of relative humidity. Reprinted with permission. Copyright 2023, Advanced Materials. 159

Figure 4-34. Pyroelectric response of YEEE Pyro-PhD to diverse VOCs as a means for sensing different polarities. Reprinted with permission. Copyright 2023, Advanced Materials. 160

Figure 4-35. Pyroelectric response of WHW Pyro-PhD to various VOCs, enabling the detection of differing polarities. Reprinted with permission. Copyright 2023, Advanced Materials. 160

Figure 4-36. Pyroelectric response of WHW Pyro-PhD under different levels of xylene. Reprinted with permission. Copyright 2023, Advanced Materials.....161

Figure 4-37. Pyroelectric response of WHW Pyro-PhD to various aromatic hydrocarbons. Reprinted with permission. Copyright 2023, Advanced Materials.....161

Figure 4-38. Pyroelectric response of YEEE Pyro-PhD to various aromatic hydrocarbons. Reprinted with permission. Copyright 2023, Advanced Materials.....162

Figure 4-39. MD simulated dipole moment of the YEEE-pVIII protein model in the presence of different hydrophilic VOCs. The change in hydrogen bonds between the loops of the YEEE-pVIII protein and the change in dipole moment of the pVIII protein are observed from 300 to 350 K. Reprinted with permission. Copyright 2023, Advanced Materials.....163

Figure 4-40. MD simulations were employed to determine the dipole moment of the WHW-pVIII protein model in the presence of different VOCs. The analysis considered the changes in hydrogen bonds between the loops of the WHW-pVIII protein and the changes in the

dipole moment of the pVIII protein across the temperature range from 300 to 350 K. Reprinted with permission. Copyright 2023, Advanced Materials..... 163

Figure 5-1. Schematic diagram of the different electrical characteristics of the M13 phage in response to different external stimuli: Piezoelectricity (mechanical stress), pyroelectricity (temperature change), and triboelectricity (contact)..... 169

List of tables

Table 1. Electrical characteristics of amino acids, including piezoelectric coefficient, *d* (pC N^{-1}), pyroelectric coefficient, *p* (μC m^{-2} K^{-1}), coercive field, E_c (GV m^{-1}), and electrical outputs of the device. Matrices in the table represent the piezoelectric tensor of the material. 43

Table 2. Electrical characteristics of amino acids, including piezoelectric coefficient, *d* (pC N^{-1}), pyroelectric coefficient, *p* (μC m^{-2} K^{-1}), coercive field, E_c (GV m^{-1}), and electrical outputs of the device. Matrices in the table represent the piezoelectric tensor of the material. 49

Table 3. Electrical characteristics of amino acids, including piezoelectric coefficient, *d* (pC N^{-1}), pyroelectric coefficient, *p* (μC m^{-2} K^{-1}), coercive field, E_c (GV m^{-1}), and electrical outputs of the device. Matrices in the table represent the piezoelectric tensor of the material. 61

Table 4. Primary structures for pVIII proteins[1]. Reprinted with permission.[2] Copyright 2021, American Chemical Society 72

Table 5. The coordinates of the center of negative and positive charges 101

Table 6. Dipole moment calculation for normal piezoelectric mode under mechanical stimulation in 3-axis direction. 107

Table 7. Dipole moment calculation for normal piezoelectric mode under mechanical stimulation in 1-axis direction. 108

Table 8. Dipole moment calculation for normal piezoelectric mode under mechanical stimulation in 2-axis direction. 108

Table 9. Dipole moment calculation for normal piezoelectric mode under mechanical stimulation in 4-axis direction. 109

Table 10. Dipole moment calculation for normal piezoelectric mode under mechanical stimulation in 5-axis direction. 109

Table 11. Dipole moment calculation for normal piezoelectric mode under mechanical stimulation in 6-axis direction. 110

Table 12. Calculation of piezoelectric coefficient of the M13 phage in various piezoelectric modes. 110

Table 13. Calculation of the frequency shifts of the M13 phage. 117

Table 14. Calculation of the surface charge density of the M13 phage. 117

Table 15. Primary structures for pVIII and pIII proteins[1,3]. 119

Table 16. Pyroelectric coefficient of known pyroelectric biomaterials. Reprinted with permission.[3] Copyright 2023, Advanced Materials 144

Table 17. Primary structures for pVIII proteins[4,5]. Reprinted with permission.[3] Copyright 2023, Advanced Materials 158

Table 18. Relative polarity of surrounding solvents. Reprinted with permission.[3] Copyright 2023, Advanced Materials 159

CHAPTER 1: INTRODUCTION

1.1 Advances in bioelectricity

The bioelectricity has developed from the observation of "animal electricity", known as the electric generation from the eel and the torpedo (electric ray).[6] Subsequently, animal electricity garnered interest, leading Luigi Galvani to demonstrate an experiment using frog fragments connected to metals to observe muscle contraction, presenting significant curiosities in bioelectrical phenomena.[7] Bioelectricity involves the generation of electrical potential and activity in biological systems.[8] The growing interest in bioelectricity originates from the development of biotechnology, which seeks to understand natural physiological processes and apply them to develop biomedical applicati ons and address energy challenges.[9-14] Biological materials hold promise for bioelectrical applications due to their inherent biocompatibility, making them suitable for bioelectronics and biomedicine.[15] Advancing bioelectricity requires understanding the mechanisms generating bioelectrical signals at the molecular level.[16] While energy conversion mechanisms in conventional materials are well-studied,[17-20] the complexity of bioelectricity arises from the intricacy and heterogeneity of biomaterials, whose electrical response mechanisms are not fully understood.[21-24] Hierarchically organized self-assembled nanostructures in biological materials result in electric dipole structures, significantly influencing their electrical properties and functionalities. These materials respond to external stimuli like mechanical stress, temperature, and electric fields, producing bioelectric potentials.[25,26] These materials respond to external stimuli, such as mechanical stress, temperature, and electric field, producing bioelectric potentials. Understanding the structure-function relationships in these materials can develop material properties to enhance energy conversion efficiency or discover new properties.

Extensive research spanning decades has focused on understanding how biological materials respond electrically, employing an array of advanced experimental tools and computational methods.[25,27-32] These tools include impedance analyzers, polarization-electric field (P-E) ferroelectric testers, dielectric spectroscopy, X-ray diffraction, Fourier-transform infrared spectroscopy, X-ray photoelectron spectroscopy (XPS), and scanning probe microscopy (SPM). Their use enables the study of both the electrical and chemical structural properties of biological materials. This comprehensive approach offers several advantages, including the ability to characterize biological materials comprehensively with complementary information across different scales, from molecules to tissues. Additionally, it enhances precision in understanding their electrical properties.[33-39] For example, SPM techniques allow researchers to visualize and analyze electrical phenomena, such as polarization, electric charge distribution, surface potential, dielectric constant, conductivity, and capacitance.[40-44] This capability is essential for deciphering the complex electrical behavior of biological systems at the nanoscale, where many critical biological processes occur.

Recent advancements in computational tools have significantly improved our understanding of how biological materials behave electrically. Techniques such as molecular dynamics (MD) simulations, finite element analysis, and density functional theory (DFT) have enabled the simulation of biological components ranging from amino acids to tissue levels.[29,45-47] These tools allow for the optimization of molecular structures under specific environmental conditions, such as varying ion concentrations, pressures, temperatures, and surrounding molecules.[3,48] Moreover, they facilitate the simulation of various electrical properties of biological materials, including energy levels, dipole moments, charge and electron distribution, electrical potential generation, conformational deformation, and molecular interactions.[2,3,47] Additionally, these simulations can reproduce responses to a variety of external stimuli, such as mechanical stresses, thermal fluctuations, optical stimulations, acoustic stimulations, and electric field applications.[29,31,49-52] Consequently, computational analyses help model intricate biological structures and systems, deepening our understanding of their underlying mechanisms and predicting their behavior under challenging experimental conditions.[53-55]

The integration of experimental and computational approaches deepens our understanding of the molecular mechanisms that govern the electrical behaviors of biological materials, bridging the gap between experimental observations and theoretical insights.[2,3,56] However, the complexity of building structures, combined with the heterogeneity found in biological tissue samples, poses a challenge in applying traditional electrical principles to biological systems.[57,58] This challenge leads to limitations in both experimental and computational analyses of comprehensive electrical characteristics. Therefore, establishing suitable biological model systems is crucial for gaining insights into molecular-level electrical characteristics within biological systems and for advancing bioelectrical applications.[59,60] These model systems, with their well-defined and adjustable structures, ability to control distinct electric dipole and polarization ordering, and capacity for precise manipulation of electrical characteristics at the molecular level, along with a range of nanostructure attributes, would be immensely valuable for advancing our understanding of the electrical properties of biological materials.

1.2. Electrical properties of materials

Electrical properties pertain to how materials interact with electric currents, generate electric charge, or respond to electric fields. Biological materials, due to their unique compositions and structures, exhibit a wide range of electrical properties. For example, tissues like muscle and nerve have intrinsic electrical conductivity, crucial for transmitting essential electrical signals.[61,62] Parameters defining these properties include conductivity, dielectric constant, and electrochemical behavior. While biological tissues generally have low conductivity (0.03-0.6 S m^{-1} for ventricular muscle, nerve, lung, cardiac, and skeletal muscle) due to being composed of amino acids, which are not inherently conductive, proteins—composed of amino acids—can indirectly influence electrical properties.[63] Proteins are

primarily composed of elongated chains of amino acids that fold into complex three-dimensional structures.[64] While some amino acids have polar or charged side chains, the overall protein structure does not promote efficient electron flow or electrical conductivity.[65] Despite this, proteins can indirectly impact the electrical properties of biological systems. For example, membrane proteins such as ion channels transport charged ions, influencing the electrical potential across cellular membranes.[66] However, proteins typically do not exhibit significant electrical conductivity in their pure form and are considered insulating materials. The ability to understand and control the electrical properties of biological materials holds promise for advancing biomedical technologies, including diagnostic tools and therapeutic interventions.[67,68] This section focuses specifically on the stimuli-responsive electrical properties of biomaterials, such as triboelectricity, piezoelectricity, pyroelectricity, and ferroelectricity (Figure 1-1).

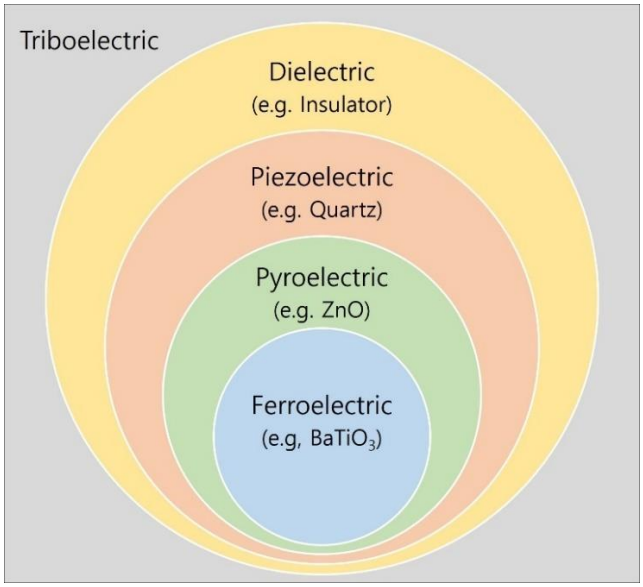

Figure 1-1. Hierarchical relationship among various subgroups of materials.

1.2.1 Triboelectricity

Triboelectrification is the phenomenon where specific materials acquire an electric charge when they come into contact and separation (Figure 1-2a).[69,70] An everyday example of triboelectricity is the creation of an electricity when brush our hair with a comb or grabbing a doorknob with hand. The ancient Greeks recognized this phenomenon more than 2500 years ago when they observed that rubbing amber could attract straw[71]. The word "electron" itself is derived from the Greek word for amber, emphasizing the historical importance of this electrical phenomenon. This phenomenon is universal to all materials and is originated in the exchange of electrons between them. When two dissimilar materials make contact, electron transfer is

driven by differences in their electronic structures – energy levels – resulting in different electron affinity and ionization energy.[72,73] Each material inherently tends to either accept or donate electrons, a characteristic highlighted in the triboelectric series (Figure 1-2b).[72,73] As materials interact, electrons transfer from a material with a preference for donating electrons (low work function) to one with a preference for accepting electrons (high work function).[74-77] Hence, the manipulation of the triboelectric effect is achievable through the careful choice of triboelectric materials, emphasizing the significance of material selection.[73,78] Enhancing the triboelectric effect is most efficiently achieved by identifying the optimal pair of materials with positive and negative properties in the triboelectric series. However, the underlying mechanisms are still under investigation and require additional theoretical and experimental validation.[79-88] Biological materials exhibit diverse capabilities in electron donation and acceptance, which stem from the presence of various charged groups or structures within them. These materials play a vital role in biological systems by engaging in triboelectric interactions, which regulate numerous natural biological functions and processes.[2] For instance, bumblebees facilitate flow pollination, immune cells combat pathogens, and viruses invade host cells.[89-92]

The triboelectric properties of materials have been extensively studied for practical applications, particularly in the advancement of energy harvesting systems.[42,52,93-96] Triboelectric energy harvesting devices use the triboelectric effect for the conversion of mechanical energy into electrical energy. The first triboelectric device, as reported by Wang et al. in 2012[97], comprised two triboelectric layers with electrodes affixed at the backside. During the subsequent contact and separation, the triboelectric layers acquire positive and negative charges, and electrons flow through an external circuit to equalize the electrical equilibrium, thus generating an electric current. This electron flow constitutes the electrical output of triboelectric devices. Triboelectric devices demonstrate versatility in harnessing various types of energy sources. Triboelectric devices can be used for environmental monitoring by harvesting mechanical energy from wind and ocean waves.[98-109] By integrating triboelectric devices into the infrastructure of buildings, bridges, or industrial machinery, they can also serve for structural safety monitoring.[110-114] Additionally, the incorporating these devices into vehicle components contributes to harvesting wasted mechanical energy and using it as a sustainable energy source for transportation systems.[115-117] Furthermore, triboelectric devices can be integrated into wearable applications to harvest mechanical energy from the body movements or monitor healthcare systems.[95,96,118-123] Since triboelectric devices can be operated by vibrations generated by ultrasound waves, they can be implanted in our bodies and used as biomedical sensors.[124-127] This adaptability and efficiency highlight the significant potential of triboelectric devices in shaping a variety of self-powered and sustainable technologies.

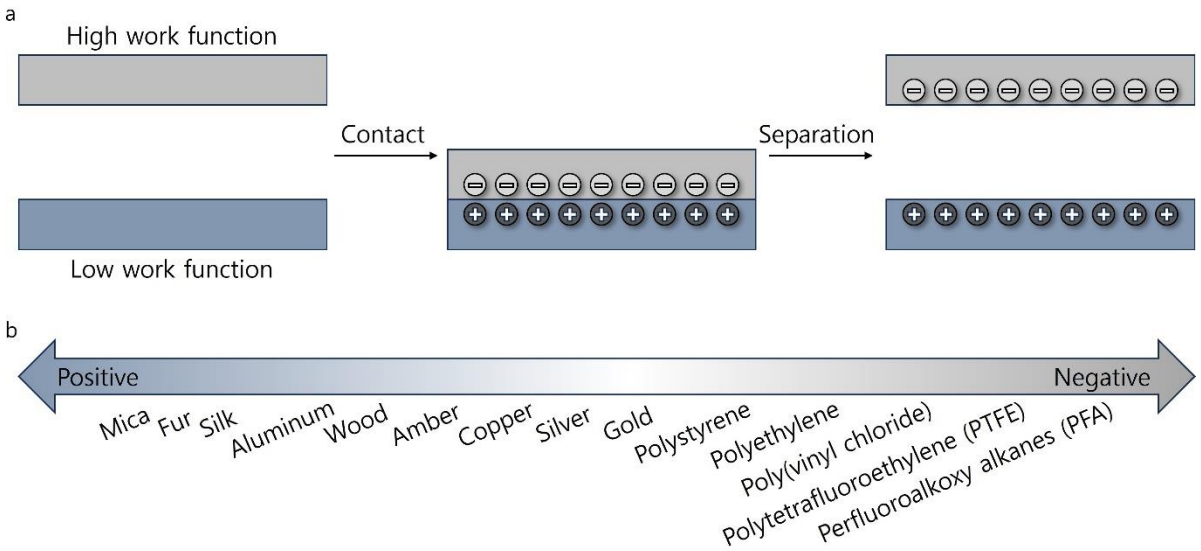

Figure 1-2. (a) Working principle of the triboelectric effect. The triboelectric effect is a phenomenon related to the generation of electric charge through the contact and separation of materials. It involves the transfer of electrons between two materials, resulting in one material acquiring a positive charge while the other acquires a negative charge. (b) Triboelectric series of conventional materials. The triboelectric series is a list that ranks materials based on their tendency to gain or lose electrons when in contact with other materials. The materials at the left of the series have a lower affinity for electrons, while those at the right have a higher affinity.

1.2.2 Dielectric

Dielectric materials have the capacity to store electrical energy when exposed to an electric field (Figure 1-3).[128] Once an external electric field is applied to a dielectric material, electric dipoles align inside the dielectric material.[129,130] The internal polarized molecule shifts from its original equilibrium state to one with higher potential energy, allowing temporary energy storage of external power source energy.[131,132] Then, when the external electric field is removed, the internal polarized molecules recover their alignment to their original states. This change in polarization of the internal molecules can be used for electric charging and discharging. The charging and discharging capability of dielectric materials can be employed as a capacitor for storing electrical energy. Therefore, enhancing the capacity of electrical storage in dielectric materials is crucial. Notably, the degree of dipole alignment of polarized molecules is affected by the strength of the external electric field, and precise electric field strength optimization should be considered due to irreversible characteristics at certain threshold points.[131,133] Thus, the capability of energy storage in dielectric materials should be carefully optimized to prevent material destruction by current leakage and a loss of energy storage capacity, requiring a profound understanding of materials properties.[134-136] In general, the efficiency of material in storing energy is equally significant to its energy storage

density.[137,138] Typically, enhancing the energy storage efficiency of dielectrics leads to reduced energy loss and improved reliability.[139-141] Several approaches have been extensively explored to improve the energy storage density in film capacitors. The energy storage density of materials can be enhanced by either increasing the dielectric constant through methods like polarity enhancement and organic-inorganic hybridization or enhancing the field strength of materials through techniques such as blending, hybridization, and the design of multilayer structures.[142-150]

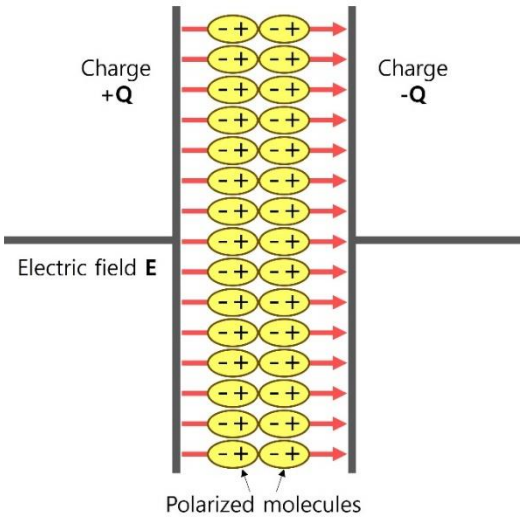

Figure 1-3. Dielectric properties in materials. When an electric field is applied to a dielectric, the electric charges within the material do not move freely as there are not loosely bound or free electrons available for drifting. Instead, they undergo a slight shift from their average equilibrium positions, leading to dielectric polarization.

1.2.3 Piezoelectricity

Piezoelectric materials can generate an electric charge in response to mechanical stress or deformation and vice versa (Figure 1-4).[151] In 1880, Jacques Curie and Pierre Curie observed electric charge generation on quartz, tourmaline, and Rochelle salt upon the application of pressure, a phenomenon known as piezoelectricity.[152] The term “piezoelectricity”, originating from the Greek word “piezein”, meaning ‘to press’, refers to the generation of electricity under pressure.[153] Following this discovery, they developed the piezoelectric quartz electrometer, a device capable of measuring the surface charges that appear on crystals when subjected to mechanical stress, enabling measurements down to tenths of a picoampere.[154,155] Since then, the piezoelectric effect has been extensively studied in crystallographic frameworks, classifying materials based on their crystal symmetry.[156-160] Particularly, the piezoelectric effect arises from certain materials lacking inversion symmetry. When mechanical stress is applied

to a piezoelectric material, the crystal lattice is deformed, leading to creation of an internal electric dipole moment. Piezoelectricity is exhibited by any material, including biological materials, that meets this structural criterion. Due to their symmetric structure, piezoelectric materials demonstrate anisotropic piezoelectric properties, which are characterized by a piezoelectric tensor (Figure 1-5). This tensor defines how mechanical stress relates to electric field in the material, encompassing longitudinal/transverse and normal/shear piezoelectric modes. The components of a piezoelectric tensor are the piezoelectric coefficients of 18 different modes, denoted as d_{ij}, where i is the direction of the induced polarization, and j is the direction of the applied stress. Longitudinal piezoelectricity (d_{ij}, where $i=j$) refers to the generation of an electric field along the same axis as the applied stress, while transverse piezoelectricity (d_{ij}, where $i \neq j$) involves the generation of an electric field perpendicular to the applied stress. Normal piezoelectricity is exhibited by materials that respond to stress in the axial direction, while shear piezoelectricity is observed in materials that respond to twist stress. The presence of piezoelectricity in biological materials plays a critical role in several biological functions. For example, in bone, mechanical stress induces piezoelectric potentials, which in turn stimulate osteoblasts. This stimulation influences the balance between bone formation and resorption, a vital process for bone remodeling and its ability to adapt to mechanical stress.[161,162] Additionally, piezoelectricity in tissues such as tendons and cartilage is essential for preserving tissue integrity and function. These tissues can sense mechanical stresses and regulate cellular responses accordingly.[163] A thorough understanding of piezoelectricity in crystallographic classification provides methods to enhance the piezoelectric properties, including poling[164-166], doping[167-169], grain size control[170-172], temperature and pressure treatments.[173-175] Additionally, computational modeling guides the optimization process, allowing for the prediction and understanding of piezoelectric properties, contributing to the advancement of technologies such as sensors, actuators, and energy harvesters.[176-178] Piezoelectric materials serve as versatile components in mechanical energy conversion applications.[179-182] These materials can be used for sensors and actuators by converting mechanical energy into electrical energy vice versa.[183-186] Additionally, piezoelectric materials can be integrated into piezoelectric energy harvesters for operating electronic devices and sensors.[187,188] Moreover, these devices can be integrated into wearable and implantable devices to harvest and monitor mechanical energy from body movements, serving as self-powered energy harvesters and sensing systems.[189-194]

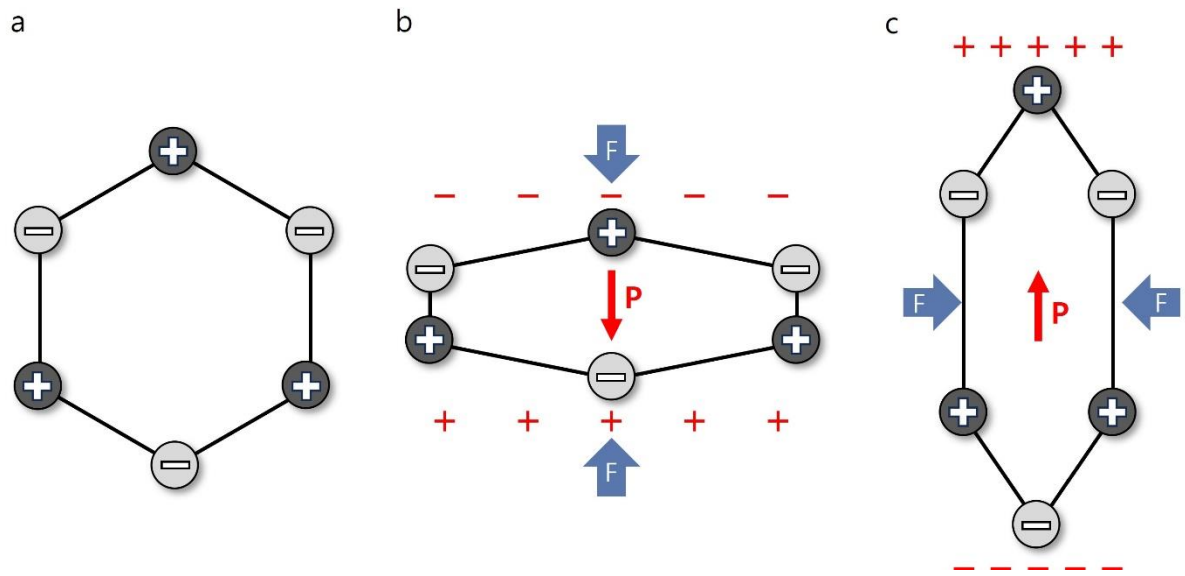

Figure 1-4. Working principle of the piezoelectric effect. When mechanical stress is applied to a piezoelectric material, it causes a deformation in the crystal lattice. This deformation leads to a displacement of positive and negative charges within the material, creating an internal electric dipole moment. The movement of charges results in the separation of positive and negative charges, breaking its electrical equilibrium.

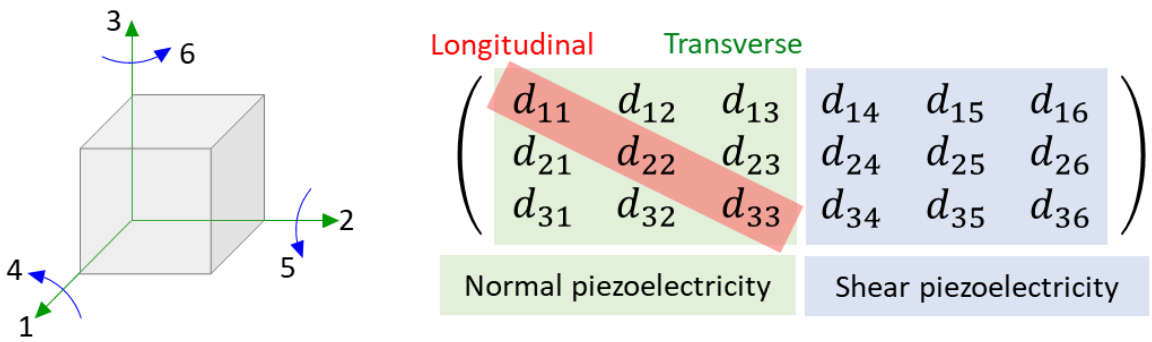

Figure 1-5. Schematic representation of a piezoelectric tensor. A piezoelectric tensor described the relationship between mechanical stress and electrical polarization in a material.

1.2.4 Pyroelectricity

Pyroelectric materials can generate electric charge in response to changes in temperature (Figure 1-6).[195] The term "pyroelectricity", derived from the Greek word "pyr", meaning "fire", denotes the generation of electricity under heat fluctuations. In the 1880s, Jacques Curie and Pierre Curie demonstrated pyroelectricity in tourmaline and quartz.[196] This pyroelectric effect is observed in materials lacking inversion symmetry and exhibiting

spontaneous polarization.[197] When these pyroelectric materials experience temperature variations, especially changes in temperature gradients or thermal fluctuations, they can develop temporary electric polarization.[198,199] During thermal fluctuations, the orientation of the electric dipole undergoes increased randomness and freedom, resulting in enhanced oscillation.[200] This change in the orientation of electric dipoles alters the distribution of electric charges within the crystal lattice, leading to the generation of an electric potential across the material.[201] Biological materials respond to temperature changes through structural changes or the breaking of weak bonds, such as hydrogen bonds, van der Waals interactions, hydrophobic interactions, and electrostatic interactions. These disruptions affect the alignment of electric dipoles within the material, leading to a pyroelectric response. Therefore, many biological materials, including bone, tendon, skin, collagen, silk, keratin, viruses, and others, exhibit pyroelectric properties. Improving the pyroelectric properties of materials requires a comprehensive and varied strategy, including temperature treatment[202,203], doping[204-206], and electric field applications.[207,208] These methods enhance pyroelectric performance by improving electric dipole orientations. Pyroelectric materials are widely used for various energy conversion and energy storage technologies. These materials are applicable to infrared sensors and thermal imaging devices, converting thermal radiation into electrical signals for diverse applications such as surveillance and medical diagnostics.[209-216] Additionally, they can be employed for ambient energy harvesting, where temperature fluctuations induce electric polarization, offering a sustainable source for low-power devices.[217,218] These devices can be integrated to harvest thermal energy from human body for wearable and healthcare applications.[219,220]

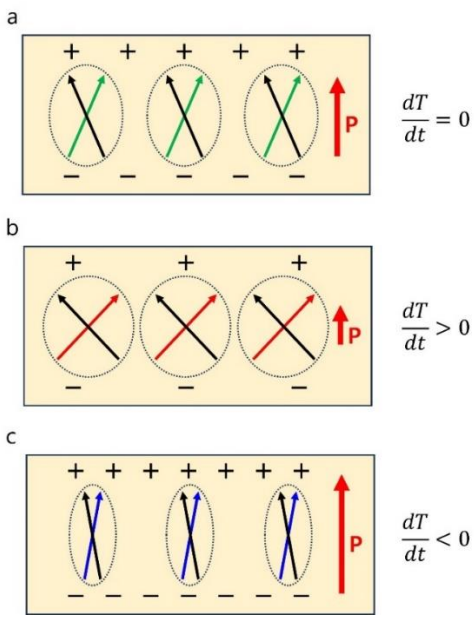

Figure 1-6. Working principle of the pyroelectric effect. Pyroelectric materials exhibit a change in their electric polarization in response to temperature fluctuations. Pyroelectric materials

exhibit a spontaneous electric polarization due to the arrangement of charges within the crystal lattice. Under the application of heat fluctuations, theses electric polarization oscillates, leading to the redistribution of electric state of the material.

1.2.5 Ferroelectricity

Ferroelectric materials exhibit spontaneous polarization that can be reversed by an external electric field (Figure 1-7).[221,222] Ferroelectricity requires a crystallographic structure lacking a center of symmetry and exhibiting a spontaneous polarization.[223-225]. Ferroelectric materials have domains with distinct polarization within their structures.[226,227] Upon the application of an external electric field, the polarization in the domains aligns with the electric field direction to varying degrees, following a hysteresis loop.[228,229] Specifically, the typical characteristics of ferroelectric materials is that this polarization can be reversed and maintain its reversed polarization even when the electric field is removed.[230,231] Additionally, remanent polarization, which is the electric polarization that remains in a ferroelectric material after the external electric field is removed, contributes to the ferroelectric behavior of the material, making it a crucial factor for various ferroelectric applications.[232] Amino acids possess intrinsic dipole moments originating from their partial positive amino- and negative acid-groups. These amino acids serve as basic building blocks for peptides, proteins, and many proteinaceous tissues. Typically, the orientation of dipole moments can be manipulated by an external electric field, while weak interactions can transiently stabilize their metastable configurations within local structures. Therefore, certain crystals or ordered structures of biological materials can exhibit ferroelectricity, such as cortical bone tissue, aorta, and elastin.[31,233-235] Enhancing ferroelectric performance of ferroelectric materials requires strategies, including doping[236,237], alloying[238], poling[239,240], and controlling the material fabrication process.[241] Additionally, recent advancements in characterization tools (e.g., piezoresponse force microscopy (PFM), X-ray diffraction (XRD)) and computational methods provided in-depth analysis on ferroelectric materials and their behaviors.[242-249] Ferroelectric materials are widely used in memory devices, specifically for "writing, reading, and erasing" based on the unique property of ferroelectricity.[250-252] Basically, the writing process involves applying an external electric field to induce a change in polarization direction, allowing for the storage of information.[253] Ferroelectric materials retain stored data even after the removal of the external electric field.[231] By applying a smaller electric field, the stored data can be read based on the resulting voltage direction.[254] Additionally, the stored data can be erased by applying an external electric field in the opposite direction to the writing process.[255] These dynamic ferroelectric characteristics make ferroelectric memory devices versatile for various memory devices.[256-263] These diverse applications highlight the versatility of ferroelectric materials in shaping the landscape of energy conversion technologies.

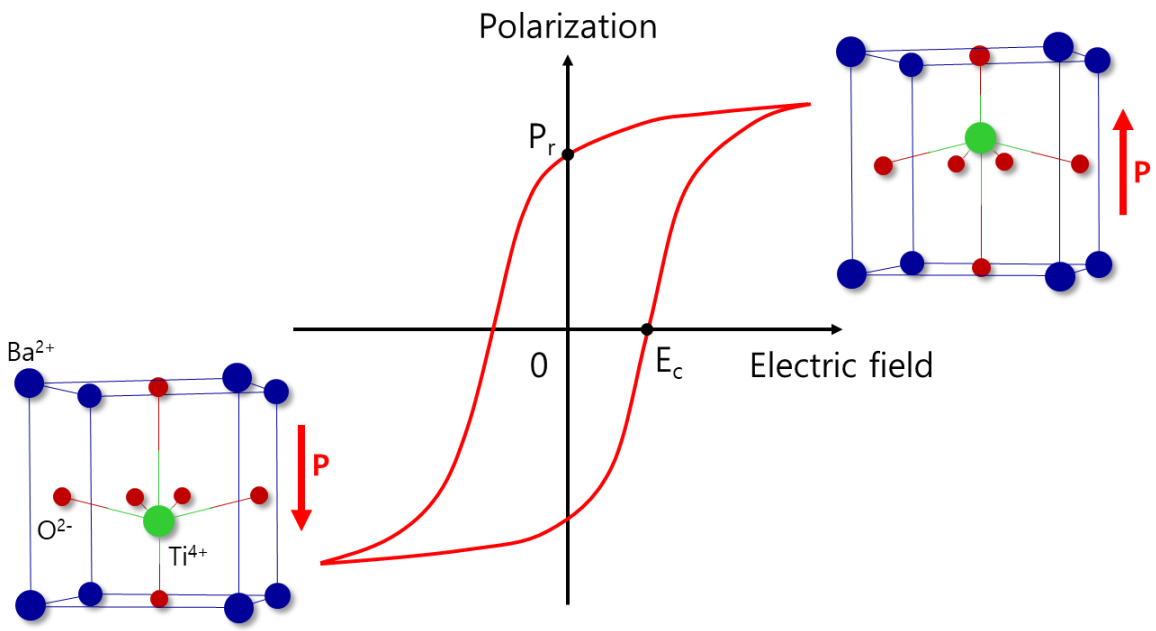

Figure 1-7. Working principle of the ferroelectric effect. The ferroelectric effect is a phenomenon observed in specific materials with non-centrosymmetric structure and spontaneous polarization. When an external electric field is applied to ferroelectric materials, their electric dipoles reorient in alignment along the electric field. After removing the external electric field, electric dipoles in ferroelectric materials maintain their reversed alignment.

1.3 Bioelectricity in amino acids

Amino acids are crucial in the structure and function of biological materials, serving as the basic components of peptides, proteins, and tissues.[264] Each amino acid comprises an α-carbon bonded to four side groups: an amino group ($-NH_2$), a carboxyl group (-COOH), a hydrogen atom, and a variable side chain (R) that differs among amino acids (Figure 1-8). The electrical properties of amino acids mainly arise from the dipole moments of their molecular structures, which arise from contributions from the the amino group, carboxyl group, and side chain.[265] In individual amino acids, the amino group ($-NH_2$) is basic and contains a lone pair of electrons on the nitrogen atom.[266] The presence of this lone pair results in a region of negative charge, leading to a partial negative charge on the nitrogen atom and influencing the overall dipole moment of the amino acid. In contrast, the carboxyl group (-COOH) is acidic and consists of a carbonyl group (-C=O) and a hydroxyl group (-OH). The oxygen atom in the carbonyl group withdraws electron density, creating a partial positive charge on the carbon atom and a partial negative charge on the oxygen atom.[266] Similarly, the oxygen atom in the hydroxyl group can induce a partial negative charge, further enhancing the overall dipole moment of the amino acid backbone. With the exception of glycine, the side chain (R group) of the amino acid can also influence its overall dipole moment[267,268], contingent upon its unique structure and properties, as discussed later. Certain side chains may contain polar functional

groups (e.g., hydrophobic, hydroxyl, negative, positive, polar groups, etc.), which can modulate the dipole moment.

Amino acids exhibit a range of electrical properties when subjected to external stimuli such as mechanical stress, temperature, and electric fields. These variations are crucial as they underlie specific electrical phenomena like piezoelectricity, pyroelectricity, ferroelectricity, and triboelectricity. With the exception of glycine, all amino acids possess a chiral structure without an inversion center, enabling them to demonstrate piezoelectric properties.[269,270] The piezoelectric resonances of different amino acids with various molecular configurations (e.g., right-handed (D), left-handed (L), and DL amino acids (racemic mixtures)) were first observed by Vasilescu et al. using a nuclear quadrupole resonance spectrometer.[271,272] They noted that most amino acids studied exhibited piezoelectric responses. Examination of amino acid crystals confirmed that those with chiral symmetry showed piezoelectric properties. Materials lacking a center of inversion and possessing spontaneous polarization demonstrate pyroelectricity and have the potential for ferroelectricity.[269,273] Materials with distinct electronic structure energy levels exhibit varying triboelectric effects.[274] As a result, amino acids demonstrate diverse electrical properties based on their structural characteristics, as outlined in Table 1. To understand the relationship between structure and function in bioelectricity, we will review the essential electrical properties of glycine as a model system and briefly extend the discussion to other amino acids.

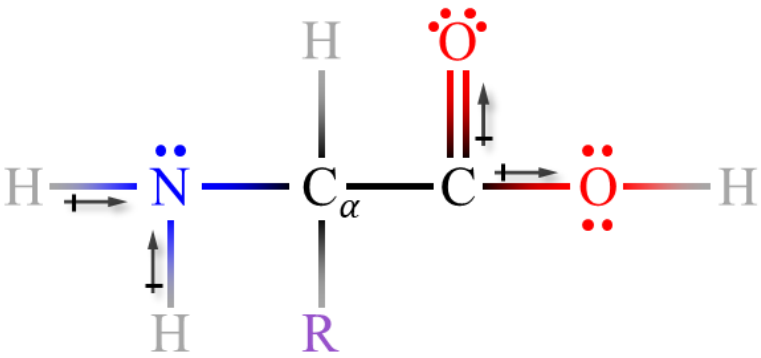

Figure 1-8. The chemical structure of an amino acid includes electron lone pairs on the nitrogen in the amino group on the oxygens in the carboxyl group, leading to the presence of partial dipole moments.

1.3.1 Glycine

Glycine is the simplest and smallest amino acid that consists of two hydrogen atoms bonded to the alpha carbon (Figure 1-9). Its compact structure is essential for constructing frameworks in biological materials, contributing to a variety of mechanical properties seen in

nature, such as those in collagen, elastin, and spider silk.[275-277] Glycine can crystallize in three different crystal lattices: α-glycine, β-glycine, and γ-glycine.[278] The space group of α-glycine is monoclinic $P2_1/c$, indicating a centrosymmetric structure (Figure 1-10a).[278-281] As a result, the dipole moments within the unit cell of α-glycine counteract each other, leading to a lack of piezoelectric effect. In contrast, β-glycine and γ-glycine have space groups of monoclinic $P2_1$ and trigonal $P3_2$, respectively, which establish a non-centrosymmetric structure conducive to exhibiting the piezoelectric effect (Figure 1-10b and 1-10c).[278-280,282-284] The piezoelectric properties of glycine were first observed in bulk powder characterization using nuclear quadrupole resonance spectroscopy. In this study, Lemanov et al. applied sequential electrical pulses to bulk glycine crystals and monitored the decrease in vibration frequency.[270] This measurement allowed them to determine how well the material mechanically responded to the electric potential stimulation. The bulk characterization confirmed that α-glycine did not exhibit piezoelectricity, while γ-glycine did exhibit a piezoelectric response. Subsequent studies observed the piezoelectric properties of β-glycine, which will be discussed later.

The development of SPM and novel crystal preparation techniques has allowed scientists to confirm the structure-dependent piezoelectric properties of glycine. Zhang et al. conducted a study on β-glycine crystals, creating crystal films using the electrohydrodynamic spray method.[285] During spraying, an electric field was applied between the nozzle tip and the conductive substrate. These films grew in a monoclinic crystal system, aligning the spontaneous polarization along the crystallographic y-axis parallel to the electric field, which maximized the out-of-plane polarization orientation and thus the piezoelectricity. The piezoelectric coefficient of β-glycine crystal films was assessed using PFM, which applies a bias to a conductive cantilever with a PFM tip, inducing a deformation that measures the piezoelectric properties of the material with nanoscale precision. The measured effective piezoelectric coefficient was 11.2 pm V^{-1}. The application of β-glycine crystal films with a large-scale out-of-plane alignment of crystal grains to piezoelectric devices resulted in an output voltage of 14.5 V, an output current of 4 μA, and a power density of 3.61 μW cm^{-2} at 2.6 MΩ under a compressive pressure of 1.5 MPa. Guerin et al. elucidated the piezoelectric properties of β-glycine using DFT calculations, determining the shear piezoelectric coefficients to be relatively high compared to normal piezoelectric coefficients.[25] Particularly noteworthy was the calculated shear transverse piezoelectric coefficient for the d_{16} mode of β-glycine, which exhibited a significantly high value of 195 pm V^{-1}. The authors attributed the piezoelectric effect to the structural properties of molecular packing, influencing the orientation of dipole moments and stiffness. The highest piezoelectric coefficient for the d_{16} mode in β-glycine was likely due to its molecular packing and relatively show elastic stiffness. Consequently, the DFT studies suggested that the loosely packed structure around the monoclinic angle could reduce resistance to deformation, enhancing piezoelectricity by promoting efficient straining. The piezoelectric properties of γ-glycine were studied using PFM measurements.[286] To grow the crystals, the slow evaporation method was employed from a supersaturated solution, resulting in the formation of pure trigonal γ-glycine crystals. Unlike

heterogeneous nucleation and random growth, the orientation of the dipole moments in these crystals was not determined. The confirmation of the piezoelectricity in γ-glycine was achieved through out-of-plane PFM measurements, which yielded an effective piezoelectric coefficient of 10 pm V^{-1}. The piezoelectric response along the crystallographic c-axis of the γ-glycine crystals was also examined.[25] Using a piezometer, a quasi-static force was applied to the (001) plane of the crystals. This device measured the voltage generated when pressure was applied using a vibrating lever or measured the lever deflection due to deformation under an applied electric field. The resulting piezoelectric coefficient for the d_{33} mode was 9.93 pm V^{-1}. Additionally, when a quasi-static force was applied to the (100) and (010) planes of the γ-glycine crystals, the piezoelectric coefficients for the d_{11} and d_{22} modes were 1.7 and -1.1 pm V^{-1}, respectively.

The pyroelectricity in γ-glycine was investigated by Lemanov.[269] Using a charge amplifier, the pyroelectric coefficient of γ-glycine crystals was determined to be 13 μC m^{-2} K^{-1} at room temperature, measuring the pyroelectric charge generation in response to heat application. Tylczynski et al. explored the pyroelectric characteristics of γ-glycine through quasi-static resonance methods.[287] They grew single crystals of γ-glycine in a trigonal crystal system slowly evaporating a saturated solution at 305 K. Their method involved measuring the change in electric charge on the surface of a glycine sample as the temperature varied from 100 to 385 K, using an electrometer. The pyroelectric coefficient of pure γ-glycine at 295 K was determined to be 21.4 μC m^{-2} K^{-1}. While these investigations confirmed the pyroelectric effect in γ-glycine, further exploration is needed for a structure-dependent nanoscale analysis. Although the pyroelectric properties of β-glycine have not been reported, it is presumed to exhibit such properties due to its association with ferroelectric materials.

The ferroelectricity in γ-glycine was studied by Heredia et al.[286] Thy grew trigonal γ-glycine crystals using the slow evaporation method from a supersaturated solution. To observe polarization switching under an external electric field, they employed switching spectroscopy PFM. Applying biases up to 25 V to the crystals, they measured resulting changes, revealing a ferroelectric hysteresis with a coercive voltage of ~10 V, indicating polarization switching in γ-glycine crystals. The researchers conducted DFT calculations and MD simulations to understand the origin of the ferroelectric behavior of γ-glycine. These computational methods determine the electronic structure of atoms and molecules by minimizing total energy, illustrating interactions between them over time and offering insights into dynamic behavior and properties of the materials. They calculated the number of switched molecules under an applied electric field ranging from 0 to 13 GV m^{-1}. MD simulation results displayed a clear transition at ~4 GV m^{-1} and complete switching in the simulation box's central region at ~8 GV m^{-1}, confirming the ferroelectric behavior in γ-glycine. Hu et al. further explored the ferroelectric properties of γ-glycine using DFT calculations and MD simulations.[288] Their computational findings revealed a spontaneous polarization of 70.7 μC cm^{-2} for trigonal γ-glycine along the crystallographic z-axis at 300 K. To investigate polarization switching, MD simulations tracked polarization changes under an external electric field along the axis ranging

from -3 to 3 GV m^{-1}. As the magnitude of the applied electric field increased, polarization switched between 1 to 2 GV m^{-1}, with a coercive field of 1 GV m^{-1}, indicating a ferroelectric behavior. The Curie temperature, at which a material loses its ferroelectric properties and becomes paraelectric, was estimated to be 630 K for γ-glycine, suggesting potential ferroelectric applications in biological systems. Computational studies on γ-glycine confirmed its ferroelectric behavior through rational design at the nanoscale, monitoring polarization switching in a time-dependent manner to systematically determine ferroelectric characteristics parameters. Investigation into the ferroelectric properties of β-glycine was excluded mainly due to its extreme instability.

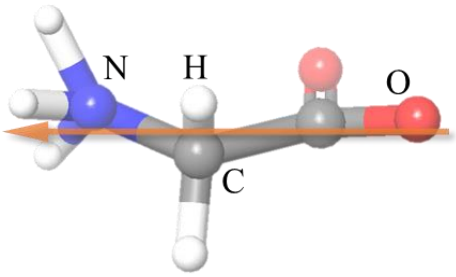

Figure 1-9. The formation of a dipole moment in glycine.

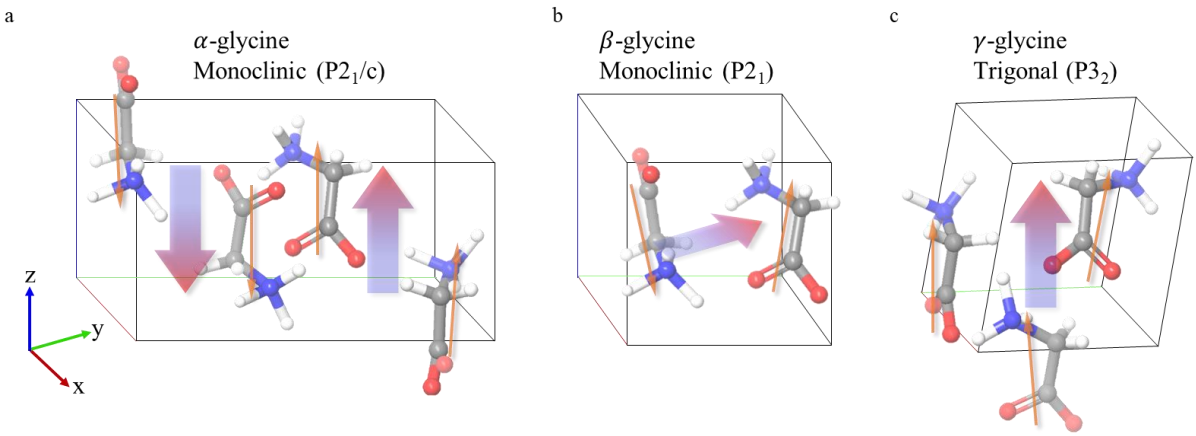

Figure 1-10. (a) α-glycine exhibit zero spontaneous polarization due to its centrosymmetric structure. The polarization of glycine molecules counteract each other, resulting in zero polarization. (b) The dipole moments in glycine molecules create a spontaneous polarization along the y-axis, contributing to an increased longitudinal 22 piezoelectric coefficient. (c) The γ-glycine unit cell exhibit a spontaneous polarization along the z-axis due to the collective alignment of dipole moments, which is directly linked to the longitudinal 33 piezoelectric coefficient.

1.3.2 Other amino acids

Amino acids exhibit diverse electrical properties based on their side chains. These side chains can be classified based on their chemical structures into nonpolar aliphatic, aromatic, positively/negatively charged, and polar uncharged groups. Amino acids with nonpolar aliphatic side chains, such as glycine, L-alanine, L-valine, L-leucine, L-isoleucine, L-proline, and L-methionine, are hydrophobic due to the absence of polar groups or bonds in their side chains. Longer or bulkier side chains tend to increase hydrophobic interactions within molecular structures.[289] However, these bulky side chains can impede close-packing arrangements, affecting the crystallinity and elasticity of materials.[290] Thus, variations in side chain structures can impact the electrical properties of amino acids. For example, L-alanine and L-proline crystallize into an orthorhombic $P2_12_12_1$ crystal system, while L-valine, L-leucine, L-isoleucine, and L-methionine crystallize into a monoclinic $P2_1$ crystal system.

Tylczyński et al. explored the piezoelectric properties of L-alanine by growing a single crystal using the slow evaporation method from a saturated solution.[291] Their study used a series resonance method to demonstrate the piezoelectric properties of L-alanine crystals. By subjecting the crystals to vibrations across various frequency ranges using an impedance meter, they measured the resulting piezoelectric resonances. The analysis of these resonances yielded elastic stiffness constants ranging from 5.34 to 6.26 GPa, which in turn led to piezoelectric coefficients of 1.92, 3.60, and 2.19 pm V^{-1} for the d_{14}, d_{25}, and d_{36} modes, respectively. Guerin et al. employed DFT calculations to study the piezoelectric properties of L-alanine.[26] They calculated elastic stiffness constants ranging from 6.87 to 8.74 GPa, consistent with experimental findings. The piezoelectric tensor of L-alanine was then determined, revealing calculated piezoelectric coefficients of -6.26, -3.78, and -6.30 pm V-1 for the d_{14}, d_{25}, and d_{36} modes, respectively. Yuan et al. investigated the piezoelectric properties of L-valine by examining its elastic stiffness constants.[292] This exploration is crucial for understanding the piezoelectric properties of the material, as the piezoelectric coefficient is inversely proportional to the elastic stiffness constants. The prediction of these constants is crucial for understanding a material's piezoelectric properties, with the piezoelectric coefficient inversely proportional to the elastic stiffness constants.[293] They used atomic force microscopy (AFM) nanoindentation techniques to measure the elastic stiffness of the crystals, revealing a stiffness value of 163.6 N m^{-1} for L-valine crystals. DFT calculations were employed to further investigate the elastic and piezoelectric constants, revealing the lowest calculated d_{22} piezoelectric coefficient of 12.3 pm V^{-1} and an effective piezoelectric coefficient of 11.4 pm V^{-1} for L-valine compared to L-leucine and L-methionine crystals, which will be discussed later. Nonpolar aliphatic amino acid-based piezoelectric devices were fabricated and tested, with L-valine-based devices producing an output voltage of 0.84 V and an output current of 35 nA under an applied force of 20 N. O'Donnell et al. conducted a study on the piezoelectric properties of L-leucine, using crystals grown through the evaporation method.[293] They measured the piezoelectric coefficient of L-leucine crystal films using a piezometer, obtaining a value of 1.57 pm V^{-1} for the d_{33} mode. Through DFT calculations, a range of 1.5 to 20 pm V^{-1} was determined for the piezoelectric

coefficients of L-leucine, with higher values attributed to the attenuation of the piezoelectric response of many single crystals in the crystalline film due to the quasi-random orientations of individual single crystals in the film. Elastic stiffness was assessed using AFM nanoindentation techniques, yielding stiffness values of 49.7 N m^{-1}.[292] The piezoelectric tensor of L-leucine was derived from the calculation of elastic constants, revealing a high shear d_{36} piezoelectric coefficient of 42.2 pm V^{-1} due to the weak hydrogen bonding interactions of the crystal. The remarkable piezoelectric properties of L-leucine crystals originates from their low stiffness and weak hydrogen bonding interactions, which promote ionic displacement under mechanical stress, leading to substantial polarization. Cheng et al. examined the piezoelectric properties of isoleucine crystals, which were produced through the evaporation method.[294] Their study included measuring the elastic stiffness constant using AFM nanoindentation techniques, yielding a value of 68.2 N m^{-1}. The molecular arrangement of L-isoleucine crystals, featuring seven hydrogen bonds between neighboring molecules, indicates their potential for piezoelectric behavior. Piezoelectric properties were evaluated using a piezometer, determining a piezoelectric coefficient of 1.2 pm V^{-1} along the normal direction of the film. Additionally, DFT calculations by Guerin et al. estimated elastic stiffness constants ranging from 0.4 to 24 GPa and a maximum calculated piezoelectric coefficient of 18.3 pm V^{-1} for L-isoleucine.[25] The piezoelectric properties of L-proline were examined using DFT calculations, as experimental data were limited.[26] The calculated elastic stiffness constants ranged from 3.28 to 8.80 GPa, resulting in calculated piezoelectric coefficients of 3.35, -0.09, and -0.4 pm V^{-1} for the d_{14}, d_{25}, and d_{36} modes, respectively. Yuan et al. investigated the piezoelectric properties of L-methionine by analyzing its elastic stiffness constants.[292] Using AFM nanoindentation techniques, they determined a stiffness value of 60.4 N m^{-1} for L-methionine crystals. Through DFT calculations, the researchers identified the elastic and piezoelectric constants, revealing a longitudinal d_{22} piezoelectric coefficient of 37.6 pm V^{-1}, attributed to the low stiffness and loose packing of the crystal. The shear d_{36} piezoelectric coefficient was notably high at 42.2 pm V^{-1} due to the weak hydrogen bonding interactions of the crystal. The piezoelectric tensor of L-methionine was established based on elastic constant calculations. Their findings indicated that L-methionine could serve as a material for nonpolar aliphatic amino acid-based piezoelectric devices, with fabricated devices generating an output voltage of 1.62 V and an output current of 55.1 nA under an application of force of 42 N, achieving a maximum power of 31.4 nW cm^{-2} at 40 MΩ.[292] Amino acids with aromatic side chains, such as L-tyrosine, L-phenylalanine, and L-tryptophan, contribute to the overall electrical properties similarly to those with aliphatic side chains. These aromatic amino acids possess a dipole moments due to the uneven electron density distribution in their aromatic rings. Their aromatic side chains can engage in hydrophobic interactions and π–π stacking with neighboring molecules. Moreover, their bulkier structures can significantly impact the crystallinity and elasticity of crystals. Specifically, L-tyrosine, L-phenylalanine, and L-tryptophan exhibit orthorhombic $P2_12_12_1$, monoclinic $P2_1$, and triclinic P1 crystal systems, respectively. Ji et al. investigated the piezoelectric properties of L-tyrosine and L-phenylalanine, determining the stiffness of the crystals through AFM nanoindentation measurements. They found that L-tyrosine exhibited a

higher stiffness of 633 N m^{-1} compared to L-phenylalanine's 84.2 N m^{-1}, indicating greater rigidity in L-tyrosine crystals.[295] This rigidity was attributed to the densely packed dimers in L-tyrosine, resulting in strong supramolecular packing. Hydrogen bonds were identified as the primary force driving the packing in both amino acids. The dimer building block in L-tyrosine crystals differed from that in L-phenylalanine in terms of hydrogen bonded units and crystal packing. DFT calculations revealed piezoelectric coefficients of L-tyrosine ranging from 5.0 to 9.7 pm V^{-1}, with the highest value observed for the d_{25} mode. In contrast, L-phenylalanine exhibited a maximum piezoelectric coefficient of 5.4 pm V^{-1} for the d14 mode.[296,297] Due to their mechanical stability, piezoelectric devices based on L-tyrosine were fabricated, demonstrating an output voltage of 0.5 V and an output current of 35 nA under an application force of 31 N. Amino acids with charged side chains can affect their electrical properties by either donating or withdrawing electron density. Mandal et al. used DFT calculations to illustrate the magnitude and direction of dipole moments in these amino acids.[298] Their study categorized amino acid structures into donor, bridge, and acceptor segments. Positively charged amino acids like L-lysine, L-arginine, and L-histidine adopt a monoclinic $P2_1$ crystal system, with the backbone, alkyl side chain, and amino or imidazole moieties serving as the donor, bridge, and acceptor, respectively. The excess positive charge on these cationic species causes dipole moments to form from the donor to the acceptor direction (Figure 1-11). Calculated dipole moments for L-lysine, L-arginine, and L-histidine were 22.7, 20.8, and 6.9 D, respectively. Conversely, negatively charged amino acids such as L-aspartate and L-glutamate crystallize into monoclinic $P2_1$ and orthorhombic $P2_12_12_1$ crystal systems, with the backbone, alkyl side chain, and carboxylate moieties acting as the acceptor, bridge, and donor, respectively. The excess negative charge on these anionic species leads to dipole moments forming from the acceptor to the donor direction (Figure 1-11). Calculated dipole moments for L-aspartate and L-glutamate were 14.4 and 17.4 D, respectively. Amino acids featuring polar uncharged side chains (e.g., L-serine, L-threonine, L-asparagine, L-glutamine, and L-cysteine) exhibit a dipole moment due to their polar functional groups, which include hydroxyl, thiol, and amide. Specifically, L-serine, L-threonine, and L-glutamine crystallize in an orthorhombic $P2_12_12_1$ system, while L-asparagine and L-cysteine adopt a monoclinic $P2_1$ crystal system. The crystal systems and piezoelectric tensors of these amino acids are outlined in Table 1. Through the use of a quadrupole spectrometer, researchers have observed a piezoelectric response in these amino acids, showcasing the presence of piezoelectricity in polar uncharged variants.[270,271] DFT calculations were employed to determine the piezoelectric coefficients of L-serine, as experimental data was not accessible.[296] These calculations revealed the piezoelectric coefficients for the d_{14}, d_{25}, and d_{36} modes of L-serine to be 4.69, 4.33, and -3.00 pm V^{-1}, respectively. Furthermore, the elastic stiffness constants of L-serine were calculated across a range of 2.3 to 12.6 GPa. The study involved examining the piezoelectric response of L-threonine crystals by using a piezometer.[296] These crystals were grown in an orthorhombic structure using the slow evaporation method from a saturated aqueous solution. Measurements on polycrystalline L-threonine crystal films revealed an effective longitudinal d_{33} piezoelectric coefficient of 0.1 pm V^{-1}. Furthermore, predictive DFT calculations were performed to

determine the piezoelectric coefficients for the d_{14}, d_{25}, and d_{36} modes of L-threonine crystals, resulting in values of 3.78, -3.40, and -4.90 pm V^{-1}, respectively. The study also determined the elastic stiffness constants of L-threonine, which ranged from 5.1 to 11.5 GPa. Guerin et al. used DFT calculations to establish the piezoelectric properties of L-asparagine, as there was no experimental measurements.[25] They found that the piezoelectric coefficients varied between 0.9 and 13.0 pm V^{-1}, with the highest value observed for the d_{16} shear mode. Additionally, the elastic stiffness constants were determined to range from 7 to 83 GPa. DFT calculations were used to determine the piezoelectric properties of L-glutamine.[296] The calculated piezoelectric coefficients for the d_{14}, d_{25}, and d_{36} modes were found to be -1.85, -3.78, and -11.40 pm V^{-1}, respectively. Additionally, the elastic stiffness constants were calculated to range from 8.1 to 16.8 GPa. DFT calculations were employed to determine the piezoelectric properties of L-cysteine.[25] The calculated piezoelectric coefficients ranged from 1.2 to 11.4 pm V^{-1}, with the highest value observed for the longitudinal d_{22} mode. Additionally, the calculated elastic stiffness constants ranged from 3 to 37 GPa. Polar uncharged amino acids exhibited minimal variation in their elastic stiffness constants, leading to minor discrepancies in their piezoelectric behaviors.

Most amino acids in proteins exhibit polar symmetry groups, suggesting they may demonstrate pyroelectric properties.[269] Although there is a lack of structure-dependent pyroelectric analyses, some amino acids have been reported to display this behavior. Yarmakin et al. studied the pyroelectric properties of L-aspartate crystals.[299] These single crystals were grown by slowly cooling saturated aqueous solutions, and then cut perpendicular to the symmetry axis. Pyroelectric measurements on the monoclinic L-aspartate crystals were conducted using a dynamic method. The crystals were illuminated with infrared light at a heat rate of 100 K min^{-1}, resulting in a measured pyroelectric coefficient of 4 μC m^{-2} K^{-1} at 295 K. Mishuk et al. conducted a study on DL-alanine crystals to demonstrate their pyroelectric properties, which were grown using the slow evaporation method.[300] These crystals have an orthorhombic structure with exposed carboxylate groups along the [001] direction. When subjected to periodic temperature changes using an infrared laser, the crystals showed pyroelectric coefficients of 5-20 μC m^{-2} K^{-1} along the [001] direction and -210 μC m^{-2} K^{-1} along the [210] direction. The authors suggested that the significant pyroelectricity along the [210] direction is due to local distortions caused by these molecules, which displace neighboring host molecules from their lattice positions and align them in a polar configuration.

The triboelectric properties of amino acids, including L-arginine, L-histidine, L-glutamate, and L-aspartate, were examined by Pal et al.[274] Kelvin probe force microscopy (KPFM), a technique that measures the contact potential difference (CPD) between a conductive tip and a sample surface, was employed to provide nanoscale insights into surface potential and variations in work function. Surface potential mapping using KPFM revealed distinct work function profiles for amino acids with different side chain structures. Positively charged amino acids, including L-arginine and L-histidine, demonstrated low work functions of approximately 3.8 eV, whereas negatively charged amino acids like L-glutamate and L-

aspartate exhibited higher values around 5 eV. Amino acids that were neither positively nor negatively charged had work functions ranging from approximately 4.4 to 4.6 eV. This variation suggests that the differing electron-donating and -accepting capabilities among amino acids lead to distinct electronic energy level structures, resulting in diverse triboelectric effects. XPS involves irradiating a sample with X-rays to release photoelectrons, the energies of which are measured to analyze the elemental composition and chemical state of the material. Through XPS analysis, they clarified the reasons for these distinctions, which include the material's atomic composition and the existence of various chemical structures in side chain functional groups. XPS characterizations analyses demonstrated that the guanidine group in the side chain of L-arginine and the imidazole group in the side chain of L-histidine exhibited electron-donating properties, while oxygen-based functional groups in L-glutamate and L-aspartate displayed electron-accepting properties. The atomic composition, particularly the nitrogen-to-oxygen ratio, was determined for these amino acids, with positively charged amino acids showing high values and negatively charged amino acids showing low values. These results emphasized the varied electron-donating and -accepting capabilities of amino acids at the atomic level, which were consistent with the observations from the work function analyses. Additionally, the triboelectric series of amino acids was established through the measurement of triboelectric transfer charges (Figure 1-12). Amino acid-based triboelectric devices were created by using amino acids as positive materials and polytetrafluoroethylene (PTFE) as the negative material, selected for its strong negative triboelectric characteristics. The quantity of generated triboelectric transfer charges was determined and found to be closely related to the work function values; materials with a greater difference in work function yielded more triboelectric transfer charges. Consequently, the triboelectric series of amino acids categorized amino acids with a high nitrogen content as positive triboelectric materials, those with a high oxygen content as negative triboelectric materials, and non-charged amino acids in between. This investigation illustrates how the atomic structure of amino acids influences their ability to donate or accept electrons in a triboelectric context. Yuan et al. investigated the influence of amino acid molecular packing on triboelectric performance using valine crystals.[301] They employed a vapor deposition process to fabricate various self-assembled molecular packing structures of L-valine, D-valine, and DL-valine. Valine molecules naturally form layered structures due to interactions between the amino and carboxyl groups, resulting in double layers parallel to the (001) plane. While L-valine and D-valine formed three-dimensional films, DL-valine formed a two-dimensional film, possibly due to differing hydrogen bonding interactions. The molecular packing of the valine crystals influenced their triboelectric properties. In the three-dimensional L-valine and D-valine crystals, the amino groups were oriented in the same direction, enhancing their electron-donating capabilities. Conversely, in the two-dimensional DL-valine crystal, the amino groups pointed in different directions, diminishing their ability to donate electrons due to the opposing negative charges from the carboxyl group. Hirshfeld surface mapping of valine crystals revealed differing electrostatic potentials for the interaction between the donor (H) atom in the amino group and the acceptor (O) atom in the carboxyl group. The potentials were measured as 0.0043, 0.0037, and 0.0030 a.u. for L-valine, D-valine,

and DL-valine, respectively, indicating higher electropositivity in the order of L-valine, D-valine, and DL-valine. KPFM measurements supported this trend, showing a higher surface potential in the same order. This suggests that triboelectric devices based on valine, particularly those with L-valine in a three-dimensional structure, exhibited superior triboelectric performance due to their high electropositivity and large contact area. For instance, the L-valine-based triboelectric device demonstrated an impressive output voltage of 112 V, an output current of 1.05 μA, and a power density of 92.9 mW m-2 at 300 MΩ under an application force of 57 N.

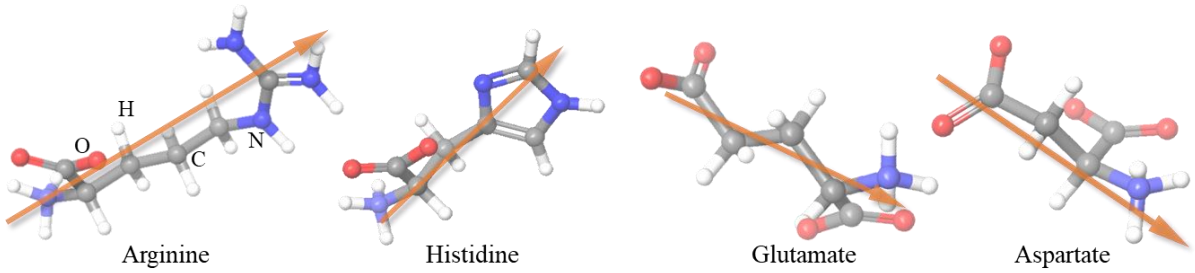

Figure 1-11. Schematic images of positively charged amino acids (arginine and histidine) and negatively charged amino acids (glutamate and aspartate) depict dipole moments. In positively charged amino acids, these dipole moments are formed from the carboxyl group toward the amino group, whereas in negatively charged amino acids, they are oriented in the opposite direction.

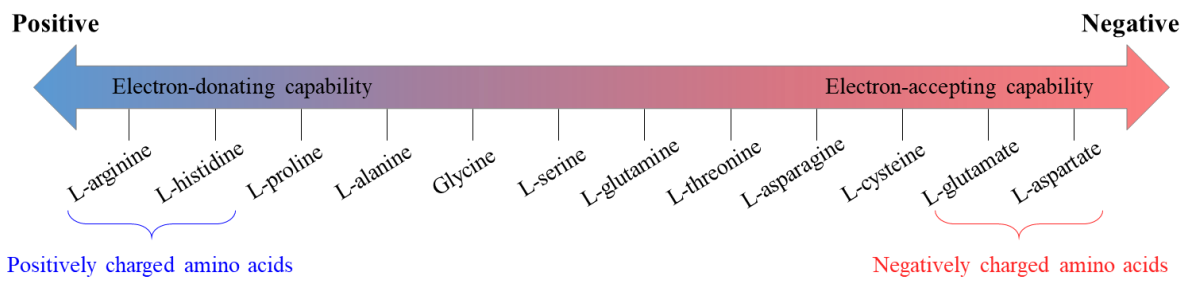

Figure 1-12. The triboelectric series of amino acids indicates that positively charged amino acids, classified as positive triboelectric materials, typically donate electrons due to their low work functions. Conversely, negatively charged amino acids, categorized as negative triboelectric materials, tend to accept electrons due to their high work functions.

Material	Electrical characteristics	Symmetry	Methods	Refs.

β-Glycine	$\begin{pmatrix} 0 & 0 & 0 & 15.8 & 0 & 195 \\ 1.8 & -5.7 & 1.9 & 0 & 5.1 & 0 \\ 0 & 0 & 0 & 1.3 & 0 & 7.5 \end{pmatrix}$	Monoclinic ($P2_1$)	DFT	[25]
	$d_{16} = -178$		Resonance method	
	$d_{33,eff} = 11.2$		PFM	[285]
	14.5 V, 4 μA, 3.61 μW cm^{-2} at 2.6 MΩ		Piezo-device	
	$E_c = 1.5 - 2$		DFT & MD	[284]
γ-Glycine	$\begin{pmatrix} 1.6 & -1.1 & 0 & -5.8 & 7.2 & 5.6 \\ 1.2 & -1.1 & 0 & 7.5 & 5.6 & -5.6 \\ -0.8 & -0.7 & 10.4 & 0 & 0 & 0 \end{pmatrix}$	Trigonal ($P3_2$)	DFT	[25]
	$d_{11} = 1.7,\ d_{22} = -1.1,\ d_{33} = 9.93$		Quasi-static method	
	$d_{33} = 5.8 - 11.6$		DFT & MD	[284]
	$d_{33} = 7.37$		Piezometer	[302]
	0.45 V at 0.172 N		Piezo-device	[25]
	$p = 13$		-	[303]
	$p = 21.4$		Quasi-static method	[287]
	$E_c = 0.03 - 0.08$		DFT & MD	[284]
	$E_c = 1$		DFT & MD	[288]
L-lysine	$d_{34} = 6.0$	Monoclinic	DFT	[297]
L-phenylalanine	$d_{14} = 5.4$	($P2_1$)		
L-tryptophan	$d_{25} = 28$	Triclinic		
		($P1_1$)		
L-arginine	$\begin{pmatrix} 0 & 0 & 0 & 0.28 & 0 & 6.52 \\ -0.71 & 3.65 & 0.36 & 0 & -0.73 & 0 \\ 0 & 0 & 0 & 2.33 & 0 & 3.64 \end{pmatrix}$	Monoclinic ($P2_1$)	DFT	[304]
L-valine	$\begin{pmatrix} 0 & 0 & 0 & 0.13 & 0 & 1.37 \\ -0.15 & -0.12 & 0.05 & 0 & 0.95 & 0 \\ 0 & 0 & 0 & 1.81 & 0 & 1.62 \end{pmatrix}$			
	$d = 11.4$		PFM	[305]
	0.84 V, 35 nA at 20 N		Piezo-device	
	$\begin{pmatrix} 0 & 0 & 0 & -7.36 & 0 & -7.7 \\ 0.16 & -12.4 & 5.75 & 0 & -3.23 & 0 \\ 0 & 0 & 0 & -5.33 & 0 & 0.61 \end{pmatrix}$		DFT	[305]
	112 V, 1.05 μA, 92.9 mW m^{-2} at 300 MΩ		Tribo-device	[301]
D-valine	100 V, 1.0 μA			
DL-valine	75 V, 808 nA			
L-asparagine	$\begin{pmatrix} 0 & 0 & 0 & 12.0 & 0 & -13.0 \\ 2.1 & 2.0 & 1.1 & 0 & -4.6 & 0 \\ 0 & 0 & 0 & -0.9 & 0 & 5.7 \end{pmatrix}$		DFT	[25]
L-aspartate	$\begin{pmatrix} 0 & 0 & 0 & 3 & 0 & 3 \\ -0.73 & -1.85 & -1.82 & 0 & 0 & 0 \\ 0 & 0 & 0 & 13 & 0 & 10 \end{pmatrix}$			
	$p = 4$		Dynamic method	[299]
L-cysteine	$\begin{pmatrix} 0 & 0 & 0 & 10.7 & 0 & 10.6 \\ 4.1 & 11.4 & 2.9 & 0 & 2.6 & 0 \\ 0 & 0 & 0 & 13 & 0 & 1.2 \end{pmatrix}$		DFT	[25]
L-histidine	$\begin{pmatrix} 0 & 0 & 0 & 4 & 0 & 18 \\ 1.6 & 1.25 & 0.43 & 0 & 6.67 & 0 \\ 0 & 0 & 0 & 2.5 & 0 & 2 \end{pmatrix}$			

L-isoleucine	$\begin{pmatrix} 0 & 0 & 0 & 12.25 & 0 & 18.3 \\ 2.6 & 10 & 1.1 & 0 & 10 & 0 \\ 0 & 0 & 0 & 25 & 0 & 3.33 \end{pmatrix}$			
L-leucine	$\begin{pmatrix} 0 & 0 & 0 & 0 & 0 & 12.5 \\ 2.7 & 8.6 & 1.5 & 0 & 12.5 & 0 \\ 0 & 0 & 0 & 20 & 0 & 12.5 \end{pmatrix}$			
	$d_{33} = 1.57$		Piezometer	[293]
L-methionine	$\begin{pmatrix} 0 & 0 & 0 & 5 & 0 & 13 \\ 2.42 & 6.9 & 4.1 & 0 & 5 & 0 \\ 0 & 0 & 0 & 15 & 0 & 0 \end{pmatrix}$		DFT	[25]
	$d = 18.0$		PFM	[292]
	1.62 V, 55.1 nA, 31.4 nW cm^{-2} at 40 MΩ		Piezo-device	[292]
	$\begin{pmatrix} 0 & 0 & 0 & 6.83 & 0 & 15.0 \\ -12.9 & 37.6 & -8.96 & 0 & 18.3 & 0 \\ 0 & 0 & 0 & 16.4 & 0 & 11.5 \end{pmatrix}$		DFT	[292]
L-proline	$\begin{pmatrix} 0 & 0 & 0 & 3.35 & 0 & 0 \\ 0 & 0 & 0 & 0 & -0.09 & 0 \\ 0 & 0 & 0 & 0 & 0 & -0.4 \end{pmatrix}$	Orthorhombic ($P2_12_12_1$)	DFT	[26]
L-alanine	$\begin{pmatrix} 0 & 0 & 0 & -6.26 & 0 & 0 \\ 0 & 0 & 0 & 0 & -3.78 & 0 \\ 0 & 0 & 0 & 0 & 0 & -6.30 \end{pmatrix}$		DFT	[296]
	$p = -0.11$		Dynamic method	[296]
DL-alanine	$\begin{pmatrix} 0 & 0 & 0 & 0 & 8.0 & 0 \\ 0 & 0 & 0 & 17.8 & 0 & 0 \\ 0.9 & -1.1 & 10.3 & 0 & 0 & 0 \end{pmatrix}$	Orthorhombic ($Pna2_1$)	DFT	[306,307]
	$d_{33} = 10.8$		PFM	[306]
	$p = 5 - 20$ along [001], $p = -210$ along [210]		Quasi-static method	[300]
L-tyrosine	$\begin{pmatrix} 0 & 0 & 0 & -5.00 & 0 & 0 \\ 0 & 0 & 0 & 0 & -9.73 & 0 \\ 0 & 0 & 0 & 0 & 0 & -5.81 \end{pmatrix}$	Orthorhombic ($P2_12_12_1$)	DFT	[296]
	0.5 V, 35 nA at 31 N		Piezo-device	[295]
DL-tyrosine	$\begin{pmatrix} 0 & 0 & 0 & 0 & -14.5 & 0 \\ 0 & 0 & 0 & -10.7 & 0 & 0 \\ -0.9 & -2.2 & -8.4 & 0 & 0 & 0 \end{pmatrix}$		DFT	[306]
	$d_{33} = 8.4$		PFM	[306]
L-glutamine	$\begin{pmatrix} 0 & 0 & 0 & -1.85 & 0 & 0 \\ 0 & 0 & 0 & 0 & -3.78 & 0 \\ 0 & 0 & 0 & 0 & 0 & -11.40 \end{pmatrix}$		DFT	[296]
L-threonine	$\begin{pmatrix} 0 & 0 & 0 & 3.78 & 0 & 0 \\ 0 & 0 & 0 & 0 & -3.40 & 0 \\ 0 & 0 & 0 & 0 & 0 & -4.90 \end{pmatrix}$			
	$p = -0.24$		Dynamic method	[206]
L-serine	$\begin{pmatrix} 0 & 0 & 0 & 4.69 & 0 & 0 \\ 0 & 0 & 0 & 0 & 4.33 & 0 \\ 0 & 0 & 0 & 0 & 0 & -3.00 \end{pmatrix}$		DFT	[296]
	$p = 0.11$		Dynamic method	[206]
L-glutamate	$\begin{pmatrix} 0 & 0 & 0 & 0.54 & 0 & 0 \\ 0 & 0 & 0 & 0 & -1.60 & 0 \\ 0 & 0 & 0 & 0 & 0 & -3.18 \end{pmatrix}$		DFT	[296]
Hydroxy-L-proline	$\begin{pmatrix} 0 & 0 & 0 & 3.72 & 0 & 0 \\ 0 & 0 & 0 & 0 & -27.75 & 0 \\ 0 & 0 & 0 & 0 & 0 & 4.55 \end{pmatrix}$			

Table 1. Electrical characteristics of amino acids, including piezoelectric coefficient, *d* (pC N^{-1}), pyroelectric coefficient, *p* (μC m^{-2} K^{-1}), coercive field, E_c (GV m^{-1}), and electrical outputs of the device. Matrices in the table represent the piezoelectric tensor of the material.

1.4 Bioelectricity in peptides

Peptides, short amino acid chains linked by amide bonds, can form a variety of structures such as dipeptides, tripeptides, and oligopeptides using the 20 natural amino acids and their analogs, each exhibiting unique dipole structures.[308,309] These structures, including nanofibers, nanotubes, and nanoribbons, can organize their dipole structures and display diverse electrical properties based on their primary structure, the arrangement of polar groups, and their response to external stimuli like mechanical stress, temperature changes, and electric fields.[269,310-313] Extensive research has focused on understanding the structural and electrical properties of dipeptides (e.g., diphenylalanine, FF) and tripeptides (e.g., PFF and OFF) (Table 2).[59,314-317] These studies aim to elucidate the various electrical properties of these hierarchically structured peptide assemblies.

Diphenylalanine (FF), composed of two phenylalanine amino acids, has the ability to self-assemble into structured nanostructures, demonstrating a range of electrical characteristics. Phenylalanine, the foundational element of diphenylalanine, crystallizes in a monoclinic crystal system and bonds to create diphenylalanine, potentially showing electrical properties due to its inherent polarization.[295,317] FF is naturally involved in the formation of amyloid-β proteins, which are associated with Alzheimer's disease.[316,318] The electrical characteristics of self-assembled FF nanotubes have been extensively studied, focusing on their structural features. FF has the ability to self-assemble into a hexagonal ring structure, where six individual FF monomers join to form a ring plane with six-fold hexagonal symmetry (space group P61). This structure is non-centrosymmetric and exhibits a spontaneous polarization of 1.3 D along the axis perpendicular to the ring plane (Figure 1-13).[317,319,320] Through a combination of hydrogen bonding and π–π stacking interactions, the FF hexagon ring can further assemble into a nanotube structure, demonstrating a dipole moment of 42-52 D along the tubular axis.[317,318,321]

Kholkin et al. were the first to discover the piezoelectric effect in FF nanotubes.[316] They created horizontally aligned FF nanotubes by dissolving FF building blocks in lyophilized form in hexafluoro propanol. A 2 μL aliquot of the resulting solution was diluted in ddH_2O, placed on a gold substrate, and then dried. The piezoelectric properties of these aligned FF nanotubes were examined using PFM measurements. They found that a 100 nm diameter tube exhibited a shear piezoelectric coefficient of 35 pm V^{-1} in the d_{15} mode, which increased to 60 pm V^{-1} when the diameter was increased to 200 nm. This increase in piezoelectric effect with larger diameter was attributed to a bulk effect. Assuming a consistent inner diameter of the FF nanotube with varying outer diameters, the change in the piezoelectric response can be explained by the transition from a thin wall to a thick wall. In the case of a thick wall, the

piezoelectric properties resemble those of a solid material, approaching what is known as the bulk piezoelectric effect. Heredia et al. investigated the piezoelectric characteristics of vertically aligned FF nanotubes.[317] They produced these vertically aligned nanotubes by dissolving FF building blocks in lyophilized form in hexafluoro propanol. A 30 μL portion of the resulting solution was deposited directly onto a substrate and allowed to dry. Using PFM measurements, they estimated the effective longitudinal piezoelectric coefficient for the d_{33} mode in vertically aligned FF tubes to be 30 pm V^{-1}. Later, Vasilev et al. established a piezoelectric tensor for FF microtubes.[322] Their study reported shear piezoelectric coefficients of 80 pm V^{-1} for the d_{15} mode and -10 pm V^{-1} for the d_{14} mode, alongside normal piezoelectric coefficients ranging from 4-18 pm V^{-1}. The larger piezoelectric coefficient for the d15 mode may have been a result of constructing larger FF nanotubes. In 2016, Nguyen et al. devised piezoelectric devices featuring polarization-controlled arrays of FF tubes.[323] These tubes were grown on a 1.25×1.25 cm^2 gold substrate and positioned between two electrodes, then subjected to cyclic compressive force. Upon applying 60 N of force, the device generated an output voltage of 1.4 V and an output current of 39.2 nA. In piezoelectric output measurements dependent on impedance with various electrical resistors ranging from 1 kΩ to 1 GΩ, the device displayed a peak power of 3.3 nW cm^{-2} at 50 MΩ, which rose to 7 nW cm^{-2} with an increasing strain rate to approximately 0.011 s^{-1}. Su et al. later improved the piezoelectric performance of FF tube-based devices by introducing an electric field during the peptide growth process.[324] This electric field enhanced the crystallinity and uniform polarization of the peptides. PFM measurements showed that the piezoelectric coefficient (d_{33}) increased proportionally with the strength of the applied electric field, reaching up to 18.91 pm V^{-1} at a growth voltage of 7 kV. The piezoelectric device was composed of FF peptide films sandwiched between silver-coated glass substrates. When subjected to an applied force of 90 N, the device produced an output voltage of 3.4 V, an output current of 235 nA, and a power density of 9.98 W m^{-3}. In 2018, Lee et al. improved the piezoelectric energy generation of FF tubes by aligning them in a unidirectional polarization manner.[325] They achieved this by controlling the nucleation of FF nanotubes using a meniscus-driven self-assembly process, which laterally aligned the FF tubes on the substrates. The optimization of the FF films was carried out by adjusting the thermodynamic and kinetic parameters of the self-assembly process. The resulting FF-based piezoelectric device produced an output voltage of 2.8 V and an output current of 37.4 nA when subjected to a force of 42 N. At 44 MΩ, the device demonstrated a maximum power output of 8.2 nW. The authors conducted finite element simulations and showed that the asymmetric geometries of FF nanotubes contribute to the strong generation of piezoelectric potential. This is due to the asymmetric shape of the tubes, which facilitates the application of axial forces and the generation of strong shear stresses, leading to the generation of electrical energy. Additionally, the replacement of hexafluoro propanol with ethanol as the solvent contributed to the eco-friendliness of the FF-based piezoelectric devices.[326] Further studies are exploring the versatility of FF-based piezoelectric applications for potential use in piezoelectric resonators, wearable devices, and biomedical devices. Concurrently, research is underway to evaluate the flexibility and degradability of these devices through experimental and

computational analyses.[327-329]

The tubular structures of FF possess pyroelectric properties due to their non-centrosymmetric structure and spontaneous polarization.[330] FF microtubes were grown by Esin et al. on a platinum substrate, with diameters ranging from 1-3 μm and lengths of 1 mm. These tubes were subjected to periodic heating and cooling using optical stimulation with varying laser intensity and frequency. Monitoring the resulting pyroelectric current with a current preamplifier revealed positive peaks during heating and negative peaks during cooling. The pyroelectric coefficient of the FF microtubes was determined to be 2 μC m^{-2} K^{-1}. The researchers showed that enhancing the pyroelectric properties is achievable by fabricating the tubes at the nanoscopic level, which prevents opposing polarization between adjacent tubes. This discovery of pyroelectricity in FF tubes holds promise for bioelectrical applications such as energy harvesting and implantable biomedical devices.

Ferroelectric behavior is observed in FF nanotubes. The Kholkin group induced the orthorhombic phase in FF nanotubes by annealing the hexagonal phase at temperatures around 140-150 °C.[331-333] While the hexagonal phase of FF nanotubes shows no polarization switching under an external electric field due to its extremely high coercive field of 0.030-0.045 GV m^{-1}, the annealed orthorhombic FF nanotubes exhibit a decrease in axial dipole moment, resulting in antiparallel orientations but a radial component of polarization when subjected to an external field.[333] Confirmation of ferroelectric hysteresis in the orthorhombic FF nanotubes was achieved through PFM measurements and MD simulations, revealing ferroelectric hysteresis characteristics and obtaining a remanent polarization of 0.8 μC cm-2 in the radial direction.[331]

FF peptide can go through dehydration and cyclization of its linear backbone to form orthorhombic cyclo-diphenylalanine (cyclo-FF), which then self-assembles into nanotubes through a vapor deposition process.[334] These nanotubes exhibit structural features with outward-facing aromatic side chains, which are a result of strong electrostatic interactions between the backbones, giving them highly hydrophobic properties.[335] Through dehydration and cyclization, the linear backbone of the FF peptide can form orthorhombic cyclo-diphenylalanine (cyclo-FF), which then self-assembles into nanotubes via vapor deposition.[336] Vertical construction of cyclo-FF nanowires on a substrate was achieved using direct thermal evaporation. These nanowires were used as the positive material in a triboelectric device, with PTFE serving as the negative material, covering an area of 12.04 cm^2. When the device underwent cyclic vertical contact and separation, the corona-treated cyclo-FF nanowire-based triboelectric device generated an output voltage of 350 V and an output current of 10 μA. The device reached its maximum power output of 73.7 mW m^{-2} at 100 MΩ. The efficiency of triboelectric charging is significantly impacted by the water content.[337-339] Slabov et al. investigated how the triboelectric properties of diphenylalanine nanotubes are influenced by the confinement of water within their nanochannels.[340] They studied the behavior of water molecules, including those bound to the peptide backbone (bound water) and those localized near the tube axis (mobile water). The researchers found that the open-circuit voltage remained

stable up to 60 °C, decreased at 115 °C, and then increased at 140 °C. In contrast, the short-circuit current decreased gradually with increasing temperature up to 115 °C but then increased at 140 °C. According to their observations, the open-circuit voltage is affected by bound water, while the decrease in short-circuit current is attributed to the evaporation of mobile water as the temperature rises. The concurrent increase in both open-circuit voltage and short-circuit current at 140 °C resulted in the device's output power increasing from 200 to 260 nW, which was attributed to enhanced electrostatic interactions during cyclization.

The helical structure of Pro-Phe-Phe (PFF) resembles the functional phenol-soluble modulin α3 (PSMα3) peptide secreted by *Staphylococcus aureus*[341], and has been engineered to exhibit strong mechanical properties, showing promise for designing functional and electrical biomaterials.[314] In 2021, Bera et al. demonstrated the discovery of the piezoelectric effect in collagen-mimicking peptide assemblies, focusing on the PFF and OFF peptides (Figure 1-14).[59] These tripeptides form single crystals that extend their structure through intermolecular hydrogen bonding (head-to-tail) and aromatic zipper packing (π–π interactions). The PFF peptide crystallizes in a monoclinic crystal system, with a molecular dipole of 7.9 D and a crystal dipole of 2.8 D along the b-axis. Its piezoelectric coefficient for the d_{34} mode is 3.1 pm V^{-1}. For the OFF peptide, hydroxylation of the OFF peptide reduces the unit cell's symmetry, leading to a triclinic crystal system. This change results in molecular and crystal dipoles of 6.7 and 1.9 D, respectively, along the b-axis. A decrease in the elastic stiffness constant causes an increase in ionic displacement under mechanical stress, leading to a rise in the piezoelectric coefficients for the d_{16} and d_{35} modes, which can reach up to 27.3 pm V^{-1}. The PFF and OFF peptides form self-assembled supramolecular structures with helical-like sheet formations, stabilized by hydrophobic interactions among the F residues. The OFF peptide assembly displays a high aspect ratio structure, featuring a diameter of 500 nm and a length of several micrometers. PFM analysis of single crystals from PFF and OFF peptide assemblies showed a longitudinal effective piezoelectric coefficient (d_{33}) of 2.15 pm V^{-1} for PFF and 4.03 pm V^{-1} for OFF. Additionally, the shear effective piezoelectric coefficient (d_{34}) for OFF was determined to be 16.12 pm V^{-1}. These assemblies were integrated into piezoelectric devices and subjected to compressive mechanical stress to evaluate their performance. The piezoelectric device based on PFF produced 1.4 V and 52 nA of output voltage and current, respectively, under a 55 N force. In contrast, the OFF-based device yielded a comparable output voltage of 0.45 V and current of 39.3 nA, but with a lower force of 23 N, showcasing superior piezoelectric performance. This research demonstrates the ability to modify the primary structure of biomaterials to influence their electrical properties.

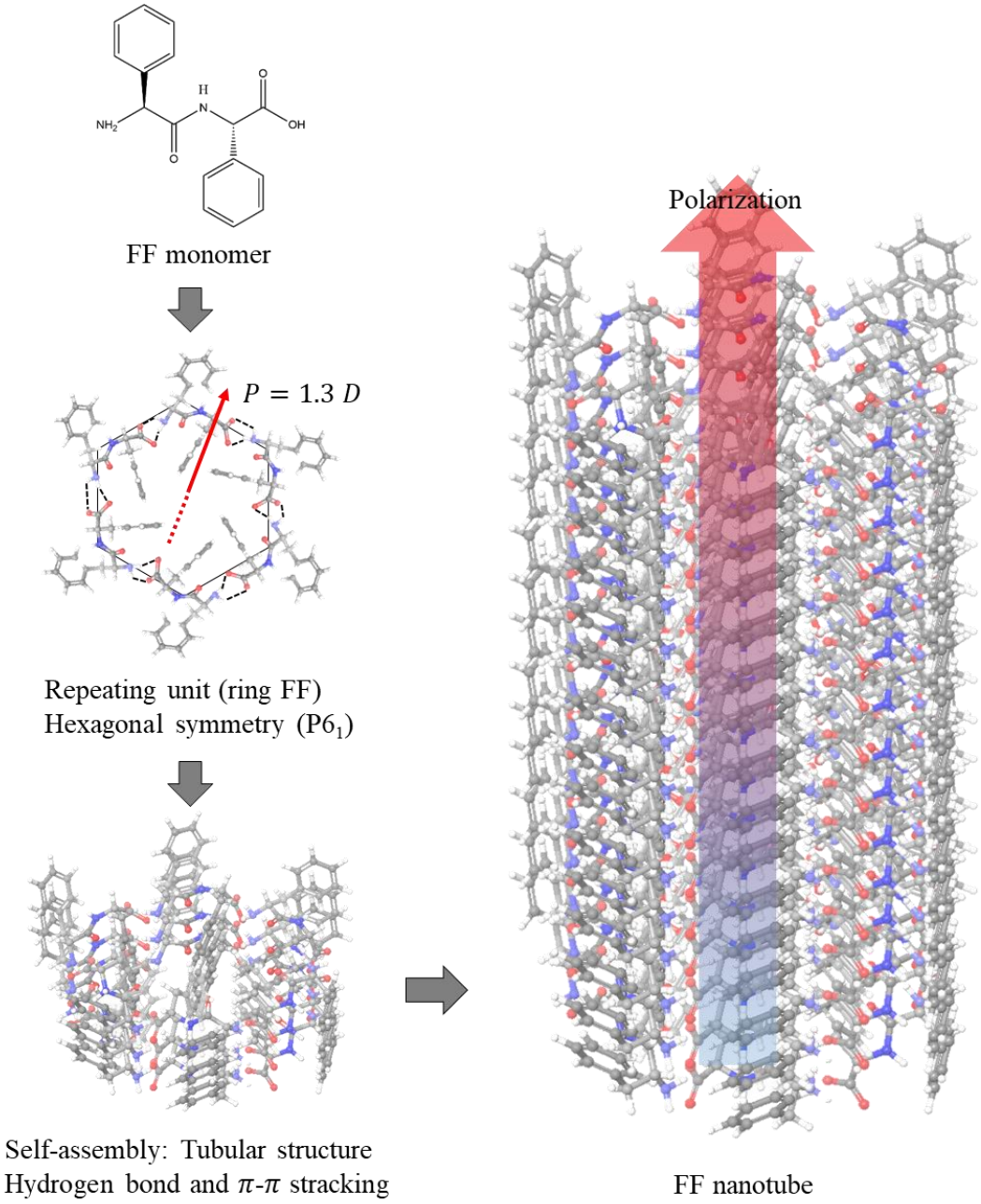

Figure 1-13. The hierarchical structures of diphenylalanine (FF) peptide assembly involve six FF monomers forming a repeating unit in a hexagonally symmetric structure. This structure exhibits a spontaneous polarization of 1.3 D perpendicular to the plane. The repeating units are stacked through hydrogen bonds and π-π stacking, resulting in self-assembled FF peptide tubular structures.

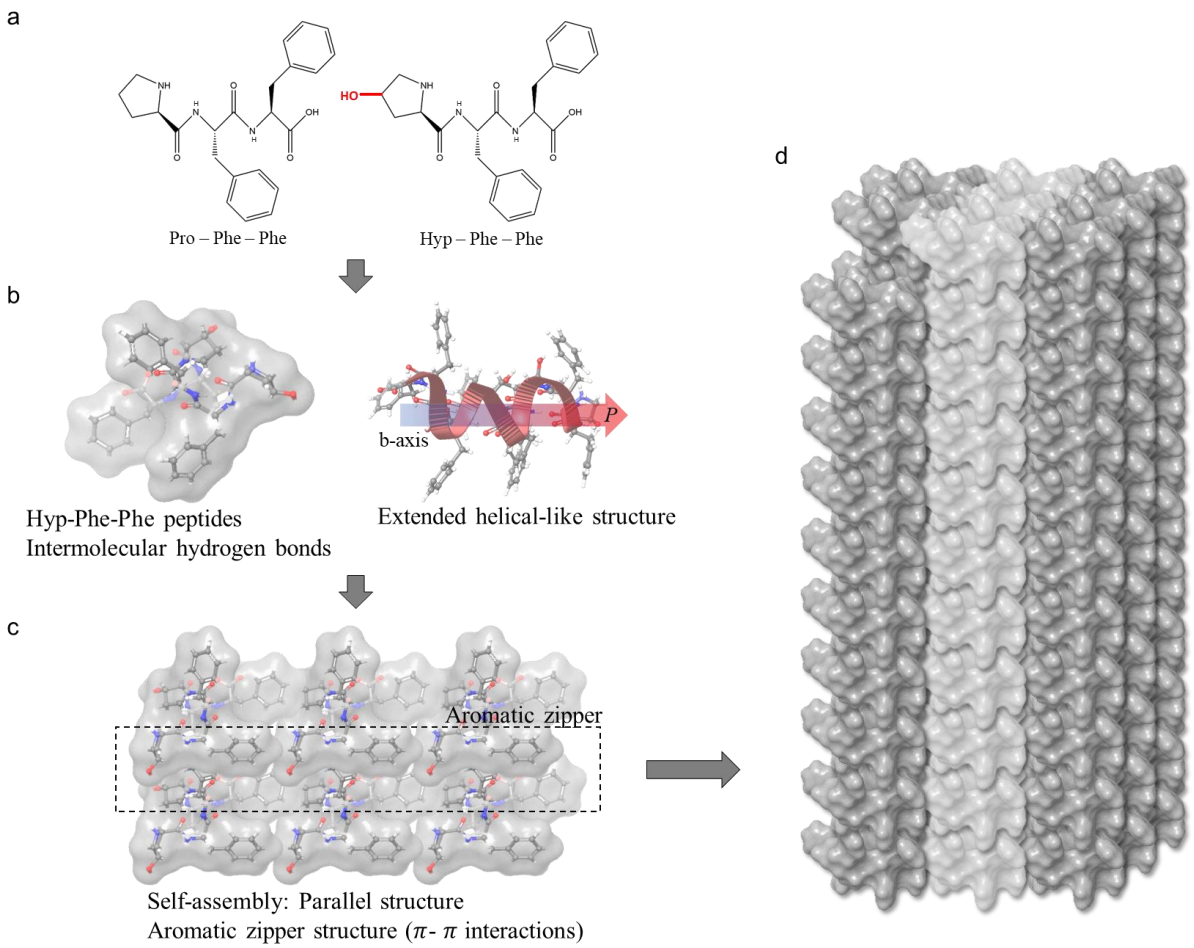

Figure 1-14. The hierarchical structures of Pro-Phe-Phe (PFF) and Hyp-Phe-Phe (OFF) peptides. (a) The chemical structures of the tripeptides PFF and OFF. (b) OFF peptides form through intermolecular hydrogen bonds, creating an extended helical-like structure. The net dipole moment of the molecule aligns along the helical axis, with molecular and crystal dipole moments of 6.7 and 1.9 D, respectively. (c) OFF peptides assemble in parallel structures using aromatic zipper structures. (d) OFF peptides self-assemble into fibrillar structures.

Material	Electrical characteristics	Symmetry	Methods	Refs.
FF	$d_{33,\mathrm{eff}} = 17.9$	Hexagonal	PFM	[323]
	1.4 V, 39.2 nA, 3.3 nW cm^{-2} at 60 N	($P6_1$)	Piezo-device	
	$d_{33,\mathrm{eff}} = 18.91$		PFM	[324]
	3.4 V, 235 nA, 9.98 W m^{-3} at 90 N		Piezo-device	
	$d_{15,\mathrm{eff}} = 60$		PFM	[316]
	$\begin{pmatrix} 0 & 0 & 0 & -10 & 80 & 0 \\ 0 & 0 & 0 & 80 & 10 & 0 \\ 4 & 4 & 18 & 0 & 0 & 0 \end{pmatrix}$		PFM	[322]
	$d_{33} = 9.9$		PFM	[342]
	$d_{15} = 46.6$		PFM	[325]
	2.8 V, 37.4 nA, 8.2 nW at 42 N		Piezo-device	
	$p = 2$		Quasi-static	[330]

			method	
	$d_{15,\mathrm{eff}} = 62.3$ (porphyrin treated)		PFM	[343]
	2.6 V, 5.8 μA cm^{-2}, 3.1 μW cm^{-2} at 20 N		Piezo-device	
	$d_{15} = 64.5$ (ethanol solvent)		PFM	[326]
	1.66 V, 19.4 nA, 19.2 nW at 40 N		Piezo-device	
Cyclo-FF	350 V, 10 μA, 73.7 mW m^{-2} at 100 MΩ	Orthorhombic ($P2_12_12$)	Tribo-device	[336]
Hyp-Phe-Phe	$\begin{pmatrix} 0 & 0.2 & -0.1 & 3.5 & 0.6 & 27.3 \\ 2.4 & -1.3 & -0.1 & -2.2 & -1.4 & 0.7 \\ -0.1 & 0.3 & 4.82 & -2.2 & -27.3 & 17.1 \end{pmatrix}$	Triclinic	DFT	[59]
	$d_{33} = 4.03,\ d_{34} = 16.12$		PFM	
	1.4 V, 52 nA at 55 N		Piezo-device	
Pro-Phe-Phe	$\begin{pmatrix} 0 & 0 & 0 & 2.4 & 0 & -1.4 \\ -2.5 & 1.9 & -0.8 & 0 & -1.0 & 0 \\ 0 & 0 & 0 & 3.1 & 0 & -2.4 \end{pmatrix}$	Monoclinic	DFT	[59]
	$d_{33} = 2.15$		PFM	
	0.45 V, 39.3 nA at 23 N		Piezo-device	
Hyp-Leu-Phe	$\begin{pmatrix} 0 & 0 & 0 & -1.6 & 0 & 0.6 \\ 0.3 & 0.4 & -0.2 & 0 & -3.5 & 0 \\ 0 & 0 & 0 & 3.6 & 0 & -3.3 \end{pmatrix}$	Monoclinic ($P2_1$)	DFT	[59]

Table 2. Electrical characteristics of amino acids, including piezoelectric coefficient, d (pC N^{-1}), pyroelectric coefficient, p (μC m^{-2} K^{-1}), coercive field, E_c (GV m^{-1}), and electrical outputs of the device. Matrices in the table represent the piezoelectric tensor of the material.

1.5 Bioelectricity in proteins

Proteins play crucial roles as structural components in the body, consisting of long amino acid chains connected by peptide bonds. These molecules have the ability to adopt a variety of structures, including α-helices, β-sheets, and random coils, as well as intricate tertiary structures. Proteins can also function as subunits in larger quaternary structures. The specific structure of each protein is dictated by its unique amino acid sequence, which is influenced by various interactions such as hydrogen bonding, hydrophobic interactions, van der Waals forces, and electrostatic forces.[344,345] While proteins themselves do not conduct electricity, their structures can exhibit diverse electrical properties when exposed to external stimuli like mechanical force, heat, and contact. This section will delve into the structure and electrical characteristics of collagen, a fundamental structural protein found in the body.

A tropocollagen, which serves as the foundational unit of collagen fibrils, is approximately 300 nm long and 1.5 nm in diameter, following a right-handed hierarchical arrangement (Figure 15).[346-348] It comprises a left-handed triple helix of polypeptides (α chains) with a glycine-X-Y repeating amino acid sequence, where X and Y represent various amino acids, primarily proline or hydroxyproline.[349-351] The tropocollagen contains electrically charged amino acid residues that create a dipole moment extending from the N-terminal to the C-terminal direction.[352] Collagen fibrils are created by cross-linking tropocollagens laterally through covalent bonds, resulting in approximately 67 nm staggered spacing between adjacent tropocollagens. This arrangement forms periodic overlap and gap regions within the fibril.[353] The arrangement of collagen fibrils enables the culmination of tropocollagen polarizations, ensuring a continuous polarization across the fibril. These fibrils then organize into collagen

fibers, forming a quasi-hexagonal structure. This structural organization results in the collective dipole moments of collagen molecules aligning, which generates a macroscopic polarization along the fiber axis.[352,354,355] Minary-Jolandan et al. investigated the piezoelectric properties of collagen at the nanoscale.[352] They used collagen samples from bovine Achilles tendon, which consisted of individual collagen type I fibrils. These fibrils displayed characteristic periodic banding structures, and their piezoelectric properties were assessed using PFM measurements. A single collagen fibril underwent lateral PFM measurements, revealing an effective shear piezoelectric coefficient of 0.6 pm V^{-1} for the d_{15} mode, with no observed piezoelectric response in the radial direction. When the collagen was rotated by 180°, the PFM phase signals exhibited a 180° phase shift, indicating axial polarization of the collagen fibril. The researchers demonstrated that the polarization of the collagen fibril occurs from the N-terminal to the C-terminal direction. They further explained that the unique shear piezoelectric response, observed solely in the collagen fibril, can be attributed to its quasi-hexagonal symmetry. Using MD simulations, Ravi et al. investigated the piezoelectricity origin in collagen.[29] Their model included diverse glycine-proline-hydroxyproline sequences to construct collagen. The researchers specifically analyzed the alteration in the dipole moment, which forms from the N-terminal to the C-terminal due to peptide bonds and the hydroxyl group in the side chain of hydroxyproline, aligned longitudinally along the collagen axis. Compression of the collagen model led to a winding of its helical structure, while stretching caused the helix to unwind. This structural deformation caused a conformational change in the dihedral angles of the backbone peptides, resulting in the reorientation of the polar groups of the collagen model. Consequently, the collagen model exhibited a shear piezoelectric effect. Zhou et al. used MD simulations to show the piezoelectric effect in a collagen fibril model.[28] Their model accurately represented a quasi-hexagonally packed structure, comprising five right-handed super-twisted tropocollagens. This structure included three α-helices with the primary sequence of type I collagen, along with the distinctive "gap" and "overlap" structural features. The study investigated how the dipole moment changes under mechanical stress. It was confirmed that collagen polarizes along the fibril axis, and polarization increased with greater tensile stress. The piezoelectric coefficient, d_{33}, was determined by analyzing the slope of induced polarization against stress, yielding values of 1.10 pC N^{-1} for a tropocollagen and 2.64 pC N^{-1} for a collagen fibril. Upon stretching, they noted that the triple-helix structure of collagen uncoiled and disentangled. This caused the side chains of the collagen residues to align along the fibril axis, leading to a reorientation and change in the magnitude of their dipole moments. These computational analyses revealed the fundamental mechanism behind the piezoelectric properties of collagen by quantitatively illustrating the polarization changes at the nanoscale level. Furthermore, the authors observed that collagen fibrils have not demonstrated ferroelectric behavior in experiments, possibly due to the difficulty of polarization switching. Vivekananthan et al. designed a piezoelectric device based on collagen nanofibrils.[356] These nanofibrils were applied onto a 9 cm^2 cotton fabric and placed between aluminum electrodes. When a 5 N force was applied, the collagen nanofibril-based piezoelectric device generated an output peak-to-peak voltage of 45 V and an output current of 250 nA.

Collagen displays pyroelectric properties because of its highly structure and the existence of spontaneous polarization arising from amino acid residues aligning from the N-terminal to the C-terminal. Plepis et al. studied the pyroelectric characteristics of natural collagen extracted from bovine serosa.[357] The samples predominantly consisted of glycine, proline, and hydroxyproline, the key amino acids in collagen. The pyroelectric coefficient was determined using a direct method, where the collagen sample was placed in a thermal chamber with temperatures ranging from 293 to 313 K and heated at a rate of 0.5 K min^{-1}. At 313 K, the pyroelectric coefficient of native collagen was found to be 37 μC m^{-2} K^{-1}.

Ravi et al. employed MD simulations to investigate how collagen fibrils exhibit pyroelectric properties.[29] Their collagen model featured amino acid sequences $[(GPP)_3\text{-}GOO\text{-}(GPP)_3]_3$, with G, P, and O representing glycine, proline, and hydroxyproline, respectively. They analyzed the alterations in dipole moment along the helical axis of the collagen model at temperatures of 300, 320, and 340 K. The simulation findings showed an increase in the dipole moment of fibril from 0.994 to 1.020 D as the temperature rose from 300 to 340 K, suggesting a temperature-dependent rise in polarization. At 360 K, a partial conformational change at the N-terminal of the collagen helix structure caused unwinding features, disrupting the symmetry of the triple helix structure of the collagen fibril. The authors demonstrated the decomposition of the pyroelectric effect into primary and secondary effects to clarify how collagen exhibits pyroelectric behavior. The primary effect involves changes in electric displacement with temperature variations under constant strain, while the secondary effect results from strain-induced alterations in electric displacement due to piezoelectric contributions from thermal effects.[358] They noted that as the temperature rose to 320 K, the collagen helix structure exhibited increased winding (approximately 0.5°), which enhanced total polarization by realigning the polar groups along the helical axis. Consequently, the pyroelectric behavior of the collagen fibril was attributed to the secondary pyroelectric effect. However, its primary effect remains unclear due to computational limitations.

Collagen demonstrates triboelectric properties. In 2022, Li et al. developed collagen-based triboelectric devices, where collagen nanofiber were created using electrospinning, sized 4 cm^2, and served as the positive triboelectric layer.[359] The negative triboelectric layer was composed of poly(vinylidene fluoride). These devices were capable of producing an output voltage of 118 V, an output current of 3.8 nA, and transferred charges of 52 nC per cycle. When tested under various electrical resistors, the device exhibited a maximum power density of 21.06 mW m^{-2} at 1 GΩ.

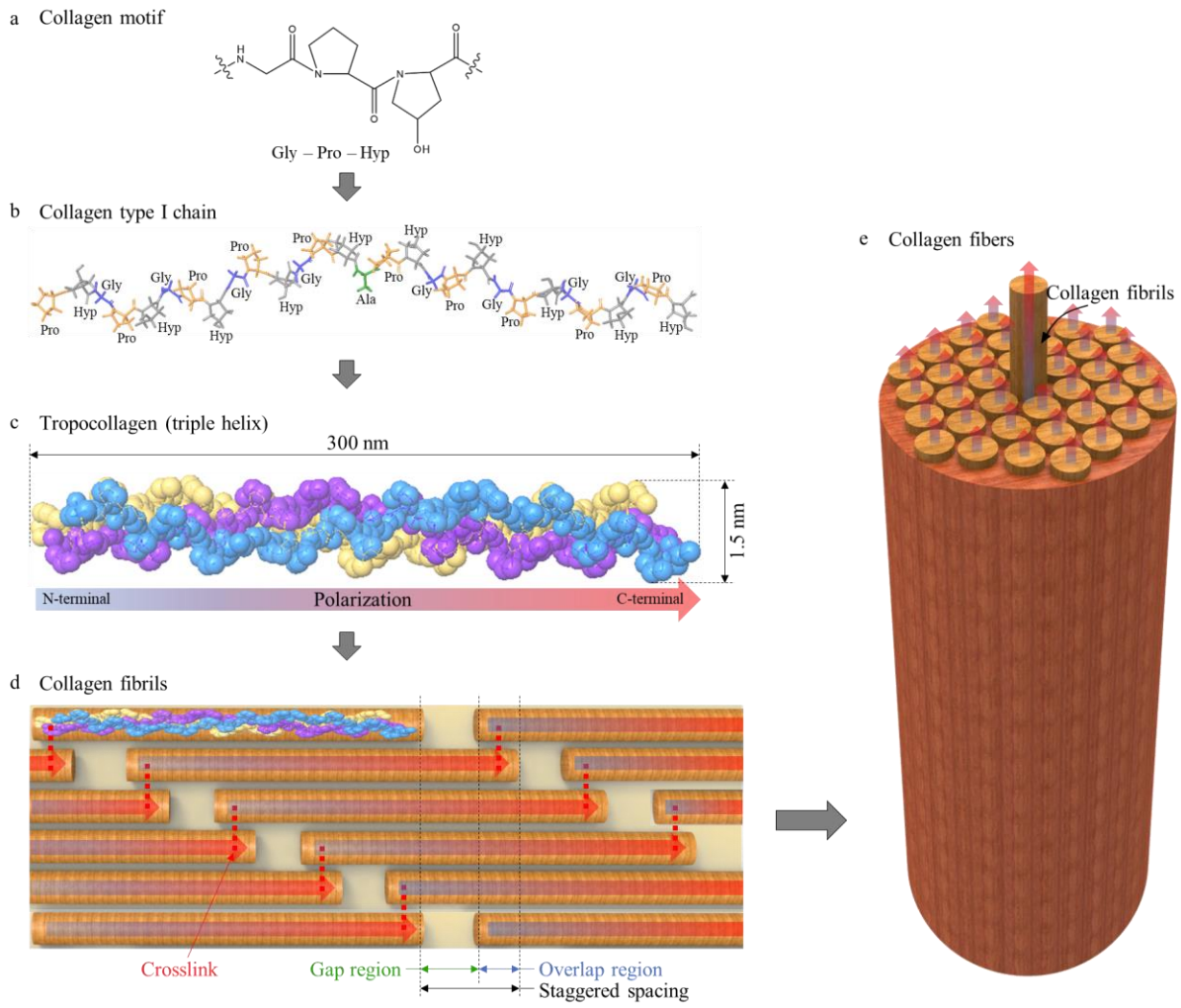

Figure 1-15. The hierarchical structures of collagen. (a) The chemical structure of the collagen motif: Gly-Pro-Hyp. (b) The chemical structure of the collagen chain, specifically Type I (PDB code: 1CAG). (c) The structure of tropocollagen, which consists of triple helices with a length of 300 nm and a diameter of 1.5 nm. (d) The structure of collagen fibrils, which are stabilized through crosslinks between collagen molecules and exhibit staggered spacing with gap and overlap regions. (e) The highly oriented structure of collagen fibers in connective tissues.

1.6 Bioelectricity in tissues

Biological tissues consist of cells and extracellular matrices, with their conductivity levels varying depending on the circumstances.[360-363] This conductivity primarily arises from the existence of ions like sodium (Na^+), potassium (K^+), chloride (Cl^-), and calcium (Ca^{2+}) dissolved in both intra- and extracellular fluids. Variations in tissue conductivity are influenced by factors such as hydration, temperature, and the concentration of specific ions. Cellular membranes also play a role by enabling the transport of ions through membrane proteins, which makes cells electrophysiologically active. For decades, electrophysiology has been a crucial

field of study in biology. This section will focus on understanding how the structural-functional relationship within extracellular matrices and other non-cellular components contributes to tissue electrical properties. Fibrous proteins such as collagen, elastin, and keratin are essential components of the matrix, imparting strength, elasticity, and structural support to tissues.[364-366] These matrix proteins are involved in creating a variety of hard and soft tissue structures throughout the body. Hard tissues are predominantly made up of organic matrices, such as collagens, along with inorganic minerals, primarily hydroxyapatite, while soft tissues are composed mainly of the matrix proteins. Differences in the proportions of these elements throughout the body impact the electrical properties of tissues. Moreover, tissues demonstrate a range of hierarchically organized structures, each displaying distinct electrical phenomena (Table 3).[367-371]

Piezoelectricity has been observed in biological tissues, both in hard tissues (e.g., bone, dentin, and cementum, etc.)[372,373] as well as soft tissues (e.g., tendon, aorta, cartilage, ligament, cornea, skin, pineal gland, intestine, etc.)[31,374-379]. Fukada et al. studied the piezoelectric effect in bone using samples from human and bovine femurs (Figure 1-16).[372] The femur bone comprises hard outer layers made of collagen and soft inner tissues. Removing the soft tissues from a bone specimen reveals a hollow structure primarily composed of highly-oriented collagen fibrils with interspersed bone minerals (hydroxyapatite). In the femur, the collagen fibrils are arranged spirally along the bone axis, with each layer alternating the direction of the spiral. This axial symmetry is evident in the properties of the bone. Applying mechanical stresses to bone specimens at different angles along the bone axis, from -90° to 90°, resulted in anisotropic piezoelectric behavior. The piezoelectric response of the bone were mainly a result of shear mechanical stresses causing the oriented collagen fibers to slip. This led to the determination of piezoelectric coefficients for the d_{14} and d_{25} modes from the piezoelectric tensor of bone, with values ranging from 0.067-0.12 pC N^{-1}. Marino et al. examined the piezoelectric properties of human cortical bone, which contains both organic and inorganic matrices.[380] Each specimen's structure was divided into three components: Bone (collagen+mineral), bone collagen, and bone mineral. The researchers investigated the anisotropic piezoelectric properties of bone by measuring its response to mechanical stress at different angles relative to the bone axis, ranging from 0 to 90°. They found that the d_{14} piezoelectric coefficients of 0.10 pC N^{-1} for bone and 1.8 pC N^{-1} for bone collagen. In contrast, the piezoelectric response for the bone mineral was negligible because of its centrosymmetric structure (space group $P6_3/m$) (Figure 1-16e). The presence of piezoelectricity in bone collagen suggests that the effect in bone is primarily attributed to the collagen matrix. The variation in the piezoelectric responses of bone collagen and bone is likely due to the lower elastic modulus of collagen compared to the higher elastic modulus of bone mineral. The research suggests that the piezoelectric properties of bone, particularly in the d_{14} mode, may be affected by its collagen content. The displacement of mineral crystals along the fibers at the collagen-mineral interface under shear stress caused by collagen could contribute to these properties. PFM measurements were employed to study the nanoscale piezoelectric properties of bones.[381]

Samples from human humerus and tibia diaphyseal fragments were prepared by cutting them in transverse (perpendicular to the diaphyseal axis) and longitudinal (parallel to the diaphyseal axis) orientations. The application of PFM measurements provided a direct method to assess the nanoscale piezoelectric characteristics within the collagen matrix of the bone specimens. A piezoelectric coefficient of 8.72 pC N^{-1} was observed in the transversely cut bone samples. This observation suggests that the piezoelectric effect primarily originates from the highly aligned collagen matrix, which facilitates the formation of peptide groups and intramolecular hydrogen bonds, leading to spontaneous polarization. The piezoelectric coefficient measured in the bone differed by two orders of magnitude from Fukada's measurement.[372] The discrepancy in measurements might be explained by the use of nanoscale PFM measurements directly on the collagen matrix, as opposed to previous measurements influenced by the microscopic scale. At the microscopic level, the presence of piezoelectric domains with different polarities could interact with adjacent fibrils, potentially reducing the overall piezoelectric response.[27] In contrast, there was no observed piezoelectricity in the longitudinally cut bone samples, which is attributed to their centrosymmetric structure. These observations are expected to deepen our understanding of how the piezoelectric effect influences bone growth, regeneration, wound healing, and tissue engineering.[13,162,382-385]

Fukada et al. demonstrated the presence of piezoelectricity in tendon using samples from bovine Achilles tendon (Figure 1-17).[374] The Achilles tendon primarily consists of collagen type I fibrils, which are highly oriented along the tendon's long axis and exhibit over 90 % crystallinity. The researchers cut the samples at various angles to investigate their anisotropic piezoelectric properties. They demonstrated the direct piezoelectric effect by applying mechanical stresses in both normal and shear directions. When normal stress was applied along the tendon axis, a piezoelectric response was observed, yielding a piezoelectric coefficient of 6.7×10^{-2} pC N^{-1} for the d_{33} mode. Conversely, applying stress perpendicular to the tendon axis resulted in a piezoelectric coefficient of 8.7×10^{-2} pC N^{-1} for the d_{31} mode. In terms of shear stresses, applying stress to cause collagen fibers to slip past each other led to a piezoelectric response both perpendicular to the shear direction and in a direction lying in the same plane as the shear stress but perpendicular to the tendon axis, with piezoelectric coefficients of 2.7 and 1.4 pC N^{-1} for the d_{14} and d_{15} modes, respectively. Fukada et al. explained this phenomenon by highlighting the helical structure of collagen fibrils, which generates a dipole moment from the N-terminal to the C-terminal through hydrogen bonds between NH and CO groups along the fibril's axis. This polarization causes collagen molecules to align in the direction of the tendon's long axis. Denning et al. investigated the piezoelectric characteristics of rat tail tendon using PFM measurements.[27] The tendon sample is comprised of collagen fibrils arranged in a hexagonal packing orientation. PFM techniques allowed for nanoscale piezoelectric characterization, enabling the determination of the piezoelectric tensor of individual collagen fibrils. Measurements were conducted on tendon sections at varying angles (0, 50, and 90°) relative to the plane perpendicular to the tendon axis. The researchers determined the piezoelectric tensor of the collagen-based tendon, revealing piezoelectric

coefficients of 0.89, -4.84, -12, and 6.21 pm V^{-1} for the d_{33}, d_{31}, d_{14}, and d_{15} modes, respectively. This study showcased a nanoscale approach to defining the piezoelectric tensor of highly symmetric collagen fibrils, indicating a narrowing of the gap between macroscopic and nanoscopic piezoelectric properties in biological materials.

Bone and tendon demonstrate potential for the pyroelectric effect, particularly due to the alignment of collagen fibers along their axes. Lang's investigation involved pyroelectric characterization of bovine femur, phalanx, and hoof tendon samples.[386] These samples are primarily composed of two major crystalline components: hydroxyapatite mineral and collagen protein. Hydroxyapatite possesses a centrosymmetric structure with a six-fold axis perpendicular to a mirror plane. The collagen molecule is classified under point group 3, which enables it to exhibit piezoelectric and pyroelectric properties. To prepare the bone and tendon samples, they were cut longitudinally and transversely along their respective axes. To remove all inorganic components, the phalanx samples underwent treatment with nitric acid. Heating and cooling of the samples were achieved by adjusting the temperature of the sample holder, while the resulting pyroelectric voltage was monitored using a vibrating reed electrometer. The pyroelectric characterization showed that longitudinally cut samples did not exhibit a pyroelectric effect. In contrast, samples cut transversely displayed a pyroelectric effect, with pyroelectric coefficients ranging from 2.5 to 4.1 nC cm^{-2} $°C^{-1}$ for phalanx, femur, and hoof tendon. These findings indicate that the pyroelectric properties are a result of the crystallographic structure of collagen orientation. Athenstaedt expanded the investigation into the pyroelectric behavior of tissues in humans and various vertebrates.[387] The study specifically explored how spontaneous polarization forms, a key requirement for showing the pyroelectric effect, in dried tissues. To measure this, pyroelectric properties were studied by observing voltage changes using a charge amplifier with precise temperature regulation. Because collagen fibrils naturally generate spontaneous polarization along their axis, the pyroelectric properties were primarily observed in the longitudinal direction of these fibrils. Interestingly, in tendons, tissues containing inorganic bone mineral exhibited lower pyroelectric properties compared to those with pure collagen structures. This difference is attributed to the organized arrangement of inorganic bone mineral within the collagen matrix. Given that inorganic bone mineral has a centrosymmetric crystalline structure that does not exhibit piezoelectricity, the pyroelectric behavior in bone tissues is mainly attributed to collagen components.

Bone tissue displays ferroelectric properties.[233] El Messiery et al. conducted a study on the ferroelectricity of bone using samples from human cortical bone in a dried state. They found that collagen fibrils in bone have varying alignments between adjacent layers, similar to the domain structure seen in ferroelectric materials. This similarity in alignment suggests a potential microscopic structural resemblance between bone and ferroelectric materials. The researchers investigated the ferroelectric characteristics of bone tissue using a ferroelectric loop tracer, following a circuit proposed by Roetschi.[388] This device measures the induced charge density when an electric field is applied. They observed a typical ferroelectric hysteresis loop in the bone tissue. The authors showed that this loop in cortical bone could be explained by the

dipolar or interspace charge electret criterion commonly seen in bone research. Later, scientists presented a more thorough illustration of ferroelectricity in the human tibia.[389] The bone specimen was obtained from the limb and dried. It was then cut into different angles according to the desired orientation. The ferroelectric analysis was carried out following Roetschi's method, but with a modification using the voltage phase shift technique to measure displacement current under an applied electric field.[388] Electric fields were applied at different angles relative to the bone axis (0, 30, 45, 60, and 90°). The researchers found that there were no differences in the ferroelectric properties based on orientation. They observed a maximum remanent polarization of 0.68 nC cm^{-2} and a coercive field of 0.95 kV cm^{-1} when the electric field was applied at a 45° angle relative to the bone axis. The bone tissue showed that it could maintain reversed polarization even after the external electric field was removed, indicating its ferroelectric properties. This suggests that the bone sample contains numerous domains with different polarization directions that can change under an external electric field. While these studies highlighted the ferroelectric nature of bone, the exact mechanism behind this behavior based on structural orientation is still unknown. Bone is mainly made up of bone collagen and bone mineral. No research has been conducted yet on the ferroelectric properties of collagen. Thus, the ferroelectric behavior of bone remains a compelling area for further investigation.

The aorta demonstrates diverse electrical properties (Figure 1-18).[31,235,376,390,391] Fukada et al. examined its anisotropic piezoelectric characteristics.[376] The elastic and robust nature of the aorta is due to its composition of fibrous elastin and collagen proteins.[392] To study its properties, samples were cut along the tubular axis and then elongated both lengthwise and widthwise. The resulting piezoelectric responses were comparable in magnitude to those of bone but with opposite polarity. The alignment of elastin and collagen fibers in the longitudinally stretched sample matched the anisotropy observed in bone. In contrast, fibers in the transversely stretched sample were oriented in the circumferential direction. Furthermore, the piezoelectric effect in elastin was verified through anisotropic piezoelectric characterization using a ligament from a bovine femur.[376] Liu et al. investigated the piezoelectric properties of the aorta at the nanoscale, focusing on its inner wall composed of fibrous elastin and collagen proteins.[235] They utilized PFM to directly measure the piezoelectric coefficient, obtaining a value of 1 pm V^{-1}. This value was found to be two orders of magnitude larger than that reported by Fukada et al. The discrepancy in results could be attributed to the nanoscale PFM measurements applied directly to the elastin and collagen matrices, contrasting with earlier measurements conducted on bulk samples.[27] In bulk samples, the opposing polarities within the piezoelectric domains might decrease the overall piezoelectric response. Furthermore, differences in sample types and levels of dryness could have also affected the results.[393]

Researchers studied the pyroelectric properties of the aorta across different temperature ranges.[376] Samples were prepared by cutting along the tubular axis both longitudinally and transversely. In both cases, the change in polarization increased linearly with temperature when the samples were dried. However, the specific mechanism behind this behavior has not yet been explored and warrants further investigation in future studies.

The ferroelectric properties of the aorta were studied using switching spectroscopy PFM.[235] Samples were taken from the porcine aortic wall, which is made up of fibrous elastin and collagen proteins. In the experiment, voltage was applied to the inner wall of the aorta samples. When a positive voltage was applied and reached the coercive voltage of 8.4 V, the polarization of the aorta reversed and persisted even after the positive bias was removed. Conversely, with a negative voltage hitting the coercive level (-10.8 V), the polarization also reversed but did not remain altered after the bias was removed. This asymmetry suggests an intrinsic outward bias in the aorta's polarization. The measurements displayed reversal hysteresis in phase and butterfly loops in amplitude, characteristic of ferroelectric materials. While collagen is thought not to exhibit ferroelectricity based on past studies[28,31,235], the ferroelectric properties observed in the aorta may stem from elastin, a crucial component of its structure. Liu et al. used PFM and MD simulations to demonstrate the ferroelectric properties of elastin and its molecular mechanism.[31] They harvested elastin samples from a porcine thoracic aorta, which exhibited a fibrous structure comprising cross-linked tropoelastin monomers. By removing collagen proteins from the sample, they obtained a pure elastin sample. The switching spectroscopy PFM measurements revealed ferroelectric hysteresis and butterfly loops, indicating that elastin maintained its ferroelectric behavior even at 473 K. MD simulations were used to investigate the polarization response and ferroelectric switching in elastin at 300 K. A model of elastin was constructed using tropoelastin chains, showing a spontaneous polarization of 801 D. When an electric field was applied perpendicular to the chain axis, the tropoelastin adjusted its configuration until its polarization aligned with the electric field, resulting in reversed polarization. The simulations demonstrated ferroelectric hysteresis under an external electric field, with an estimated Curie temperature of 580 K. These computational analyses enhanced the understanding of the aorta's ferroelectric mechanism by illustrating how the polarization of elastin building blocks changes under an electric field.

Recent discussions have emerged regarding the ferroelectric nature of the aorta. In 2017, Lenz et al. proposed the argument that the aorta may not exhibit ferroelectric properties.[394] They conducted examinations of ferroelectric and piezoelectric effects using a multiferroic tester and piezometer. The results showed that the electric displacement had a linear relationship with the electric field up to 6 MV m^{-1}, indicating dielectric behavior rather than the characteristic hysteresis of ferroelectric materials. Similarly, the strain displayed a parabolic response to the electric field, lacking the typical butterfly loop feature of ferroelectricity. Based on these findings, the authors suggested that the aorta is neither ferroelectric nor piezoelectric, but rather behaves as a dielectric material. These controversial results may be due to common artifacts such as Maxwell strain and electrostriction.[394-396]. Maxwell strain is the result of polar molecules or ions reorienting in response to an electric field, leading to temporary dipole moments and material deformation. Unlike in ferroelectric materials, this induced dipole moment and resulting strain in non-ferroelectric materials are reversible and linearly correlated with the applied electric field, returning to their original state once the field is removed. Electrostriction, in contrast, does not involve permanent

reorientation or switching of polarization; it results in reversible deformation due to dipole reorientation in response to the electric field. These findings emphasize the intricate nature of studying ferroelectricity in biological tissues and highlight the necessity for further research using well-defined biological systems and molecular-level characterization.[397]

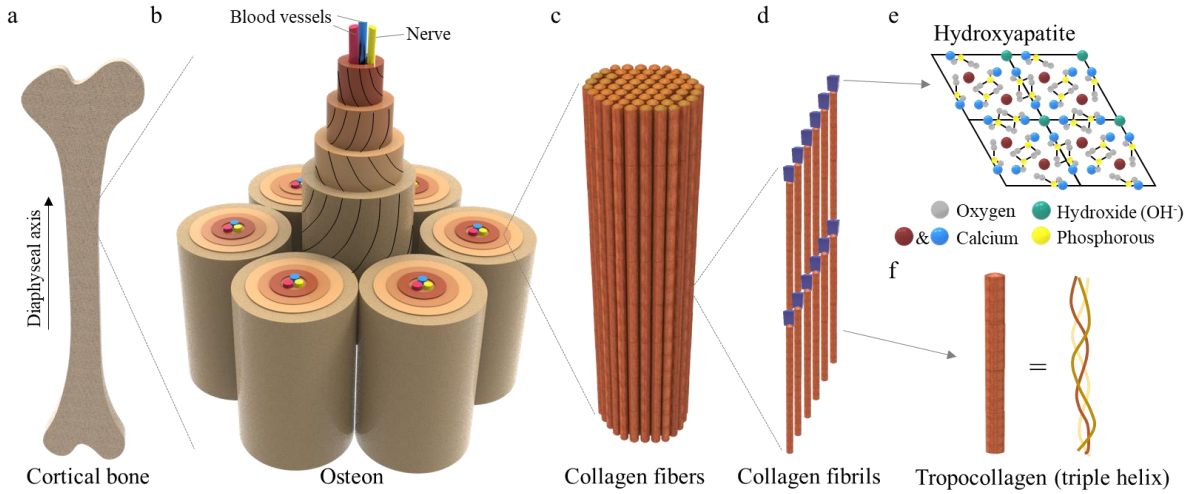

Figure 1-16. The hierarchical structures of bone. (a) Schematic image of bone. (b) The basic structural unit of bone, known as the osteon, is composed of concentric layers of bone matrix called lamellae. (c) Collagen fibers are the primary structural component of bone, composed of collagen fibrils. (d) Collagen fibrils are bundles of collagen molecules (tropocollagens) arranged in a staggered, overlapping pattern. (e) Hydroxyapatite, a mineral in bone, has crystals deposited between the collagen molecules in a hexagonal centrosymmetric structure. (f) Tropocollagen is the basic unit of collagen in tissues, forming a triple helix structure consisting of three polypeptide chains.

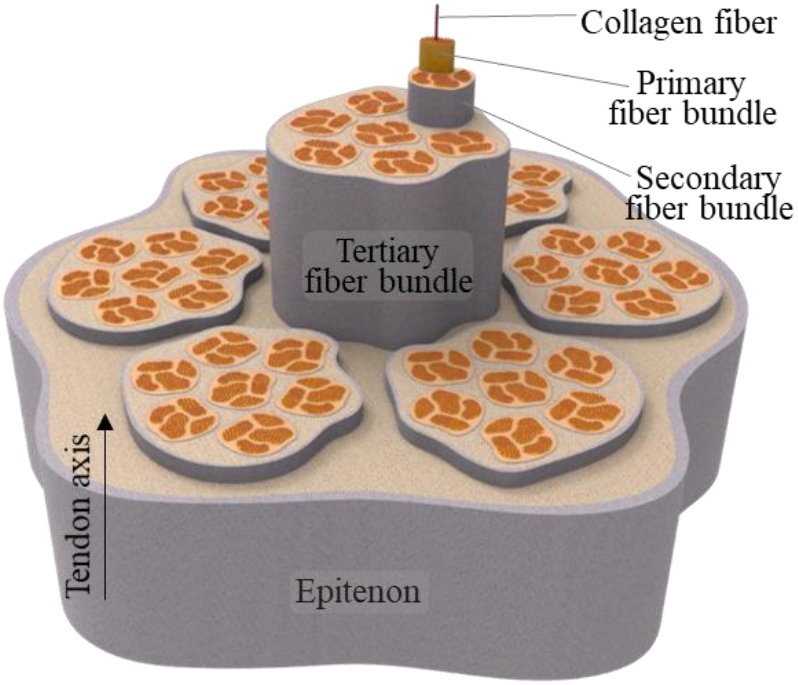

Figure 1-17. The hierarchical structure of a tendon includes collagen fibers as the primary structural component, aligned parallel to each other. Individual collagen fibers group together to form primary fiber bundles, which are surrounded by a thin layer of connective tissue called endotenon. Primary bundles then group to form secondary fiber bundles, surrounded by a thicker layer of connective tissue called peritenon. Tertiary fiber bundles, formed by grouping secondary bundles, are surrounded by a layer of loose connective tissue containing blood vessels and nerves, known as epitenon.

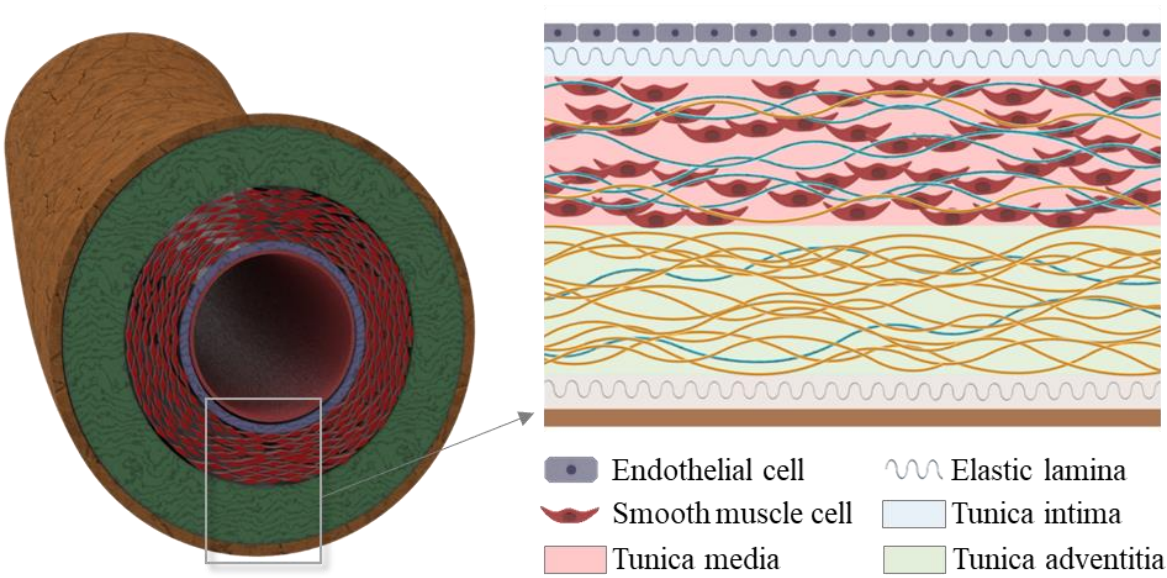

Figure 1-18. The hierarchical structure of aorta. It consists of an innermost layer lined by a single layer of endothelial cells. The tunica intima, a thin connective tissue layer, maintains the artery wall's integrity and regulates substance passage between blood and surrounding tissues. The tunica media, the thickest layer, is separated from the tunica intima by an elastic lamina and is composed of collagen fibers, elastin fibers, and smooth muscle cells. The outermost layer, the tunica adventitia, provides structural support to the artery and mainly consists of collagen fibers.

Material	Electrical characteristics	Methods	Refs.
Bone (man)	$d = 0.067 - 0.12$	Quasi-static & dynamical method	[372]
Bone (bovine)	$d = 0.2$	Dynamical method	
Demineralized phalanx (bovine)	$p = 0.0038$	Vibrating reed electrometer	[386]
Femur (bovine)	$p = 0.0036$		
Bone (human tibia)	$E_c = 0.95$	Sawyer method	[389]
Enamel (human teeth)	$d = 0.25 - 0.51$ (with organic material) $d = 0.04 - 0.26$ (without organic material)	PFM	[398]
Dentine (human teeth)	$d = 0.49 - 0.69$ (with organic material) $d = 0.13 - 0.22$ (without organic material)		
Dentine (human teeth)	$d = 0.15 - 0.25$	PFM	[399]
Dentine and cementum (human teeth)	$p = 0.0015 - 0.025$	Electrometer	[400]
Tendon (bovine Achilles)	$d_{14} = -2.7,\ d_{15} = 1.4,$ $d_{33} = 0.067,\ d_{31} = 0.087$	Dynamical method	[374]
Tendon (horse Achilles)	$d_{14} = -1.9,\ d_{15} = 0.53,$ $d_{33} = 0.067,\ d_{31} = 0.013$		
Femur (horse)	$d_{14} = -0.22,\ d_{15} = 0.043,$ $d_{33} = 0.0033,\ d_{31} = 0.0033$		
Tendon (rat tail)	$\begin{pmatrix} 0 & 0 & 0 & -12.00 & 6.21 & 0 \\ 0 & 0 & 0 & 6.21 & 12.00 & 0 \\ -4.84 & -4.84 & 0.89 & 0 & 0 & 0 \end{pmatrix}$	PFM	[27]
Tendon (bovine hoof)	$p = 0.0041$	Vibrating reed electrometer	[386]
Collagen type I (bovine Achilles)	$d_{15} = 0.6$	PFM	[352]
Collagen type I (bovine Achilles)	$d_{15} = 2.2$	PFM	[401]
Collagen type II (chicken sternum cartilage)	$d_{15} = 0.7$		
Collagen (bovine serosa)	$d_{14} = 0.096$	Resonance measurement	[402]

	$p = 37$	Direct method	[357]
Scleral collagen (bovine and human)	$d_{31} = 12.6 - 31.8$	Rheolograph solid	[377]
Tropocollagen (Collagen type I)	$d_{33} = 1.10$	MD	[28]
Collagen microfibril (9 tropocollagens)	$d_{33} = 2.64$		
Collagen film	45 V, 250 nA at 5 N	Piezo-device	[356]
Collagen film	118 V, 3.8 nA, 21.06 mW m^{-2} at 1 GΩ	Tribo-device	[359]
Elastin (murine lung)	$d_{33,eff} = 0.1$	PFM	[403]
Elastin (porcine aorta)	400 μC m^{-2} K^{-1}	PFM	[31]
Human skin	$d_{14} = 0.01 - 0.03$ (Epidermis)	Quasi-static method	[404]
	$d_{14} = 0.05 - 0.1$ (Dermis)		
Human skin (Epidermis)	$d_{33} = 0.02 - 0.19$	Quasi-static method	[378]
	$p = 0.021 - 0.27$		
Gelatin (porcine skin)	$d_{33} = 24$ (interlocked film)	Ferroelectric tester	[405]
	$d_{33} = 4$ (planar film)	Piezo/pyro-device	
	$p = 13$ (interlocked film)		
	$p = 1.1$ (planar)		
Keratin	$d_{14} = 1.8$	Quasi-static method	[406]
Silk	$d_{33} = 8.39$	PFM	[407]
Silk (Spider silk)	$d_{33,eff} = 0.36$	PFM	[408]
	21.3 V, 0.68 μA, 4.56 μW cm^{-2} at 14 MΩ	Piezo-device	
Silk (Bombyx mori silkworm)	$d_{14} = 0.01 - 1.50$	Quasi-static method	[409]
	~15 V, 2.5 μA, 4.3 mW m^{-2} at 5 MΩ	Tribo-device	[410]
Lysozyme	19.3 pC N^{-1}	PFM	[411]
Lysozyme	$p = 1441$	Quasi-static method	[412]

Table 3. Electrical characteristics of amino acids, including piezoelectric coefficient, d (pC N^{-1}), pyroelectric coefficient, p (μC m^{-2} K^{-1}), coercive field, E_c (GV m^{-1}), and electrical outputs of the device. Matrices in the table represent the piezoelectric tensor of the material.

1.7 Virus model system

1.7.1 Virus-based nanomaterials

A virus is an infectious microorganism that replicates within a host cell.[413] Traditionally, viruses have been considered invaders that threaten living organisms.[414,415] Nowadays, researchers use them as programmable biomolecules for myriad biological applications due to their well-defined structure (e.g., shape, size, and symmetry) and tenability.[416-419] Essentially, viruses have genetic material, such as DNA or RNA, covered by coat proteins in diverse shapes, sizes, and symmetries, including filamentous, spherical,

enveloped, and complex structures.[420-422] Filamentous viruses (e.g., M13 bacteriophage (phage), tobacco mosaic virus, and influenza A virus) have a high-aspect ratio in helical arrangements.[423-425] Spherical viruses (e.g., cowpea chlorotic mottle virus, adenovirus, and herpesvirus) exhibit a spherical shape with icosahedral symmetry.[418,426-428] Enveloped viruses (e.g., coronavirus, influenza virus, human immunodeficiency virus, and zika virus) have an additional outer envelope derived from the host cell membrane, exhibiting shapes like spheres, irregular shapes, or long filaments.[429-435] Complex viruses (e.g., T7 phage, poxvirus, and geminivirus) combine icosahedral or helical structures.[436-438] The structural features of these viruses are well-defined, sophisticated, and studied, showcasing highly ordered coat protein assemblies.[439-442] Notably, the variability of virus structures exhibits unique electronic characteristics due to their diverse surface charge properties.[443-446] A tremendous characteristic of viruses in biotechnology is their tunability for use as programmable tools, achievable through genetic engineering.[417,447,448] The fundamental principle of protein expression in viruses involves manipulating specific genes of interest within the viral genome.[449,450] Once the gene of interest is cloned into a plasmid, it can be inserted into the viral genome through recombinant DNA technology.[451-454] Through bacterial infection of the resulting genetically modified viral genome, viruses are reconstructed by assembling genetically modified coat proteins.[455] This tunable characteristic enables a wide range of programmable biomolecule fabrication in a precisely controlled manner.[456-459] Therefore, the structural flexibility of viruses makes it possible to understand the structure-function relationship of bioelectrical phenomena and develop various virus-based nanomaterial fabrications and bioelectrical applications.

1.7.2 M13 bacteriophage model system

1.7.2.1 Structural features of the M13 phage

M13 phage serves as an excellent model system for studying the structure-function relationship in bioelectricity. M13 phage is a bacterial virus that infects *Escherichia coli* (*E. Coli*) bacteria.[460,461] With a filamentous shape measuring 880 nm in length and 6.6 nm in diameter, this structure provides a large surface area for functionalization and interaction with different materials (Figure 1-19a).[462] Comprising 2700 copies of α-helical major coat proteins (pVIII), M13 phage encloses its single-stranded DNA genome, consisting of 50 residues, generates spontaneous polarization from the N-terminal to C-terminal direction, establishing it as an intrinsic polarization biomolecule.[3] Assembled in a five-fold rotational and two-fold screw symmetry with a ~20° tilt angle relative to the long axis of the phage, M13 phage exhibits a non-centrosymmetric structure (Figure 1-19b and 1-19c).[1,3,423] The minor coat proteins (e.g., pIII, pVI, pVII, and pIX) of M13 phage play a critical role in its function. These proteins, distinct from the major coat proteins, participate in various aspects of the phage's life cycle, including host recognition, infection, and assembly.

Genetic engineering of the M13 phage offers a variety of advantages and applications

in biotechnology (Figure 1-20).[463] Modifying these proteins allows researchers to customize the phage for specific applications, enhancing its interaction with certain materials or enabling specific functions within bioelectrical devices.[1-3] Genetically engineered M13 phage, displaying desired peptides and proteins, can serve as a building block for bioelectrical studies.[1,3-5,464-466] The M13 phage has been used as a template for bioelectrical applications, such as electrodes for batteries[467-470] and solar cells.[471-474] The performance can be enhanced through the genetic engineering of the phage by displaying specific binding motifs on the protein surface. Additionally, the use of phages in bioelectric studies is particularly advantageous because the surface charge and dipole moment can be precisely tuned through genetic engineering.[1-3,444] This precise control extends from the nanoscopic subunit, exemplified by the pVIII protein, to the macroscopic scale, encompassing the entire M13 phage.[1-3] Moreover, the structure of the M13 phage, including its shape, dimension, and size, can be precisely tuned through genetic engineering.[423,475] This control over the surface charge, dipole moment, and structural characteristics provides researchers with the unique advantage of optimizing the electrical and physical properties of the phage across multiple length scales.[2,3,423,444,475] The ability to manipulate these characteristics from the molecular to the macroscopic level enhances the versatility of M13 phages, making them invaluable for exploring and manipulating bioelectric phenomena in various research applications.[476-479]

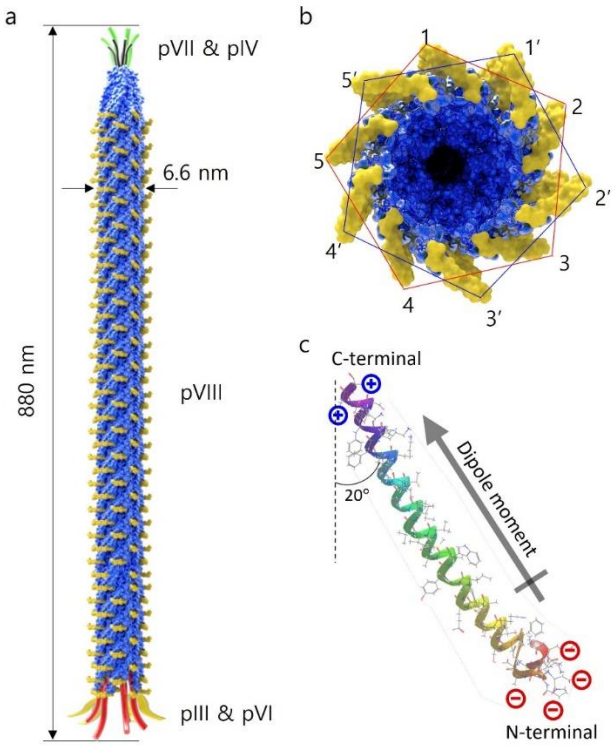

Figure 1-19. The structure of the M13 phage. (a) M13 phage has a filamentous shape measuring 880 nm in length and 6.6 nm in diameter. (b) and (c) It is composed of 2700 copies

of pVIII proteins with five-fold rotational and two-fold screw symmetry, exhibiting a non-centrosymmetric structure. pVIII protein consists of 50 residues and forms a dipole moment from the N-terminal to C-terminal direction.

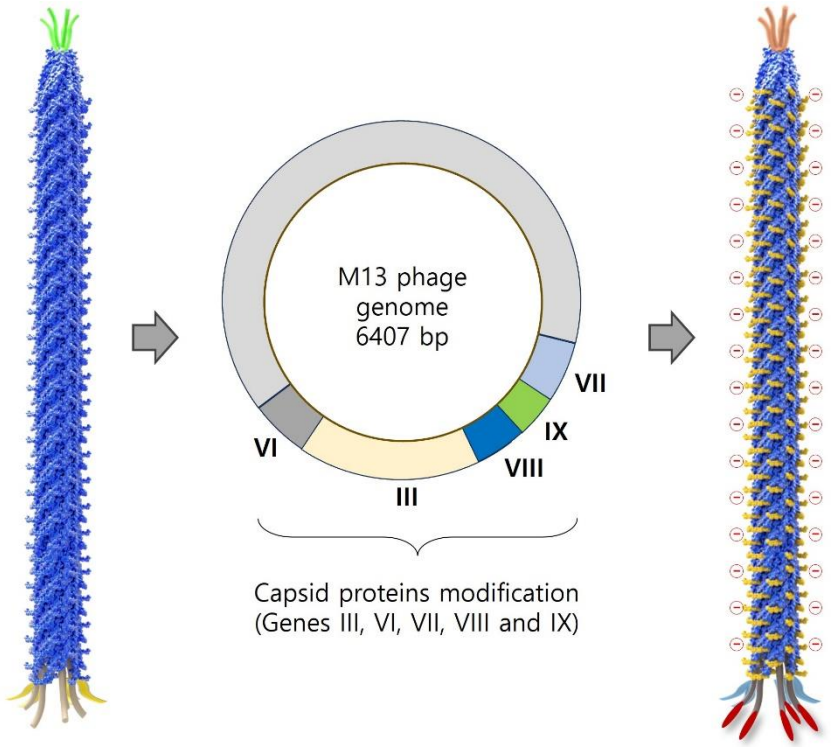

Figure 1-20. Schematic of the M13 phage depicting the arrangement of coat proteins. The surface structure of these coat proteins can be modified through genetic engineering techniques. This allows for the customization of the molecular configurations of the phage surface to align with specific characteristics, enabling the presentation of the corresponding peptide motif on the coat proteins of the phage.

1.7.2.2 Biocompatibility and mass production

M13 phages are generally considered to be biocompatible due to being non-pathogenic to humans and other organisms, signifying their well-tolerance by biological systems (Figure 21).[478] This characteristic is essential for applications where the phage interacts with living cells or tissues, such as in bioelectrical devices[478] and biomedical devices.[480-482] Moreover, the capacity of M13 phage for mass production is a significant advantage.[461] The phage naturally replicates within its bacterial host, allowing for efficient and cost-effective production on a large scale (Figure 1-21). This scalability is crucial for biomaterial research, enabling researchers to obtain substantial quantities of the phage for systematic and reproducible studies. Specifically, it is invaluable that we can produce identical genetically programmed

biomolecules in massive amounts. The ease of production with genetically engineered biomolecules can contribute to the feasibility of conducting experiments with statistically significant sample sizes and electronic characteristics, thereby enhancing the reliability and robustness of the findings.

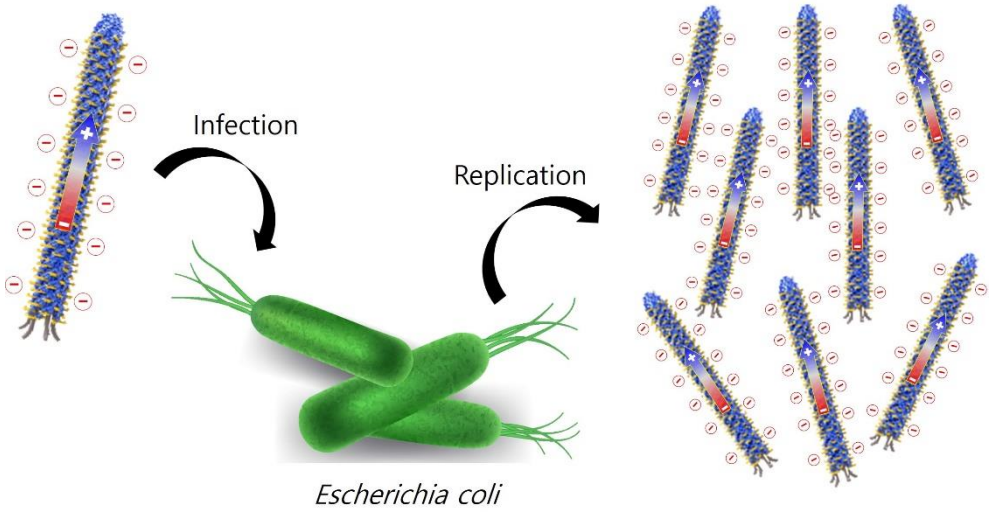

Figure 1-21. M13 phages can be efficiently produced in large quantities through bacterial infection, providing a cost-effective means of generating a significant number of phages. The life cycle of the M13 phage involves rapid replication, allowing for quick and scalable production of the phage.

1.7.2.3 Self-assembled nanostructures

High ordered building blocks are critical for the fabrication of self-assembled nanostructures, providing precise control over the size, shape, and arrangement, and ensuring a reproducible process.[423,462,483,484] The M13 phage has been widely studied as a building block, serving as a framework for bioelectrical applications.[1,3,4,466] The body of the M13 phage is constructed by pVIII proteins in a helical manner with a high-aspect ratio, resulting in a highly organized surface with regular structural characteristics that facilitate consistent and predictable nanostructure.[423,462] Additionally, the positively charged domain of the pVIII proteins covers the phage DNA, exposing the negatively charged domain to the surface of the phage.[2,423] This imparts negative characteristics to the phage surface at the exterior and contains spontaneous polarization at the interior of the proteins.[3] The M13 phage is highly organized not only in coat protein structures but also in surface charge and electric polarization structures.[3] The pVIII proteins interact with each other non-covalently, imparting monodispersive characteristics to the M13 phage and enabling various interactions (e.g., hydrogen bonding, hydrophobic-hydrophobic interactions, electrostatic interactions) during the self-assembly process.[462-464,485] The pVIII protein, consisting of 50 amino acids with varying numbers of positively or negatively charged and hydrophobic amino acids, make the

monodispersity of the phage sensitive to variations in pH, temperature, and ionic strength.[462,466,486,487] By controlling these parameters in the phage solution, the M13 phage undergoes varying self-assembly mechanisms, influencing the fabrication of diverse self-assembled nanostructures.[462,466,486,487] Furthermore, surface modification of the M13 phage can be achieved through both genetic engineering and chemical modification.[463,488] The M13 phage can be genetically modified by incorporating specific peptide motifs on its surface, contributing to the self-assembly process by changing the monodispersive characteristics of the phage and exhibiting specific interactions between the pVIII proteins and counter materials.[467,468,489] Chemical modification allows the M13 phage to be functionalized to display specific chemical functional groups on its surface.[490,491] The ability to transform its structure makes the M13 phage diverse in self-assembled nanostructure fabrication.[490,491] Therefore, the highly organized helical structure and surface characteristics of the M13 phage, particularly he pVIII proteins, make it a crucial and versatile building block for self-assembled nanostructures, with controllable features influenced by environmental factors.

1.7.2.4 M13 phage-based piezoelectric energy generation

Due to its well-defined shape and tunability for displaying functional peptides or proteins on the coat proteins[1], the M13 phage has been widely used in bioelectrical energy generating systems.[1,3,4,466] In 2012, Lee et al. In 2012, Lee and colleagues explored the piezoelectric properties of the M13 phage by subjecting it to electric pulses and then measuring the resulting mechanical responses with PFM measurements.[1] They utilized lateral and vertical PFM measurements to examine both the axial and lateral components of the phage's piezoelectricity. Initially, a monolayer of M13 phage film was developed on gold substrates. Their lateral PFM analysis indicated a strong signal when the PFM tip moved parallel to the long axis of the phage alignment, whereas scanning perpendicular to this direction resulted in a weaker signal due to the antiparallel alignment of the monolayer phage film. Furthermore, vertical PFM characterization confirmed the phage's capability to generate out-of-plane piezoelectric signals. The researchers demonstrated that modifying the phage's charge through genetic means could enhance its piezoelectric response. Introducing additional negatively charged residues, such as glutamate, significantly improved its piezoelectric properties. The engineered phage with four glutamate residues (4E) exhibited a 2.3 times increase in piezoelectric response compared to the wild-type (WT) phage. Moreover, as they produced thicker phage films, they observed an increase in the piezoelectric response up to 200 nm (about 30 layers of phages), after which the piezoelectric signal saturated. This saturation phenomenon was attributed to the reduced clamping effect with increasing film thickness, allowing for greater deformation and consequently a higher piezoelectric response. Hence, both chemical and physical structure manipulations can enhance the piezoelectric properties of phage films. Subsequently, in 2019, Heo et al. created hierarchically structured piezoelectric thin films with a two-dimensional (2D) dot pattern.[466] They achieved this pattern by using a self-templating

technique that controlled the ionic strength and phage concentration. This technique induced finger instability and stick-slip motion at the air-liquid-solid interface, allowing for localized phage deposition at the substrate's meniscus. The resulting 2D-dot patterned 4E-phage-based piezoelectric devices showed an output voltage of 0.95 V and an output current of 94 nA. The improved piezoelectric performance was attributed to the greater crystallinity of the smectic-ordered nanofiber bundles, which possessed a pseudo-hexagonally packed crystalline structure leading to alignment of dipole moments. Furthermore, in 2019, Lee et al. reported that the M13 phage exhibited a significantly higher vertical piezoelectric coefficient compared to its lateral counterpart.[4] To explore this vertical piezoelectric behavior, they modified the minor coat proteins of the phage by introducing six-histidine (6H) residues capable of binding to nickel-nitriloacetic acid (Ni-NTA). Through a self-assembly process using polydimethylsiloxane (PDMS) templates, they arranged the phages in a vertical orientation on gold electrodes. These vertically engineered phages demonstrated a 3.3 times increase in effective piezoelectric coefficients compared to the laterally aligned ones (13.2 and 3.96 pm V^{-1}, respectively). The researchers attributed this improved piezoelectric behavior to the unique structural arrangement of the pVIII major coat protein, which is tilted at a 20° angle along the phage's long axis, resulting in a stronger piezoelectric response in the vertical direction.

Despite considerable progress in optimizing the piezoelectric performance of the phage, a comprehensive understanding of the intrinsic piezoelectric properties of the phage at the molecular level remains elusive. Hence, further investigation into the molecular mechanisms of phage piezoelectricity under different modes of mechanical stimulation is essential for comprehending its role in applications related to mechanical energy conversion.

1.8 Challenges in the structure-function relationship in biomaterials

Biological systems produce electrical signals through various mechanisms, including mechanical stresses, temperature variants, biochemical reactions, and electric fields.[1-3,31,371,492] The increasing importance of using these biological signals for electricity generation holds promise for bioelectrical applications, such as biomedical devices, biosensors, and bioelectronic devices, especially applicable for living tissues and cells.[493-495] Biomaterials, in particular, are attractive for harvesting energy due to their distinctive characteristics that can be leveraged to develop sustainable, biocompatible, and versatile energy technologies.[1-4,191,496,497] However, despite the growing demand for biological energy harvesting systems, biomaterials typically present challenges such as low power output, limited efficiency, and structural intricacy when compared to traditional energy sources.[479,498,499] Furthermore, optimizing their performance lacks a straightforward approach.[500-502] Understanding the fundamental molecular mechanisms of bioelectrical systems remains a formidable task due to the intricate nature of biological systems.[500-502] Biological building blocks such as nucleic acids, proteins, and tissues, exhibit diverse electrical responses to various external stimuli.[269,499,503-505] Nucleic acid exhibits electrical responses due to their inherent electric potential distribution

along their phosphate backbones.[21,506] The change in electric potential upon external stimuli allows nucleic acids to be used for nucleic acid machines[507], nucleic acid-based sensors[508], and carriers used for controlled drug release.[509] The electric potential of proteins can be manipulated under structural deformation, temperature change, and electric field applications. These electrically responsive phenomena of proteins can be applied to protein mechanics[510], soft robotics[511], energy harvesters[189,512], and molecular sensing systems[3]. At the tissue level, tissues exhibit electric potential generation under mechanical stresses, temperature variations, and electric field application. These electrically responsive phenomena of tissues can be observed in bone and tissue regeneration[513,514], and cell membrane regulation.[515,516] Understanding the underlying mechanisms of each elementary component is crucial because these biomaterials react in highly complex ways, resulting in intricate and often unpredictable outcomes in bioelectricity.[21,369,378,517-520] This inherent complexity makes unraveling the intricacies of bioelectricity more challenging.[369,520] Nevertheless, since this understanding forms the basis of biological energy conversion technologies, it is important to comprehend their underlying molecular mechanisms.[521-525] In contrast, conventional organic/inorganic materials, while possessing relatively simple structures and well-documented characteristics, lack the dynamic properties and versatility of biological systems.[526,527] The intricacy and heterogeneity of biological systems make it challenging to accurately reproduce them using organic/inorganic materials. Furthermore, the ability to modify materials at the molecular level is constrained by the scarcity of inherent functional groups, strong bonding characteristics, and limited reactivity.[528-530] Therefore, a suitable model system is required to understand and optimize biological electricity at the molecular level.

1.9 Thesis outline

My work focuses on investigating the structure-function relationship in biomaterials using the M13 phage as a model system. The filamentous structure of the phage provides a significant surface area with 2700 copies of genetically engineerable major coat proteins. These proteins assemble into a non-centrosymmetric structure with spontaneous polarization, exhibiting interesting stimuli responsive electrical properties. Phage genome engineering allows precise customization, providing control over surface charge and dipole moment and offering researchers unprecedented control for exploring the electrical responses to external stimuli (e.g., friction, mechanical stress, heat, and chemical environment). This represents bioelectrical energy conversion mechanisms at the molecular level. In the upcoming chapters, the exploration of triboelectricity, piezoelectricity, and pyroelectricity in the context of M13 phage bioelectrical applications will unfold.

In Chapter 2, I demonstrate the triboelectric properties of the M13 phage, which involve the generation of electrical charge resulting from frictional interactions. This chapter will delve into the molecular mechanisms and potential applications of triboelectricity in M13 phage-based triboelectric devices. Firstly, the triboelectric charging and discharging behavior

of the M13 phage, characterized by the KPFM technique, is described. Next, the underlying principle of the triboelectric effect of the phage is studied by demonstrating the energy levels through computational methods. Lastly, the output performance of the phage-based triboelectric device is demonstrated.

In Chapter 3, I investigate the piezoelectric properties of the M13 phage, focusing on its ability to generate electric fields in response to mechanical stress. This section will discuss the fundamental principles of piezoelectricity in the phage and its applications. To begin, a computational study on the dipole moment of the phage—the origin of the piezoelectric effect—and its directional dependence under various mechanical stresses is examined. Next, the relationship between surface charge engineering, dipole moment, and the piezoelectric response of the phage is explored using electrostatic force microscopy (EFM) and PFM. Finally, the directional dependence of the piezoelectric output is illustrated by fabricating M13 phage-based piezoelectric devices.

In Chapter 4, I explore the pyroelectric properties of the M13 phage, which enable it to generate electric charge in response to temperature changes. This discussion will encompass the underlying pyroelectric mechanisms of the phage and highlight the applications of pyroelectric properties in areas such as energy harvesting and molecular sensing systems. First, the pyroelectric effect of the M13 phage, characterized by the KPFM technique, is demonstrated. Next, the molecular mechanisms of the pyroelectric effect in the M13 phage, studied through MD simulations and circular dichroism (CD) spectroscopy, are examined. Lastly, the applications of phage-based pyroelectric devices for energy harvesting and molecular sensing systems are explored.

In Chapter 5, I summarize the achievements presented in my Ph.D. dissertation and discuss the future perspectives of my research, along with recommendations for further work based on this thesis. I anticipate that my research will convey a comprehensive understanding of the molecular mechanisms underlying bioelectric phenomena and will serve as inspiration for future innovative investigations aimed at developing novel bioelectrical properties.

CHAPTER 2: Triboelectricity in M13 bacteriophage

Reprinted with permission. Han Kim et al., M13 Virus Triboelectricity and Energy Harvesting. *Nano Letters* 21, 6851-6858 (2021). Copyright 2021, American Chemical Society.

2.1 Introduction

Triboelectricity refers to the phenomenon of generating electric potentials during the contact and separation of different materials.[69,70] In modern society, electricity is indispensable, and the generation of triboelectric energy has been identified as a promising method to harness widespread mechanical energy.[43,95,97,126,531-537] Additionally, triboelectric and contact-induced electrostatic interactions play a crucial role in regulating various biological functions and processes in nature, such as bumblebees pollinating flowers, immune cells engulfing pathogens, and viruses infecting host cells.[89-92] Given that many of these interactions rely on biological structures, even minor alterations like single amino acid mutations can completely change biological behaviors and functions.[538,539] Despite the well-established understanding of the electrical properties of inorganic and organic materials over several decades, our comprehension of the electrical properties in biological materials remains elusive. This gap in knowledge persists because natural biomaterials are complex, and there are few model systems available to precisely modify their chemical and physical structures and study their electrical properties at the molecular level.[540]

In this chapter, I will illustrate the phenomenon of triboelectricity exhibited by viral particles upon interacting with metals and other materials. Employing the M13 phage as a programmable biomaterial, I created precisely defined physical and chemical structures, allowing me to study their triboelectric properties. By genetically engineering glutamate fusions ranging from one to four on the N-terminus of the major coat proteins of the M13 phage, I generated monolayer and multilayer phage films. Subsequently, I explored their ability to generate triboelectric potential upon contact with a Ti/Pt-coated AFM tip, observing charge generation in the range of 2-4 $\mu C\ m^{-2}$. Using KPFM, I presented that more negatively charged phages exhibit a higher triboelectric potential and faster charge diffusion compared to less negatively charged phages. The relative polarity analysis of the engineered phages, coupled with computational simulation results, confirms that an increase in engineered glutamates leads to a lower lowest unoccupied molecular orbital (LUMO) energy level. Consequently, these phages can readily accept electrons from counter materials upon contact. Additionally, my demonstration revealed that phage-based triboelectric devices (Tribo-PhD) can generate approximately 76 V of voltage and around 5.1 μA of current, powering 30 light-emitting diode devices through the application of mechanical forces. My findings suggest that viral particles can induce triboelectric potential upon contact, and this characterization opens avenues for

harvesting ubiquitous mechanical vibrational energy and presents an innovative approach for detecting specific viruses in the future.

2.2 The structure of genetically engineered M13 phages

The M13 phage serves as an excellent tunable model system for exploring the structure-function relationship of triboelectricity in biomaterials. The filamentous shaped M13 phage is covered by 2700 pVIII proteins, exhibiting large surface area of the protein surface (Figure 2-1a-c).[460,462,541,542] The N-terminus of the pVIII major coat protein is exposed on the outer surface of the phage (Figure 2-1b). In this study, I used genetically engineered phages with varying numbers of negatively charged amino acids (E), ranging from one glutamate to four glutamates, denoted as 1E-, 2E-, 3E-, and 4E-phage, respectively (Figure 2-1b and Table 4).[1] Since 21 amino acids of the pVIII protein at the N-terminus are exposed externally on the phage surface[543] (Figure 2-1c), the surface charge density of the phage can be predicted. With an estimated surface area of approximately 18,700 nm², the net electric charge of the pVIII coat protein at pH 7.5 is calculated to be -2.2, -3.2, -4.2, and -5.2e (where *e* is the elementary charge) for the 1E-, 2E-, 3E-, and 4E-phages, respectively. The corresponding surface charge densities are estimated as 50.8, 73.9, 97.0, and 120 mC m^{-2} for the 1E-, 2E-, 3E-, and 4E-phages, respectively. This demonstrates that the structural modification of the pVIII protein with varying amounts of charged residues allows for control over the electrical properties of the phage.

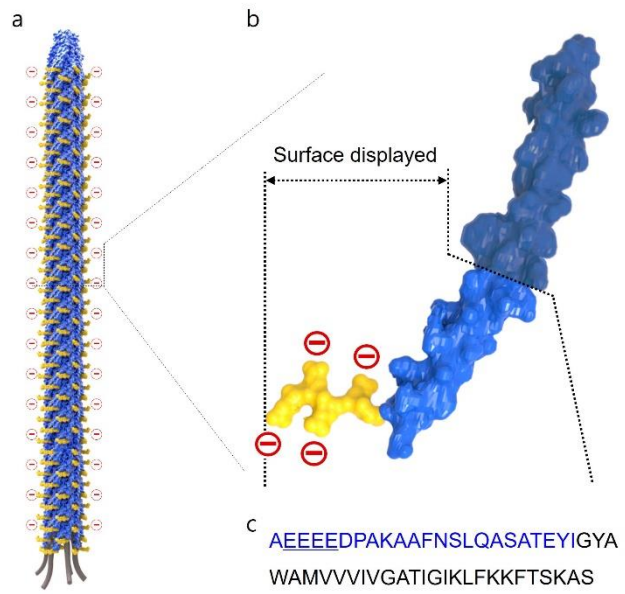

Figure 2-1. Schematic of the M13 phage structure and surface charges. (a) The M13 phage possess a filamentous structure, measuring 880 nm in length and 6.6 nm in diameter, and is

encased by 2700 copies of pVIII major coat proteins. (b) Side view of the pVIII protein of 4E-phage highlighted with the surface exposed area (light blue color) and the engineered peptides (yellow color). (c) Primary structure of the major coat protein for the 4E-phage. The engineered four glutamates (4E) are underlined. Amino acids displayed on the surface are indicated in blue. Reprinted with permission.[2] Copyright 2021, American Chemical Society.

Phage type	Primary structure of pVIII proteins*
WT	AEGDDPAKAAFNSLQASATEYIGYAWAMVVVIVGATIGKLFKKFTSKAS
1E	A*EG*DPAKAAFNSLQASATEYIGYAWAMVVVIVGATIGKLFKKFTSKAS
2E	A*EEG*DPAKAAFNSLQASATEYIGYAWAMVVVIVGATIGKLFKKFTSKAS
3E	A*EEEG*DPAKAAFNSLQASATEYIGYAWAMVVVIVGATIGKLFKKFTSKAS
4E	A*EEEE*DPAKAAFNSLQASATEYIGYAWAMVVVIVGATIGKLFKKFTSKAS

Table 4. Primary structures for pVIII proteins[1]. Reprinted with permission.[2] Copyright 2021, American Chemical Society.

*The primary structure of the pVIII protein of the M13 phage and the insert is *underlined and italicized.*

2.3 Characterization of the triboelectricity in M13 phage

2.3.1 Triboelectric effect using Kelvin probe force microscopy

I conducted a thorough examination of the triboelectric properties exhibited by the phage. To elucidate how mechanical contact influences the manifestation of triboelectric properties in the phage, I performed KPFM in conjunction with AFM (Figure 2-2). This approach involved visualizing the surface potential of the phage based on the contact potential difference (CPD) between the AFM tip and the phage film.[544,545] KPFM was employed to measure the surface potential of the monolayer phage film. For characterizing the triboelectric properties, I applied a single line of contact forces by 200 nm (indicated by the red dotted box in Figure 2-3a and 2-3b) to the phage film with a force of 1.4 nN and a scan rate of 0.50 Hz. This was achieved using a Ti/Pt-coated AFM tip with an approximate radius of ~28 nm in contact mode. I observed the induction of electric potential and its changes through time-lapse KPFM imaging. The work function of the phage, denoted as ϕ_{phage}, is defined by equation (1).[546-548]

$$\phi_{phage} = \phi_{AFM\ tip} - eV_{CPD} \qquad (1)$$

where $\phi_{AFM\ tip}$ is the work function of the Ti/Pt-coated AFM tip, e is the electric charge, and V_{CPD} is the measured CPD. I determined the triboelectric potential, defined as the net variations of the surface potential with reference to that of the non-friction region, by measuring

the surface potential of the rubbed phage. The dark brown color in the KPFM images illustrates the spatial distribution of negative electric charges on the 4E-phage monolayer film (Figure 2-3b). From the first scanning of the KPFM measurement following the application of force, I observed the development of 48.8 mV of electric potential. Using the same experimental setup, the triboelectric potentials of the 1E-, 2E-, and 3E-phages were determined to be 22.9, 32.8, and 40.3 mV, respectively.

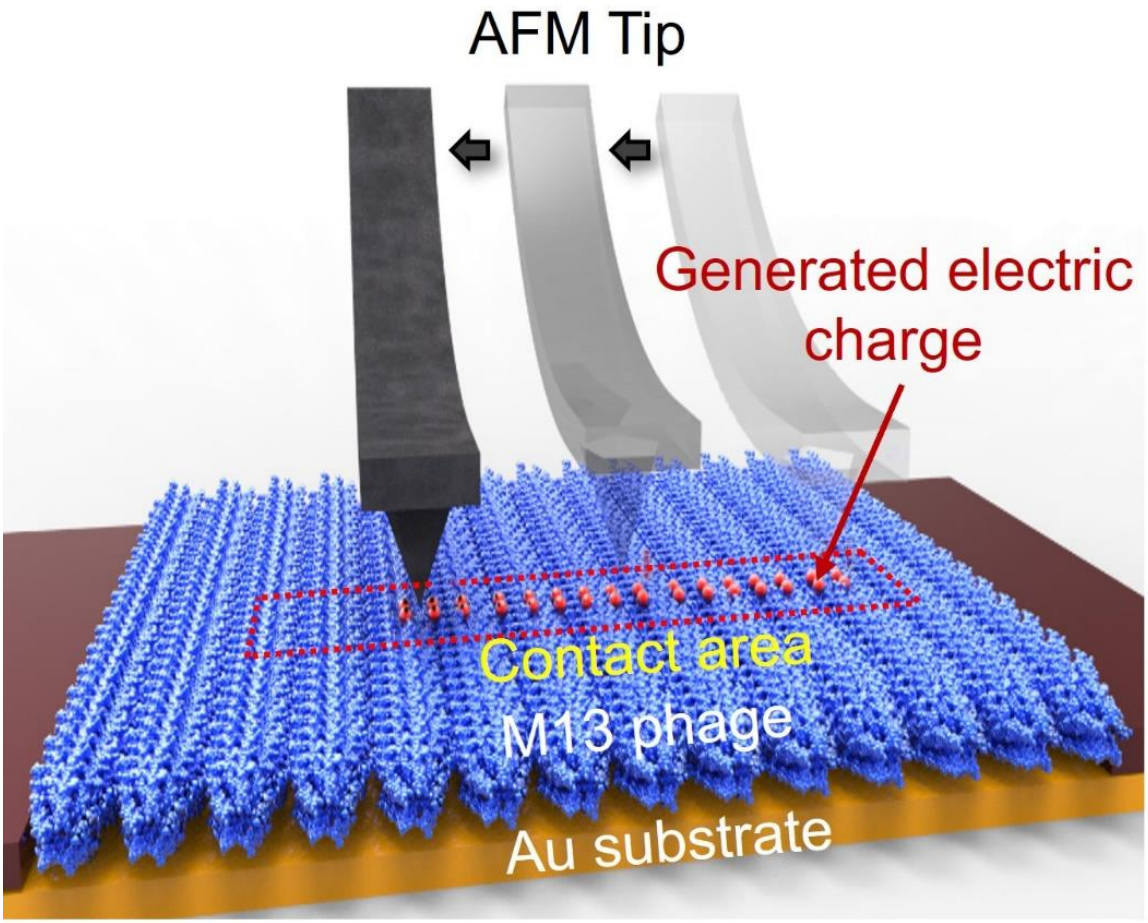

Figure 2-2. Characterization of the triboelectrification of the M13 phage using a Ti/Pt-coated AFM tip. Reprinted with permission.[2] Copyright 2021, American Chemical Society.

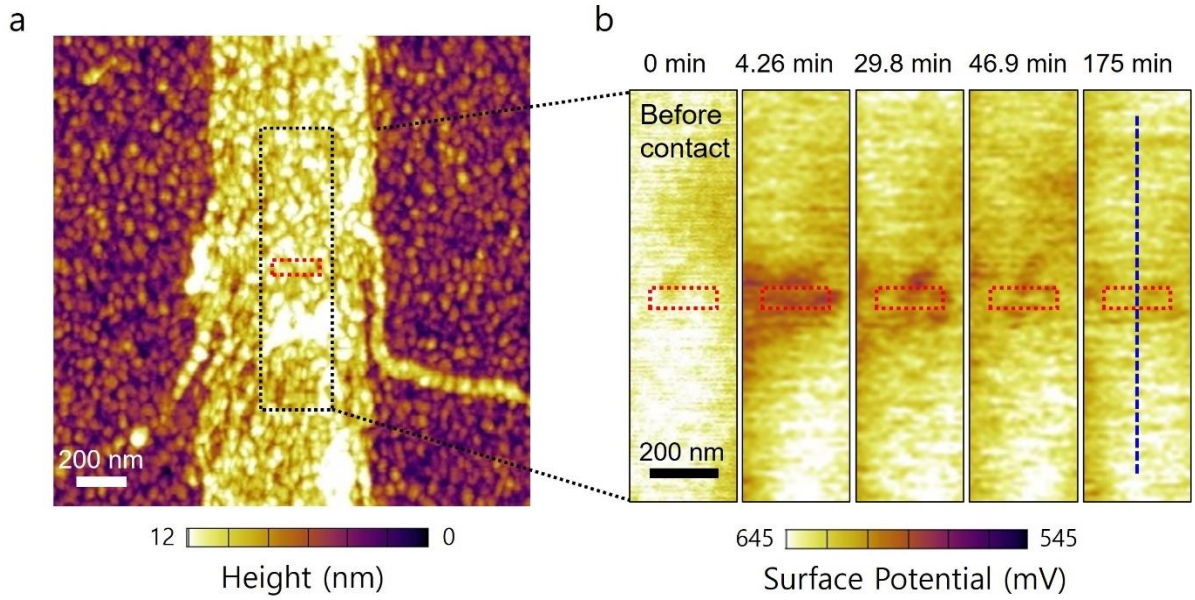

Figure 2-3. Characterization of triboelectrification of the M13 phage. (a) AFM height profile image of a monolayer phage film, where mechanical force was applied within the red dotted box, and the triboelectric charges were observed in the black dotted box. (b) Time-lapse KPFM images capturing the evolution of triboelectric charges on the surface of the M13 phage within the region outlined by the dotted box in (a). Reprinted with permission.[2] Copyright 2021, American Chemical Society.

2.3.2 Diffusion of the triboelectric charges

I conducted an analysis of the diffusion of triboelectric potentials using time-lapse KPFM. Following the application of friction on the monolayer phage film with an AFM tip, I continuously monitored the surface potential of the phage film over time. The observations revealed that the contact-induced electric charges diffused over time, as evidenced by the triboelectric potential profiles as a function of time. Remarkably, the surface potential recovered to a state similar to the initial condition after 175 minutes (Figure 2-3b). For a quantitative analysis of the diffusion of contact-induced electric charges (Figure 2-4), I assumed that these charges predominantly diffuse on the surface in two dimensions rather than through the bulk.[549] The two-dimensional diffusion model to characterize the surface charge diffusion coefficient is expressed by equation (2).

$$\sigma = \frac{A}{t-t_0} \exp\left[-\frac{(x-x_0)^2+(y-y_0)^2}{4D(t-t_0)}\right] \qquad (2)$$

where σ is the surface triboelectric charge density of point (x,y) at time t, A is the constant, D is the diffusion coefficient. To estimate the diffusion coefficient, we applied Gaussian fitting to the one-dimensional surface potential profile with the Gaussian distribution function, $f(x)$, as

expressed by equation (3).

$$f(x) = B \cdot exp\left[-\frac{(x-x_0)^2}{2w^2}\right] \qquad (3)$$

where B is the constant and w is the diffusing distance. In consideration of equations (2) and (3)[545,549], I obtain equation (4).

$$D(t - t_0) = \frac{1}{2}w^2 \qquad (4)$$

By plotting Dt for different diffusing times, I obtained the diffusion coefficient of the triboelectric charges through linear fitting, with the slope representing the diffusion coefficient. The calculated diffusion coefficient of the 4E-phage was 5.20×10^{-18} m^2 s^{-1}. By analyzing differently charged phages (1E-, 2E-, and 3E-phage), I could characterize the chemical structure-dependent triboelectric potential generation and its diffusion. The observed diffusion coefficients for the 1E-, 2E-, and 3E-phages were 0.517×10^{-18}, 1.50×10^{-18}, and 3.57×10^{-18} m^2 s^{-1}, respectively.

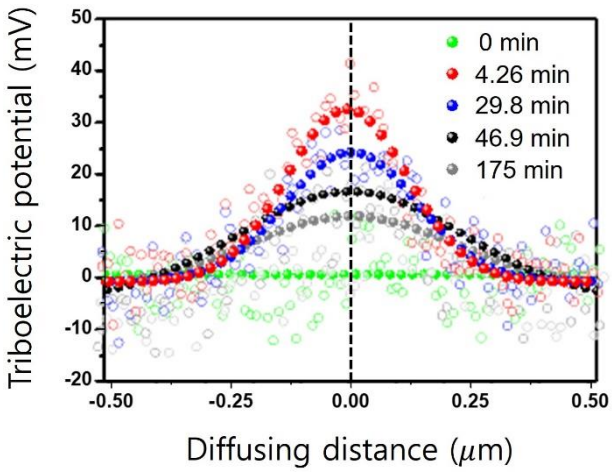

Figure 2-4. Time-dependent triboelectric potential profiles of the phage surface along the dashed line in Figure 2-3b. The contact area is indicated by the dotted line, measured as 0 μm. Reprinted with permission.[2] Copyright 2021, American Chemical Society.

2.3.3 Triboelectric charge characterization

I determined the intrinsic triboelectric potential and generated charge density of the engineered phage films through the analysis of discharging plots. Since I observed the initial triboelectric potential after 4.26 minutes from the application of force, and the potential diffused over time, I drew a trend line on the charge discharging plot for each type of phage

(Figure 2-5) to obtain the corresponding equation and values. By considering the diffusing time at 0 minute, I estimated the intrinsic triboelectric potential of the phages (Figure 2-5). Consequently, the calculated intrinsic triboelectric potentials were found to be 29.1, 40.3, 46.5, and 52.5 mV for 1E-, 2E-, 3E-, and 4E-phage, respectively (Figure 2-6). To further analyze these measurements, I calculated the density of the generated electric charge on the surface of the phage films using equation (5).[550]

$$\sigma_{surface\ triboelectirc\ charge\ density} = \frac{\Delta Q}{A} = \frac{C\Delta V}{A} = \varepsilon_0 \varepsilon_{phage} \frac{\Delta V_{CPD}}{d} \quad (5)$$

where ΔQ is the quantity of generated electric charge on the surface, A is the friction area, C is the capacitance of the phage, ε_0 is the vacuum permittivity, ε_{phage} is the dielectric constant of phage, ΔV_{CPD} is the triboelectric potential and d is the thickness of the phage film. The calculated density of generated electric charge of the engineered phages was 2.44, 3.38, 3.90, and 4.40 μC m^{-2} for 1E-, 2E-, 3E-, and 4E-phage, respectively.

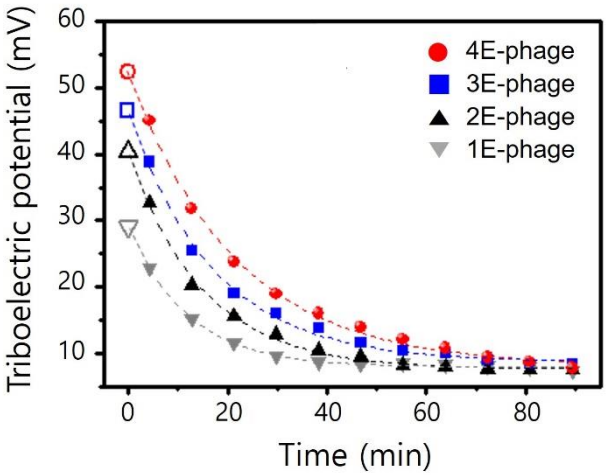

Figure 2-5. Time-dependent electric discharging and diffusion behavior in the 1E- to 4E-phages. Experimentally measured data is represented by filled markers, while calculated data is indicated by open markers. Reprinted with permission.[2] Copyright 2021, American Chemical Society.

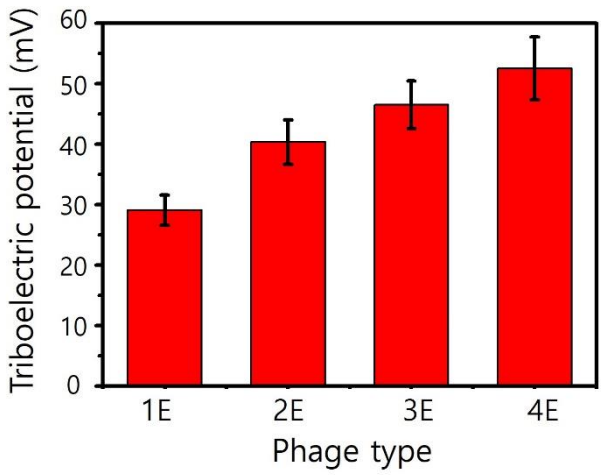

Figure 2-6. Intrinsic triboelectric potentials for the 1E- to 4E-phages were computed. The mean values from seven replicates are specified. Reprinted with permission.[2] Copyright 2021, American Chemical Society.

2.4 Molecular mechanisms of the triboelectricity in M13 phage

2.4.1 Relative triboelectric charging behaviors of phage films

Because the engineered phage films, with varying amounts of glutamate, demonstrate distinct electrical properties, I proceeded to characterize the relative polarity and magnitude of the triboelectric potentials among the 1E- to 4E-phages. Initially, I deposited the desired phages on indium tin oxide (ITO) electrodes, each having an area of 70 mm^2 and a thickness of approximately 300 nm.[1] Subsequently, I subjected the phage films to a dynamic mechanical test using a system. The electric potentials generated by successive contact and separation of two materials were measured and compared, applying a force of 5 N at a distance of 4 mm (Figure 2-7). I assessed the relative electric charging behavior of the materials based on the direction and magnitude of the output voltage signals. Specifically, I used 1E-phage as the bottom substrate against 1E-, 2E-, 3E-, and 4E-phages as the top substrates, all serving as triboelectric materials. An electrometer was employed for this purpose. Connecting the positive material to the probe tip and linking the negative material to the ground lead resulted in a negative voltage signal upon contact and a positive signal upon separation. During the contact of two triboelectric layers, an electrostatic phenomenon generated positive and negative charges on the surfaces of each side of the layers. Subsequently, upon the separation of the two substrates, electrons tended to flow through the external load from the positively electrified electrode (the bottom electrode in Figure 2-7) to the negatively electrified electrode (the top electrode in Figure 2-7) until the system reached an electrical equilibrium. In this process, a negative voltage was observed, signifying that electron flowed from the more negative phage layer toward the more positive phage layer, inducing positive electric charges on the surface of

the more positive layer upon contact with the phage surface. After reaching equilibrium, there was no electron flow. Upon the contact of the two substrates, a positive voltage was exhibited, indicating that the electrons flowed in the opposite direction compared to the previous step.

The output voltage from electrification between identical phage types (e.g., 1E-phage against 1E-phage) is minimal (0.01 V). However, when 1E-phage contacts 2E-, 3E-, and 4E-phages, positive polarity is observed during contact-separation, with magnitudes of 0.56, 0.79, and 1.26 V, respectively. Contact with more negatively charged phages (2E-, 3E-, and 4E-phages) results in the generation of positive charges on the surface of the 1E-phage. Additionally, the greater the disparity in the number of glutamates on the phages, the larger the quantity of generated charges (Figure 2-8). This outcome indicates that the 1E-phage, being relatively positive, tends to donate electrons to the counter, relatively negative phages (e.g., 2E-, 3E-, and 4E-phages) upon contact, resulting in a larger electric potential. This principle is confirmed across various combinations of different phages (Figure 2-9 and Figure 2-10). In the case of 2E-phage against 1E-phage, a negative voltage of -0.65 V is observed, signifying the generation of negative electric charges on the surface of the 2E-phage and positive charges on the 1E-phage. Similar to the scenario of 1E against 1E-phage, electrification between 2E-phage against 2E-phage yields negligible potential (0.01 V). The signal polarity for 2E-phage against 3E- and 4E-phages is reversed compared to the 1E-phage, with output values of 0.63 and 0.92 V. Similarly, in 3E- and 4E-phages, the electric potential between identical phage types is negligible, but the signal polarity reverses when the phage interfaces with a more negatively charged counterpart (Figure 2-9 and Figure 2-10). Analyzing the relative output voltage signal between each phage, I conclude that the electric properties can be systematically controlled based on the engineered glutamates on the phages at the single amino acid level. The phages exhibit a tendency to generate more negative electric charges in the order of 4E-, 3E-, 2E-, and 1E-phages.

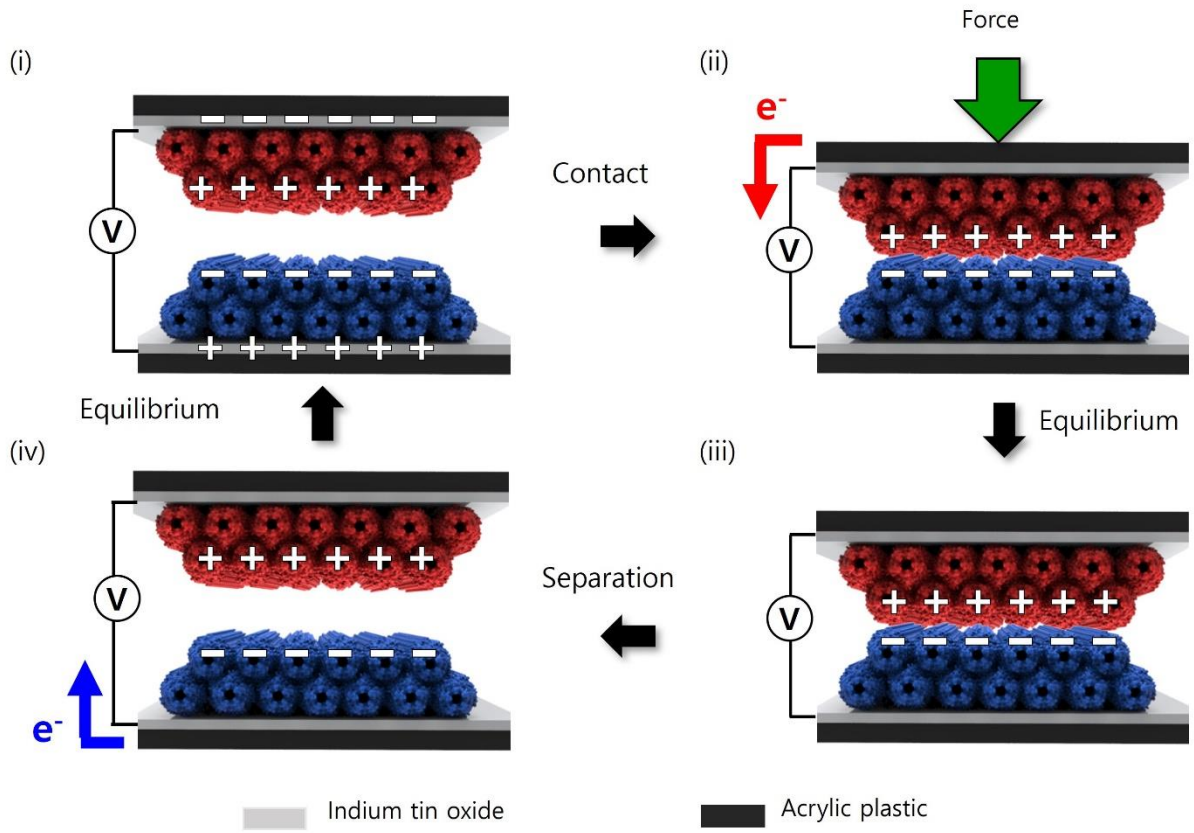

Figure 2-7. Working principle of a Tribo-PhD. Reprinted with permission.[2] Copyright 2021, American Chemical Society.

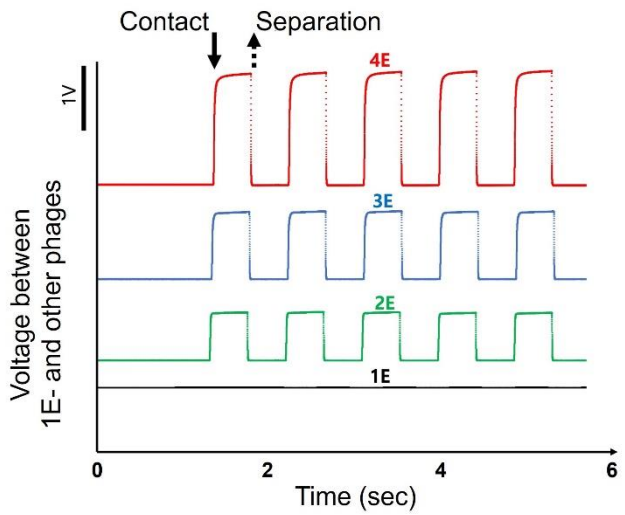

Figure 2-8. Triboelectric voltage observed during the contact and separation of the 1E-phage (bottom substrate) with the 1E- to 4E-phages (top substrate). Reprinted with permission.[2] Copyright 2021, American Chemical Society.

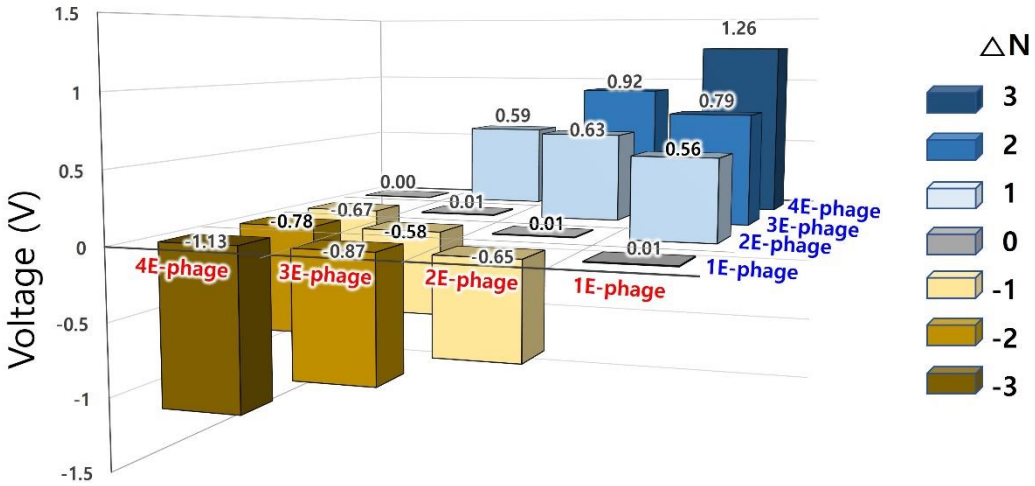

Figure 2-9. Generation of Relative triboelectric voltage among different phage types. ΔN represents the disparity in glutamate numbers between the engineered phages at the top and bottom. Reprinted with permission.[2] Copyright 2021, American Chemical Society.

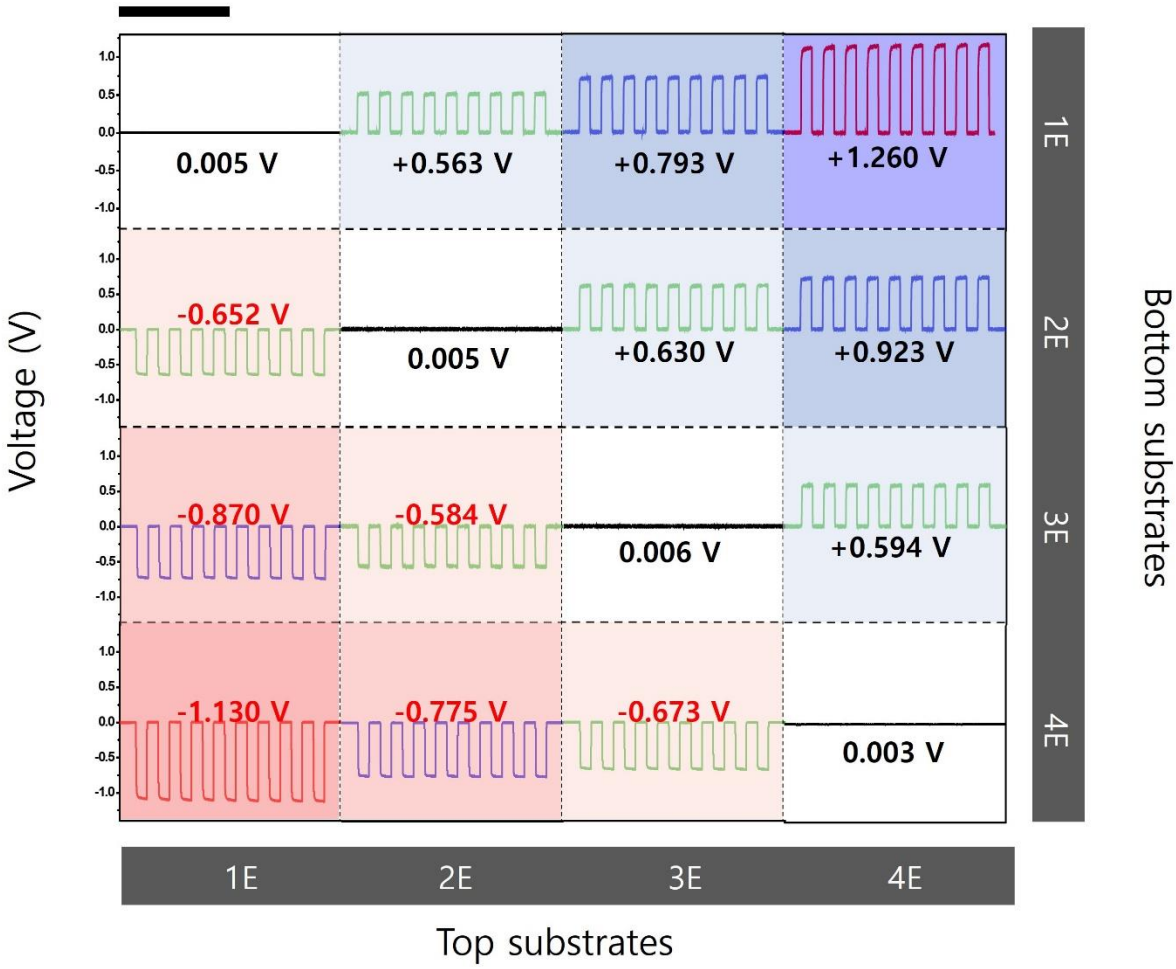

Figure 2-10. The relative triboelectric charging characteristics of each phage in relation to other phage types (1E-4E-phages). Scale bar represents 5 seconds. Reprinted with permission.[2] Copyright 2021, American Chemical Society.

2.4.2 Computational analysis – Extended semiempirical tight-binding calculations

To understand the variations in electric charging behavior among the glutamate-engineered phages, I employed an extended semiempirical tight-binding calculation (GFN2-xTB).[551] The modeling approach involved extracting the pVIII protein structure from the molecular configuration of the M13 phage, as obtained from the Protein Data Bank (PDB code: 1IFJ). I used the mutagenesis function in Pymol 2.4.0 software to manipulate the genetically engineered segment of the pVIII protein, creating both the molecular structure with the complete amino acid sequences of the pVIII coat protein and partial sequences modified through genetic engineering. Following geometric optimization, we employed GFN2-xTB with the Gaussian 16 package interface for xTB code at 300 K. This investigation focused on the variance in the LUMO energy level, representing the electron acceptor energy state, up to the LUMO+4 level in response to the glutamate insertion changes. The LUMO levels of the pVIII

coat protein were found to be -7.82, -7.84, -7.86, and -8.04 eV for 1E-, 2E-, 3E-, and 4E-phages, respectively (Figure 2-11). It was observed that the LUMO level decreased with an increase in the number of inserted glutamates, indicating a heightened inclination to accept electrons. I also demonstrated the LUMO level of the inserted peptides (ranging from one to four glutamates) of the pVIII protein, revealing a consistent trend with the pVIII protein itself that the LUMO level decreased with an increasing number of glutamates (Figure 2-12). Thus, alterations in the LUMO of the engineered glutamates on the pVIII protein play a role in controlling electric properties, aligning with experimental results that highlight the 4E-phage's increased tendency to accept electrons from the counter material in contact electrification.

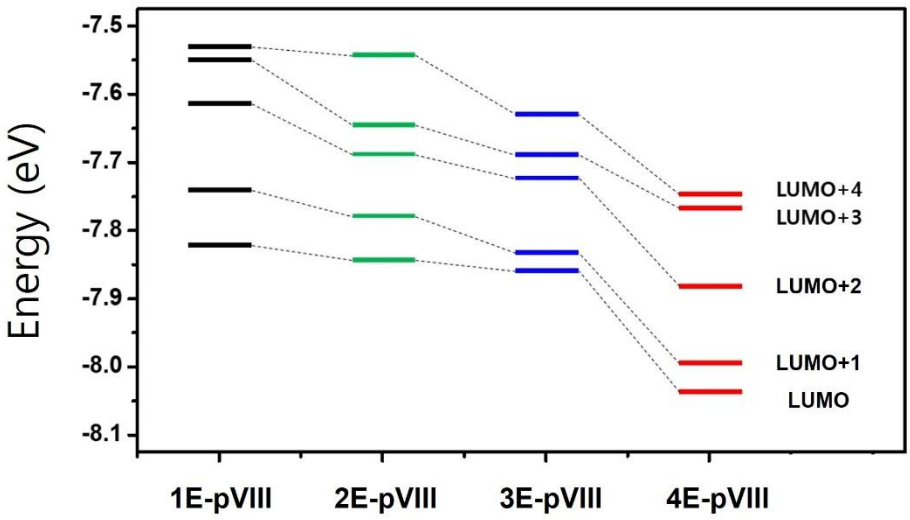

Figure 2-11. Extended semiempirical tight-binding calculations reveal the LUMO level of the pVIII coat protein in the 1E- to 4E-phages. Reprinted with permission.[2] Copyright 2021, American Chemical Society.

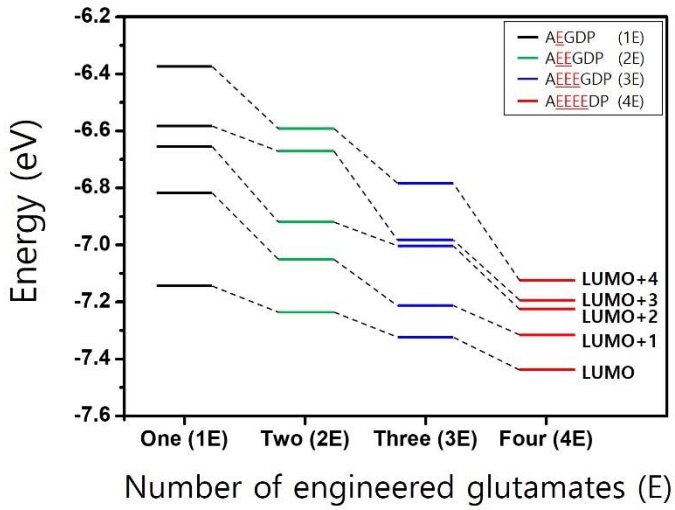

Figure 2-12. The extended semiempirical tight-binding calculation results to show the LUMO level of the N-terminus peptides of the pVIII coat protein. The LUMO levels for AEGDP, AEEGDP, AEEEGDP, and AEEEEDP are -7.14, -7.24, -7.32, and -7.44 eV, respectively. Reprinted with permission.[2] Copyright 2021, American Chemical Society.

2.4.3 Triboelectric series

To determine the relative order of the phage material in the conventional triboelectric series, I examined its triboelectric behavior in comparison to representative materials within the series.[72] Multiple measurements of phage film output were conducted with the same contact area, focusing on the 4E-phage against five different materials: nylon, polyethylene (PET), polyimide (PI), PTFE, and perfluoroalkoxy (PFA) (Figure 2-13a). In electrification with other materials, those on the positive side (left) of the series typically donate electrons to those on the negative side (right). The output voltage signals from the phage-nylon and phage-PET pairs exhibited positive voltages, while the pairs of phage-PI, phage-PTFE, and phage-PFA displayed negative voltages (Figure 2-13b). Therefore, the phage under investigation falls between PET and PI in the triboelectric series, elucidating how the phage generates triboelectric charges in interactions with various materials.

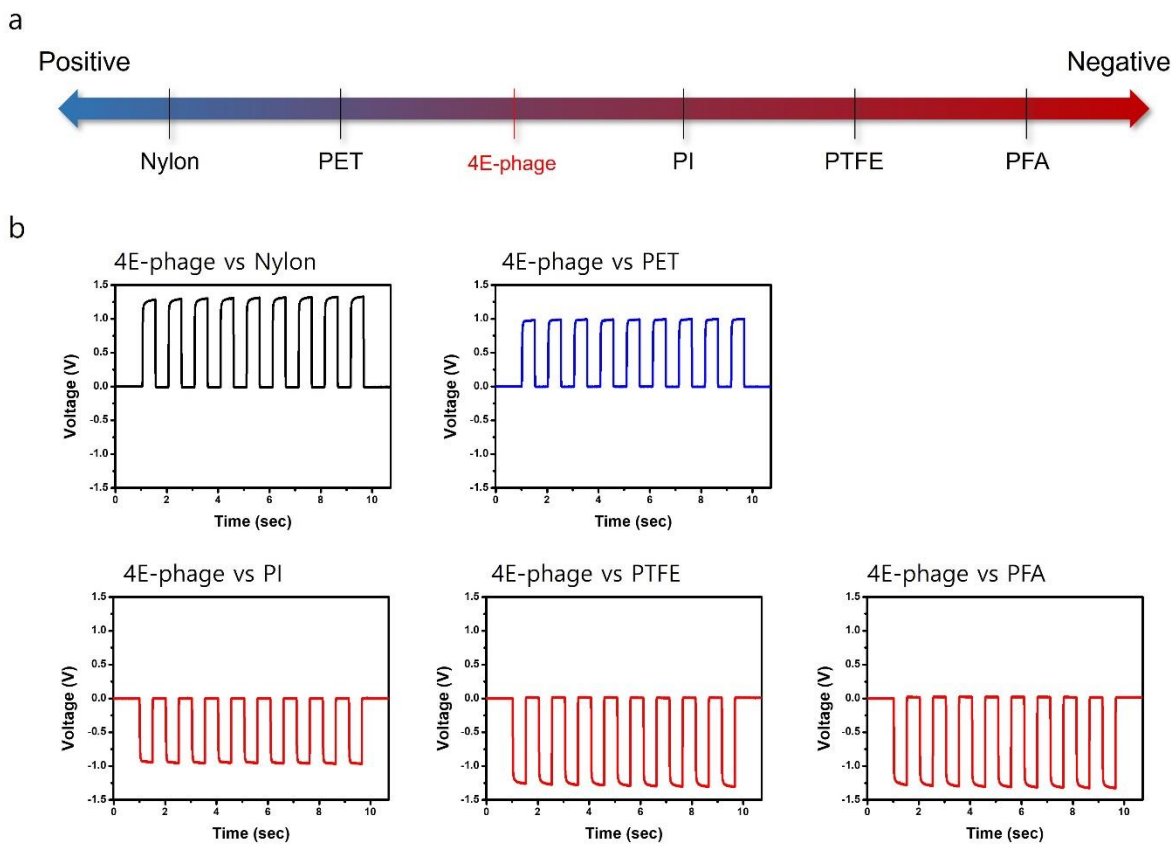

Figure 2-13. The relative triboelectrification of the 4E-phage in relation to traditional triboelectric materials such as nylon, polyethylene terephthalate (PET), polyimide (PI), polytetrafluoroethylene (PTFE), and perfluoroalkoxy (PFA). Reprinted with permission.[2] Copyright 2021, American Chemical Society.

2.5 Characterization of phage-based triboelectric nanogenerators

I constructed a Tribo-PhD and assessed its triboelectric energy generation. Briefly, I prepared a 5.0 mg mL^{-1} film of 4E-phage covering an area of 25 cm^2 on an ITO electrode using the drop-casting method, which was then air-dried for 2 days. Another ITO counter electrode of equal size was positioned facing the first electrode (Figure 2-14). Applying a force of 7.5 N to the Tribo-PhD typically resulted in an observed voltage of 76 V and a current of 5.1 μA (Figure 2-15a and 2-15b). The polarity of the voltage and current signals switched when they were connected in reverse, confirming that the output signals were attributable to the triboelectrification from the Tribo-PhD (Figure 2-16). Given the known piezoelectricity of the M13 phage[1], the piezoelectric effect can contribute to the Tribo-PhD output under the application of a compressive force.[552] When both compressive and tensile forces were applied to the attached Tribo-PhDs, an approximate 0.5 V output voltage was observed. However, it was confirmed that the contribution of the piezoelectric effect is significantly lower than that

of the triboelectric effect (Figure 2-17). As the electrical output of the Tribo-PhD varies with the load level in the system, the output voltage and current of the Tribo-PhD were measured under various electrical resistors ranging from 10 kΩ to 1 GΩ (Figure 2-18). As the external load resistance increased, the voltage gradually increased while the current gradually decreased. The instantaneous power ($W=I^2R$) reached its maximum at a load resistance of 100 MΩ, with a calculated maximum power density of 6.7 μW cm^{-2} (Figure 2-19). Durability tests demonstrated that the Tribo-PhD could produce continuous electricity over approximately 10,000 applications of compressive forces with minimal change in output power (Figure 2-20). Due to the protein-covered surface of the M13 phage, it is sensitive to ambient humidity and temperature. Voltage and current characteristics of the Tribo-PhD were characterized under various humidity and temperature conditions, revealing that both output voltage and current gradually decreased with increasing humidity and temperature (Figure 2-21). Furthermore, the generated charge could be stored in capacitors. The direct current (DC) output obtained by rectifying the alternating current (AC) output generated from the P-TENG successfully charged a 4.7 μF capacitor to 2.1 V within 25 s (Figure 2-22). Finally, I demonstrated the practical application of our P-TENG by operating multiple light-emitting diodes (LEDs). By connecting 30 LEDs to the Tribo-PhD, the word "CAL" was displayed, and upon the application of force, all 30 LEDs turned on simultaneously (Figure 2-23). Similarly, the Tribo-PhD was applied to operate flexible organic LED (OLED) devices (Figure 2-24).

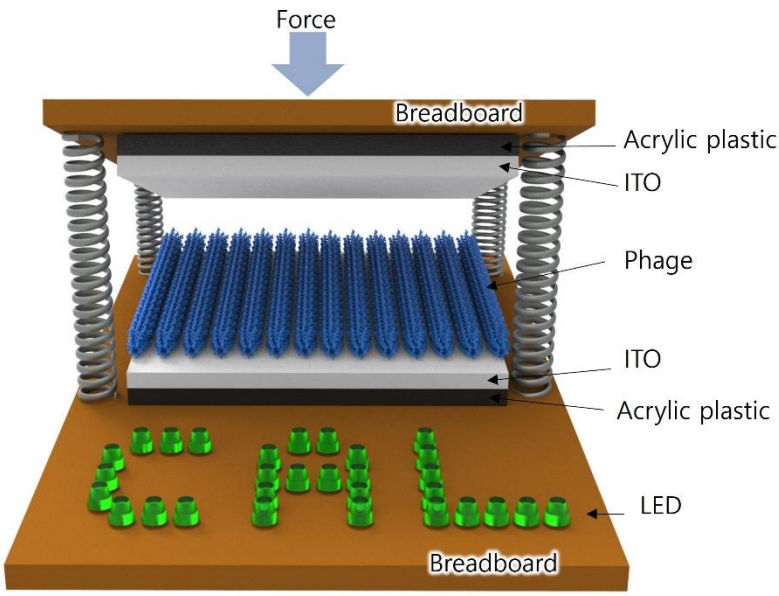

Figure 2-14. Schematic figure of a large-scaled Tribo-PhD. Reprinted with permission.[2] Copyright 2021, American Chemical Society.

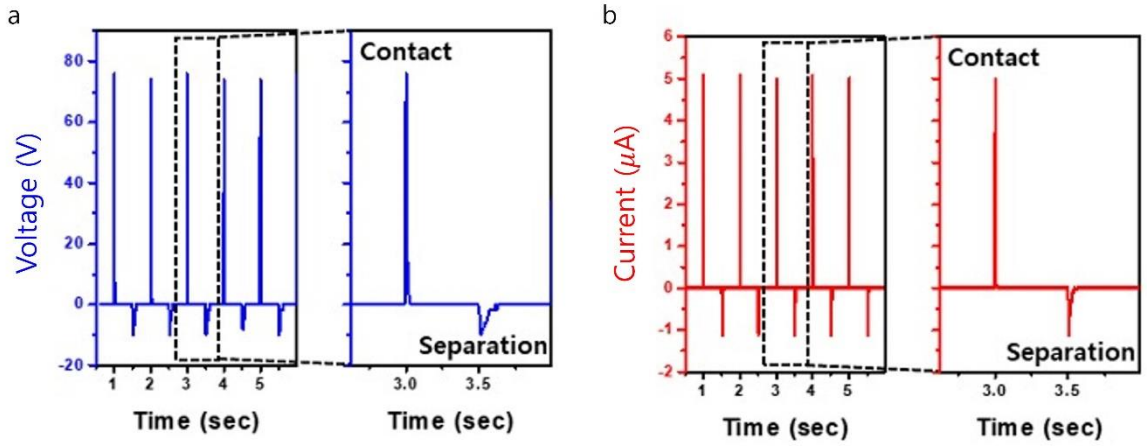

Figure 2-15. Output voltage and current of the Tribo-PhD. Reprinted with permission.[2] Copyright 2021, American Chemical Society.

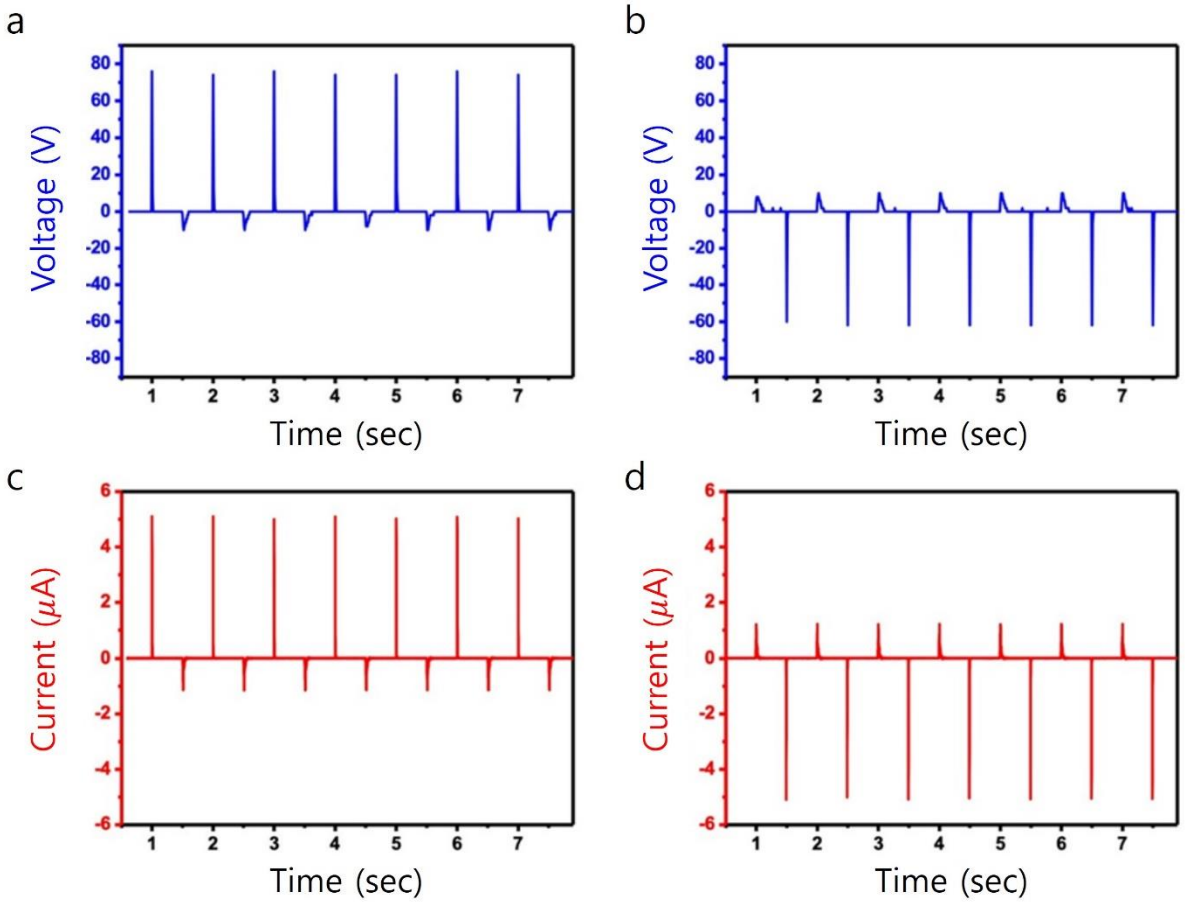

Figure 2-16. Switching polarity test on the Tribo-PhD. Output voltage (a) and (b) and current

(c) and (d) were measured by connecting the probes in the opposite orientation to the Tribo-PhD, demonstrating the reverse polarity changes. Reprinted with permission.[2] Copyright 2021, American Chemical Society.

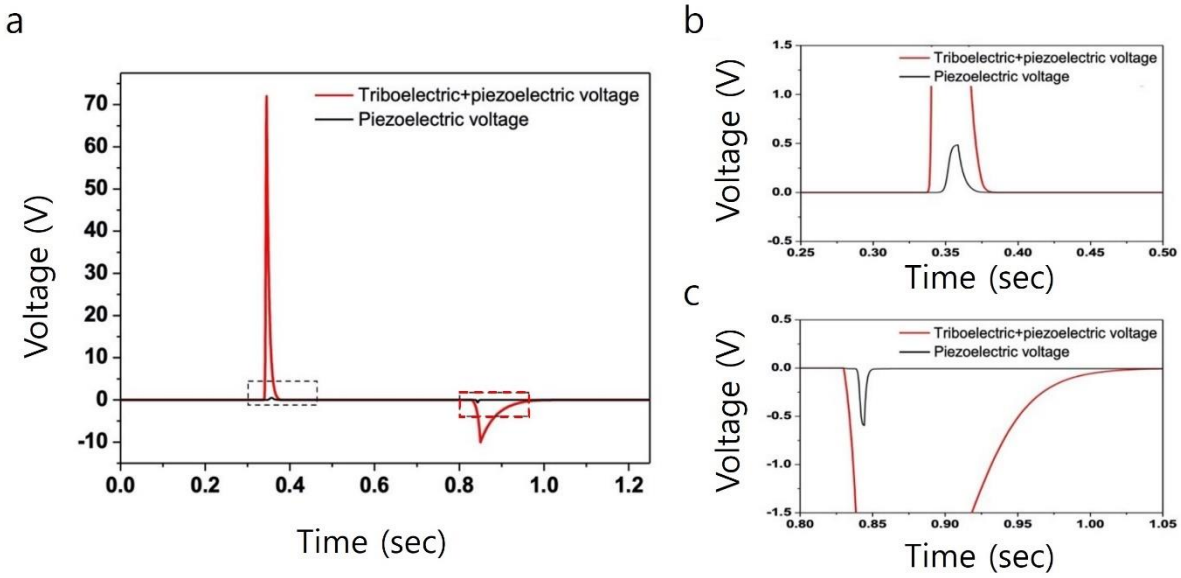

Figure 2-17. Contrasting the impact of piezoelectricity and triboelectricity on the output voltages of a Tribo-PhD. (a) Output voltage of Tribo-PhD resulting from both piezoelectric and triboelectric sources. (b-c) Enlarged output voltage signals extracted from the black- and red-dashed boxes in Figure 2-16a. Reprinted with permission.[2] Copyright 2021, American Chemical Society.

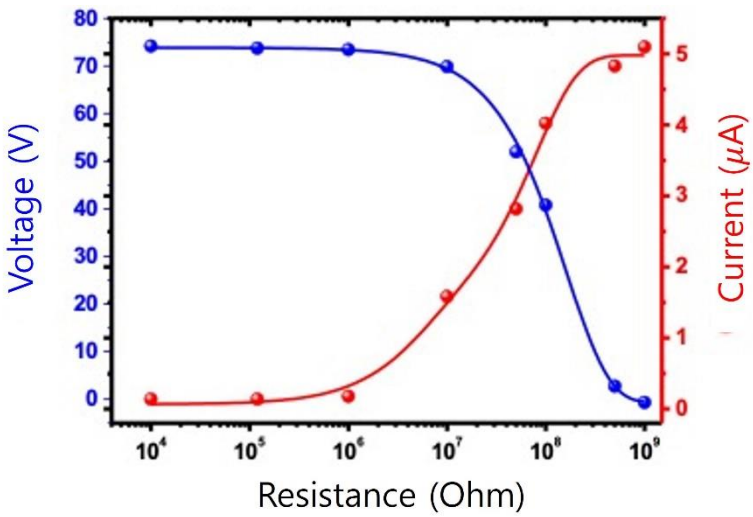

Figure 2-18. Output voltage and current observed across various external resistances, ranging

from 10 k Ω to 1 GΩ, in the Tribo-PhD. Reprinted with permission.[2] Copyright 2021, American Chemical Society.

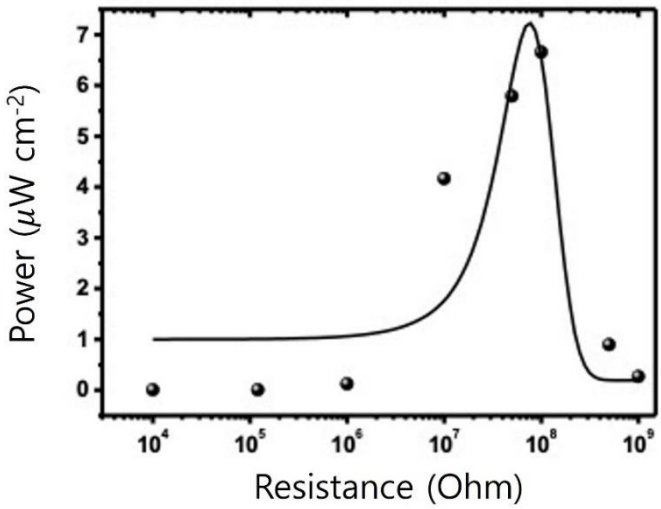

Figure 2-19. Analysis of power density based on resistance reveals that the highest power density is attainable at 100 MΩ. Reprinted with permission.[2] Copyright 2021, American Chemical Society.

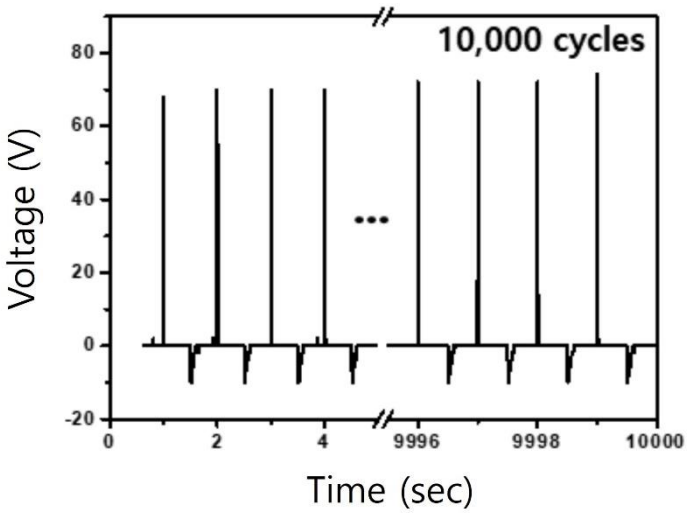

Figure 2-20. Evaluation of the durability of the Tribo-PhD through a 10,000-cycle test. The mechanical durability assessment, conducted under a compressive force of 7.5 N and a frequency of 1.0 Hz, demonstrates outstanding stability and resilience in the Tribo-PhD. Reprinted with permission.[2] Copyright 2021, American Chemical Society.

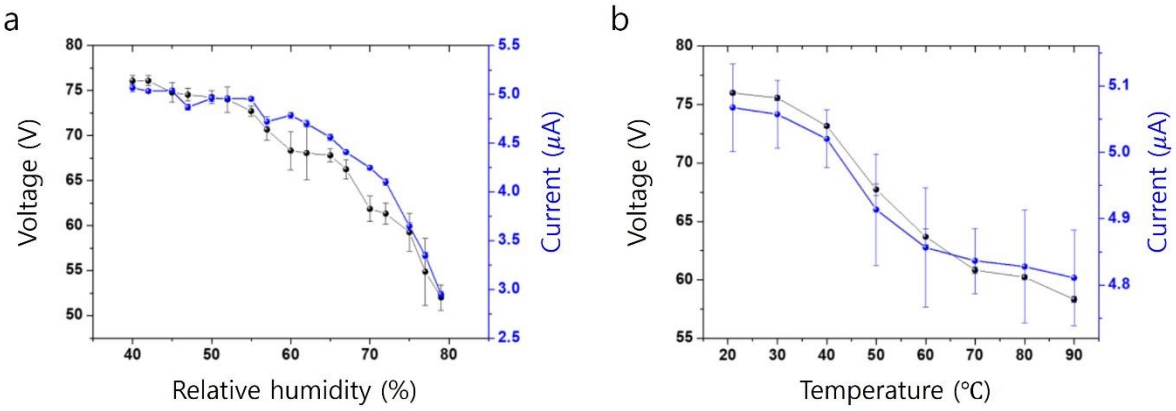

Figure 2-21. Triboelectric characterization of the Tribo-PhD in relation to humidity and temperature. (a) With an increase in humidity from 40 to 80 %, both voltage and current decreased from 76 to 52 V and from 5.1 to 2.9 μA, respectively. (b) With a temperature rise from 20 to 90 °C, the voltage and current decreased from 76 to 58 V and 5.1 to 2.9 μA, respectively. Reprinted with permission.[2] Copyright 2021, American Chemical Society.

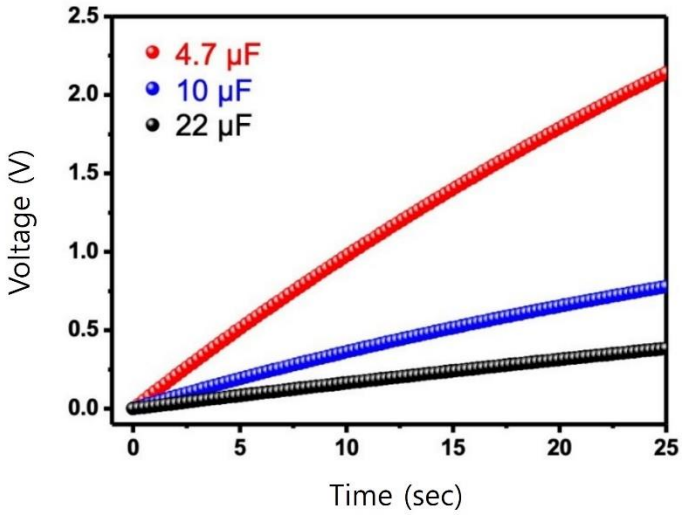

Figure 2-22. Charging characteristics of the Tribo-PhD device across various capacitors. Reprinted with permission.[2] Copyright 2021, American Chemical Society.

Figure 2-23. Photographs of 30 LEDs connected to the Tribo-PhD. The images show the LEDs when the room light was switched on (left) and off (right). Reprinted with permission.[2] Copyright 2021, American Chemical Society.

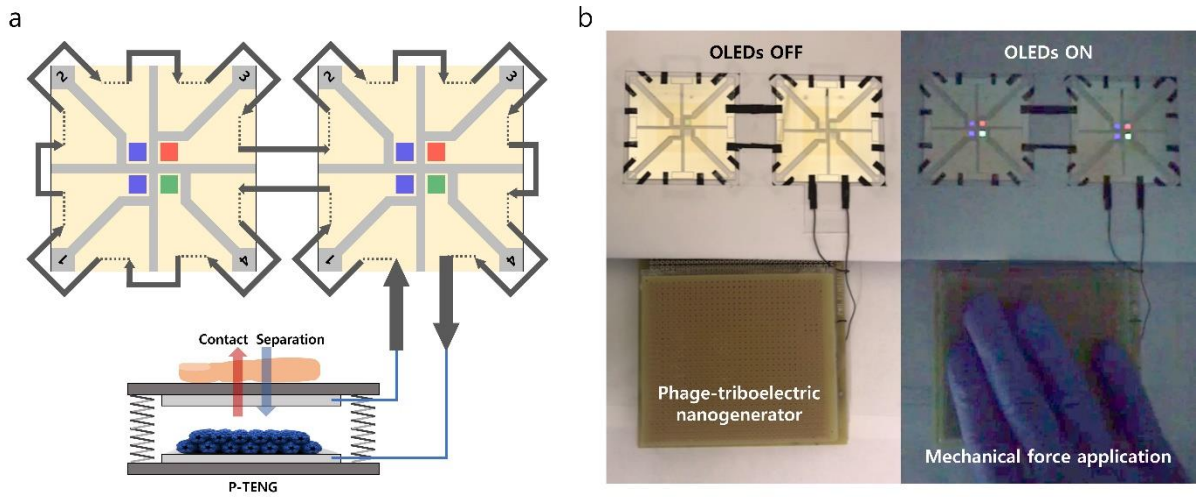

Figure 2-24. (a) Diagram illustrating the connections between the OLEDs and the Tribo-PhD. 8 OLEDs were linked in series to the Tribo-PhD. (b) Images capturing the operation of the OLEDs. All 8 OLEDs emitted light when manual compressive force was applied. The photos show the OLEDs in both illuminated (left) and non-illuminated (right) conditions with the room light on and off, respectively. Reprinted with permission.[2] Copyright 2021, American Chemical Society.

2.6 Conclusion

In summary, I present findings indicating that virus particles possess the capability for triboelectrification, thus qualifying them for application in energy harvesting materials. This study involved the creation of precisely defined phage structures to investigate triboelectrification and to characterize the electric potential behaviors. I observed that more negatively charged phages not only exhibited higher triboelectric potential generation but also demonstrated faster charge mobility compared to their less negatively charged counterparts. The distinct differences in polarity and triboelectric potential magnitude between various glutamate-engineered phages were evident at the level of a single amino acid. Additionally, I successfully augmented the electrification property of M13 phages through genetic engineering. These approaches, harnessing the triboelectricity of viral particles, offer a promising avenue for sustainable energy harvesting and present a novel methodology for detecting specific viruses in future applications.

2.7 Methods

2.7.1 Genetic engineering of M13 phage

I investigated the triboelectric properties of the M13 phage by adapting genetically engineered phages used in our previous work.[461] The pVIII protein was engineered using recombinant DNA techniques. A variable number of negatively charged glutamates (E) (from one (1E) to four (4E)) was incorporated into the first alanine and aspartate of WT-pVIII protein. To facilitate genetic engineering, a *PstI* restriction site (CTGCAG) was utilized by introducing mutations to the M13KE vector (New England Biolabs, Ipswich, MA) through site-directed mutagenesis (QuickChange® Kit, Stratagene, La Jolla, CA). Primers (IDT, Coralville, IA) were created to incorporate the desired genetic information. The polymerase chain reaction (PCR) was carried out using PhusionTM High-Fidelity DNA polymerase (Finnzymes, Espoo, Finland), along with the primers and the M13 KE vector. Subsequently, the resulting digestion products underwent separation via agarose gel electrophoresis, followed by digestion with the PstI enzyme (New England Biolabs, Ipswich, MA), and ligation using T4 DNA Ligase (New England Biolabs) overnight at 16 °C. The ligated DNA vector was then introduced into XL 1-Blue electroporation competent cells (Stratagene, La Jolla, CA). Following the verification of the DNA at the DNA sequencing facility located at the University of California, Berkeley, CA, I proceeded to amplify the engineered phage of interest through bacterial amplification.

2.7.2 Surface charge estimation

I used Protein Calculator v3.4 (C. Putnam, Scripps Research Institute, USA) to estimate the theoretical net charge on the surface of the engineered phage at various pH levels. This calculation was based on the outermost 21 amino acids among its overall primary structure.

The calculation assumes that all three residues have identical pKa values as the individual amino acids. To determine the surface charge density of the phage, I multiplied the net charge value at pH 7.5 by the number of copies of the major coat proteins and then divided by the surface area of the phage.

2.7.3 Fabrication of the monolayer M13 phage films

I created monolayer phage films through a soft-lithography technique and the phage self-templating assembly method.[1,462] Initially, a 1-μm patterned PDMS (Slygard 184 silicone elastomer) stamp was crafted using a silicon dioxide wafer that had been patterned through photolithography. With the stamp, we generated octadecanethiol (ODT) layers on a gold-coated silicon substrate (300 nm gold layer on a 50 mm Cr adhesion layer) from Platypus Technologies in Madison, WI. Following the ODT patterning, I cleansed the substrate with ethanol and deionized water, and subsequently dried it using N_2 gas. Then, utilizing a 5.0 μg mL^{-1} phage solution, I applied a monolayer of phage onto the ODT-patterned substrate through the self-templating assembly process.[1]

2.7.4 Phage quantification

The M13 phage concentration was determined using the following equation (6), as outlined in our previously published literature.[461]

$$\frac{mg\ \ of\ \ phage}{mL} = \frac{(A_{269} - A_{320})}{3.84} \qquad (6)$$

where A_{269} is the UV absorbance at 269 nm, and A_{320} is the UV absorbance at 320 nm.

2.7.5 Triboelectric characterization using Kelvin probe force microscopy

I explored the triboelectric properties of the phage using KPFM coupled with AFM on the MFP-3D AFM system from Asylum Research in Santa Barbara, CA. AC240TM-R3 AFM tips coated with Ti/Pt (Oxford Instruments) were employed, featuring a tip radius of approximately 28 nm and a force constant of around 2 N m^{-1}. The surface potential of the phage was measured using KPFM with a scan rate of 1.0 Hz, a scan size of 3 μm × 3 μm, and a distance of 300 nm from the phage film surface. Triboelectric charges were generated by a single line of friction in contact mode, using an AFM tip with a force of 1.4 nN and a scan rate of 0.50 Hz. The work function of the phage, denoted as ϕ_{phage}, is defined as equation (7).[546-548]

$$\phi_{phage} = \phi_{AFM\ \ tip} - eV_{CPD} \qquad (7)$$

where $\phi_{AFM\ \ tip}$ is the work function of the Ti/Pt-coated AFM tip, *e* is the electric charge, and

V_{CPD} is the measured CPD. The triboelectric potential, indicating the net variations in surface potential with reference to the non-friction region, was obtained by measuring the surface potential of the rubbed phage. KPFM measurements were conducted under consistent conditions in a time-lapse manner post-friction. All experiments were carried out at atmospheric pressure at 20 °C and 40 % relative humidity.

2.7.6 Fabrication of the multilayer M13 phage films

I generated multilayer phage films using the phage self-templating assembly method.[462] Phage films were produced on an ITO substrate (Sigma-Aldrich) using a phage solution with a concentration of 1.5 mg mL^{-1} and a pulling speed of 20 μm min^{-1}.

2.7.7 Calculation of the energy levels of M13 phage

I performed the extended semiempirical tight-binding calculation (GFN2-xTB) to investigate the LUMO level of the pVIII coat protein of the M13 phage. I designed the modeling the pVIII protein by extracting from the molecular structure of the M13 phage obtained from the Protein Data Bank (PDB code: 1IFJ). I manipulated the genetically engineered part of the pVIII protein using the mutagenesis function of Pymol 2.4.0 software. I designed the molecular structure with the full amino acid sequences of the pVIII coat protein. The LUMO level of the protein model was calculated using GFN2-xTB with the Gaussian 16 package (Revision A. 03). After importing the protein model into GaussView 6.0.16 software, I set up the Optimization to a minimum and the Force constants to Default in the Job Type tab. Additionally, I selected Ground State, Zero charge, and Doublet spin in the Method tab. After the geometric optimization, the LUMO level of the protein model was calculated under 300 K.

2.7.8 Device fabrication and output characterization

I constructed Tribo-PhDs by utilizing a 4E-phage film and an ITO film. The ITO layer, measuring 5 cm × 5 cm with a PET substrate, was completely coated with a 5.0 mg mL^{-1} solution of 4E-phage using a drop-casting method and allowed to air-dry for 2 days. To ensure a flat contact surface, the PET side of the electrode was affixed to acrylic plastics of the same dimensions. As an alternative contact material, a 5 cm × 5 cm ITO film from Sigma-Aldrich, attached with 1.5 mm thick acrylic plastics (TAP Plastics), was employed. The ITO side of the electric materials was wired, and the two electrodes were connected. To enhance durability under repeated compressive forces, the two triboelectric materials were combined with four springs. The Tribo-PhD was loaded onto a dynamic mechanical test system (Electroforce 3200, Bose, MN), and cyclic force was applied to establish contact and separation within the device. The gap distance between contact surfaces was set at 4 mm, the contact area was 25 cm^2, and

the applied compressive force amounted to 7.5 N. Output voltage was measured using an oscilloscope (Tektronix TDS 1001B) and Keithley 6514 System Electrometer, while output current was measured with a Low-Noise Current Preamplifier (Stanford Research SR570). All experiments were conducted at 20 °C and 40 % relative humidity.

CHAPTER 3: Piezoelectricity in M13 bacteriophage

3.1 Introduction

Electric responses originating from biological materials demonstrate intricate and complex reactions to diverse external stimuli, presenting a remarkable spectrum of manifestations. Recently, the exploration of harnessing this bioelectricity has gained considerable attention due to its potential to address key challenges in diverse applications, including biomedical devices, biosensors, and bioelectronic devices interfacing with living tissues and cells.[553-556] Biomaterials have emerged as particularly promising candidates for energy harvesting systems, given their unique properties that offer opportunities to develop biocompatible, sustainable, and versatile energy technologies.[22,557-559] For instance, materials like collagen, bone, spider silk, and plant proteins have been utilized to harvest energy from mechanical movements.[195,356,408,560-564] However, despite the increasing demand for biological energy harvesting systems, biomaterials generally demonstrate limited power output, efficiency, and structural complexity compared to conventional energy sources.[479,497,498] These limitations originate from the lack of precise molecular-level control over their structure and bioelectrical properties.[565-568] In contrast, conventional inorganic piezoelectric materials (e.g., PZT, $BaTiO_3$, ZnO, PMN-PT, $pBNb_2O_6$, and $NiNbO_3$) possess well-defined structures, forming a solid foundation for understanding the fundamental principles of the piezoelectric effect.[179,569-579] Consequently, they are widely employed in various piezoelectric applications due to their high piezoelectric coefficients, durability, and stability.[558,580-583] Extensive research has explored methods to enhance the piezoelectric properties of materials, including crystal structure modification through doping or texturing, stoichiometry optimization during crystal growth, and domain alignment through poling or mechanical/thermal treatments during the fabrication process.[165,167,285,584-592] However, applying conventional piezoelectric theories and methodologies to understand piezoelectric structure-function relationships in biomaterials poses challenges.[368,369,520] Thus, there is a clear need for an appropriate model system to comprehend and optimize the piezoelectric properties of biomaterials at the molecular level.

In our prior works, we demonstrated the structurally advantageous features of the M13 phage, making the groundbreaking discovery of the piezoelectric effect in the M13 phage[1]. This was achieved by constructing liquid crystalline phage matrices on top of electrodes, demonstrating that mechanical stimulation could generate an electric potential. Through genetic engineering, we also enhanced its energy harvesting capabilities.[4,466] More recently, we have confirmed that M13 phages exhibit triboelectricity and pyroelectricity.[2,3] Despite significant progress in understanding phage-based electric performance, a molecular-level understanding of the intrinsic electrical properties of the M13 phage remains elusive. Consequently, unraveling the structure-function relationship of viral electricity and understanding how different modes of mechanical stimulation contribute to the conversion of

mechanical energy into bioelectricity remains a complex challenge.

In this chapter, I will elucidate a molecular-level exploration into the source of piezoelectricity in the M13 phage, utilizing a combination of MD simulations and the verification of piezoelectricity through SPM characterization of phage films. My investigation leverages the M13 phage as a programmable biomaterial, delving into its bio-piezoelectric properties and unraveling the structure-function relationship. Initially, I conducted MD simulations to calculate all possible piezoelectric tensors within the M13 phage, assessing its response to various mechanical stresses. Specifically, I constructed a model repeat unit consisting of ten α-helical pVIII coat proteins with varying numbers of negatively charged glutamate residues. I computed the contribution of the dipole moment resulting from surface charges and α-helical proteins. Additionally, through the application of different directional mechanical deformations, I calculated 18 modes of piezoelectric constants, demonstrating how the distribution of surface charges on the phage surface influences dipole moment and subsequent changes in the piezoelectric effect under different mechanical stresses. To experimentally verify these effects, I employed EFM and PFM, confirming observable piezoelectric effects in both individual phages and vertically oriented monolayered phage films. The results highlighted that genetic engineering of the negatively charged amino acids on the outer coat proteins significantly contributes to the enhancement of piezoelectricity. Notably, the phage engineered with four glutamate residues exhibited a surface charge density of 16.8 $\mu C\ cm^{-2}$ and effective piezoelectric coefficients of 14.5 and 4.31 pm V^{-1} in the vertical (normal longitudinal d_{33}) and horizontal (normal longitudinal d_{11}) modes, respectively. I conducted additional measurements on the piezoelectric outputs of the phage films across various modes (such as vertical, horizontal, and shear). The outcomes revealed a stronger piezoelectric response in the vertical mode as opposed to shear and horizontal modes, attributed to its greater changes in dipole moment. This engineered phage, with its four-glutamate modification in vertical piezoelectric mode, demonstrated enhanced piezoelectric performance, generating 43.2 V and 208 nA, resulting in 4.2 $\mu W\ cm^{-2}$ under 8.6 N of mechanical stress. The integration of computational analysis and surface probe microscopy characterization in our study of the M13 phage unveils the molecular-level origin of piezoelectricity. This comprehensive approach significantly contributes to our understanding of how nature generates electric potential in biological systems in response to mechanical stimulation. Moreover, the ability to harness different piezoelectric modes of biomaterials can find applications in various fields, from energy harvesting to sensing technologies, making a critical contribution to materials science and biotechnology.

3.2 Piezoelectric structure of M13 phage

The M13 phage is covered by 2700 copies of pVIII proteins, organized in a pattern involving both five-fold rotational and two-fold screw symmetry that make its piezoelectric properties (Figure 3-1a and 3-1b). The pVIII protein is arranged at an angle of approximately

20 degrees relative to the long axis of the M13 phage (Figure 3-1c).[1,3,423] The WT-pVIII protein is composed of 50 amino acids with varying charges, where negatively charged amino acids are predominantly situated at the outward-facing N-terminal, while positively charged amino acids are concentrated at the inward-facing C-terminal. This configuration results in the creation of a surface charge dipole moment from the N-terminal to the C-terminal, indicated by the red arrow in Figure 3-1c. Concurrently, the pVIII protein's backbone forms an α-helical structure through hydrogen bonds, generating a core dipole moment in the opposite direction, as denoted by the blue arrow in Figure 3-1c. The overall dipole moment of the pVIII protein is established in the direction from the N-terminal to the C-terminal, arising from a combination of the surface charge and core dipole moments, as represented by the gray arrow in Figure 3-1c. Due to the 20-degree tilted angle between the coat protein and the long axis of the M13 phage, the collective dipole moments of these proteins culminate in a macroscopic polarization aligned with the long axis of the phage.[3,4]

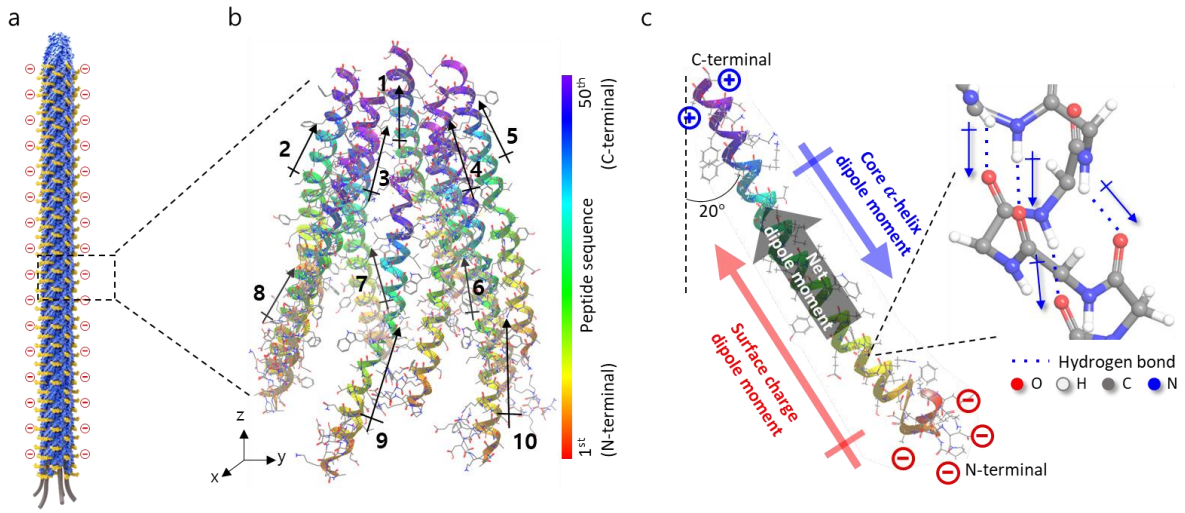

Figure 3-1. Schematic diagram of the M13 phage and its piezoelectric properties. (a-b) The M13 phage has a non-centrosymmetric structure due to its five-fold rotational and two-fold screw symmetry of pVIII proteins. (c) Schematic representation of a pVIII protein. The formation of the net dipole moment from the N-terminal to the C-terminal is ascribed to the surface charge dipole moment and core dipole moment, which arise from the surface charges and the α-helical protein structure, respectively.

3.3 Molecular mechanism of the piezoelectricity in M13 phage

3.3.1 Dipole moment of genetically engineered M13 phages

The M13 phage exhibits a directional piezoelectric effect in response to various mechanical stresses (Figure 3-2a-c). A piezoelectric tensor, depicted in Figure 3-3, serves as a

mathematical representation of the relationship between mechanical stress and electric polarization in piezoelectric materials. While conventional research has predominantly focused on inorganic and organic piezoelectric materials, biomaterials present unique challenges due to their departure from conventional crystallographic frameworks.[593-595] The symmetric structure of the M13 phage deviates from traditional classification (Figure 3-4). To address this knowledge gap, I conducted MD simulations to explore the piezoelectric tensor of the M13 phage and investigate changes in its dipole moment under mechanical stimulation. To calculate the dipole moment of the phage, I constructed a model repeat unit (RU) featuring ten α-helical pVIII coat proteins (Figure 3-5). This calculation was based on one RU of the phage. Our previous research demonstrated a linear correlation between one RU calculation and bulk bioelectric properties, such as pyroelectricity, in the M13 phage due to its repeating structures.[3] Various phage models were created, introducing different numbers of negatively charged glutamates, ranging from one-glutamate (1E) to four glutamates (4E), to modulate the dipole strength. The net dipole moment of 1 RU of the WT-phage was determined to be 4.57 kD, with 8.27 kD majorly attributed to the surface charge dipole moment and -3.75 kD to the core dipole moment (Figure 3-5). The partial dipole moment produced by C_α of the 1 RU made a minimal contribution, accounting for approximately 3%. In the investigation of 1E- to 4E-phages, the surface charge dipole moment and core dipole moment ranged from 6.33 to 10.5 kD and from -3.61 to -3.96 kD, respectively. As the number of inserted glutamates increased, a corresponding rise in the net dipole moment of the engineered phages was observed, resulting in values of 2.80, 4.25, 5.76, and 6.52 kD for the 1E-, 2E-, 3E-, and 4E-phages, respectively. The introduction of charges into a protein influenced the center of positive and negative charges, impacting the overall charge distribution.[267,596,597] From 1E- to 4E-RU, the addition of glutamates led to an increase in the displacement of the center of positive and negative charges, constituting the dipole moment, from 1.45 to 2.05 Å (Figure 3-6 and Table 5). Consequently, computational results indicate a significant increase in the dipole moment with the introduction of charges to the side chain of the phage, while the contribution from the α-helical backbone remains minimal.

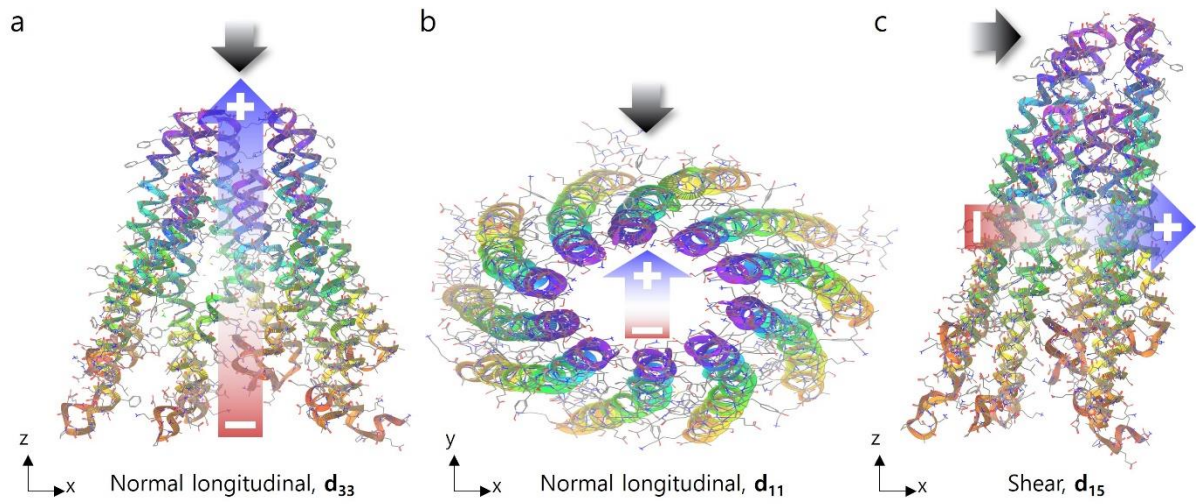

Figure 3-2. (a-c) The polarization of the phage reacts to diverse mechanical stresses, resulting in the manifestation of a directional piezoelectric effect.

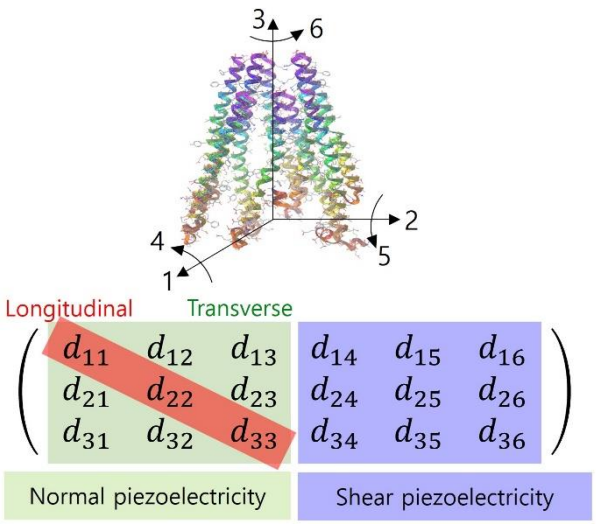

Figure 3-3. Schematic representation of a piezoelectric tensor.

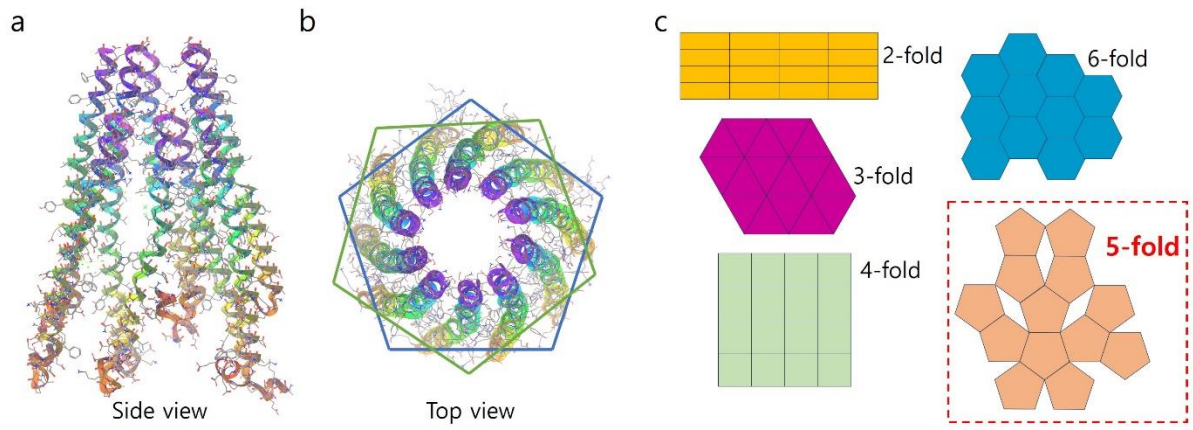

Figure 3-4. (a) and (b) The M13 phage structure with five-fold rotational and two-fold screw symmetry. (c) The structure of the M13 phage does not fit into the traditional crystallographic framework.

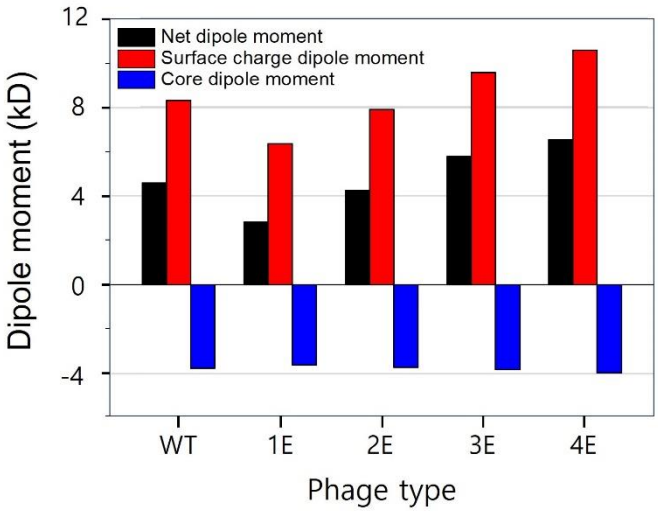

Figure 3-5. The calculated dipole moment of a 1 repeating unit (RU) of the M13 phage.

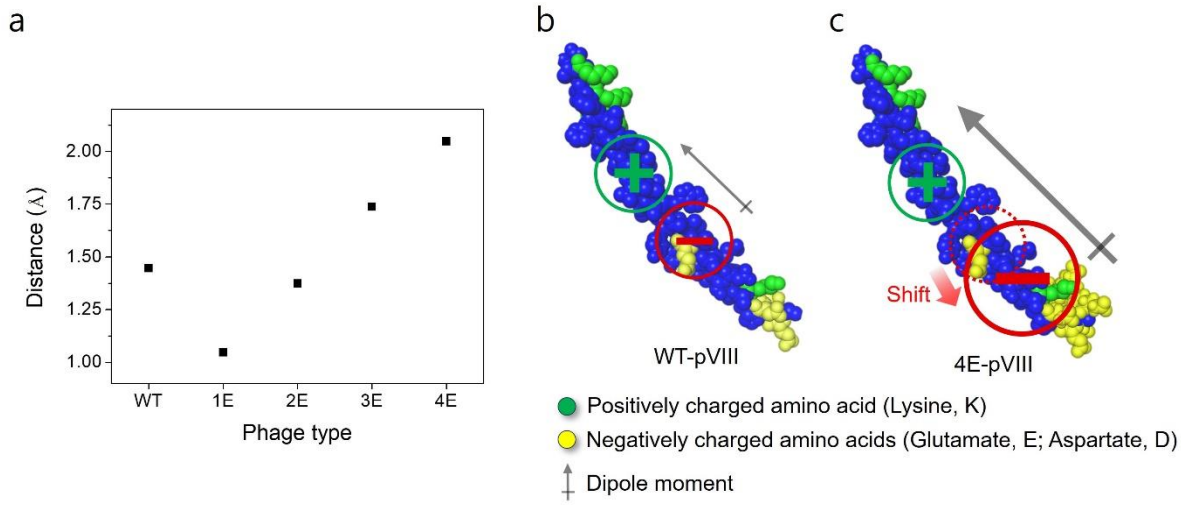

Figure 3-6. (a) The shift between the center of positive and negative charges within a pVIII protein. (b) and (c) The displacement of the charge center expands with the integration of negatively charged residues on the protein surface, leading to an elevation in the dipole moment.

Phage type	Center of negative charge			Center of positive charge charge			Displacement
	x	y	z	x	y	z	[Å]
WT-pVIII	-1.75	-0.137	25.1	-0.725	-0.0437	26.1	1.44
1E-pVIII	-1.24	-0.0657	25.9	-0.557	-0.0247	26.7	1.05
2E-pVIII	1.59	0.122	25.1	0.638	0.0429	26.0	1.31
3E-pVIII	-1.98	-0.222	24.2	-0.722	-0.0418	25.4	1.75
4E-pVIII	2.19	0.271	23.8	0.710	0.0504	25.2	2.05

Table 5. The coordinates of the center of negative and positive charges.

3.3.2 Directional dependency of the dipole moment of M13 phage

I calculated the magnitude of the change in the dipole moment (Δdipole moment) of one RU of the 4E-phage for different piezoelectric modes (e.g., normal longitudinal, normal transverse, and shear) (Figure 3-7a-c). To investigate the different modes of piezoelectric behavior of the phage, I created deformed phage structures for each piezoelectric mode (Figure 3-8). Because the dipole moment and strain exhibit a linear relationship, I demonstrated the Δdipole moment of the phage across a range of strains from 0 to 0.20. To ensure the reliability of phage models in maintaining protein structures under mechanical stimulation (e.g., vertical (normal longitudinal d_{33}), horizontal (normal longitudinal d_{11}), and shear deformation), I

investigated atomic distances and dihedral angles at a strain of 0.20 (Figure 3-9 and 3-10). All atomic distances (e.g, C_α-C, N-C_α, and C-O) in a deformed pVIII protein are measured, exhibiting negligible changes during deformation (Figure 3-9). The dihedral angles (e.g., psi (ψ), phi (ϕ), and omega (ω)) in a deformed pVIII protein are investigated, presenting negligible changes during deformation (Figure 3-10a and 3-10b). Furthermore, I plotted Ramachandran plot for the deformed pVIII proteins. The measurements revealed the pVIII proteins maintain their protein structure upon deformation (Figure 3-10c-f). These results support the suitability of our deformed phage models for piezoelectric analysis. The Δdipole moment for the vertical mode (d_{33}) exhibited a significant increase upon strain, with a Δdipole moment of 529 D at a normal strain of 0.20 (Figure 3-7a and Table 3). In contrast, the Δdipole moment for the horizontal modes (d_{11} and d_{22}) increased by 48.4 and 45.8 D at a strain of 0.20, indicating a minor change (Figure 3-7a and Table 4 and 5). The Δdipole moment in normal transverse piezoelectric modes (d_{12}, d_{13}, d_{21}, d_{23}, d_{31}, and d_{32}) increased with normal strain, ranging from 28.8 to 132 D at a normal strain of 0.20 (Figure 3-7b and Table 6-8). Figure 3-7c shows the Δdipole moment in shear piezoelectric modes (d_{14}, d_{15}, d_{16}, d_{24}, d_{25}, d_{26}, d_{34}, d_{35}, and d_{36}). The Δdipole moment for d_{15}, d_{24}, d_{26}, and d_{16} modes increased with shear strain, ranging from 73.7 to 226 D at a shear strain of 0.20 (Figure 3-7c and Table 9-11). However, the Δdipole moment for the remaining shear piezoelectric modes (d_{14}, d_{25}, d_{34}, d_{35}, d_{36}) showed negligible change, ranging from 3.67 to 14.8 D at a shear strain of 0.20. Piezoelectric coefficients for various piezoelectric modes were calculated based on the dipole moment calculations. The d_{33} mode exhibits the highest value among the normal longitudinal modes, ranging from 1.97 to 22.8 pC N^{-1} (Figure 3-11a and Table 9). In contrast, the d_{32} mode exhibited the highest value for normal transverse modes, ranging from 0.656 to 2.89 pC N^{-1}, while the d_{15} piezoelectric mode had the highest value for shear modes, ranging from 0.156 to 15.5 pC N^{-1} (Figure 3-11b, 3-11c and Table 12). This computational analysis suggests that the piezoelectric properties of the phage are tunable through molecular engineering of the charged structures and exhibit multiple different modes of piezoelectric behavior that are sensitive to strain.

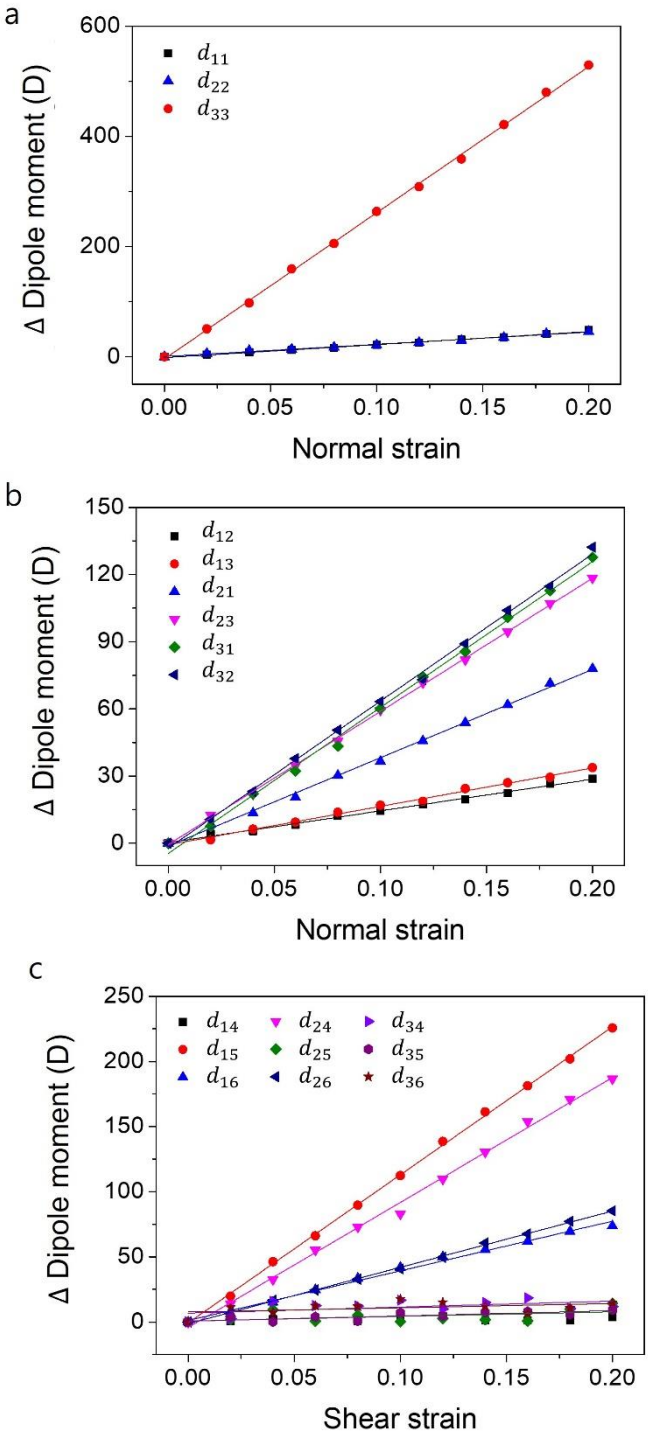

Figure 3-7. (a-c) The change in the dipole moment of 1 RU in normal longitudinal, normal transverse, and shear orientations.

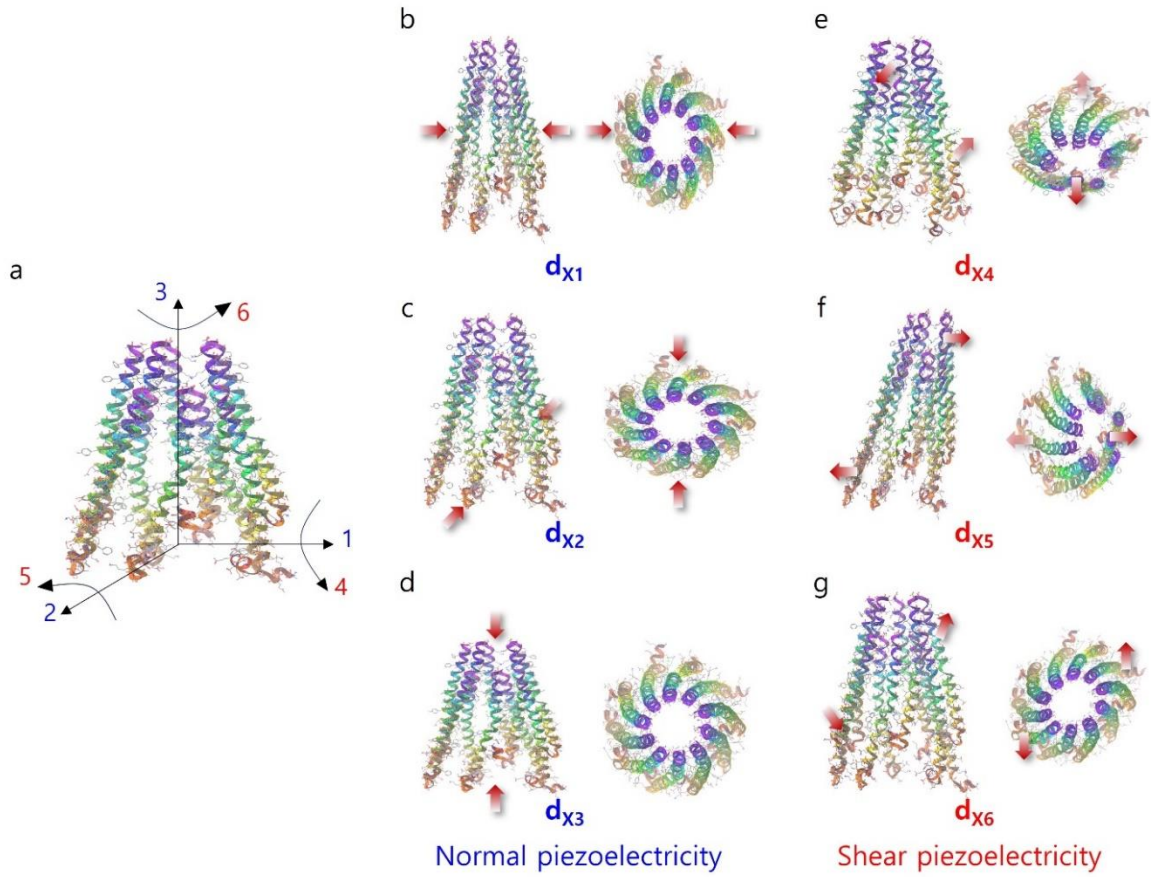

Figure 3-8. (a) The model of an unstrained 1 RU of the M13 phage. (b-d) The structural modifications in normal piezoelectric modes. (e-g) The structural adjustments in shear piezoelectric modes.

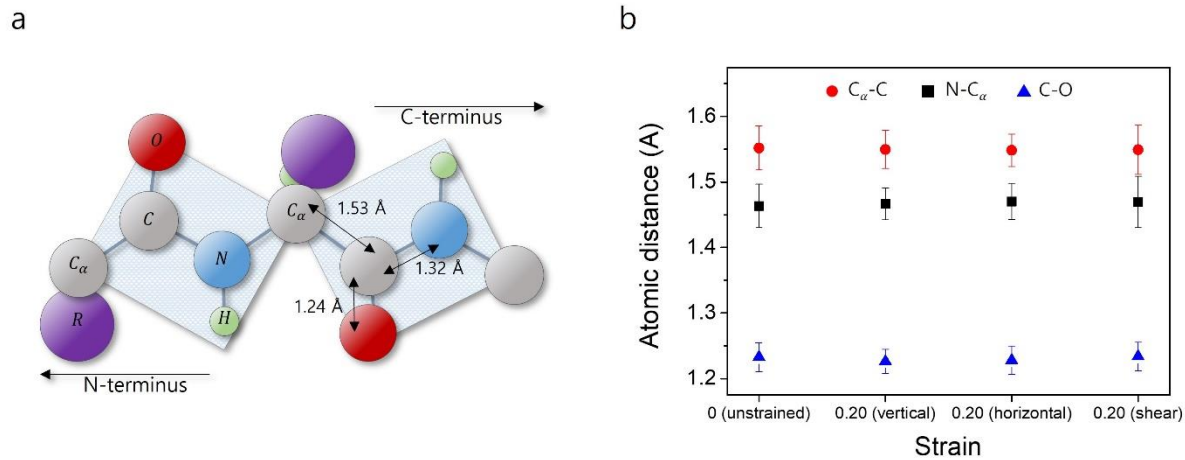

Figure 3-9. (a) Atomic configurations within the peptide bond. (b) Variations in atomic distance for the unstrained, vertical (normal longitudinal d_{33}), horizontal (normal longitudinal

d_{11}), and shear d_{15} piezoelectric modes. The minimal changes in atomic distance suggest that the pVIII protein retains its structural integrity under mechanical stresses.

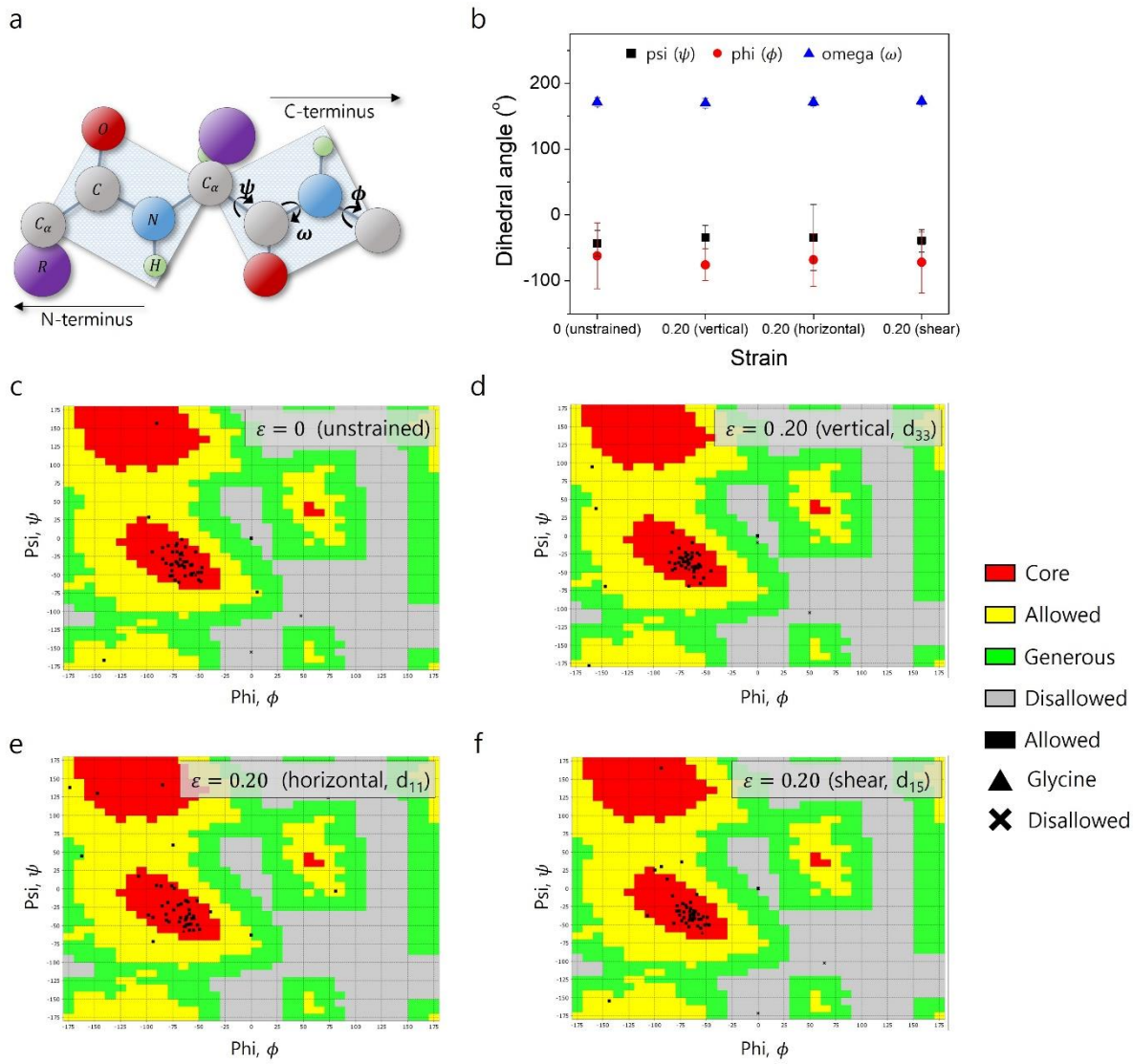

Figure 3-10. (a) Dihedral angles within the peptide bond. (b) Dihedral angle for the unstrained, vertical (normal longitudinal d_{33}), horizontal (normal longitudinal d_{11}), and shear d_{15} piezoelectric modes. The minimal changes in dihedral angle suggest that the pVIII protein retains its structural integrity under mechanical stresses.

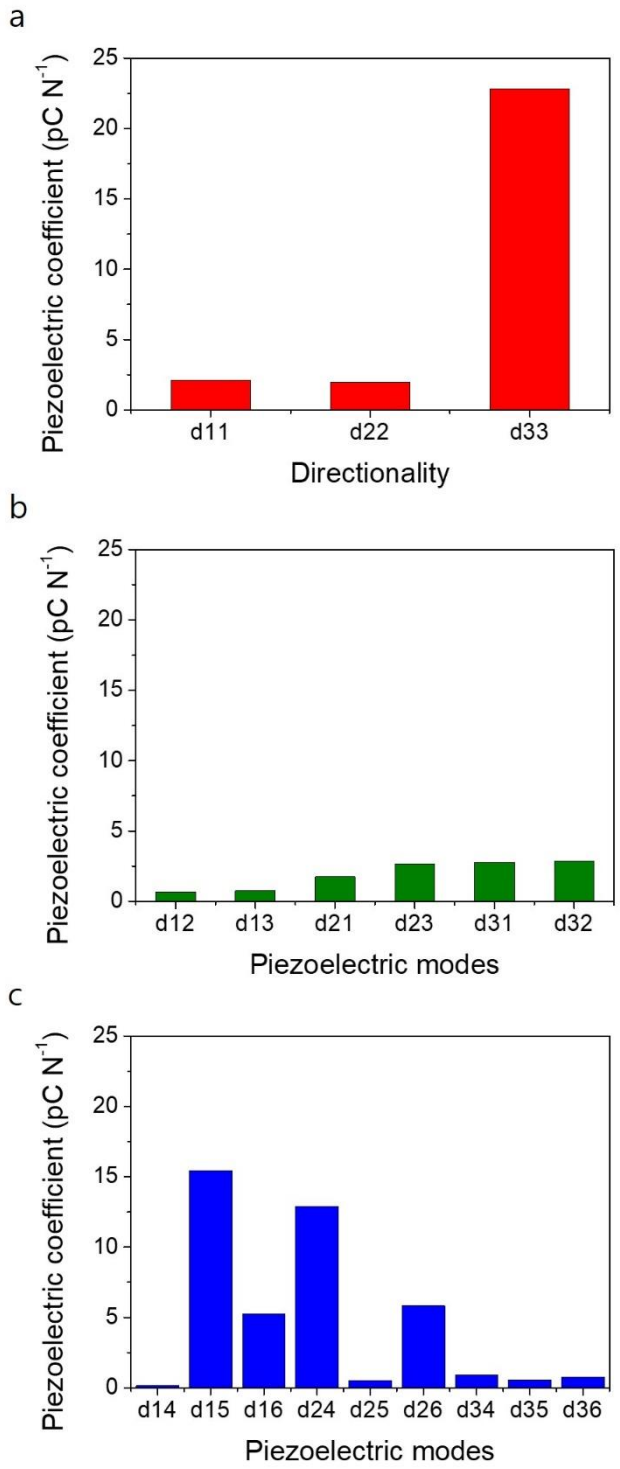

Figure 3-11. The calculated piezoelectric coefficients for different piezoelectric modes for (a) normal longitudinal, (b) normal transverse, and (c) shear piezoelectric modes.

Strain	Dipole moment (unstrained) [D]			Dipole moment (strained) [D]			Dipole moment change [D]		
	1-axis	2-axis	3-axis	1-axis	2-axis	3-axis	1-axis (d_{13})	2-axis (d_{23})	3-axis (d_{33})
0.02				178	441	5938	1.55	12.6	-50.4
0.04				183	450	5891	6.28	21.9	-97.8
0.06				186	463	5829	9.35	34.6	-159
0.08				190	474	5783	13.8	45.5	-206
0.10	176	428	5989	193	488	5725	17.0	59.4	-263
0.12				195	500	5680	18.7	71.7	-309
0.14				201	510	5630	24.4	81.9	-359
0.16				203	523	5568	27.1	94.5	-421
0.18				206	536	5509	29.5	107	-480
0.20				210	547	5460	33.7	118	-529

Table 6. Dipole moment calculation for normal piezoelectric mode under mechanical stimulation in 3-axis direction.

Strain	Dipole moment (unstrained) [D]			Dipole moment (strained) [D]			Dipole moment change [D]		
	1-axis	2-axis	3-axis	1-axis	2-axis	3-axis	1-axis (d_{11})	2-axis (d_{21})	3-axis (d_{31})
0.02				173	437	5996	-3.93	8.53	7.60
0.04				168	442	6011	-8.22	13.5	22.1
0.06				165	449	6021	-11.9	20.6	33.2
0.08				160	459	6032	-16.1	30.3	43.4
0.10	176	428	5989	155	465	6049	-21.5	36.6	60.0
0.12				151	474	6063	-25.2	45.8	74.3
0.14				146	482	6074	-30.9	53.9	85.5
0.16				142	490	6090	-34.9	61.8	101
0.18				135	500	6102	-41.8	71.4	113
0.20				128	506	6117	-48.4	77.9	128

Table 7. Dipole moment calculation for normal piezoelectric mode under mechanical stimulation in 1-axis direction.

Strain	Dipole moment (unstrained) [D]			Dipole moment (strained) [D]			Dipole moment change [D]		
	1-axis	2-axis	3-axis	1-axis	2-axis	3-axis	1-axis (d_{12})	2-axis (d_{22})	3-axis (d_{32})
0.02				181	423	5999	4.27	-5.78	10.6
0.04				182	417	6012	5.47	-11.2	23.1
0.06				185	415	6027	8.31	-13.9	37.7
0.08				189	411	6039	12.1	-17.5	50.4
0.10	176	428	5989	191	407	6052	14.4	-21.5	63.2
0.12				194	402	6062	17.3	-26.2	72.9
0.14				196	399	6078	19.5	-29.9	89.0
0.16				199	393	6093	22.5	-35.3	104
0.18				203	386	6014	26.7	-42.1	115
0.20				205	383	6121	28.8	-45.8	132

Table 8. Dipole moment calculation for normal piezoelectric mode under mechanical stimulation in 2-axis direction.

Strain	Dipole moment (unstrained) [D]			Dipole moment (strained) [D]			Dipole moment change [D]		
	1-axis	2-axis	3-axis	1-axis	2-axis	3-axis	1-axis (d_{14})	2-axis (d_{24})	3-axis (d_{34})
0.02				177	442	5992	0.331	14.0	2.56
0.04				174	461	6005	2.20	32.5	15.7
0.06				180	484	6002	3.20	55.2	12.6
0.08	176	428	5989	176	501	6002	0.352	72.9	12.3
0.10				172	511	6006	4.05	82.9	16.7
0.12				181	538	5999	4.13	110	9.89
0.14				175	559	6004	1.17	130	14.9

0.16				178	582	6008	1.06	154	18.5
0.18				177	599	6000	0.973	171	10.5
0.20				173	615	6001	3.67	187	12.0

Table 9. Dipole moment calculation for shear piezoelectric mode under mechanical stimulation in 4-axis direction.

Strain	Dipole moment (unstrained) [D]			Dipole moment (strained) [D]			Dipole moment change [D]		
	1-axis	2-axis	3-axis	1-axis	2-axis	3-axis	1-axis (d_{15})	2-axis (d_{25})	3-axis (d_{35})
0.02				196	427	5993	19.8	1.92	3.97
0.04				223	438	5989	46.2	9.40	0.130
0.06				243	428	5993	66.2	0.596	3.94
0.08				266	423	5990	89.6	5.32	0.810
0.10	176	428	5989	289	429	5996	112	0.355	6.97
0.12				315	431	5993	139	2.72	4.57
0.14				338	430	5996	161	1.79	7.37
0.16				358	428	5997	181	0.696	8.01
0.18				378	438	5995	202	9.98	5.92
0.20				402	443	5998	226	14.3	9.30

Table 10. Dipole moment calculation for shear piezoelectric mode under mechanical stimulation in 5-axis direction.

Strain	Dipole moment (unstrained) [D]			Dipole moment (strained) [D]			Dipole moment change [D]		
	1-axis	2-axis	3-axis	1-axis	2-axis	3-axis	1-axis (d_{16})	2-axis (d_{26})	3-axis (d_{36})
0.02				170	435	6001	-6.42	6.66	11.2
0.04	176	428	5989	161	445	5997	-15.1	16.5	7.42
0.06				152	453	6002	-24.6	24.5	12.4

0.08	143	461	6001	-33.5	32.7	11.9
0.10	135	469	6007	-41.9	40.7	17.7
0.12	126	478	6004	-50.0	49.6	15.1
0.14	121	489	6001	-55.6	60.7	12.1
0.16	115	496	5996	-61.8	67.6	6.51
0.18	107	506	6000	-69.5	77.2	10.6
0.20	103	514	6004	-73.7	85.2	14.8

Table 11. Dipole moment calculation for shear piezoelectric mode under mechanical stimulation in 6-axis direction.

Piezoelectric mode		Dipole moment of 1 RU at given stress [D]	Dipole moment of 1 M13 phage [C m]	Unit cell volume [m^3]	Stress [N m^{-2}]	Piezoelectric coefficient [pC N^{-1}]
Normal longitudinal	d_{11}	-48.4	-4.36×10^{-26}			-2.09
	d_{22}	-45.8	-4.12×10^{-26}			-1.97
	d_{33}	-529	-4.77×10^{-25}			-22.8
Normal transverse	d_{21}	40.3	3.63×10^{-26}			1.74
	d_{31}	64.1	5.78×10^{-26}			2.76
	d_{12}	15.2	1.37×10^{-26}			0.656
	d_{32}	67.0	6.04×10^{-26}			2.89
	d_{13}	17.4	1.57×10^{-26}			0.750
	d_{23}	62.1	5.59×10^{-26}	4.84×10^{-23}	4.32×10^{8}	2.67
Shear	d_{14}	3.61	3.25×10^{-27}			0.156
	d_{15}	359	3.23×10^{-25}			15.5
	d_{16}	-122	-1.10×10^{-25}			-5.24
	d_{24}	299	2.69×10^{-25}			12.9
	d_{25}	11.9	1.07×10^{-26}			0.513
	d_{26}	135	1.22×10^{-25}			5.83
	d_{34}	21.4	1.93×10^{-26}			0.923
	d_{35}	13.3	1.20×10^{-26}			0.574
	d_{36}	17.9	1.62×10^{-26}			0.773

Table 12. Calculation of piezoelectric coefficient of the M13 phage in various piezoelectric modes.

3.4 Surface charge to piezoelectric response studies using scanning probe microscopy

3.4.1 Dielectric constant characterization

To verify the outcomes of the MD simulations, I used SPM techniques to characterize the piezoelectric properties of the phage. Initially, I created monolayer phage films on gold substrates and evaluated their electric potential using EFM.[2] When a surface probe tip encounters the inherently charged phage, a Coulomb force arises between the tip and the phage (Figure 3-12). Consequently, when a DC voltage is applied between the tip and the sample, deflection occurs in the cantilever due to capacitance contributions.[598,599] The local dielectric constant of the monolayer phage film can be calculated using the theoretical capacitive model, and the formula can be demonstrated through SPM and finite element simulations.[600] The total energy of the system, E_T, can be expressed by equation (8).

$$E_T = E_K + E_{vdw} - E_C \quad (8)$$

where E_K is the recovering elastic energy, E_{vdw} is the remaining energy contributed by Van der Waals force, and E_C is the electrostatic probe-sample energy. I made approximations assuming that Van der Waals forces are negligible due to the long distance between the AFM tip and the sample.

$$E_T = \frac{1}{2}k(z_0 - z)^2 - \frac{1}{2}C_T V^2 \qquad (9)$$

where k is the spring constant of the cantilever, z is the AFM tip-sample distance, C_T is the total capacitance, and V is the applied bias. The minimum energy with respect to z can be calculated.

$$\frac{\partial E_T}{\partial z} = -k(z_0 - z) - \frac{1}{2}\frac{\partial C_T}{\partial z}V^2 = 0 \qquad (10)$$

where

$$\frac{\partial C_T}{\partial z} \approx -F - f(z) = \frac{\partial(C_l + C_c)}{\partial z} - f(z) \qquad (11)$$

and

$$\frac{\partial C_{apex}}{\partial z} = -f(z) = -\frac{2\pi\varepsilon_0 R\tilde{R}}{(z+\tilde{R}+\frac{h}{\varepsilon_r})(z+\frac{h}{\varepsilon_r})} \qquad (12)$$

with $\tilde{R} = R(1 - \sin\theta)$ where R is the tip radius, h is the thickness of the capacitive layer, ε_0 is the vacuum permittivity, C_l is the cantilever capacitance and C_c is the cone capacitance. By substituting equation (11) and (12) into equation (10), we obtain the following equation (13) for the local dielectric constant, ε_r, as a function of the cantilever deflection, D.

$$\varepsilon_r(D) = 2h\left\{-2z - \tilde{R} + \left([2z + \tilde{R}]^2 - 4z(z + \tilde{r}) + \frac{4(V_{tip} - V_{sp})^2 \pi \varepsilon_0 R\tilde{R}}{k(D - D_0)}\right)^{\frac{1}{2}}\right\}^{-1} \quad (13)$$

where h is the diameter of the phage, z is the AFM tip-phage distance, V_{tip} is the applied voltage, and V_{sp} is the surface potential of the phage film. The calculated dielectric constant of WT- and engineered phages was approximately 3.95±0.15 (4 measurements were performed for each type of phage; total 20 measurements), indicating a negligible difference resulting from genetic modification (Figure 3-13).

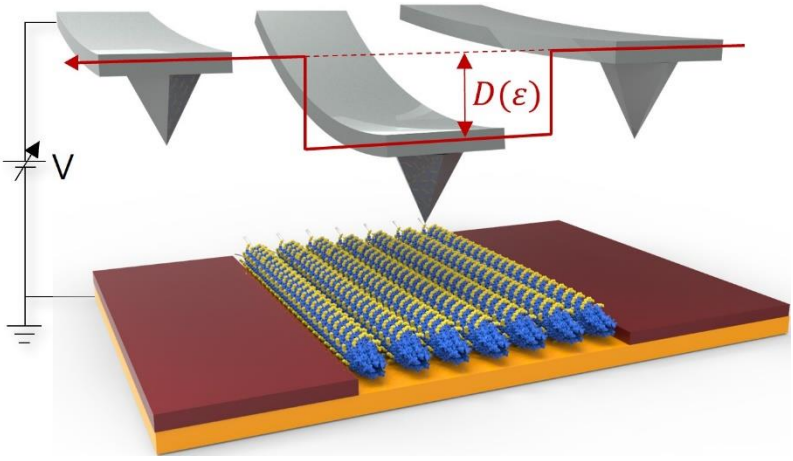

Figure 3-12. Diagram illustrating the setup of the EFM system used for dielectric constant characterization.

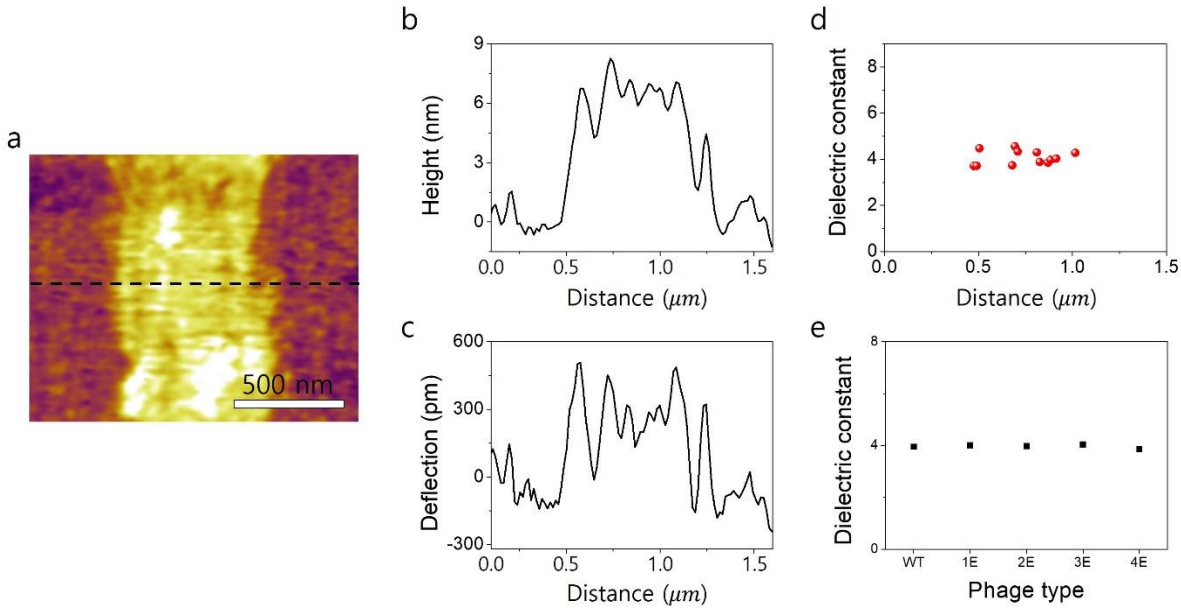

Figure 3-13. (a) EFM image of the horizontally aligned WT-phage film. (b-c) Profiles indicating height and deflection along the dashed line in (a) for the horizontally aligned WT-phage film. (d) Dielectric constant of the WT-phage calculated from (b) and (c). (e) Dielectric constants computed for WT- and engineered phages.

3.4.2 Surface charge density characterization

I prepared individual phage samples on gold substrates and evaluated their electric potential using EFM (Figure 3-14). The tip measured the force gradient in the vertical direction, and consequently, the shift in frequency (Δf) relative to the resonant frequency of the cantilever (f_0) was monitored. The surface charge density was determined based on the Coulomb force between the AFM tip and the sample. When the AFM tip interacted with the charged phage, it recorded the force gradient in the vertical direction ($F'(z) = \partial F/\partial z$), resulting in a frequency shift (Δf). This allowed us to obtain the frequency shift relative to the resonant frequency of the cantilever (f_0).

$$\frac{\Delta f}{f_0} = -\frac{\partial F/\partial z}{2k} \qquad (14)$$

To calculate the surface charge density of the phage, a parallel plate model was employed.[601,602] The Coulomb force driven by the charged phage during the EFM measurement was given by equation (15).

$$F(z) = \frac{A}{(z+t/\varepsilon)^2} \times \left(-\frac{t^2\sigma^2}{2\varepsilon_0\varepsilon^2} + \frac{2tV_{tip}\sigma}{\varepsilon} + \frac{\varepsilon_0 {V_{tip}}^2}{2}\right) \qquad (15)$$

where A is the surface area of the charged region, z is the AFM tip-sample distance, t is the thickness of the capacitive layer, and ε is the dielectric constant. By combining equation (14) and (15), the formula for the $\Delta f(\sigma)$ is obtained as equation (16).[601,602]

$$\Delta f = \frac{f_0 A}{k(z+t/\varepsilon)^3} \times \left[-\frac{t^2\sigma^2}{2\varepsilon_0\varepsilon^2} + \frac{2tV_{tip}\sigma}{\varepsilon} + \frac{\varepsilon_0 {V_{tip}}^2}{2}\right] \qquad (16)$$

At a resonant frequency of 70.938 kHz, the oscillation frequency decreased upon the AFM tip encountering the phage. In the case of the 4E-phage, the phage background displayed a frequency of -153 Hz, indicating an average frequency difference of 6.80 Hz between the phage and background area (Figure 3-15a and 3-15b). Consequently, I observed that the actual frequency of the 4E-phage with respect to the free-air resonant frequency was -146 Hz. The frequency shifts of WT-, 1E-, 2E-, and 3E-phages were observed as -93.7, -68.3, -92.1, and -104 Hz, respectively (Figure 3-15a and 3-15b and Table 13). Subsequently, I employed an electrostatic analysis of the EFM system, using a parallel plate model to calculate surface charge density.[603] The calculated surface charge densities were determined to be 15.1, 14.2, 15.0, 15.4, and 16.7 μC cm^{-2} for WT-, 1E-, 2E-, 3E-, and 4E-phages, respectively (Figure 3-16 and Table 14). The surface charge properties of the phages were further elucidated using gel

electrophoresis. Figure 3-17 illustrates that both the WT-phage and engineered phages migrated towards the anode due to their negatively charged surfaces. It was observed that 1E- and 2E-phages migrated less towards the anode, indicating lower surface charge than the WT-phage. Conversely, 3E- and 4E-phages migrated towards the anode more than the WT-phage due to their abundant surface charge. Additionally, the surface charge properties of the phages were characterized using the isoelectric point, revealing that phages with more negative charges on their surfaces exhibited stronger surface charge characteristics, aligning with the consistent trend observed in the EFM analysis (Figure 3-18). To further confirm the surface charge characteristics of the phages, zeta potential measurements were employed. Figure 3-19 indicates that the zeta potential of the WT-phage was -31.9 mV, confirming its negatively charged nature. The phages with different numbers of glutamate insertions (1E-4E) exhibited sequentially different zeta potentials of -17.1, -26.6, -35.3, and -45.7 mV, respectively. These results affirm that the structural modification of the pVIII protein with varying amounts of charged residues can indeed control the surface charge properties of the phage.

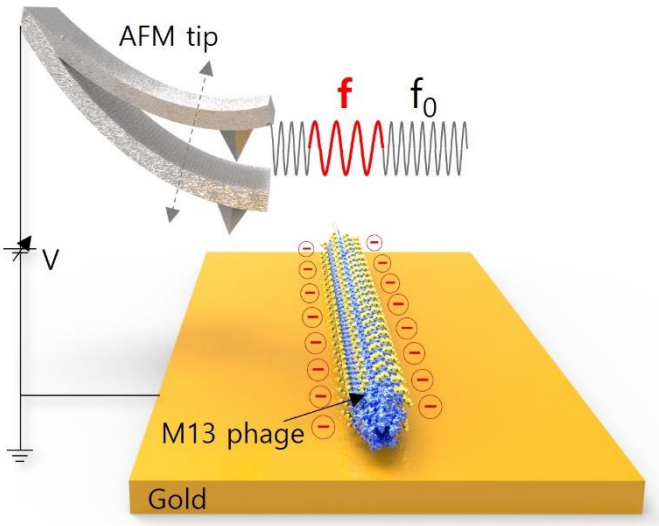

Figure 3-14. Schematic of the EFM system used for surface charge density characterization.

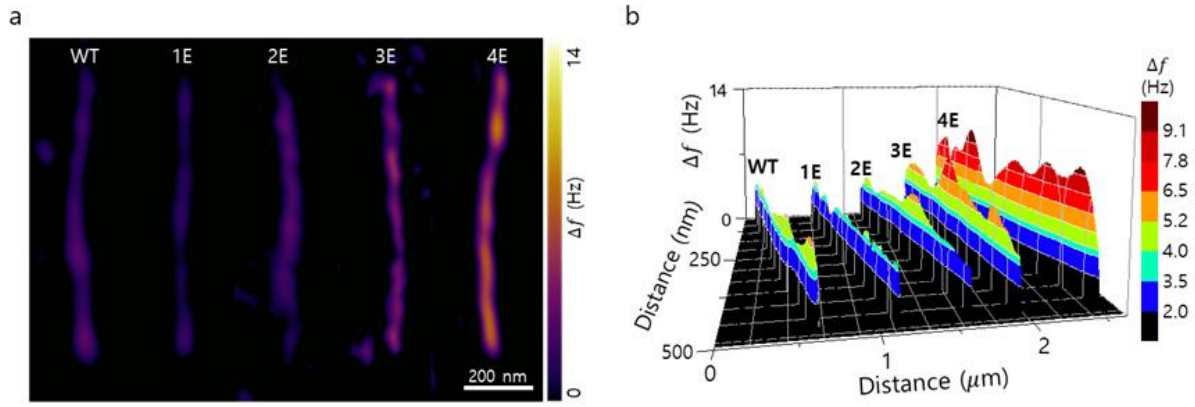

Figure 3-15. (a) The frequency images of WT- and engineered phages. (b) Frequency profiles of the WT- and engineered phages from (a).

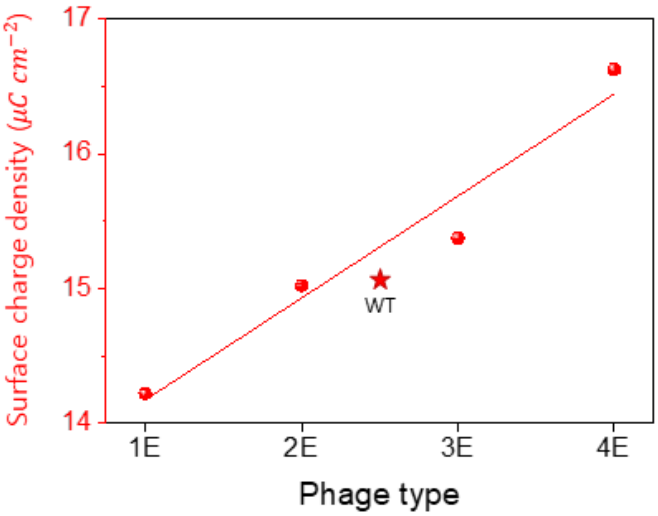

Figure 3-16. Calculated surface charge densities of the WT- and engineered-phages. Error bars indicate one standard deviation.

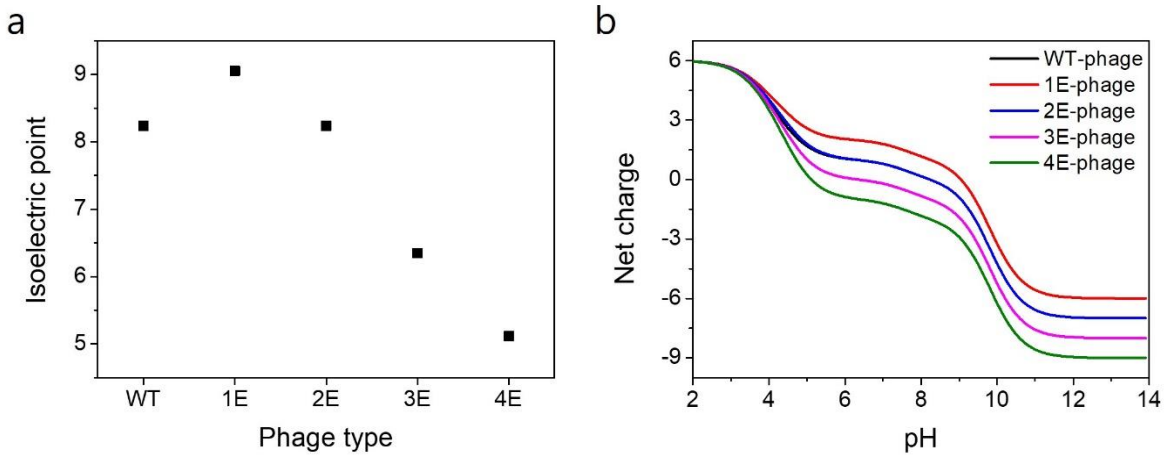

Figure 3-17. Isoelectric point calculations for WT- and engineered-phages.

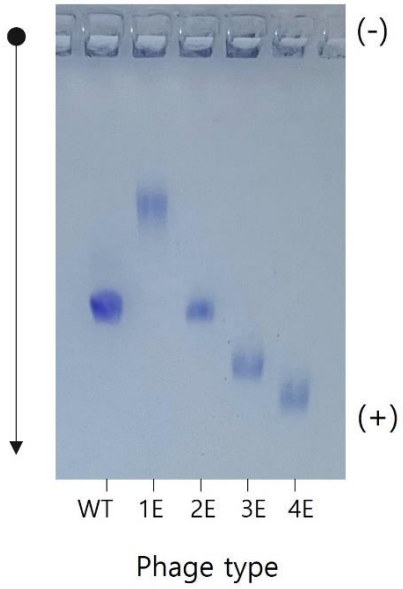

Figure 3-18. Gel electrophoresis measurements for WT- and engineered-phages.

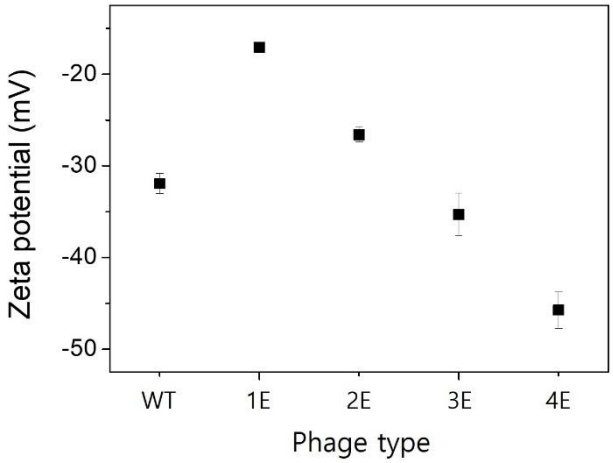

Figure 3-19. Zeta potential measurements for WT- and engineered-phages.

Phage type	$\Delta f_{phage-droplet}$ [Hz]	f_0 [Hz]	$\Delta f_{droplet-f_0}$ [Hz]	Actual Δf ($\Delta f_{phage-f_0}$) [Hz]
WT	4.04		-97.7	-93.7
1E	3.08		-71.4	-68.3
2E	3.90	70938	-96.0	-92.1
3E	5.06		-109	-104
4E	6.80		-153	-146

Table 13. Calculation of the frequency shifts of the M13 phage.

Phage type	Actual Δf ($\Delta f_{phage-f_0}$) [Hz]	A [m^{-2}]	k [N m^{-1}]	z [nm]	t [nm]	ε	V_{tip} [V]	Surface charge density [μC cm^{-2}]
WT	-93.7							15.1
1E	-68.3							14.2
2E	-92.1	5.81×10^{-15}	2.43	118	6.60	3.95	5.00	15.0
3E	-104							15.4
4E	-146							16.7

Table 14. Calculation of the surface charge density of the M13 phage.

3.5 Vertical and horizontal piezoelectric output characterization

I carried out PFM to investigate how the surface charge modifications of the phage contribute to its piezoelectric behavior, examining both vertical and horizontal piezoelectric modes. Employing pIII tail-engineered phage with 6 histidine (6H), I fabricated vertically standing phage films using the capillary force-driven self-assembly method, introducing a varying number of glutamates (ranging from 1E to 4E) (Table 15).[3,4] This approach ensures a unidirectional arrangement of phage polarization, facilitating the measurement of the vertical (normal longitudinal d_{33}) piezoelectric mode. By applying different voltages ranging from 0 to 7 V between the PFM tip and substrate, I monitored the forces generated based on the phage type and their mechanical responses.[1,4] In the vertical mode (d_{33}) of piezoelectric characterization, the effective piezoelectric coefficients were measured to be 12.2, 11.6, 12.2, 12.9, and 15.4 pm V^{-1} for WT-, 1E-, 2E-, 3E-, and 4E-phage films, respectively (Figure 3-20). This outcome suggests that phages with higher surface charges form a larger dipole moment, indicating stronger piezoelectricity. Additionally, I fabricated horizontally aligned phage films to measure the horizontal piezoelectric mode (d_{11} and d_{22} modes are randomly mixed). Given that the piezoelectric response of horizontally aligned phage film is established to be independent of thickness at 100 nm or beyond[1], I carried out the measurements within the thickness range of 300 nm. The resulting effective piezoelectric coefficient in the horizontal mode (d_{11}) measured to be 3.49, 3.32, 3.52, 3.96, and 4.31 for WT-, 1E-, 2E-, 3E-, and 4E-phage films, respectively (Figure 3-21). The PFM measurements were calibrated using a periodically-poled lithium niobate (PPLN).

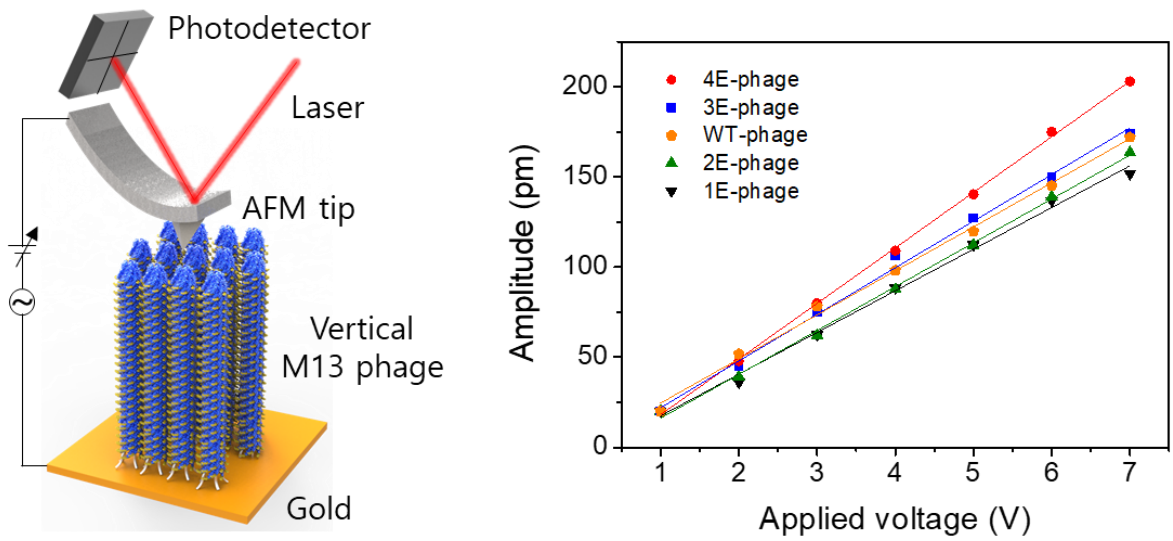

Figure 3-20. Comparison of PFM amplitude versus applied voltage for WT- and engineered phages along the normal longitudinal d_{33} piezoelectric mode.

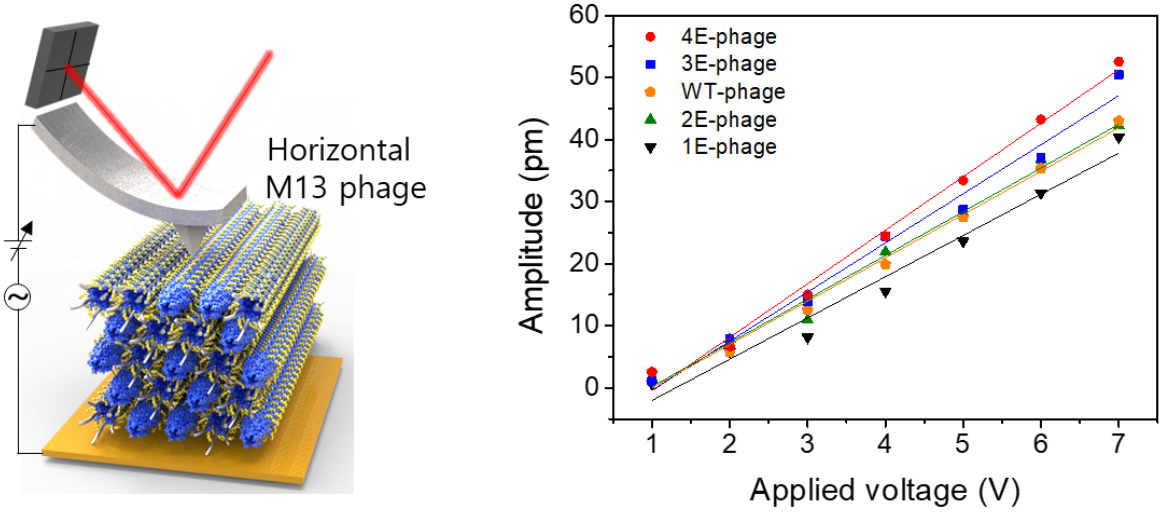

Figure 3-21. Comparison of PFM amplitude versus applied voltage for WT- and 4E-phages along the normal longitudinal d_{11} piezoelectric mode.

Phage type	Primary structure of pVIII proteins*
WT	AEGDDPAKAAFNSLQASATEYIGYAWAMVVVIVGATIGIKLFKKFTSKAS
1E	A*EG*DPAKAAFNSLQASATEYIGYAWAMVVVIVGATIGIKLFKKFTSKAS
2E	A*EEG*DPAKAAFNSLQASATEYIGYAWAMVVVIVGATIGIKLFKKFTSKAS
3E	A*EEEG*DPAKAAFNSLQASATEYIGYAWAMVVVIVGATIGIKLFKKFTSKAS
4E	A*EEEE*DPAKAAFNSLQASATEYIGYAWAMVVVIVGATIGIKLFKKFTSKAS
Phage type	**Primary structure of pIII proteins***
All	*HHHHHH*GGGSAETVESCLAKSHT

Table 15. Primary structures for pVIII and pIII proteins[1,3].

*The primary structure of the pVIII and pIII proteins of the M13 phage and the insert is *underlined and italicized.*

3.6 Shear piezoelectric output characterization

I studied the shear piezoelectric properties of the M13 phage using vertically aligned monolayered 4E-phage films. By varying the magnitude and direction of forces using PDMS

molds tilted at angles of θ = 15, 30, 45, and 60° (Figure 3-22a-c), I measured the generation of piezoelectric potential. At a 0° tilted angle, the vertical (d_{33}) piezoelectric output was measured, as the forces in this mode are purely vertical. Increasing the tilt angles up to 60° resulted in piezoelectric outputs that combined vertical and shear contributions (Figure 3-23 and 3-24). The measured outputs initially increased linearly with force up to 3 N, after which they exhibited a nonlinear increase due to the nonlinear elasticity and dipole moment change of the phage film, consistent with my previous findings. The shear piezoelectric output, calculated by subtracting the vertical contribution, exhibited a trend towards a specific force-dependent shear piezoelectricity. In this characterization system, the shear piezoelectric output was found to be negative, which is attributed to the opposite signs of the piezoelectric coefficients of the vertical and shear modes as determined by MD simulations. The mechanical-to-electrical conversion values for the vertical (d_{33}) and shear (d_{34}) modes of phage piezoelectricity at low forces (< 3 N) were 8.5 V N^{-1} (38 nA N^{-1}) and 2.1 V N^{-1} (9.7 nA N^{-1}), respectively. To compare with the horizontal mode (d_{11}), I also fabricated horizontally aligned phage films and measured their piezoelectric outputs, which yielded a mechanical-to-electrical conversion value of 0.066 V N^{-1} (2.3 nA N^{-1}) (Figure 3-23c, 3-24c, and 3-25).

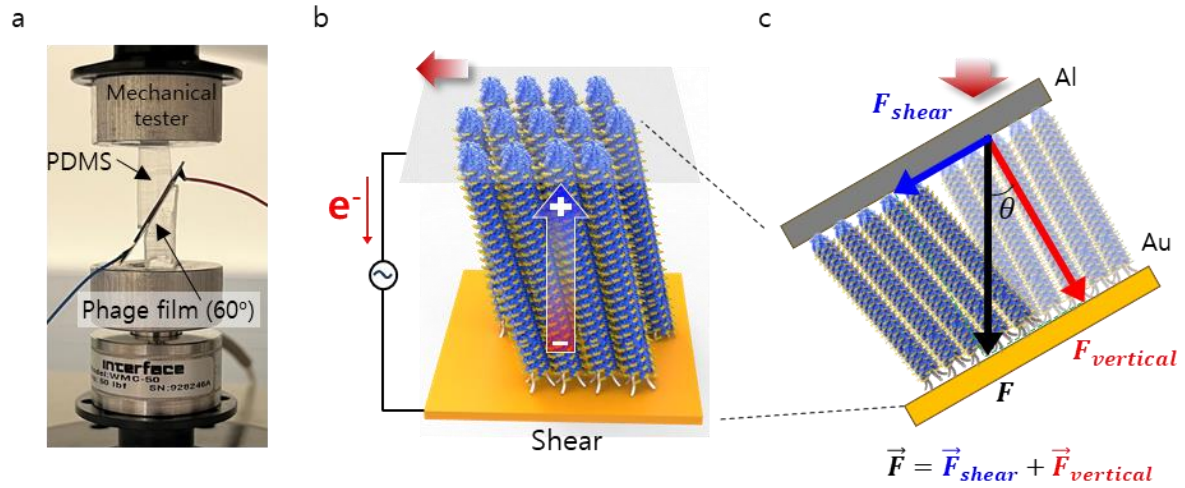

Figure 3-22. Schematic representation of Piezo-PhD in shear orientation.

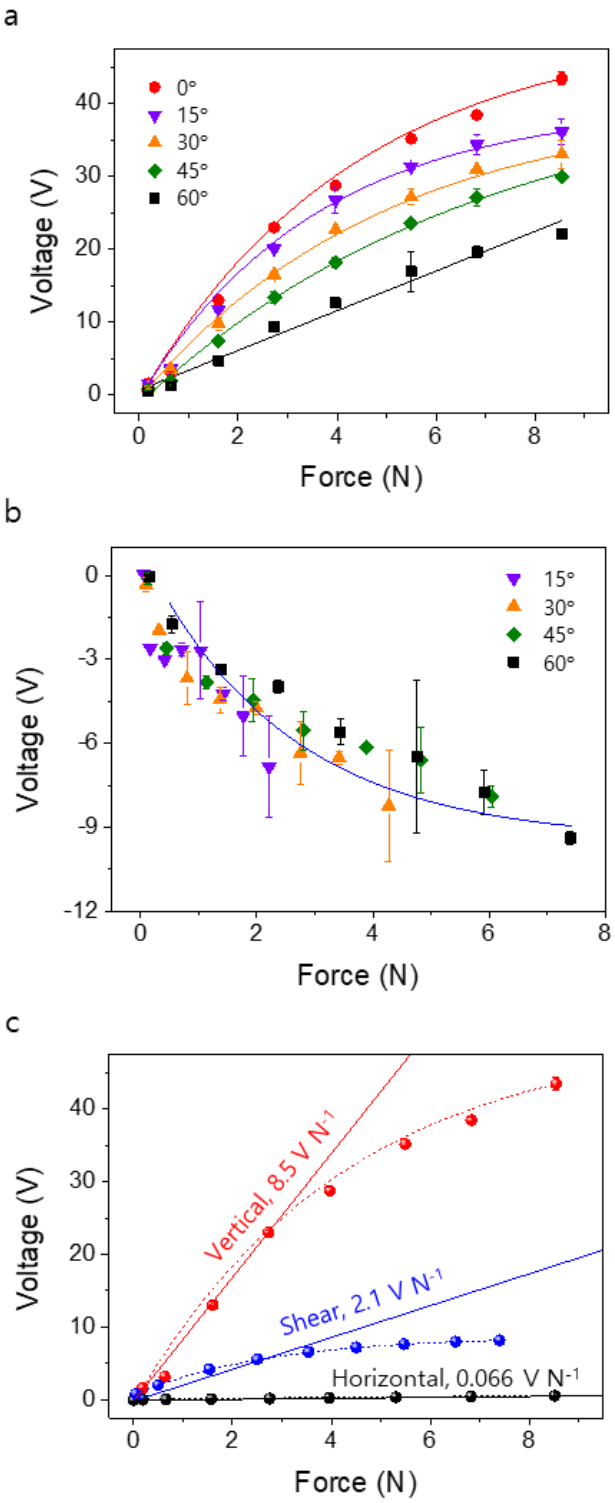

Figure 3-23. Shear output voltage measurements of Piezo-PhDs. (a) Shear output voltage of Piezo-PhDs at different tilted angles. (b) Calculated shear output voltage from (a). (c) Comparison of piezoelectric output voltage among vertical, shear, and horizontal modes.

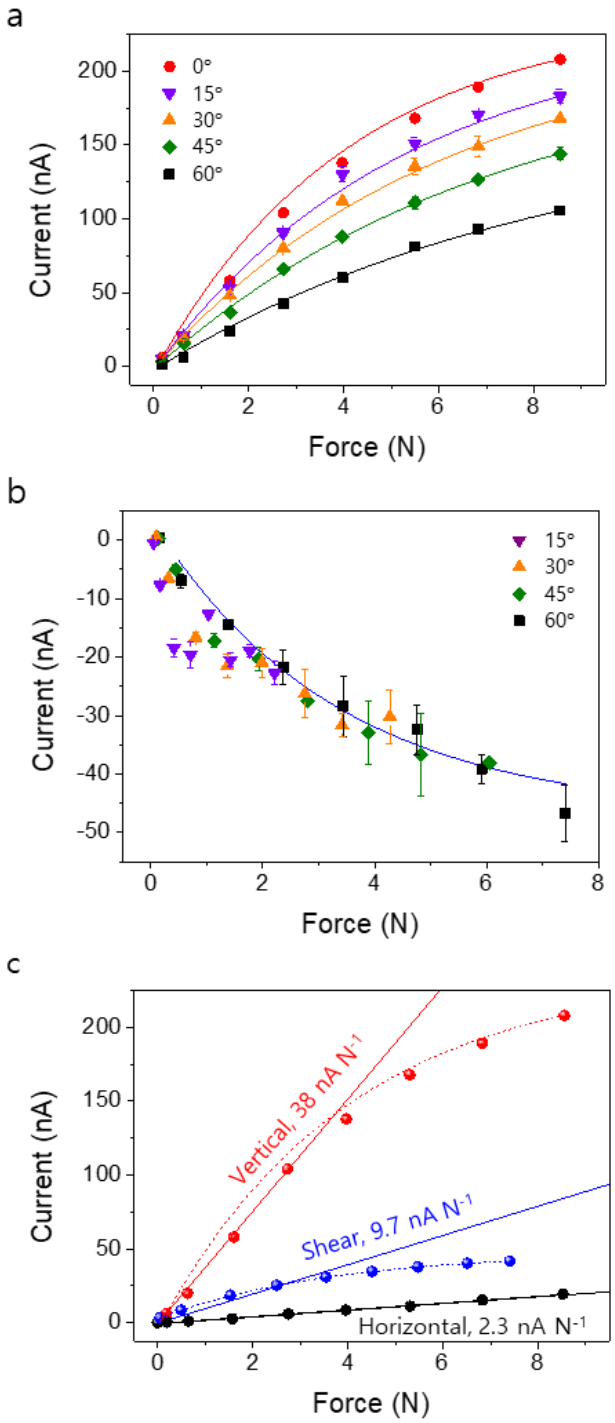

Figure 3-24. Shear output current measurements of Piezo-PhDs. (a) Shear output current of Piezo-PhDs at different tilted angles. (b) Calculated shear output current from (a). (c) Comparison of piezoelectric output current among vertical, shear, and horizontal modes.

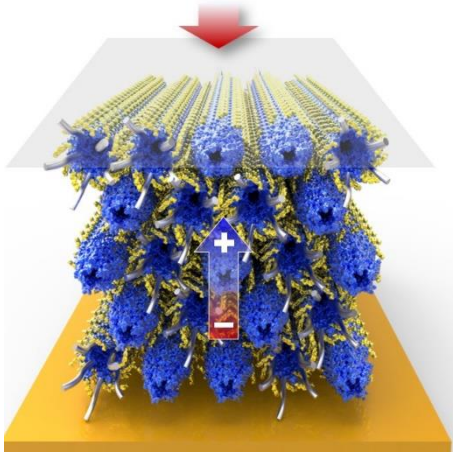

Figure 3-25. Schematic representation of Piezo-PhD in horizontal orientation.

3.7 Characterization of phage-based piezoelectric devices

I produced energy harvesting devices based on phages and assessed their piezoelectric performance using vertically standing 4E-Piezo-PhDs (Figure 3-26a-c). I measured the output voltage and current of the Piezo-PhDs under periodic mechanical force applications (Figure 3-27). With the application of 8.6 N of force, I observed an output voltage of 43.2 V and an output current of 208 nA (Figure 3-28). When the probes were connected in reverse, resulting in the reversal of the polarities of the voltage and current (Figure 3-29), it indicated that the output signal is a consequence of the piezoelectric effect of the Piezo-PhD. Through impedance-dependent piezoelectric output measurements across various electrical resistors ranging from 120 to 1 Gohm, the Piezo-PhD demonstrated a maximum power density of 4.6 μW cm^{-2} at 50 Mohm (Figure 3-30). Rectifying the alternating current (AC) generated from the phage-based piezoelectric device into a direct current (DC) output allowed us to charge a 1 μF capacitor to 2.5 V within 60 s (Figure 3-31). The Piezo-PhD generated sufficient electrical energy to illuminate 22 LEDs upon mechanical stimulation, surpassing phage-based Piezo-PhDs published to date (Figure 3-32).

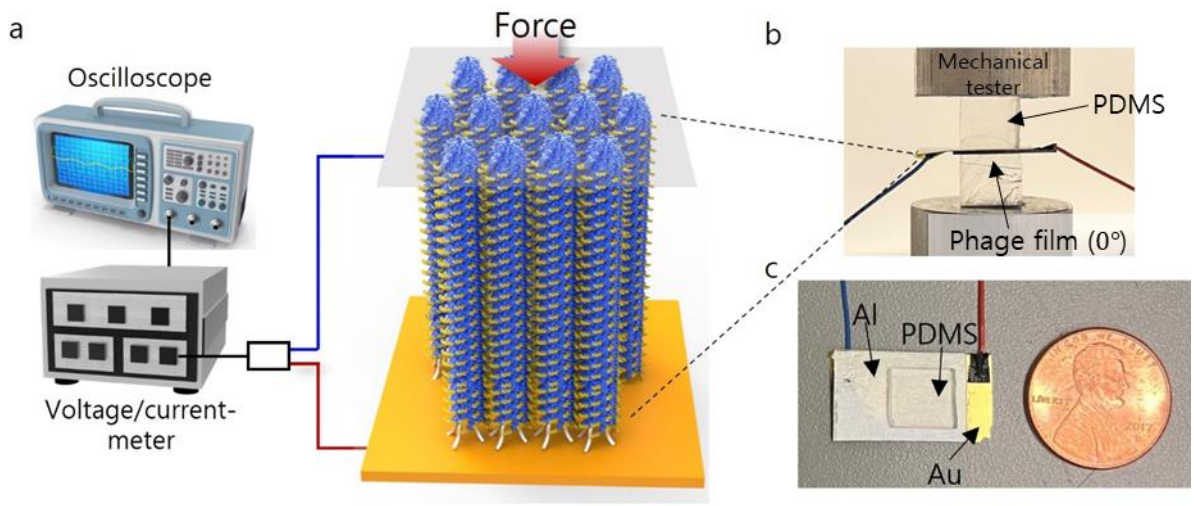

Figure 3-26. (a) and (b) Schematic of piezoelectric output characterization measurement setup. (c) Photograph of a Piezo-PhD.

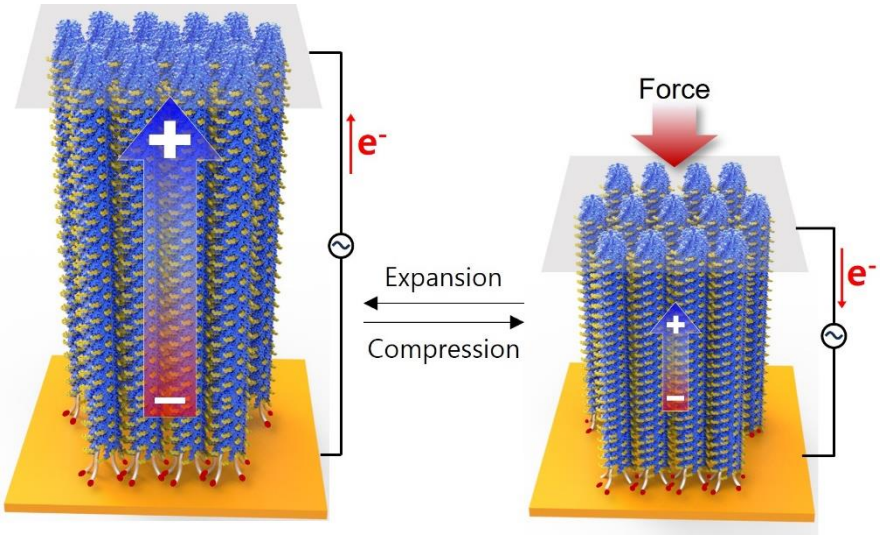

Figure 3-27. Working principle of a Piezo-PhD. Upon applying mechanical force to the piezoelectric device based on phages, the polarization of the phages undergoes a shift. Consequently, electrons migrate through the external conductive wire to establish electrical equilibrium.

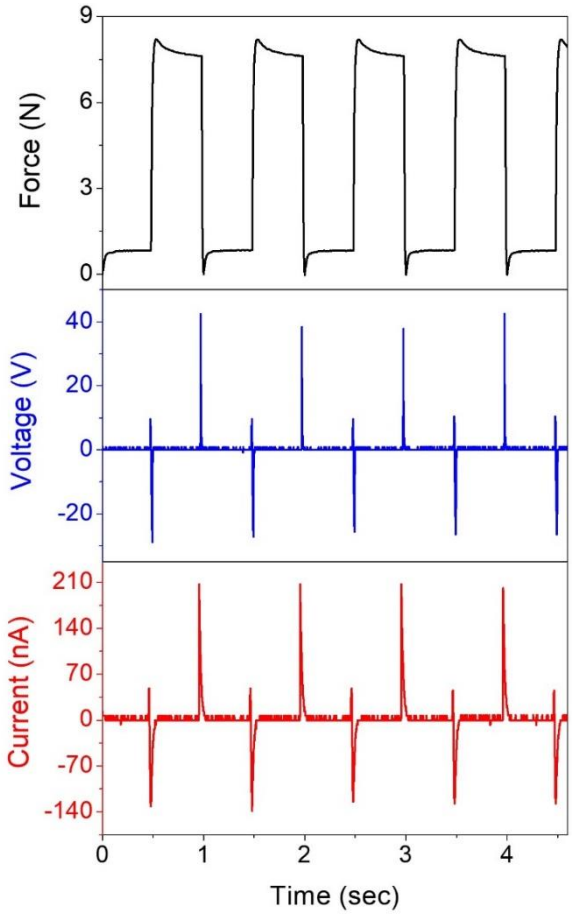

Figure 3-28. Application of mechanical force to the Piezo-PhD and the resultant generation of voltage and current.

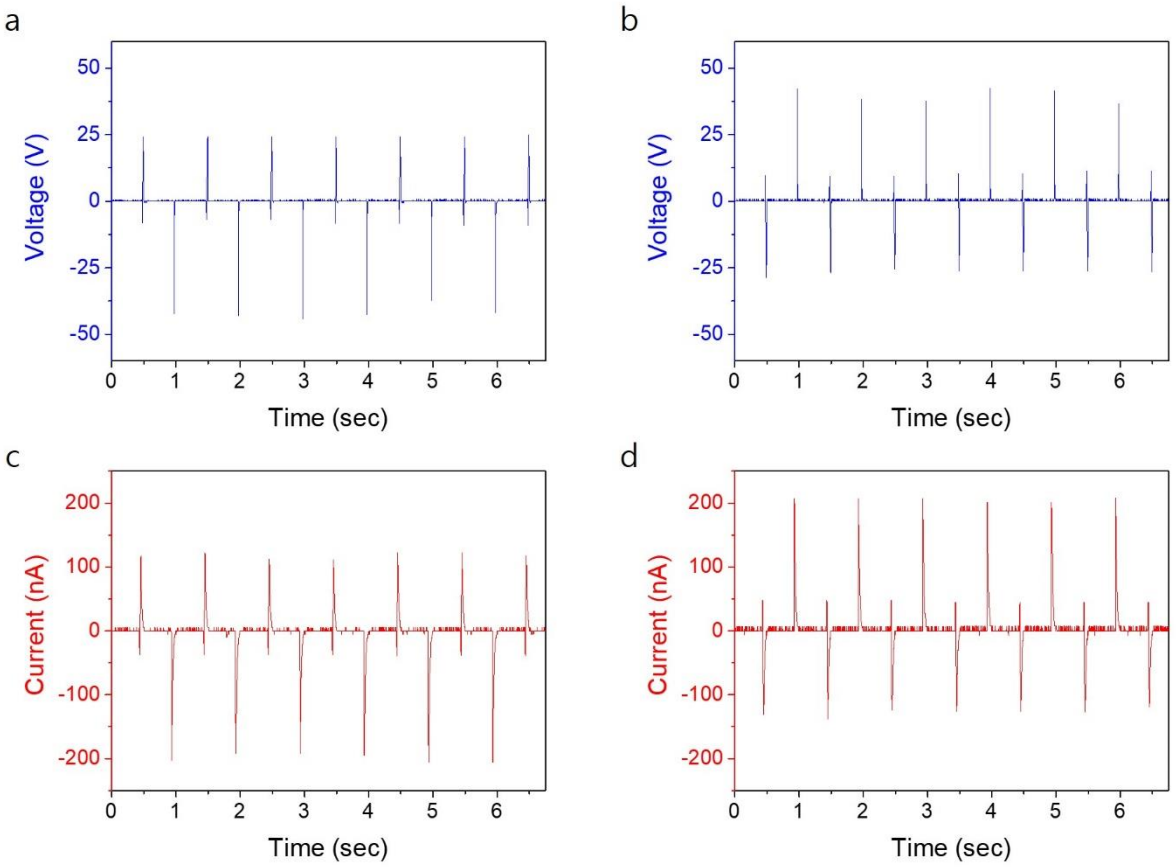

Figure 3-29. Polarity switching test on the Piezo-PhD. Output voltage (a) and (b) and current (c) and (d) were recorded by connecting the probes in the opposite orientation to the Piezo-PhD, presenting the reverse polarity changes.

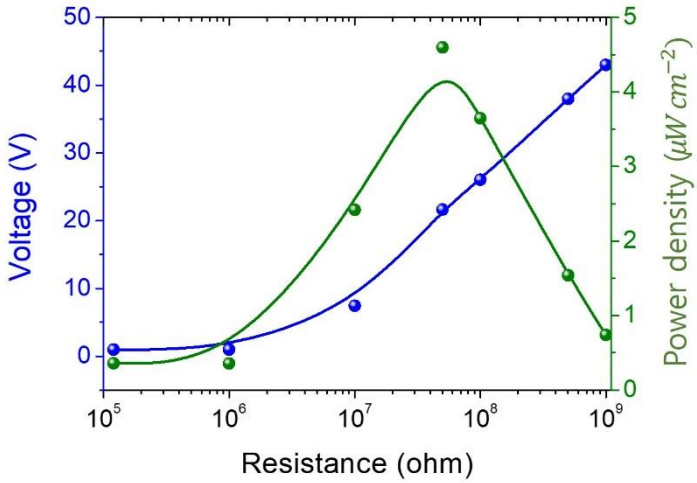

Figure 3-30. Output voltage and power density observed across various external resistances,

ranging from 120 kΩ to 1 GΩ, in the Piezo-PhD.

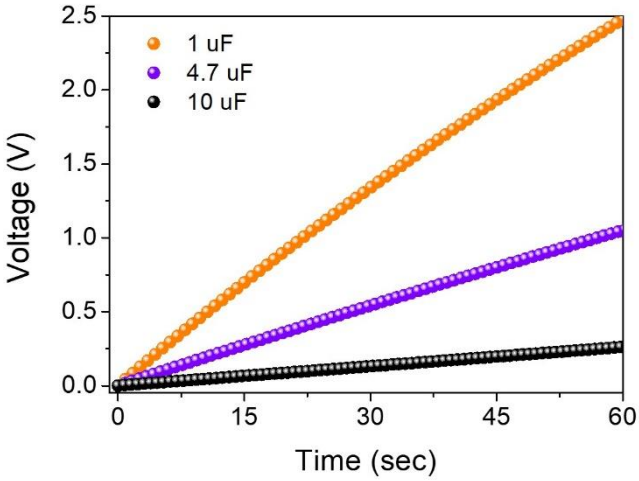

Figure 3-31. Charging characteristics of the Piezo-PhD device across various capacitors.

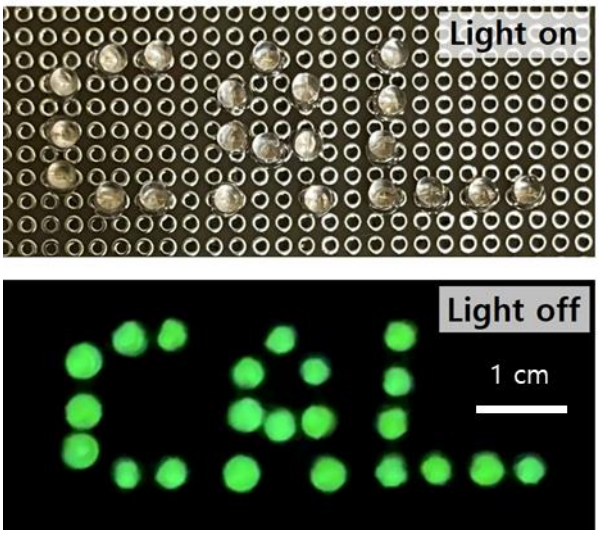

Figure 3-32. Photographs of 22 light-emitting diodes illuminating by the operation of the Piezo-PhD.

3.8 Conclusion

The challenging aspect of understanding the molecular mechanisms responsible for the complex piezoelectric response in biomaterials originates from the diverse and intricate hierarchical structures they possess. To overcome this barrier, an essential solution requires a

systematic approach and molecular-level analysis. This study addresses these challenges by providing a comprehensive understanding of the molecular mechanisms underlying the piezoelectric capabilities of the M13 phage at the molecular level, particularly in response to various mechanical stimulations. Through computational analysis, I revealed the M13 phage's electrical response to various external mechanical stresses by defining its piezoelectric tensor. Demonstrating the impact of tuning the surface charge of genetically engineered phages, I illustrated how surface charge contributes to the formation of the dipole moment and how these dipole moment components collectively result in a macroscopic polarization of the phage. Additionally, I fabricated vertical and horizontal self-assembled phage films, quantifying the directional dependency of the piezoelectric effect of the phage. In this study, validated by both computational analysis and measurements of piezoelectric output, demonstrated that the piezoelectric effect is more pronounced in the normal longitudinal d_{33} mode compared to the shear mode. This difference is primarily attributed to the greater changes in dipole moment associated with the former. This bioengineering approach, encompassing surface charge engineering, genetic modification, and precise polarization control, proves pivotal in optimizing the piezoelectric effect. Beyond advancing phage-based triboelectric and pyroelectric energy harvesting systems, our approach broadens horizons for designing and producing bioelectrical materials. These materials hold promise for diverse applications, including energy harvesting, bioelectronics, and bio-inspired devices.

3.9 Methods

3.9.1 Computations of the dipole moment of the M13 phage

I employed MD simulations using the Maestro package (Maestro release 2021-2 by Schrödinger) and Desmond MD to investigate the internal electrical properties of the genetically engineered phages. The pVIII protein model, sourced from the Protein Data Bank (PDB code: 1IFJ), underwent manipulation of the genetically modified segment using Maestro software. A repeating unit of pVIII protein assembly was constructed with five-fold rotational and two-fold screw symmetry, comprising ten pVIII proteins. After geometric optimization, dipole moments were computed using Desmond MD with the Maestro software interface over a 10 ns period at 300 K. The partial dipole moments generated by the side chains, backbones, and C_α atoms of the repeating unit were calculated. The formula used for computing the dipole moment of a collection of point charges is expressed as equation (17).

$$\sum_{i=1}^{N} q_i(r_i - r) \quad (17)$$

where q_i is the charge, r_i is the position of a charge, and r is the reference point, using the average atom position. For computing the centers of charge, the formula used is expressed as equation (18).

$$R = \frac{1}{Q}\sum_{i=1}^{n} q_i \cdot r_i \qquad (18)$$

where $Q = \sum_{i=1}^{n} q_i$ is the total charge of all the particles. The displacement of positive and negative charges was calculated based on the three-dimensional coordinates of the net positive and negative charges. The displacement of the center of positive and negative charges was calculated as the distance between the three-dimensional coordinates of the charges (see Appendix A.1). Subsequently, deformed phage models were prepared for normal longitudinal, normal transverse, and shear strain manners by converting the unit cell into a triclinic unit cell with variable lengths and angles (see Appendix A.2). The lengths and angles of the deformed structure were calculated, and the dipole moment was compared to that of the unstrained model. The assumed Poisson's ratio of the M13 phage was 0.5.

3.9.2 Gel electrophoresis

I used agarose gel (1 wt %) with 0.5X Tris-acetate-EDTA (TAE) buffer solution to apply WT- and engineered phage solutions at a concentration of 0.2 mg mL^{-1}. Subsequently, I subjected the gel to a voltage of 30 V for 8 hours and stained it using Coomassie-blue staining. After a 15-minute staining period, I removed the stain using a destaining buffer composed of deionized water, methanol, and acetic acid in a ratio of 70/20/10 (v/v/v).

3.9.3 Isoelectric point

The isoelectric point of the M13 phage was calculated using an isoelectric point calculator (https://www.protpi.ch/Calculator/ProteinTool#Results).

3.9.4 Zeta potential

I conducted zeta potential measurements through dynamic light scattering (DLS) using a disposable cuvette (ZEN0040, Malvern Instruments Ltd, Westborough, MA). The DLS characterization of the M13 phage took place in a Tris buffer containing 20 mM Tris and 10 mM NaCl.

3.9.5 Dielectric constant measurements

I examined the dielectric constant of the M13 phage using EFM coupled with AFM (MFP-3D AFM, Asylum Research Santa Barbara, CA). Ti/Pt-coated AC240TM-R3 (Oxford Instruments) AFM tips, featuring a radius of approximately 28 nm and a spring constant of around 2 N m^{-1}, were employed. The EFM was conducted at a scan rate of 1.0 Hz, with 256 scan lines, capturing the topography and deflection of the phage. The initial AFM tip-substrate distance was set at 40 nm, and an applied voltage of 10 V was used. To eliminate topographical errors, only the thickness of the phage film within a 3 % error range of the phage diameter was

considered. The calculated dielectric constant for both WT- and engineered phages was determined to be 4.0, aligning closely with the reported dielectric constant for bulk phage samples (ε_{phage}=2.8)[2].

3.9.6 Surface charge density measurements

I assessed the surface charge density of the M13 phages through EFM combined with AFM using the MFP-3D AFM system from Asylum Research in Santa Barbara, CA. For this analysis, Ti/Pt-coated AC240TM-R3 (Oxford Instruments) AFM tips, featuring a radius of around 28 nm and a spring constant of approximately 2 N m^{-1}, were employed. The topography and frequency of the phage were acquired at an applied voltage of 5 V, a scan rate of 0.80 Hz, and 256 scan lines, maintaining a tip-sample distance of 118 nm. The frequency data of the phages illustrated in Figure B16 were processed using a flatten function in the MFP3D Igor 6.38B01 software (version 16.14.216).

3.9.7 Fabrication of the vertically standing phage films

I fabricated phage films with unidirectional polarization using a template-assisted self-assembly technique.[3,4] I fabricated Ni-NTA functionalized gold substrates to induce a specific binding between the Ni-NTA layer and 6-His on the pIII of the M13 phage.[3,4] Rinsed gold substrates were immersed in a solution of 1 mg mL^{-1} of 3,3′-dithiodipropionic acid di(N hydroxysuccinimide ester) (Sigma Aldrich) in dimethyl sulfoxide (DMSO) for 15 min. I rinsed the substrate with pure DMSO and dried it with nitrogen gas. The substrate was immersed in an aqueous solution of 150 mM Nα,Nα-bis(carboxymethyl)-L-lysine hydrate (Sigma Aldrich) in 0.5 M K2CO3 buffer (pH 9.8) for 1 hr. I rinsed the substrate with deionized water and dried it with nitrogen gas. Then, I incubated the NTA-terminated surface with 50 mM nickel (II) sulfate heptahydrate (Sigma Aldrich) solution for 10 min. Finally, I rinsed the Ni-NTA/gold substrate with deionized water and dried it with nitrogen gas. Next, I drop-casted 30 mg mL^{-1} of phage solution on the Ni-NTA/gold substrate. Subsequently, I stamped the phage solution using a micropatterned PDMS mold and exposed it to ultraviolet light for 2 hours. The incubation process leveraged the specific binding between the pIII protein and the substrate, promoting the upright orientation of phages through capillary forces. After removing the PDMS mold, I covered it with an Al-ITO-coated PET substrate (Sigma Aldrich) as the top electrode and applied a PDMS layer to prevent damage to the phage film.

3.9.8 Fabrication of the horizontally aligned phage films

I prepared horizontally oriented phage films using the phage self-templating assembly method[2]. I created these films on gold substrates by applying a phage solution with a

concentration of 10 mg mL^{-1} and a pulling speed in the range of 10-20 μm min^{-1}.

3.9.9 Characterization of the piezoelectric coefficient of M13 phage film

To explore the piezoelectric coefficient of the phage films, I conducted PFM combined with AFM using the MFP-3D AFM system by Asylum Research. In this process, Ti/Pt-coated AC240TM-R3 (Oxford Instruments) AFM tips, featuring a radius of around 28 nm, a spring constant of approximately 2 N m^{-1}, and a free-air resonance frequency of about 70 kHz, were utilized. An applied voltage ranging from 0 to 7 V was used on the AFM tip to measure the piezoelectric coefficient of the phage films. Calibration was performed using periodically poled lithium niobate (PPLN), with a known d_{33} value of 14.1 pm V^{-1}, consistent with previously reported values.[1,4]

3.9.10 Characterization of phage-based piezoelectric devices.

The phage-based piezoelectric devices underwent testing on a dynamic mechanical test system (Electroforce 3200, Bose, MN), where mechanical forces were applied to the devices. I used an oscilloscope (Tektronix TDS 1001B), a Keithley 6514 system electrometer, and a low-noise current preamplifier (Stanford Research SR570) to measure the resulting output voltage and current. For shear measurements, tilted angled PDMS holders were employed, capturing both normal and shear outputs. The isolation of the shear output involved subtracting the normal output portion, determined by the standard curve derived from the normal longitudinal d_{33} piezoelectric mode measurements. The standard curves for output voltage and current of the d_{33} piezoelectric device were represented by a generic exponential equation, as indicated by the trend line as expressed by equation (19).

$$y = A_1 \cdot \exp\left(-\frac{F}{t_1}\right) + y_0 \qquad (19)$$

where y is the output, F is the force, A_1, t_1, and y_0 are constants. Specifically, for output voltage, these constants were 48.03134, -48.03134, and 3.72268, while for output current, they were 254.48634, -254.48634, and 5.02915.

CHAPTER 4: Pyroelectricity in M13 bacteriophage

Reprinted with permission. Han Kim et al., Virus-based pyroelectricity. *Advanced Materials* 35, 2305503 (2023). Copyright 2023, John Wiley and Sons.

4.1 Introduction

Designing functional materials based on viruses provides a versatile platform to address real-world challenges in environmental, energy, and health-related fields. Viruses offer unique advantages in material design and synthesis compared to traditional materials. By encapsulating genetic material (DNA/RNA) within a protein coat, viruses can rapidly replicate identical copies of materials on a large scale through host cell infection.[604,605] Genetic engineering techniques allow viruses to be customized for fabricating materials with specific biological functions or evolving to acquire novel functionalities.[460,606] Additionally, viruses possess self-assembly capabilities, enabling the formation of diverse supramolecular structures that exhibit various optical and photonic properties.[486,487,607] These advantageous material features have led to the use of viruses in bioenergy applications[1,468,469,473,474], biosensors[486,487], and biomedical materials.[608,609]

In my previous works, I explored the M13 bacteriophage as a model system to investigate bioelectricity in biomaterials. I demonstrated the triboelectric and piezoelectric properties of M13 phage, allowing them to generate electricity by touch or sensing pressure, respectively.[2,466] Through genetic engineering of the coat protein structures, I successfully enhanced their triboelectric and piezoelectric performance.[2,466] While M13 phages do not directly sense heat, they undergo structural changes in response to thermal stimuli. Due to the non-centrosymmetric structure of M13 without an inversion center[1], I hypothesize that M13 exhibits pyroelectricity—a phenomenon where an electric potential is generated upon heat-induced polarization changes. Extensive research and characterization efforts have contributed to our understanding of pyroelectricity in a wide range of inorganic and organic materials.[198,610-615] The molecular-level mechanisms of pyroelectricity have been comprehensively elucidated through theoretical models and experimental investigations.[198,616,617] Although pyroelectricity has been observed in various biological entities such as cells, tissues, and proteins[29,30,269,387,618], understanding the molecular mechanisms underlying the biological pyroelectric effect has been limited due to the complex nature of biological structures and the lack of tools for manipulating desired structures and properties.

In this chapter, I will present the first demonstration of generating pyroelectric potential in a virus, using the M13 phage as a model system. To explore the pyroelectric properties of the phage, I conducted genetic modifications on the tail segment of pIII minor coat proteins by introducing six histidine (6H) residues. This led to the creation of

unidirectionally polarized phage structures on Ni-NTA-coated gold substrates through template-assisted self-assembly (ref 17). Using KPFM, I characterized the surface potential generation of the unidirectionally polarized phage films when subjected to heating. Through additional engineering of the major coat protein with varying numbers of negatively charged glutamates, I demonstrated the structure-dependent pyroelectric properties of the phage. Specifically, the phage engineered with four glutamates demonstrated pyroelectricity with a pyroelectric coefficient of 0.13 μC m^{-2} °C^{-1}. Computational modeling and CD spectroscopy analysis validated that heat-induced changes led to the unfolding of α-helices in the pVIII proteins, causing polarization changes along the long axis of the phage. By genetically modifying the phage with molecular recognition elements, I also demonstrated the potential of pyroelectric phage as an innovative sensing modality for detecting various volatile organic chemicals (VOCs). This phage-based approach enhances our understanding of the thermo-bioelectrical behaviors of biomolecular materials and sets the stage for the development of novel bionanomaterials with applications in biosensors and energy harvesting.

4.2 Pyroelectric structure of M13 phage

4.2.1 Microscopic pyroelectric structure of M13 phage

The categorization of pyroelectric materials is based on their crystallographic symmetry, specifically characterized by the absence of inversion symmetry and the presence of spontaneous polarization. The M13 phage is covered by 2700 copies of α-helical pVIII proteins with five-fold rotational and two-fold screw symmetry, which exhibits a non-centrosymmetric structure (Figure 4-1). Additionally, the net dipole moment in pVIII protein forms a spontaneous polarization of the entire phage. Therefore, the M13 phage is expected to exhibit the pyroelectric effect (Figure 4-2).

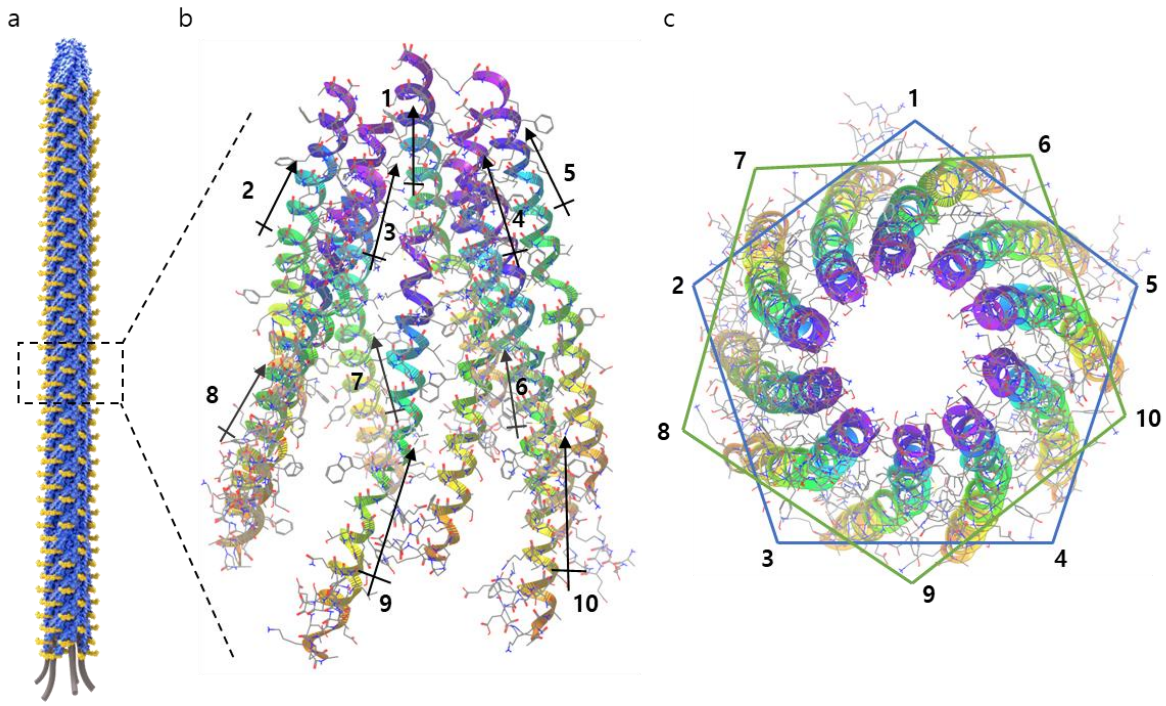

Figure 4-1. (a) Schematic diagram of the M13 phage and its pyroelectric properties. (b) and (c) The M13 phage has a non-centrosymmetric structure due to its five-fold and two-fold screw symmetry of pVIII proteins. Additionally, the M13 phage has a spontaneous polarization due to the intrinsic dipole moment of the pVIII protein. Reprinted with permission.[3] Copyright 2023, John Wiley and Sons.

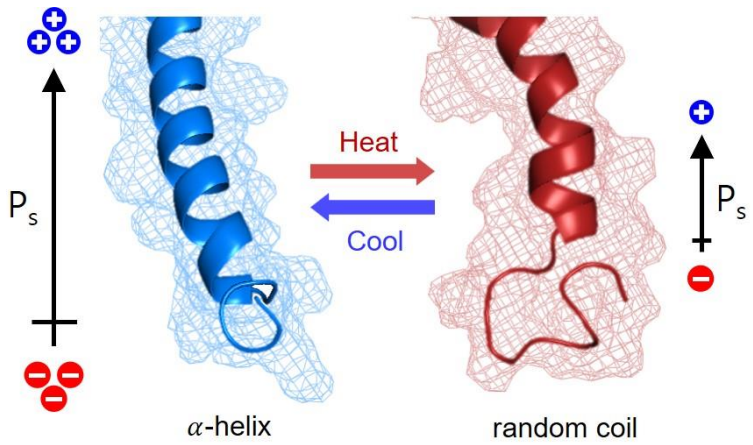

Figure 4-2. The α-helical protein structures of the pVIII protein impart it with inherent polarization. When the secondary structure transitions from an α-helix to a random coil, the spontaneous polarization diminishes. Reprinted with permission.[3] Copyright 2023, John Wiley and Sons.

4.2.2 Macroscopic pyroelectric structure of M13 phage film

While a single M13 phage molecule is anticipated to display pyroelectricity, achieving a macroscopic characterization of phage pyroelectric properties necessitates the engineering of a polar structure with unidirectionally aligned dipoles. To create such nanostructures with tunable surface charges, I conducted dual engineering on the pIII minor coat and pVIII major coat proteins of the M13 phage (Figure 4-3). The minor coat protein (pIII tail) was genetically modified with six-histidine to facilitate specific binding to Ni-NTA coated on gold substrates. Furthermore, by additional engineering of the major coat protein with varying numbers of glutamates (ranging from one (1E) to four (4E)), I adjusted the quantity of negative charges on the outer surface of the M13 phage (Figure B3). Using these engineered phages, alongside the WT-phage, I fabricated vertically standing phage films on Ni-NTA-coated gold substrates.

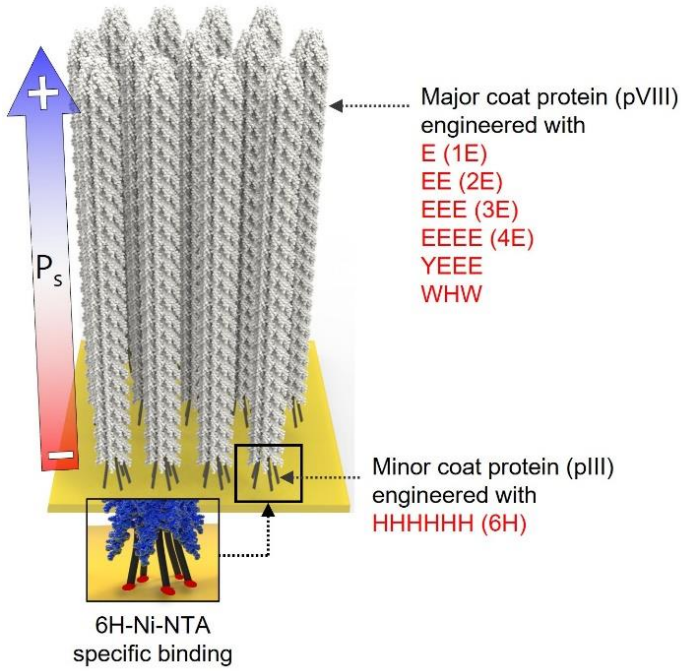

Figure 4-3. Schematic diagram of a vertically standing M13 phage film. Through the implementation of specific binding between the pIII proteins and the substrate using 6H-Ni-NTA, the phage film demonstrates a unidirectional arrangement of spontaneous polarization (P_s). Reprinted with permission.[3] Copyright 2023, John Wiley and Sons.

4.2.3 Pyroelectric characterization of the vertically standing phage films

The AFM and KPFM were employed to assess the topographic and electric potential profiles of a vertically standing phage film (Figure 4-4). The height profile of the phage film revealed that its height corresponds to a single phage length (~980 nm), implying a monolayer

alignment of phages on the substrate (Figure 4-5). The resultant monolayer film displayed a consistent surface potential (Figure 4-6). Additionally, I conducted a comprehensive analysis of their surface roughness, mechanical properties, and compactness. The resulting phage films exhibited comparable roughness, Young's modulus, and Fourier-transform infrared spectroscopy (FT-IR) with minimal variation (Figures 4-7–4-9). These findings suggest that the pyroelectric properties of the phages were analyzed under standardized conditions.

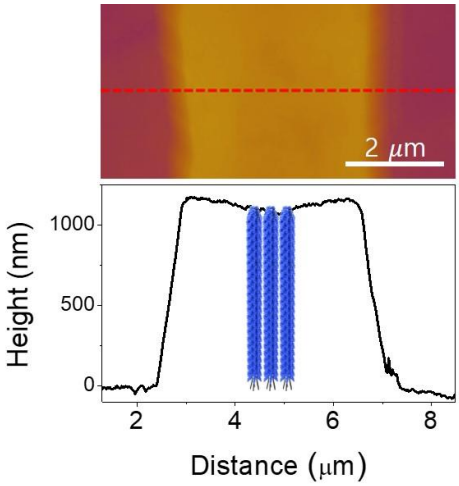

Figure 4-4. AFM topographic image of a vertically standing phage film. The height of the phage film aligns closely with the length of an individual phage, as illustrated by the red dotted lines. Reprinted with permission.[3] Copyright 2023, John Wiley and Sons.

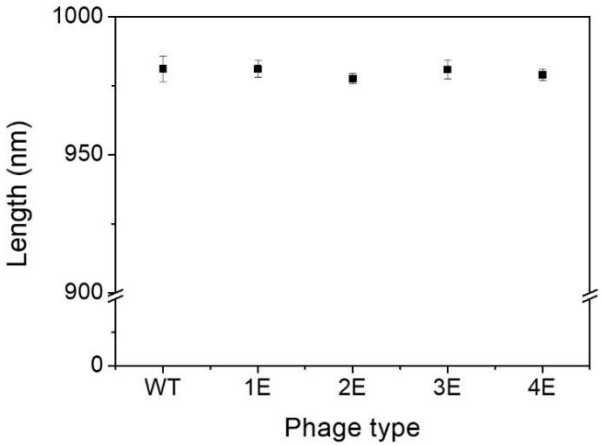

Figure 4-5. Individual phage length profiles for both wild-type and engineered phages. All phages exhibited a length of approximately 980 nm with minimal variations. Reprinted with permission.[3] Copyright 2023, John Wiley and Sons.

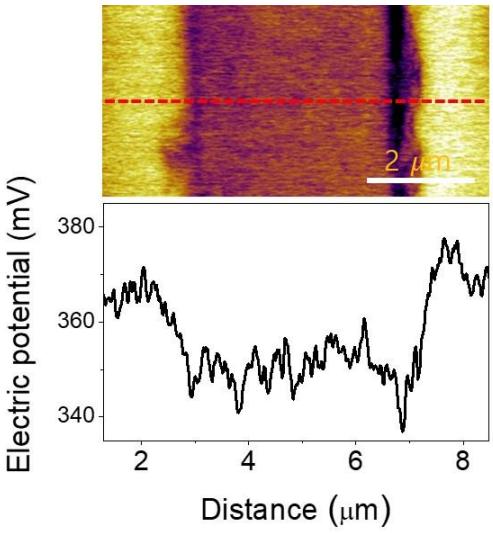

Figure 4-6. KPFM surface potential images of a vertically standing phage film. The surface potential of the phage film demonstrates a consistent electric potential throughout its surface, as highlighted by the red dotted lines. Reprinted with permission.[3] Copyright 2023, John Wiley and Sons.

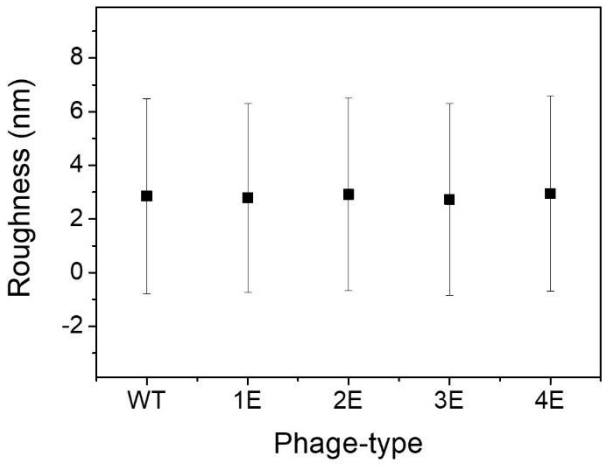

Figure 4-7. Surface roughness characterization of vertically standing phage films. The variation of the roughness for different phage types was negligible. Reprinted with permission.[3] Copyright 2023, John Wiley and Sons.

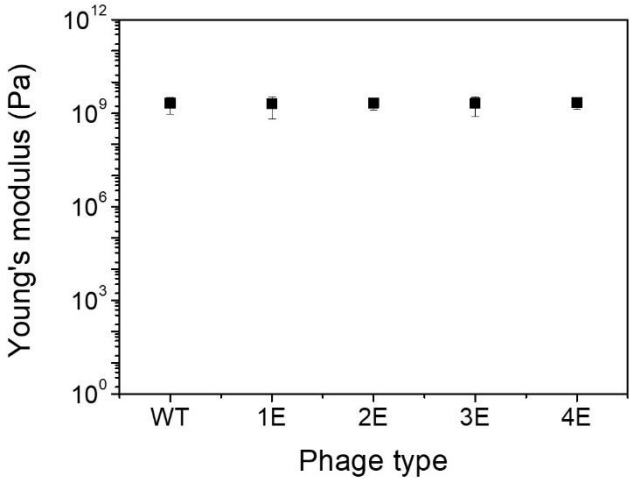

Figure 4-8. Young's modulus characterization of vertically standing phage films. The variation of the Young's modulus for different phage types was negligible. Reprinted with permission.[3] Copyright 2023, John Wiley and Sons.

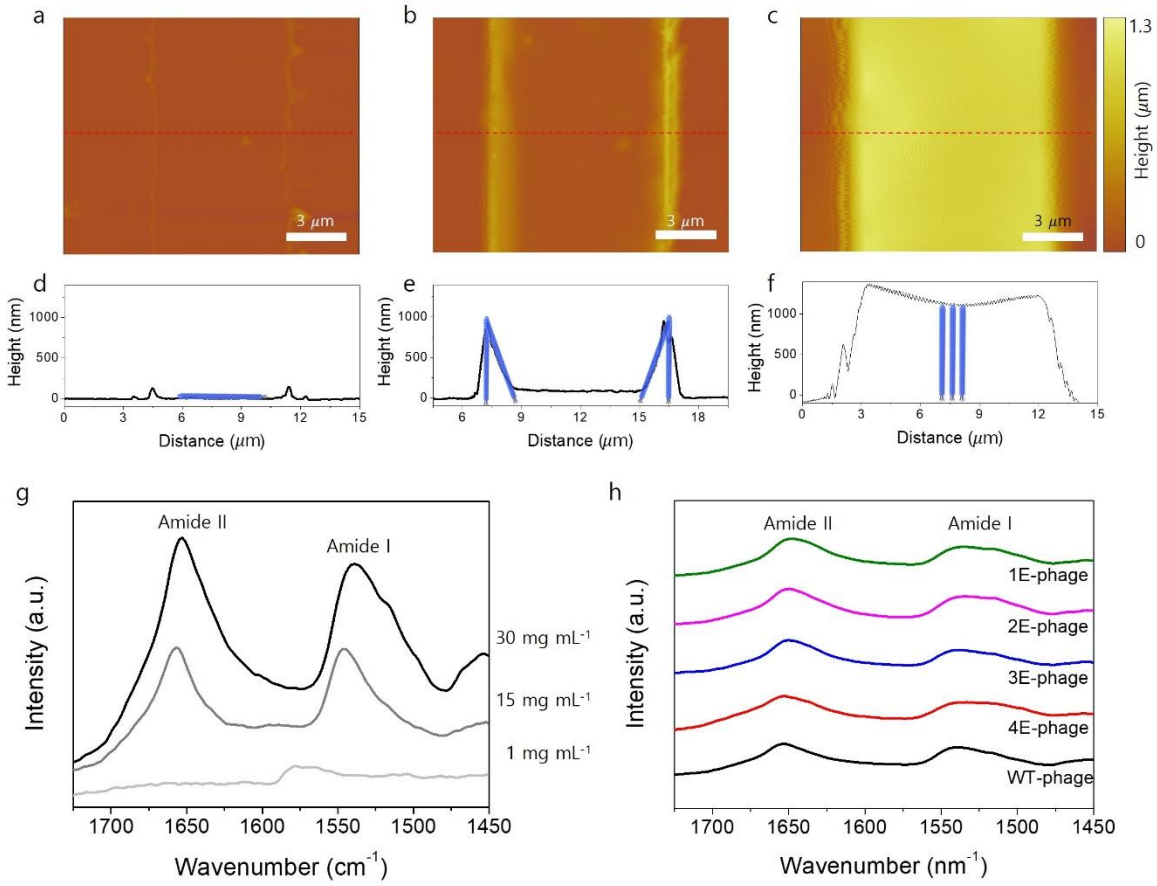

Figure 4-9. AFM height profile images and FT-IR spectra of vertically standing phage films.

AFM height images and profiles of vertically standing phage were created using phage concentrations of (a) and (d) 1 mg mL^{-1}, (b) and (e) 15 mg mL^{-1}, and (c) and (f) 30 mg mL^{-1}. Schematic representations of the phages illustrate their potential orientations within the films. (g) FT-IR spectra of the vertically standing phage film on gold substrates, corresponding to the concentrations indicated in AFM images (a-f). (h) FT-IR spectra of the 1E-, 2E-, 3E-, 4E-, and WT-phage films prepared using a phage concentration of 30 mg mL^{-1}. Reprinted with permission.[3] Copyright 2023, John Wiley and Sons.

4.3 Pyroelectric potential studies using Kelvin probe force microscopy (KPFM)

4.3.1 Pyroelectric potential characterization

I examined the pyroelectric surface potential variations in WT and genetically modified phages (1E~4E-phage) utilizing KPFM. A temperature controller was positioned beneath the vertically standing phage film, and heat was administered to the film (Appendix A.3). Prior to heat application, the phage film displayed a uniform equipotential surface across its entire area (Figure 4-10). Subsequently, I measured the surface potential at the same position of the phage film during temperature modulation, defining the surface potential change magnitude as the pyroelectric potential. An observed pyroelectric potential of 16.3 mV was recorded with a temperature change variation rate (dT/dt) of 1.14 °C min^{-1}, signifying a reduction in phage film polarization (Figure 4-11). Once the set temperature was reached, and the temperature variation rate became zero, no further pyroelectric potential generation occurred. The surface potential reverted to its initial state through charge redistribution on the phage surface. Similar charge redistribution was noted in the triboelectric charge generation of the phage films.[2,619] Conversely, the surface potential of the randomly aligned phage film remained unchanged under equivalent heat application (Figure 4-12). This is attributed to the negligible net polarization and pyroelectric effect when individual phages are randomly aligned in the control sample.

Distinct pyroelectric potential generation and charge redistribution were observed among different phage types (Figure 4-13). At a temperature variation rate of 1.08 °C min^{-1}, a higher pyroelectric potential was observed in the order of 4E-, 3E-, WT-, 2E-, and 1E-phages. Comparing the pyroelectric potential magnitude among phage types revealed that a greater pyroelectric potential was generated when more negative charges were distributed on the phage surface. Additionally, applying varying degrees of heat to vertically standing phage films demonstrated an increased pyroelectric effect with rising temperature change. Moreover, phages with more negative charges on their surfaces yielded a larger pyroelectric potential (Figure 4-14).

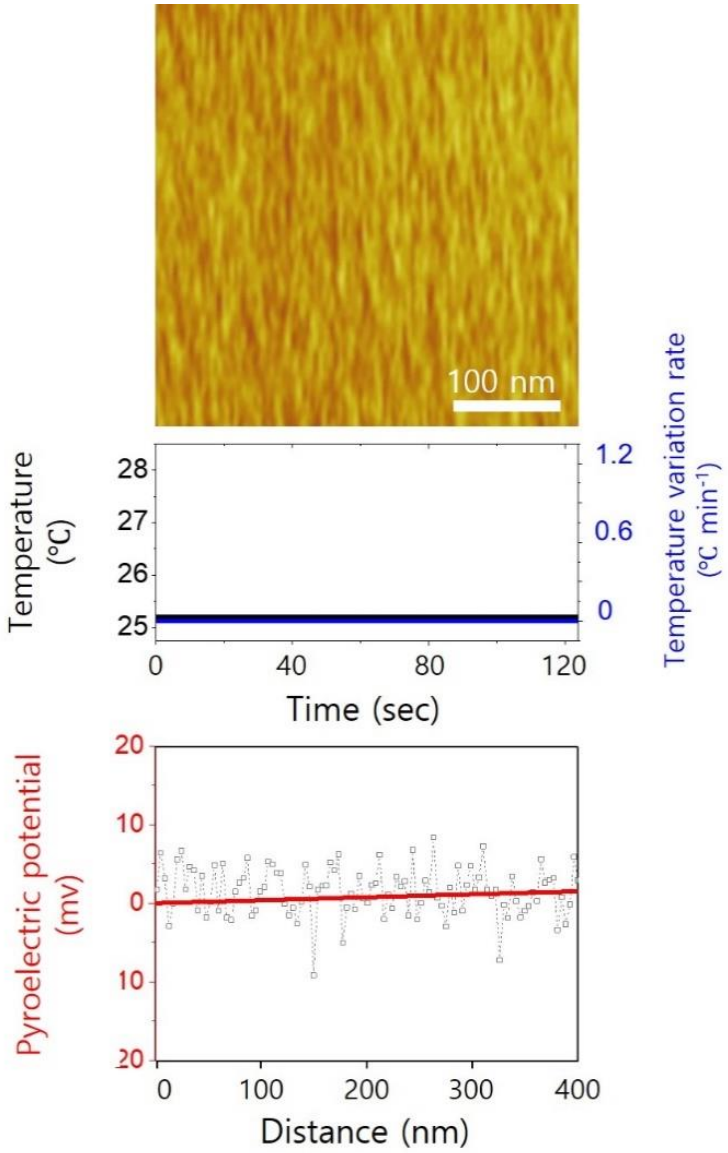

Figure 4-10. Surface potential representation of a vertically standing phage film without the application of heat using KPFM. The associated profiles of pyroelectric potential, temperature, and temperature variation rate for the phage film are graphed. Reprinted with permission.[3] Copyright 2023, John Wiley and Sons.

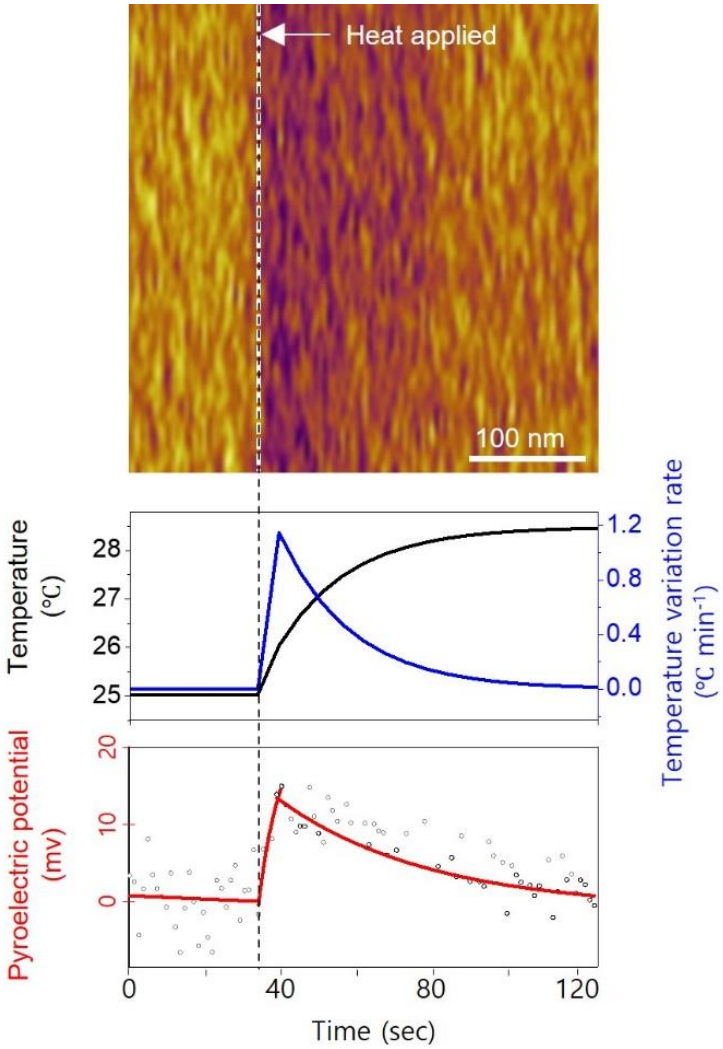

Figure 4-11. KPFM image of a 4E-phage film while subjected to heat. The accompanying profiles illustrate the pyroelectric potential, temperature, and temperature variation rate of the phage film. Reprinted with permission.[3] Copyright 2023, John Wiley and Sons.

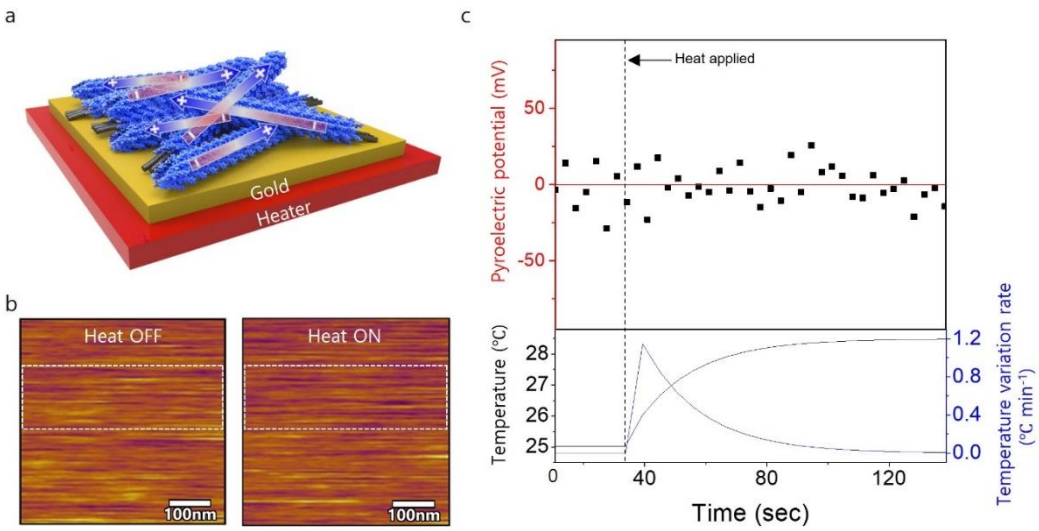

Figure 4-12. Pyroelectric assessment of M13 phage with randomly organized structures. (a) Illustration of the pyroelectric characterization using KPFM. By applying a 4E phage solution on Ni-NTA coated Au films, we generated randomly oriented phage films with minimal net polarization. (b) KPFM images of a randomly oriented phage film, showing the surface potential of the 4E phage film (a) without heat application and (b) under heat application at a temperature variation rate of 1.14 °C min^{-1}. (c) The pyroelectric potential of the phage film depicted in (b). The corresponding profiles of pyroelectric potential, temperature, and temperature variation rate for the phage film are illustrated. The pyroelectric potential is negligible due to the randomly aligned polarization of the phage film. Reprinted with permission.[3] Copyright 2023, John Wiley and Sons.

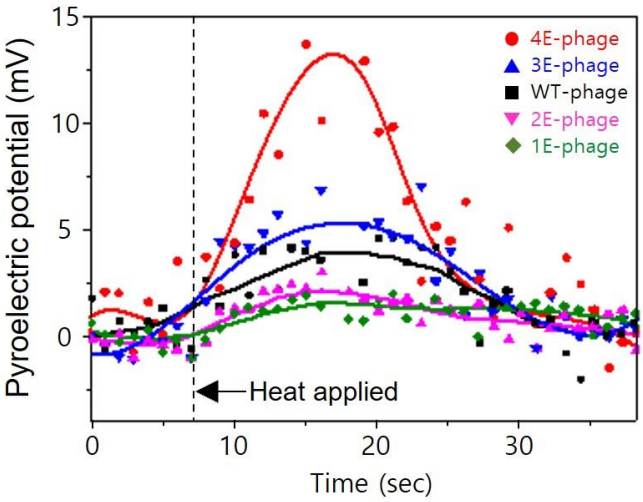

Figure 4-13. Pyroelectric potentials of various phage films under heat exposure with a temperature variation rate of 1.08 °C min^{-1}. Reprinted with permission.[3] Copyright 2023, John

Wiley and Sons.

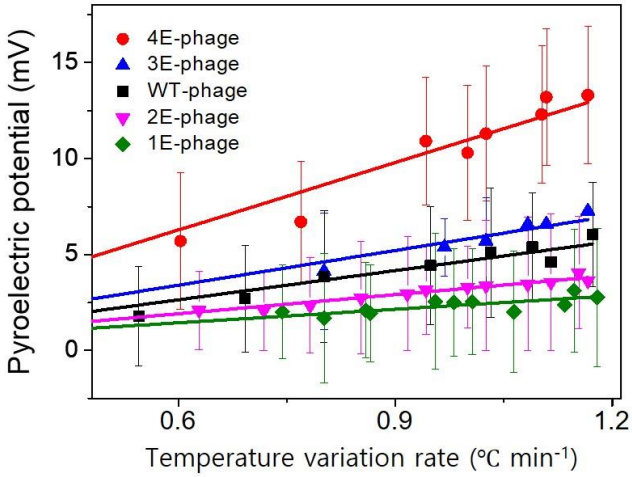

Figure 4-14. Pyroelectric potentials exhibited by different types of phage films in response to diverse temperature fluctuations. Reprinted with permission.[3] Copyright 2023, John Wiley and Sons.

4.3.2 Pyroelectric coefficient calculation

I conducted a quantitative analysis of the pyroelectric coefficient of the phages based on their temperature-dependent pyroelectric potentials, applying Equation (20).[619]

$$p_{phage} = \frac{1}{\Delta T}\frac{\Delta V}{d}\varepsilon_0\varepsilon_{phage} \qquad (20)$$

where ΔT is the temperature change, ΔV is the surface potential change induced by the change in the spontaneous polarization, d is the thickness of the pyroelectric layer along the polar axis, ε_0 is the vacuum permittivity, and ε_{phage} is the dielectric constant of the phage film, with a value of 2.84[2]. The determined pyroelectric coefficients were 0.13, 0.066, 0.058, 0.040, and 0.028 μC m^{-2} °C^{-1} for 4E-, 3E-, WT-, 2E-, and 1E-phages, respectively. These findings illustrate that the pyroelectric properties of phages can be clarified through the manipulation of charged peptides on the phage surface and the adjustment of spontaneous polarization within the phage. While the observed pyroelectric coefficients of the phages surpass those of most natural biological materials, they are smaller than those of inorganic or organic crystalline biomaterials (e.g., hydroxyapatites, γ-glycine, and lysozymes) (Table 16).[30,195,378,405,620-628] This is likely due to the unidirectionally aligned polarizations of the vertically standing phage nanostructures.

Known pyroelectric biomaterials	Pyroelectric coefficient ($\mu C\ m^{-2}\ K^{-1}$)	Category	Refs.
Lysozyme film	1441∓536	Organic	30
Hydroxyapatite ceramics	150-640	Inorganic	620
Hydroxyapatite thin film	12	Inorganic	621
Porcine skin gelatine	13	Organic	405
γ-glycine	13	Organic	30
Wheat	3.5-4.6	Organic	622
Human skin	2.1-27.0	Organic	378
Cellulose nanocrystal	0.58	Organic	623
Periplaneta americana	0.20-3.5	Organic	624
M13 bacteriophage	**0.028-0.13**	**Organic**	**-**
Fluorapatite/gelatin	0.05	Organic/inorganic composite	625
Dentine and cementum	0.025-0.0015	Organic/inorganic composite	627
Rhododendron leaf	0.02-0.15	Organic	624
Encephalartos villosus	0.0129	Organic	628
Hoof tendon	0.0041	Organic	195
Demineralized phalanx	0.0038	Organic/inorganic composite	195
Femur	0.0036	Organic/inorganic composite	195
Encephalartox leaves	0.005-0.06	Organic	624

Table 16. Pyroelectric coefficient of known pyroelectric biomaterials. Reprinted with permission.[3] Copyright 2023, John Wiley and Sons.

4.4 Molecular mechanism of the pyroelectricity in M13 phage

4.4.1 Molecular dynamics simulations

To explore the molecular mechanisms underlying the pyroelectric effect in the M13 phage, I employed MD simulations. These simulations encompassed the computation of temperature-dependent alterations in the secondary structure of a single pVIII coat protein and multilayers of repeating units of the M13 phage. Dipole moments were also calculated through Desmond MD simulation. The MD simulations unveiled that the pVIII protein primarily adopts α-helical structures and manifests a dipole moment of 355.0 D at 300 K (Figure 4-15a and 4-15b). With an increase in temperature to 350 K, the hydrogen bonds between the loops of the α-helices weakened (Figure 4-16). Consequently, the N-terminal end of the pVIII protein adopted a random coil conformation, leading to a reduction in the dipole moment to 226.9 D. To assess the polarization changes in the supramolecular structure of the pVIII protein within

the M13 phage, I constructed a model of supramolecular structures consisting of repeating units composed of 10 pVIII proteins with a five-fold rotational and two-fold screw symmetry. Simulating the dipole moment changes in these supramolecular structures with increasing numbers of repeat units revealed a decrease in the dipole moment for each repeating unit within the temperature range of 300 to 350 K. These trends aligned with those observed in the single pVIII protein simulations (Figure 4-17). Additionally, simulations of the changes in the distance between the loops of the α-helices of the pVIII protein as the temperature increased indicated a negligible standard deviation of 0.23 Å during the temperature change from 300 to 350 K (Figure 4-18). Thus, the study demonstrates that the variation in the dipole moment of a phage is directly linked to the secondary structure changes of the major coat proteins in response to temperature fluctuations, rather than being influenced by the thermal expansion effect of the major coat proteins.

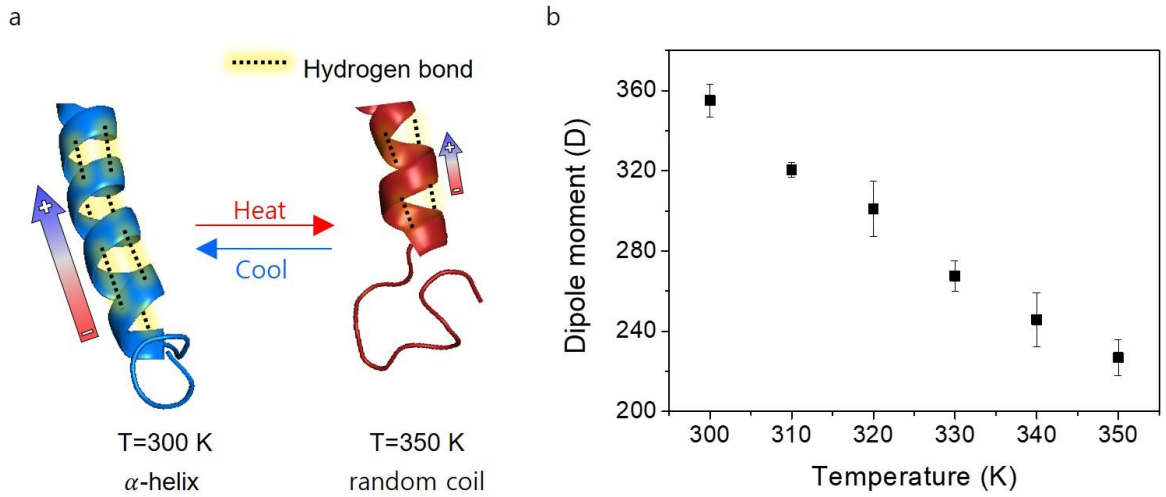

Figure 4-15. Temperature-dependent polarization change in the M13 phage. (a) MD simulated structures of a pVIII protein at 300 K and 350 K. The unfolding of the α-helical structure of the pVIII protein leads to a reduction in the polarization of the M13 phage. (b) MD results depicting the temperature-dependent dipole moment of an individual pVIII protein. Reprinted with permission.[3] Copyright 2023, John Wiley and Sons.

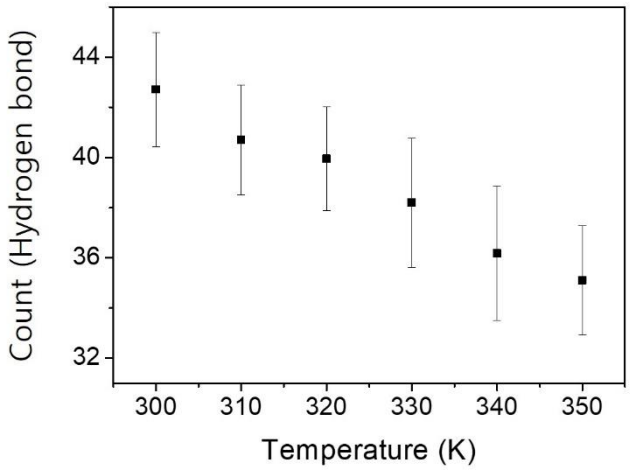

Figure 4-16. Assessment of the quantity of hydrogen bonds existing within the loops of the pVIII protein. With the rise in temperature, the number of hydrogen bonds steadily diminished, attributed to the structural transformation from α-helices to random coils. Reprinted with permission.[3] Copyright 2023, John Wiley and Sons.

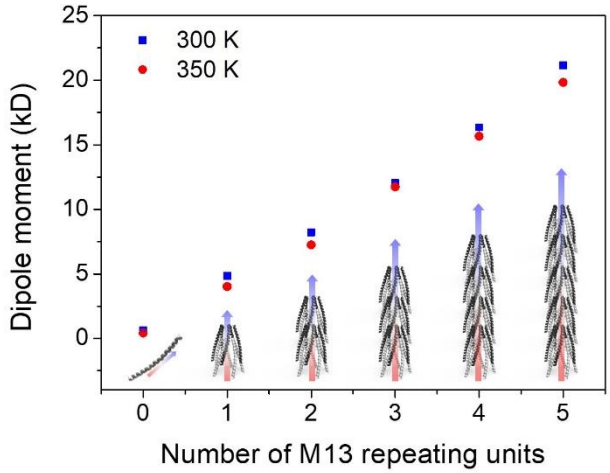

Figure 4-17. Determination of the dipole moment of the M13 phage at temperatures of 300 K and 350 K. Dipole moments were computed in supramolecular structures with escalating repeating units. The dipole moment exhibited a consistent decrease with increasing temperature. 0 repeating unit signifies a single pVIII protein. Reprinted with permission.[3] Copyright 2023, John Wiley and Sons.

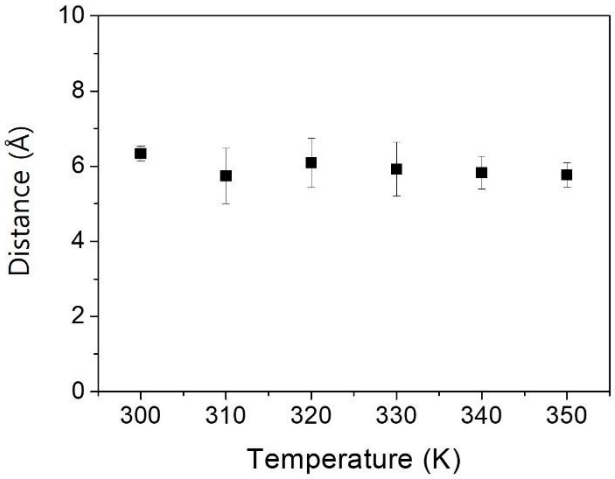

Figure 4-18. Variation in the spacing between the loops of the pVIII protein based on temperature. The change in the polarization of the M13 phage is attributed to the modification in the secondary structure of the major coat proteins, rather than a thermal expansion effect in these proteins. Reprinted with permission.[3] Copyright 2023, John Wiley and Sons.

4.4.2 Circular dichroism spectroscopy

To validate the structural alterations of the coat proteins, CD spectroscopy was employed on the M13 phage. With an increase in temperature, the characteristic α-helical structure of the pVIII protein diminished (Figure 4-19). Specifically, the CD signals at 208 and 222 nm increased from −49.9 to −40.1 mdeg and 78.6 to 56.6 mdeg, respectively, while the signal at 193 nm decreased from 119 to 3.98 mdeg as the temperature rose from 293 to 353 K, indicating a reduction in the α-helical structure of the pVIII protein.[629,630] All engineered phages utilized in this study exhibited a similar decrease in α-helical content during heating (Figure 4-20). Dynamic light scattering (DLS) analysis revealed no alteration in particle size distribution in the phage solution throughout the heating and cooling process, suggesting that the unfolded pVIII protein tail structure does not induce phage aggregation due to the intrinsic negative charge repulsion of phage surfaces (Figures 4-21 and 4-22). The conformational change observed through CD analysis aligns with the results of MD simulations, indicating changes in the dipole moment of the phage upon heating. Both CD spectroscopy and MD simulations indicate that the pyroelectricity of the M13 phage results from the weakening of the α-helical characteristics of the pVIII protein and the subsequent reduction in dipole moment during heating. Consequently, the conformational changes within the phage structure and the pyroelectric response with varying degrees of heat application exhibit a clear correlation. Thus, the primary factor influencing the pyroelectric effect in the phage is the conformational changes within the phage structure, rather than being influenced by the presence or migration of salt or buffer residues in the phage films.

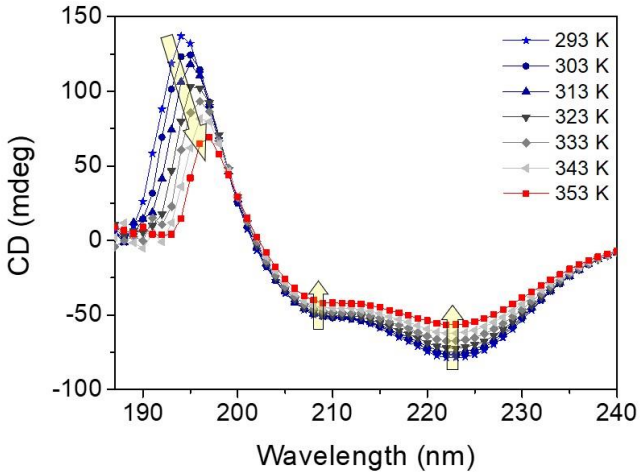

Figure 4-19. Circular dichroism spectra of the WT-phage exhibiting a temperature-dependent structural transition from an α-helix to a random coil configuration during heating. Reprinted with permission.[3] Copyright 2023, John Wiley and Sons.

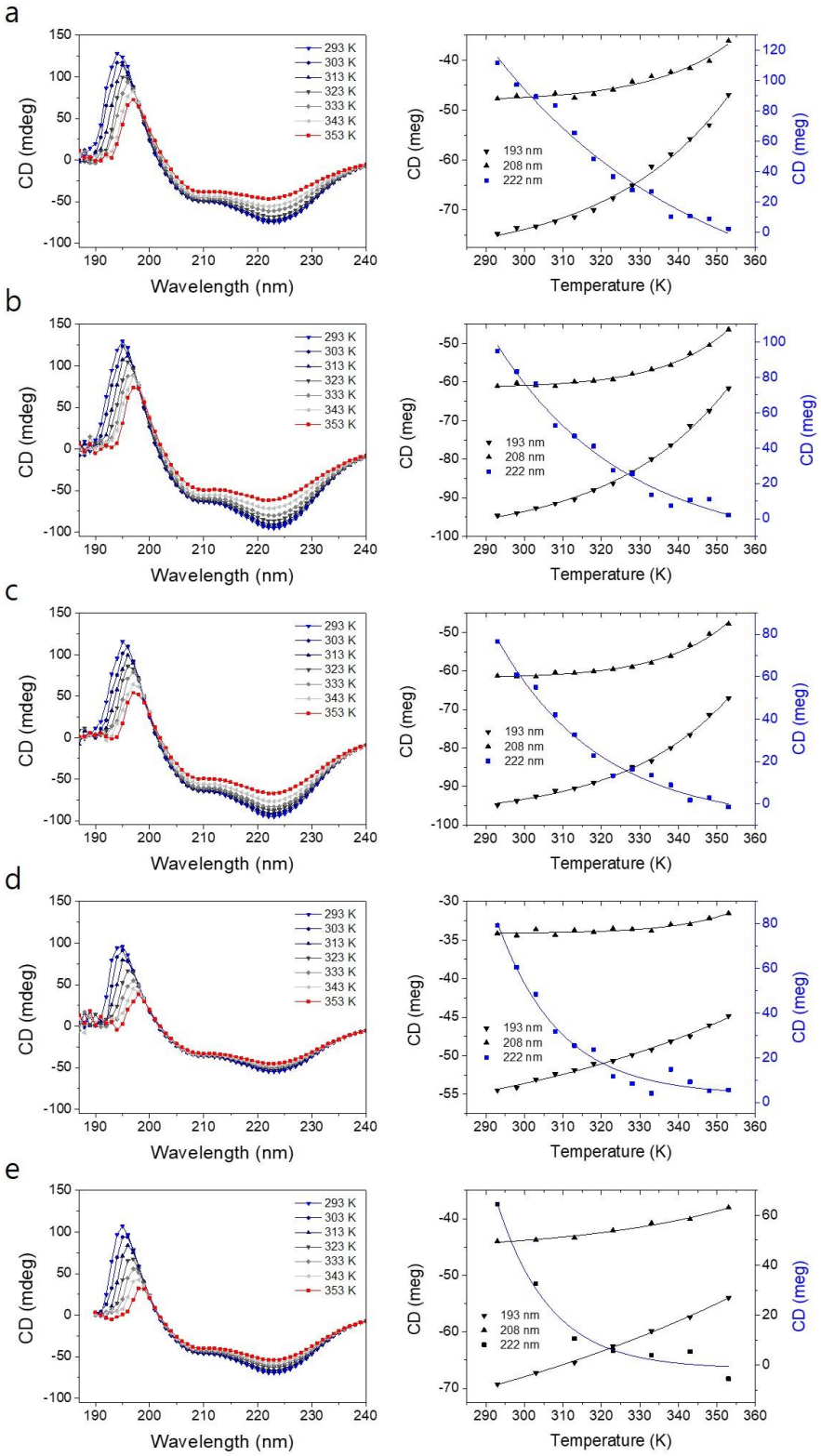

Figure 4-20. Temperature-dependent CD spectra of the wild-type M13 phage illustrating the shift from an α-helix to a random coil configuration during heating. Additionally, CD spectra for various genetically engineered phages are depicted: (a) 1E phage, (b) 2E phage, (c) 3E

phage, (d) 4E phage, and (e) YEEE phage. The CD spectra reveal the structural transformation from an α-helix to a random coil for each type of phage. Reprinted with permission.[3] Copyright 2023, John Wiley and Sons.

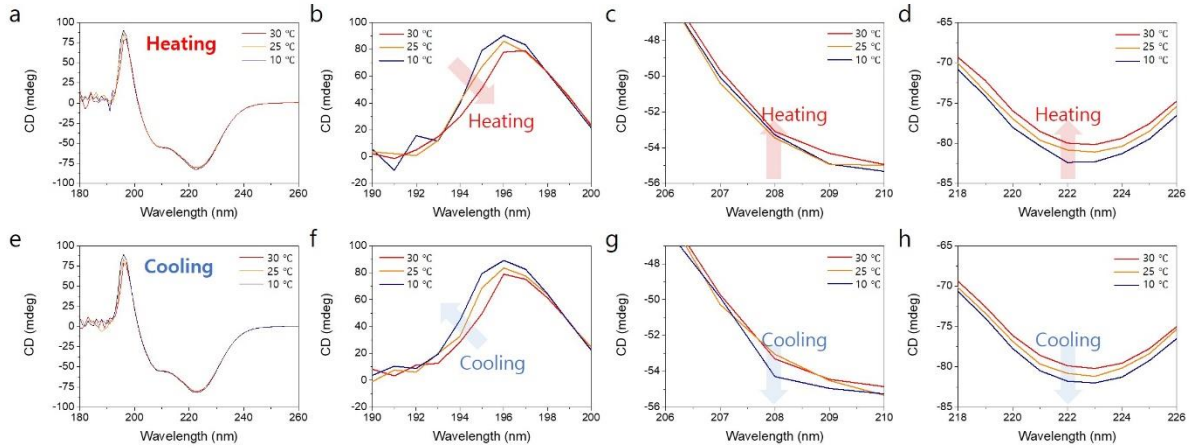

Figure 4-21. CD spectra of the M13 phage. (a) Changes in the CD signal during the heating process. (b-d) CD spectra at specific wavelength regions (193, 208, and 222 nm), revealing a decrease in the α-helical structural feature of the pVIII protein. (e) The CD signal during the cooling phase. (f-h) CD spectra at typical wavelength regions (193, 208, and 222 nm), illustrating a restoration of the α-helical structural characteristic of the pVIII protein to its initial state. These findings indicate a reversible structural transformation. Reprinted with permission.[3] Copyright 2023, John Wiley and Sons.

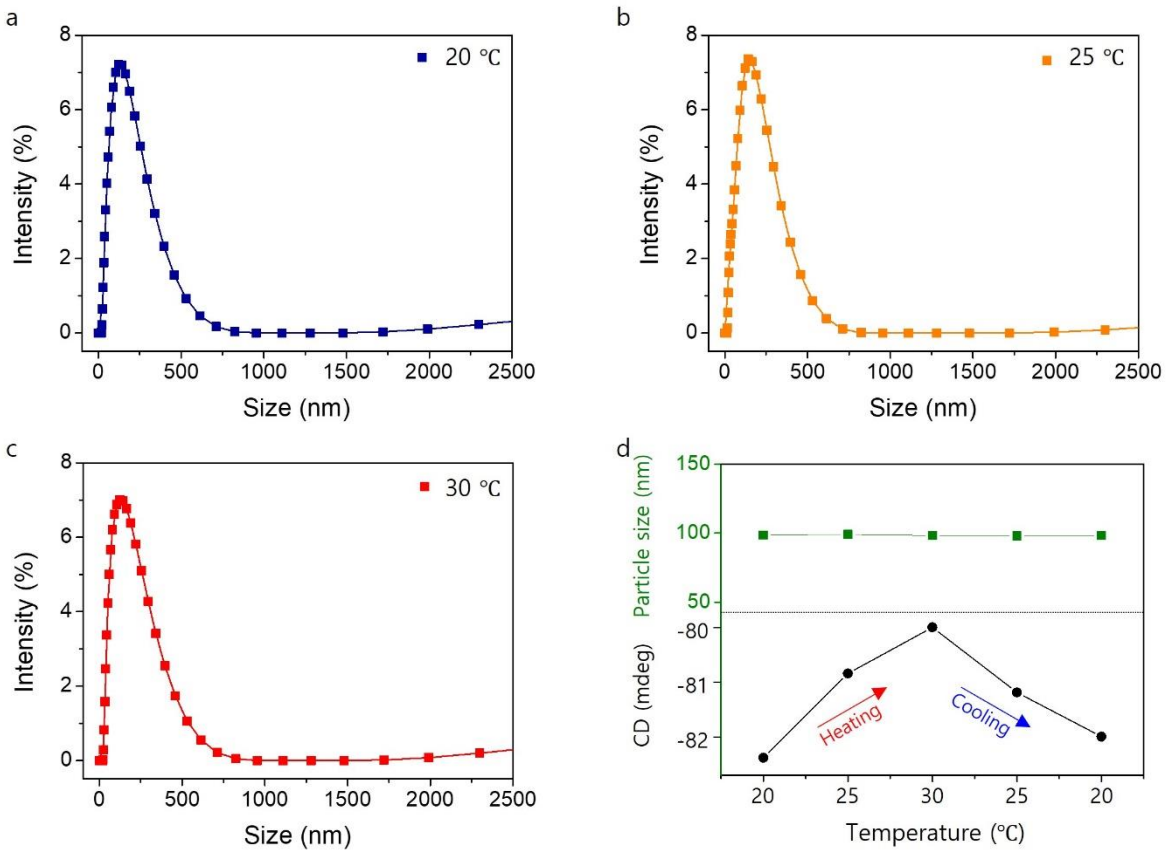

Figure 4-22. DLS analysis during the heating and cooling sequences. The DLS results indicate the absence of phage aggregation during both the heating and cooling phases. DLS characterization of the M13 phage was conducted in a Tris buffer (12.5 mM Tris and 37.5 mM NaCl) at (a) 20 °C, (b) 25 °C, and (c) 30 °C. Despite minimal adjustments in particle size throughout the heating and cooling procedures, alterations were observed in the CD signal at 222 nm. Reprinted with permission.[3] Copyright 2023, John Wiley and Sons.

4.5 Pyroelectric signal measurement using near-infrared (NIR) heat

4.5.1 Infrared heating mechanism

To demonstrate the potential generation of pyroelectric phage-based devices (Pyro-PhDs), I created vertically standing phage films on Ni-NTA-coated gold substrates and applied heat to the Pyro-PhDs (Figure 4-23). For more precise control over the heating and cooling processes, I investigated the pyroelectric characteristics of M13 phage under optical stimulation using a Near-Infrared laser (808 nm). To elucidate the mechanism of infrared heating for the pyroelectric characterizations of M13 phage, I employed spectrophotometry. A UV-vis spectrophotometer was used to measure the absorbance of M13 phage and the gold film at 800 nm, close to the wavelength of the NIR laser setup. In the absorbance spectra, a peak at

269 nm was observed for the phage film deposited on the gold thin film, and a separate peak was seen for the gold thin film with a glass substrate baseline (Figure 4-24). Notably, the phage film deposited on the gold thin film exhibited a higher absorbance peak, as confirmed by the baseline absorbance at 269 nm. The average absorbance was 2.0 at 800 nm for the gold thin film with a glass substrate as the baseline and approximately 0.12 at 800 nm for the phage film with the gold thin film as a baseline. Thus, there is minimal absorbance of NIR irradiation by the phage film, suggesting its insignificance for heat transfer. Instead, in the NIR laser setup, heat transfer primarily occurs through the gold thin film absorbing NIR irradiation and conducting heat to the phage film. The absorption spectra of the gold thin film were compared to literature values, revealing a decrease in absorbance near 500 nm and an increase from 500 to 800 nm, in line with increasing wavelengths at which absorption peaked with rising gold thin film thickness.[631]

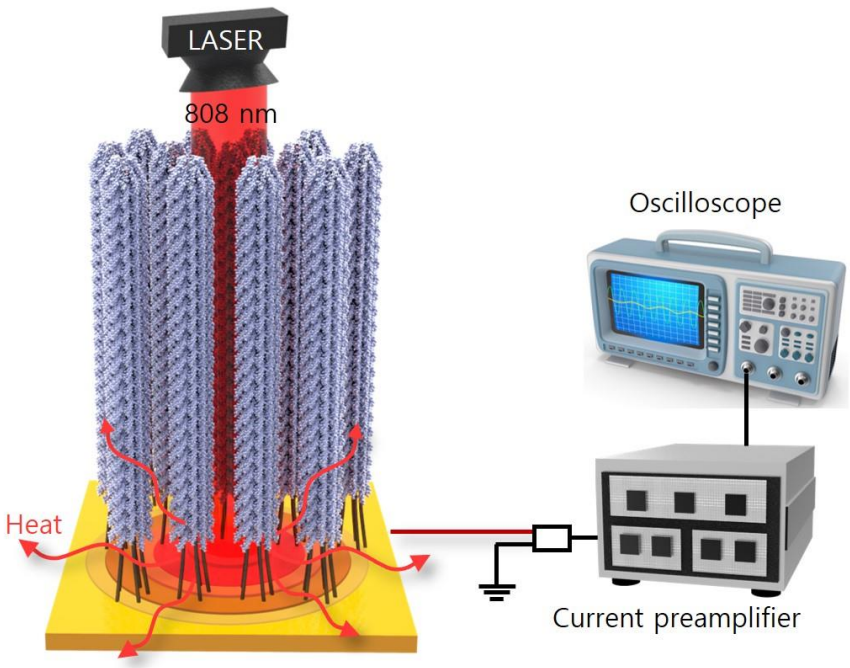

Figure 4-23. Pyroelectric characterization of a Pyro-PhD. Schematic diagram depicting the generation of pyroelectric potential. Schematic illustration outlining the pyroelectric characterization of a vertically standing Pyro-PhD through NIR laser thermal stimulation. Reprinted with permission.[3] Copyright 2023, John Wiley and Sons.

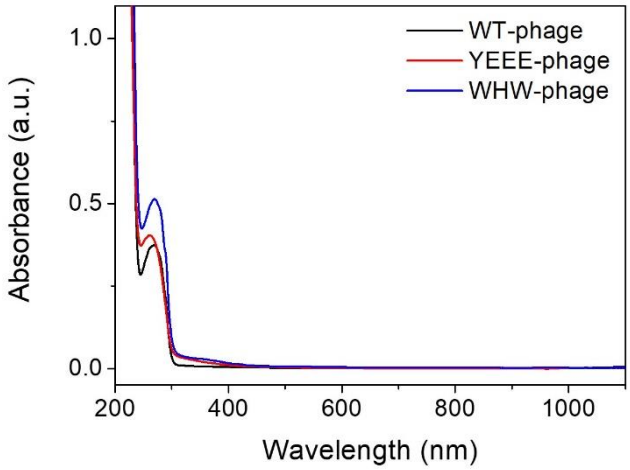

Figure 4-24. UV-vis spectra of M13 phages. The absorbance at the wavelength of 808 nm is minimal. Reprinted with permission.[3] Copyright 2023, John Wiley and Sons.

4.5.2 Pyroelectric output characterization

I employed a vertically standing YEEE-phage film for potential application as a gas sensor. Through periodic optical stimulation, I induced periodic heating and cooling with a pulse frequency of 0.10 Hz (Figure 4-25 and 4-26). During the heating process, the polarization of the phage decreased, prompting electrons to flow through the external load from the ground to the electrode until the temperature variation rate reached zero. Conversely, during the cooling process, the polarization of the phage increased, causing electrons to flow in the opposite direction compared to the heating process until the temperature variation rate reached zero.[615] At a temperature variation rate of 1.31 °C s^{-1}, I observed a voltage of 69.7 mV and a current of 50.6 pA (Figure 4-27). The pyroelectric voltage and current gradually increased with the laser intensity rising from 0.70 to 2.6 W cm^{-2} (Figure 4-28), aligning with the temperature variation rates (Figure 4-29). In a control experiment using a randomly aligned phage film, no output voltage or current was observed from the device, confirming that the electric signals were indeed generated by the pyroelectric effect along the polar direction of the phage (Figure 4-30). Notably, the M13 phage does not absorb 808 nm light (Figure 4-24). However, I could remotely induce pyroelectricity in the vertically standing phage films by heating the gold substrate. To assess the durability of Pyro-PhDs, I examined the performance of the Pyro-PhD under 3000 cycles of laser illumination (Figure 4-31). The output voltage and current showed negligible degradation. Therefore, the pyroelectric outputs under varied thermal conditions are well-defined and robust, making Pyro-PhDs suitable for further applications involving pyroelectric phages.

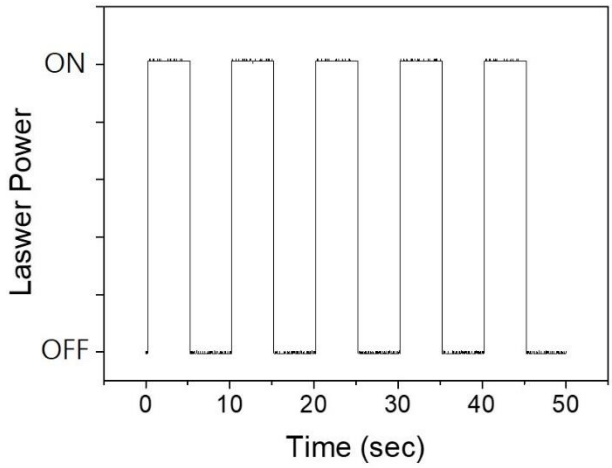

Figure 4-25. Temperature fluctuation generated by a NIR laser (808 nm) with a square function. Reprinted with permission.[3] Copyright 2023, John Wiley and Sons.

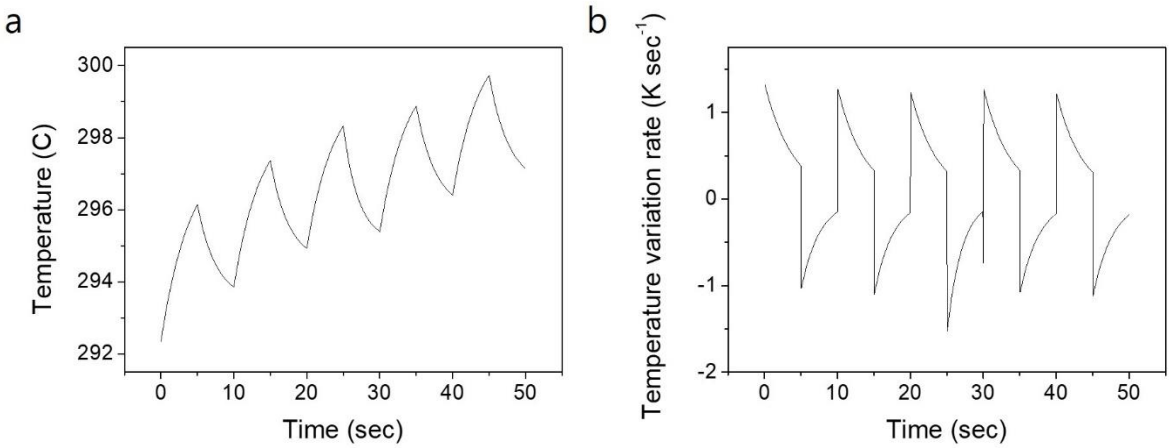

Figure 4-26. (a) Temperature profile under laser irradiation. (b) Temperature variation rate under laser irradiation. Reprinted with permission.[3] Copyright 2023, John Wiley and Sons.

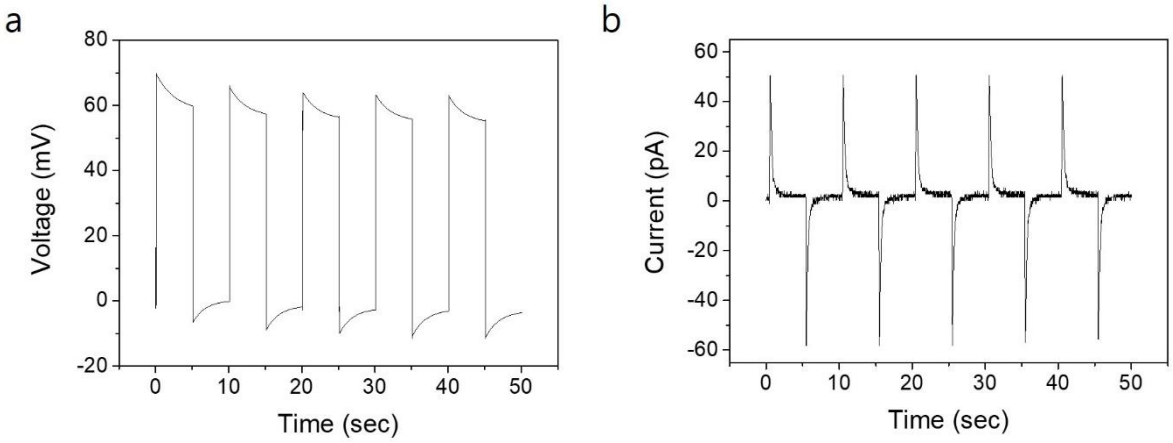

Figure 4-27. (a) Output voltage of the Pyro-PhD. (b) Output current of the Pyro-PhD. Reprinted with permission.[3] Copyright 2023, John Wiley and Sons.

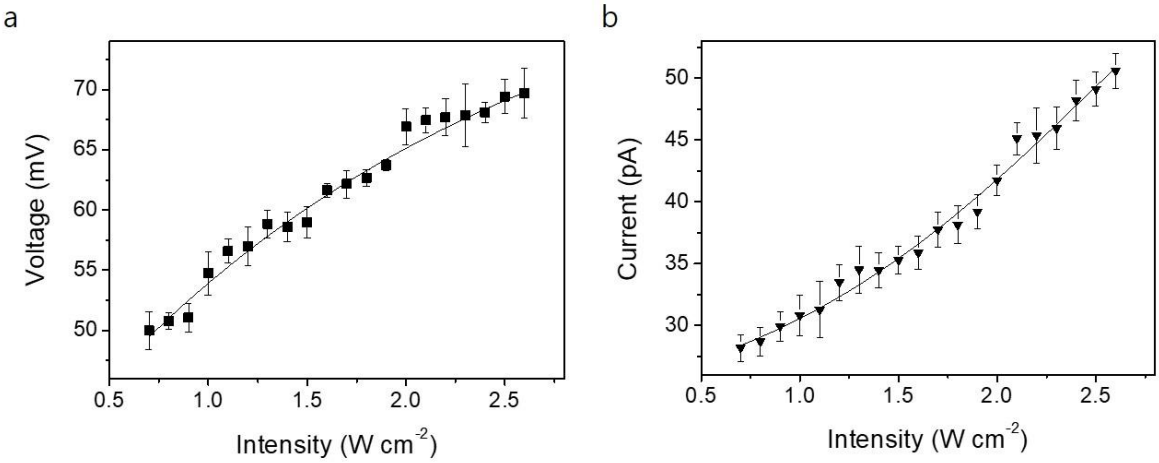

Figure 4-28. (a) Output voltage of the Pyro-PhD under different NIR intensities. (b) Output current of the Pyro-PhD under varying NIR intensities. Reprinted with permission.[3] Copyright 2023, John Wiley and Sons.

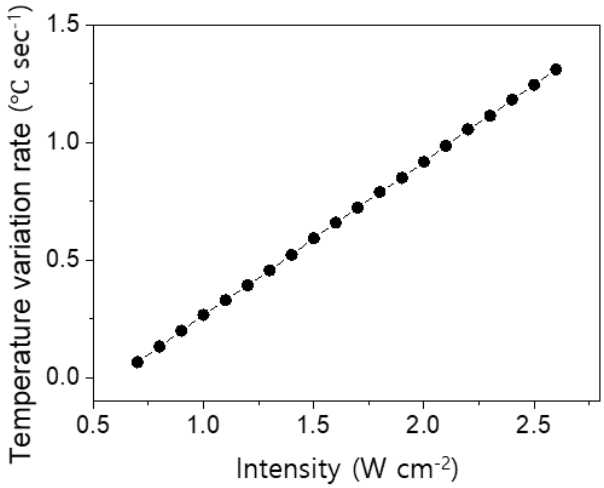

Figure 4-29. Temperature variation rates of the Pyro-PhD under varying levels of NIR intensity irradiation. Reprinted with permission.[3] Copyright 2023, John Wiley and Sons.

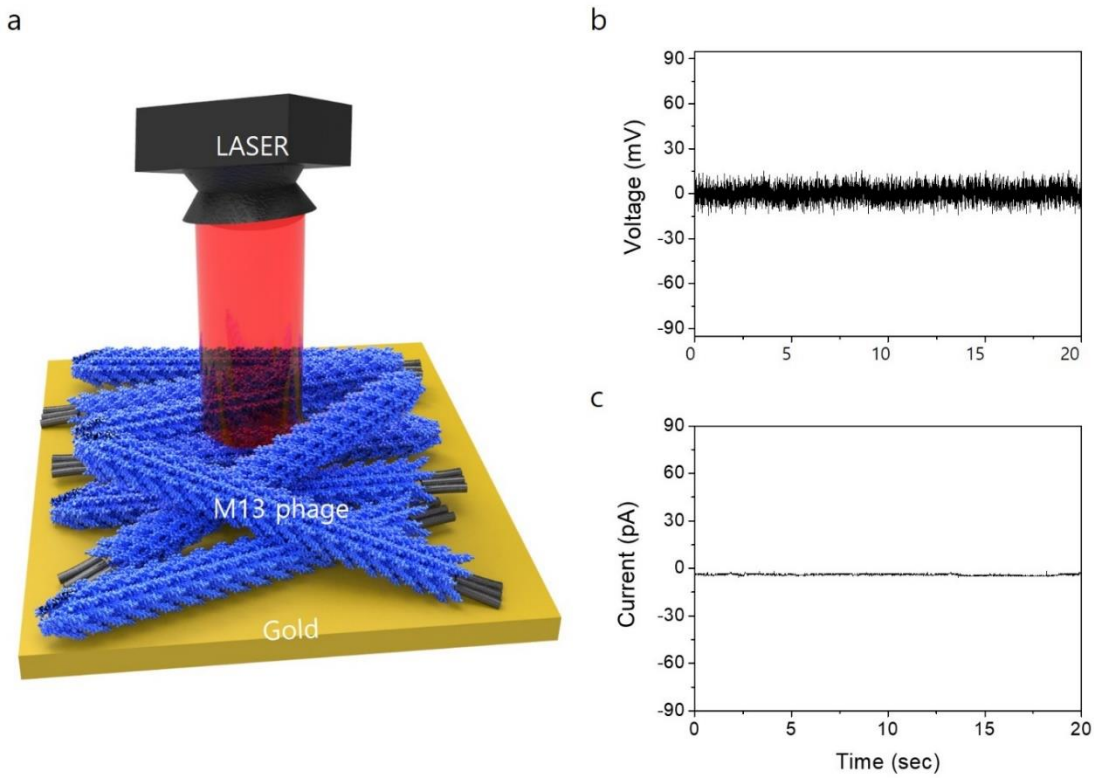

Figure 4-30. Pyroelectric analysis of a randomly aligned Pyro-PhD during infrared heating. (a) Diagram illustrating the pyroelectric characterization of a randomly aligned Pyro-PhD under NIR laser thermal stimulation. (b) Temperature fluctuations induced by a NIR laser with a square function. (c) and (d) Temperature and temperature variation rate during laser application.

(e) and (f) Output voltage and current of the Pyro-PhD. Reprinted with permission.[3] Copyright 2023, John Wiley and Sons.

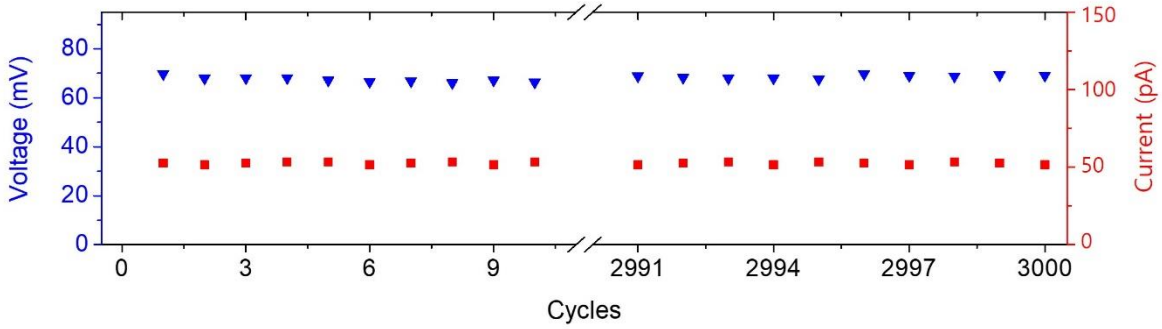

Figure 4-31. Durability test of the Pyro-PhD for 3000 cycles. Reprinted with permission.[3] Copyright 2023, John Wiley and Sons.

4.6 Pyroelectric responses to molecular interactions

4.6.1 Introduction

M13 phage exhibits remarkable genetic adaptability, allowing the presentation of specific peptide motifs on its surface and customizable interactions with external molecules. I observed notable alterations in pyroelectric response due to the interaction of the engineered motifs with external organic vapors. Leveraging this feature of the M13 phage, it becomes feasible to detect VOCs based on their pyroelectric responses. Previous investigations have demonstrated that YEEE- and WHW-engineered phages exhibit heightened sensitivities for detecting hydrophilic and aromatic VOCs (Table 17).[464,487] In this study, I engineered YEEE- and WHW-peptides onto the major coat protein of the M13 phage, in conjunction with 6-His on the minor coat proteins. Subsequently, Pyro-PhDs featuring vertically standing and unidirectionally polarized phage nanostructures were developed. Employing the same NIR laser setup, we monitored the pyroelectric response (changes in pyroelectric current, $|\Delta I_p|$) upon exposure to the specified VOCs (Table 18). The application of VOCs was systematically controlled by mass flow controllers (MFCs) (Figure 4-32).

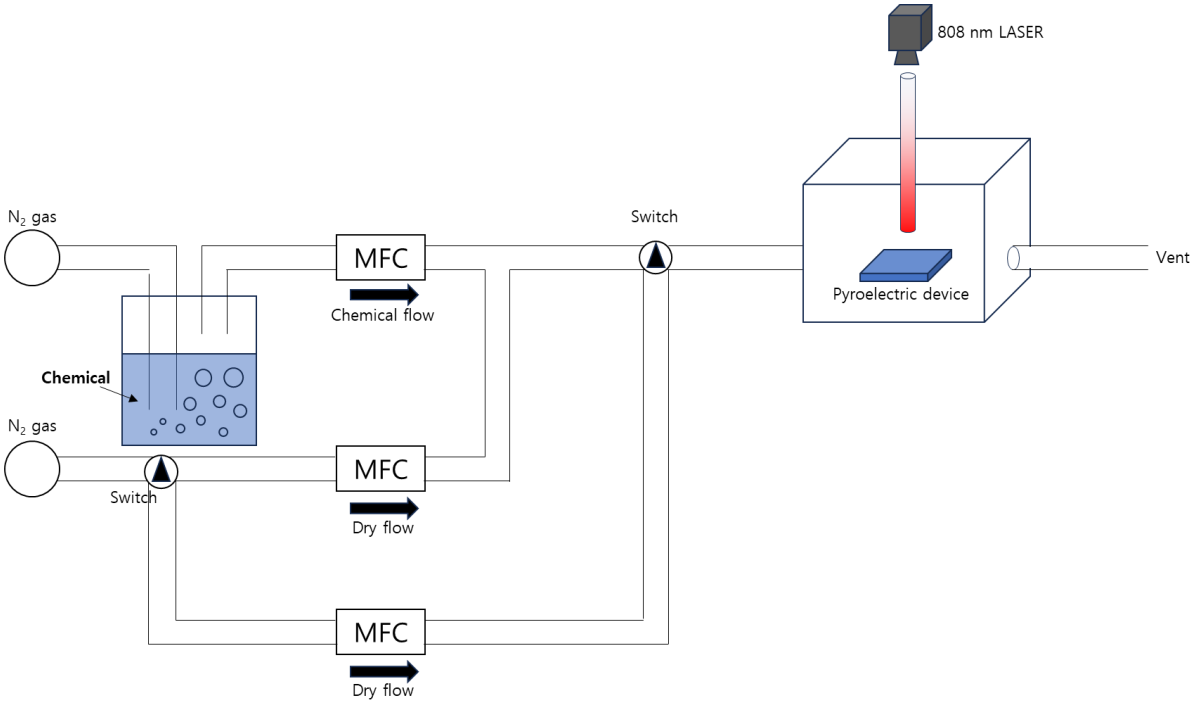

Figure 4-32. Configuration for molecular sensing experiments employing Pyro-PhDs. A Pyro-PhD is enclosed within a cage, and the introduction of target VOCs is regulated using MFCs.

Phage type	Primary structure of pVIII proteins*
YEEE	A*GYEEERGT*DPAKAAFNSLQASATEYIGYAWAMVVVIVGATIGKLFKKFTSKAS
WHW	A*DDWHWQEG*DPAKAAFNSLQASATEYIGYAWAMVVVIVGATIGKLFKKFTSKAS

Table 17. Primary structures for pVIII proteins[4,5]. Reprinted with permission.[3] Copyright 2023, John Wiley and Sons.

*The primary structure of the pVIII protein of the M13 phage and the insert is *underlined and italicized.*

Surrounding solvents*	Relative polarity
Water	1.00
Methanol	0.762
Ethanol	0.654
Octanol	0.537
Acetone	0.355
Diethyl ether	0.117
Benzene	0.111
Toluene	0.099

Xylene	0.077
Hexane	0.009

Table 18. Relative polarity of surrounding solvents. Reprinted with permission.[3] Copyright 2023, **John Wiley and Sons**.

*The aromatic hydrocarbons are *underlined and italicized*.

4.6.2 Hydrophilic molecular interactions

Figure 4-33 illustrates the pyroelectric response curve of the YEEE Pyro-PhD in different environments characterized by varying relative humidity (RH). The developed YEEE Pyro-PhD demonstrated the ability to differentiate between 0 and 100 % RH. As humidity levels increased from 0 to 100 %, the change in pyroelectric current exhibited a gradual increase, with a more pronounced rate of change observed in the higher humidity ranges (50–100 %). Additionally, I explored the pyroelectric response and the associated dipole moment of the YEEE Pyro-PhD in the presence of various hydrophilic VOCs. Exposure to 8000 ppm of different polar solvents was conducted for both YEEE- and WHW-Pyro-PhDs, and the resulting changes in pyroelectric current were observed. Notably, the YEEE-Pyro-PhD displayed a more substantial pyroelectric response compared to the WHW-Pyro-PhD when exposed to more polar solvents, indicating stronger hydrophilic interactions with the phage surface (Figure 4-34 and Figure 4-35).

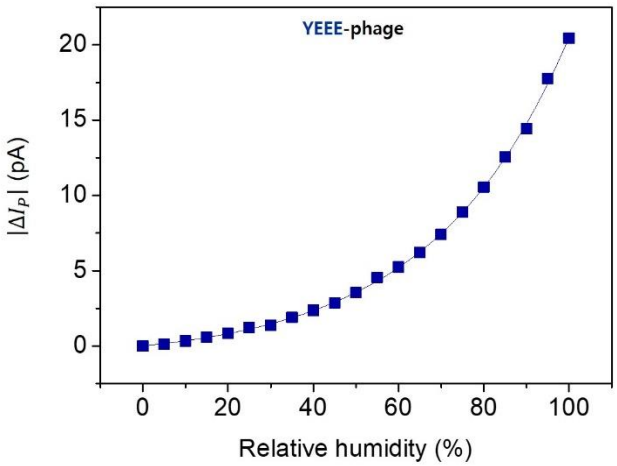

Figure 4-33. Pyroelectric response of YEEE Pyro-PhD under different levels of relative humidity. Reprinted with permission.[3] Copyright 2023, John Wiley and Sons.

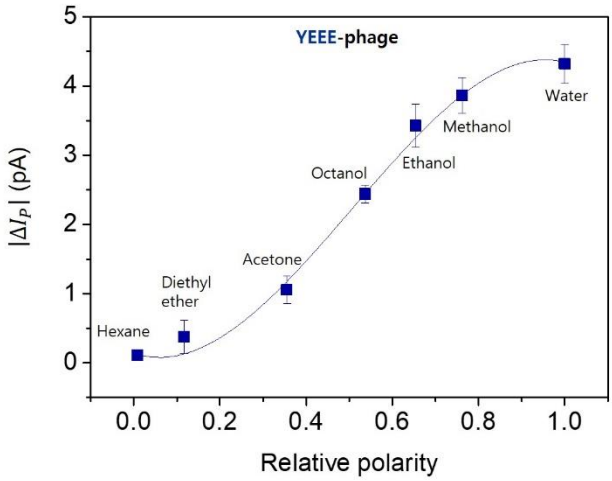

Figure 4-34. Pyroelectric response of YEEE Pyro-PhD to diverse VOCs as a means for sensing different polarities. Reprinted with permission.[3] Copyright 2023, John Wiley and Sons.

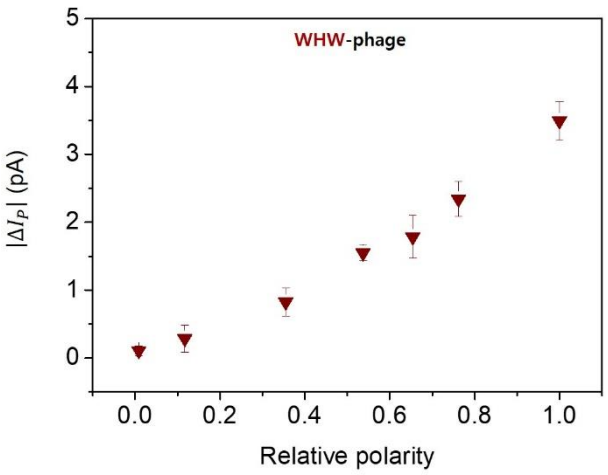

Figure 4-35. Pyroelectric response of WHW Pyro-PhD to various VOCs, enabling the detection of differing polarities. Reprinted with permission.[3] Copyright 2023, John Wiley and Sons.

4.6.3 Aromatic molecular interactions

To enhance the pyroelectric sensing capability of the phage for toxic aromatic molecules, I incorporated the previously identified aromatic molecule-responsive peptide (WHW) onto the Pyro-PhD.[5,465,486,487] Exposure to various concentrations of xylene revealed a rapid increase in the pyroelectric response between 0–120 ppm, followed by a gradual increase

in the 200–1000 ppm range (Figure 4-36). Given the known toxicity and carcinogenicity of xylene, I assessed the detection limit of the Pyro-PhDs for xylene. The resulting WHW-Pyro-PhD demonstrated a detection limit of 50 ppm, which is half the permissible exposure limit level. When subjected to 8000 ppm of other aromatic solvents, including xylene, toluene, and benzene, the pyroelectric response of the WHW Pyro-PhD measured 1.4, 1.2, and 0.83 pA, respectively (Figure 4-37). In contrast to the observed trend for hydrophilic interactions, the pyroelectric response of the WHW-Pyro-PhD increased as the relative polarity of the molecules decreased, while the YEEE-Pyro-PhD exhibited negligible pyroelectric response (Figure 4-38).

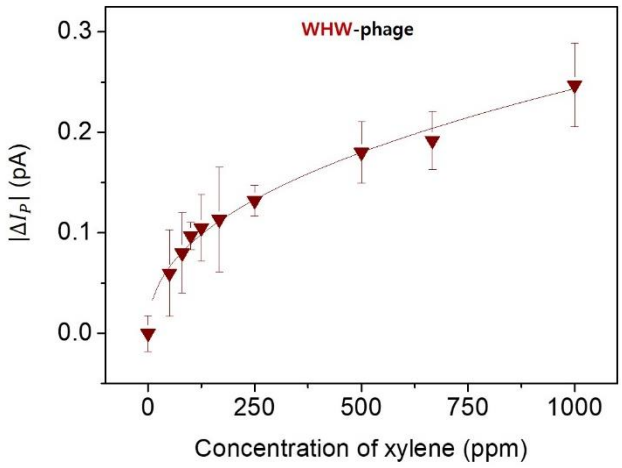

Figure 4-36. Pyroelectric response of WHW Pyro-PhD under different levels of xylene. Reprinted with permission.[3] Copyright 2023, John Wiley and Sons.

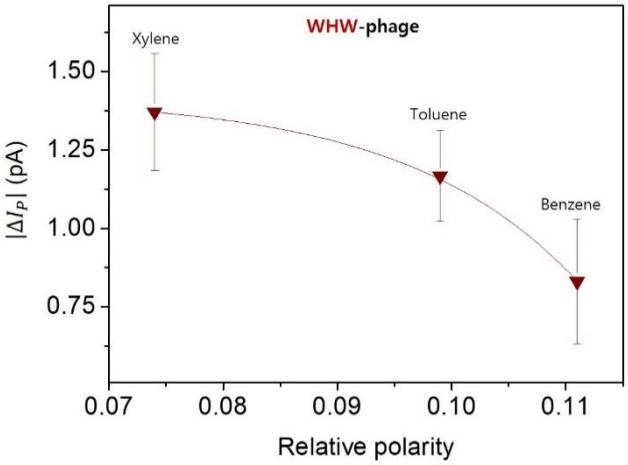

Figure 4-37. Pyroelectric response of WHW Pyro-PhD to various aromatic hydrocarbons. Reprinted with permission.[3] Copyright 2023, John Wiley and Sons.

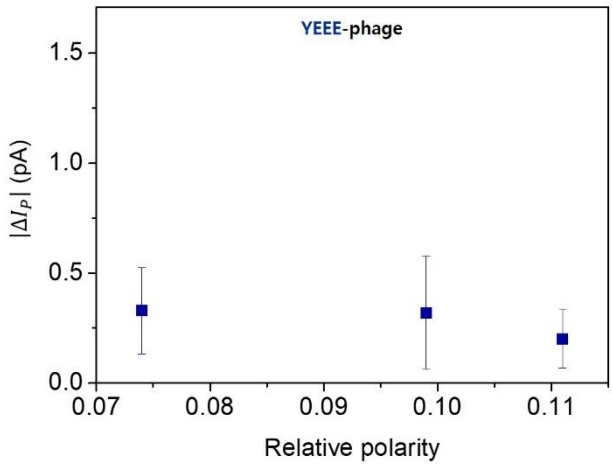

Figure 4-38. Pyroelectric response of YEEE Pyro-PhD to various aromatic hydrocarbons. Reprinted with permission.[3] Copyright 2023, John Wiley and Sons.

4.6.4 Mechanisms of the molecular interactions

To enhance our understanding of the specific pyroelectric signal generation triggered by molecular interactions in the Pyro-PhDs, I conducted MD simulations to examine the structural changes and variations in dipole moment of the engineered phages when exposed to solvents within the temperature range of 300 to 350 K. The YEEE-phage exhibited a more pronounced change in the number of hydrogen bonds with molecules of higher relative polarity, resulting in a greater change in dipole moment (Figure 4-39). This implies that a stronger hydrophilic interaction between the phage and surrounding molecules induces more substantial structural changes and a heightened pyroelectric response. Similarly, when the phage was genetically engineered with the aromatic-interacting WHW peptide, structural changes in the WHW-phage were observed upon exposure to aromatic molecules. The WHW phage displayed more significant changes in the number of hydrogen bonds and dipole moment, following the order of xylene, toluene, and benzene (Figure 4-40). Intriguingly, the structural changes were less pronounced with more polar molecules. This can be attributed to the strong aromatic interaction observed with xylene, resulting in a more significant structural change and a heightened pyroelectric response in the WHW-phage. Hence, I demonstrate that the M13 phage exhibits pyroelectric characteristics based on polarization changes resulting from molecular structural deformation. Through genetic modifications of the phage surface and the introduction of preferred molecular interactions, I have showcased its potential application as a novel VOC sensing system.

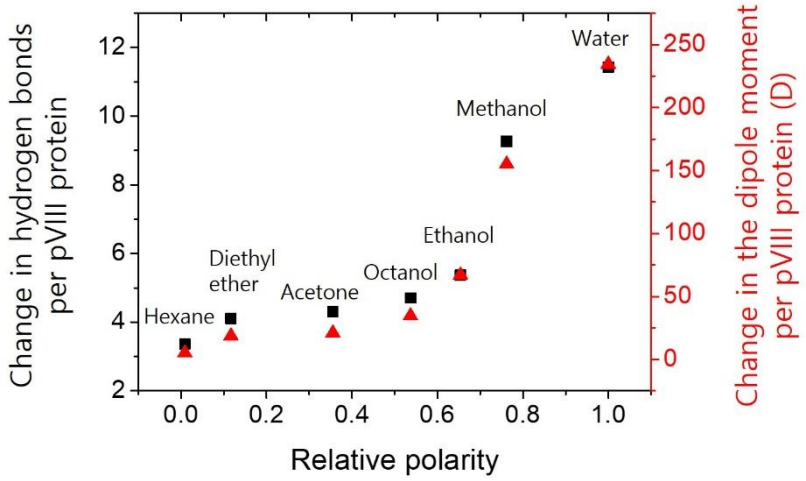

Figure 4-39. MD simulated dipole moment of the YEEE-pVIII protein model in the presence of different hydrophilic VOCs. The change in hydrogen bonds between the loops of the YEEE-pVIII protein and the change in dipole moment of the pVIII protein are observed from 300 to 350 K. Reprinted with permission.[3] Copyright 2023, John Wiley and Sons.

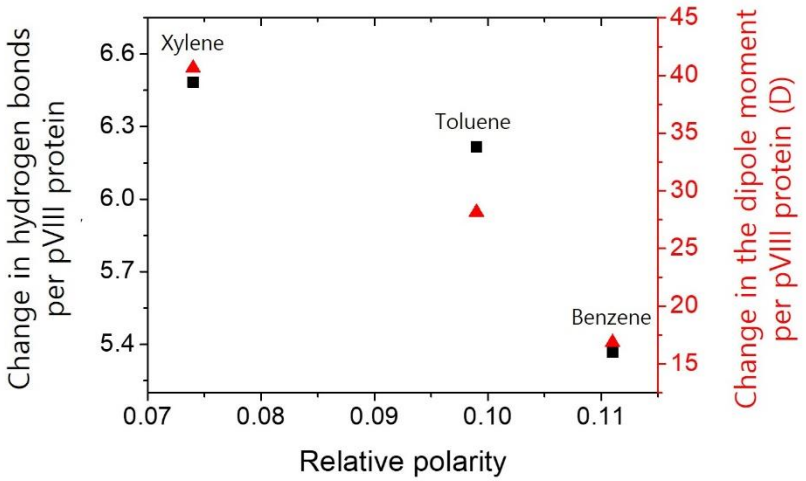

Figure 4-40. MD simulations were employed to determine the dipole moment of the WHW-pVIII protein model in the presence of different VOCs. The analysis considered the changes in hydrogen bonds between the loops of the WHW-pVIII protein and the changes in the dipole moment of the pVIII protein across the temperature range from 300 to 350 K. Reprinted with permission.[3] Copyright 2023, John Wiley and Sons.

4.7 Conclusion

Currently, the molecular-level comprehension of pyroelectricity in biomaterials remains elusive.[369,378,520] The intricate and heterogeneous hierarchical structure of biomaterials poses challenges in exploring their intrinsic material properties. Moreover, unlike inorganic piezoelectric materials, the tools available for manipulating desired structures and characterizing their properties are limited. In this investigation, we present the novel insight that viruses can sense heat through pyroelectricity, utilizing them as a model system to probe the structure-function relationship of bio-pyroelectricity at the molecular level. Through surface potential measurements, computational modeling, and spectroscopy, we demonstrate that virus particles undergo structural changes upon the application of heat. These changes lead to alterations in spontaneous polarization and the generation of pyroelectric potential. By focusing on the M13 phage and its inherent dipole structures, our study offers valuable insights into the connection between viral structures and electrical properties. This discovery suggests the potential application of our established bio-pyroelectric modality for detecting various viral particles and biomaterials. Such an approach could have significant implications for developing innovative technologies to detect new virus strains in biomedical applications, diagnostics, and biosensors. Furthermore, our strategy of engineering phages with tailored pyroelectric properties broadens the scope for designing and fabricating bioelectric materials in diverse fields, including bioelectronics, energy harvesting, and bio-inspired devices in the future.

4.8 Methods

4.8.1 Single phage length measurements

I conducted quantitative analysis of AFM images to determine the length of individual phages. For each type of phage (1E-, 2E-, 3E-, 4E-, and WT-phages), I deposited 2 μL of dialyzed phage solutions, allowing them to air-dry overnight. Employing Ti/Pt-coated AC240TM-R3 (Oxford Instruments) AFM tips, I performed topography imaging at a scan rate of 0.80 Hz. Using ImageJ software, I calculated the lengths of the engineered phages, and the measured lengths were approximately 980 nm.

4.8.2 Mechanical property characterization of phage films

I explored the mechanical characteristics of the phage films through AFM using the MFP-3D AFM system from Asylum Research in Santa Barbara, CA. To image the surface of the phage films, I employed Ti/Pt-coated AC240TM-R3 (Oxford Instruments) AFM tips with a radius of approximately 28 nm and a force constant of about 2 N m^{-1}. The AFM software (Asylum Research version 16.14.216) was used for the analysis of the roughness of the phage films. Additionally, I conducted nanoindentation for assessing the Young's modulus of the phage films, employing RTESP-525 (Bruker) AFM tips with a radius of around 8 nm and a force constant of about 200 N m^{-1}.

4.8.3 Fourier-transform infrared (FT-IR) spectroscopy

To assess the density of the phage films, I employed Fourier-transform infrared spectroscopy (FTIR) using a Shinmadzu IR Tracer-100 instrument. The measurements were conducted with a diamond attenuated total reflection (ATR) accessory featuring a diameter of 1.8 mm.

4.8.4 Pyroelectric characterization using Kelvin probe force microscopy

I explored the generation of surface charge induced by the pyroelectric effect in M13 phage, employing KPFM combined with AFM using an MFP3D AFM system from Asylum Research in Santa Barbara, CA. For imaging the surface, I used Ti/Pt-coated AC240TM-R3 AFM tips with a radius of approximately 28 nm and a force constant of about 2 N m^{-1}. The surface potential of the phage film was assessed using KPFM with a scan rate of 1.5 Hz for Figure 4-11 and 1.0 Hz for Figure 4-13 and 4-14, and scan lines of 512 and 128, respectively. A temperature controller was positioned between the sample and the AFM stage, and heat was applied to the sample by controlling the temperature controller. The temperature of the phage film was monitored using a thermoprobe attached to the sample surface and Arduino software (version 1.8.13). The pyroelectric potential, defined as the absolute value of the net variations in surface potential with reference to that of the non-heated region, was obtained by measuring the surface potential of the heated region.

4.8.5 Molecular dynamics simulations

To unravel the molecular mechanism behind pyroelectricity in the M13 phage, I conducted MD simulations using the Maestro package (version 2021-2 by Schrödinger). The M13 phage was designed using Pymol 2.4.0 software and subsequently imported into Maestro. MD simulations were executed using Desmond MD within the Maestro software interface, spanning the temperature range of 300 to 350 K for a duration of 20 ns. Dipole moments were computed for both a single pVIII protein and multilayers of pVIII layers. Additionally, I assessed the change in distance between M13 repeating units to ascertain whether alterations in spacing at the phage level contributed to changes in dipole moment. The results indicated that the variation in the dipole moment of phage was attributable to the pyroelectric effect rather than the thermal expansion effect.

4.8.6 Structural analysis using circular dichroism spectroscopy

I examined changes in the secondary structure of the M13 phage through CD

spectroscopy, employing a J-815 CD spectrometer by JASCO. Wavelength scans were conducted across the range of 170 to 900 nm, with temperatures varying from 293 to 353 K, utilizing a 0.1 cm cuvette and a 200 μL solution containing 0.2 mg mL^{-1} of the phage. The acquired data were analyzed for structural changes in the phage using CDtoolX software.[630]

4.8.7 Structural analysis using dynamic light scattering

I explored the impact of temperature on the particle size of the M13 phage using DLS with a disposable cuvette (ZEN0040, Malvern Instruments Ltd, Westborough, MA). The Z-average of the phage was determined through Zetasizer software (version 8.1, Malvern). The DLS analysis of the M13 phage was carried out in a Tris buffer (12.5 mM Tris and 37.5 mM NaCl) within the temperature range of 20-30 °C.

4.8.8 Pyroelectric characterization upon near-infrared heating

I assessed the electrical responses of vertically standing Pyro-PhDs by subjecting them to periodic heating. This was achieved using a transistor-transistor logic (TTL)-modulated NIR laser (Lasever LSR808NL-FC-3W), connected to a laser diode driver (Lasever LSR-PS-II) and waveform function generator (Rigol DG1022). This setup allowed for precise and systematic control of laser thermal stimulation. The output voltage and current were monitored using an oscilloscope (Tektronix TDS 1001B), Keithley 6514 System Electrometer, and a Low-Noise Current Preamplifier (Stanford Research SR570), respectively. The heat generation profiles were examined with a Thermal imager (Klein Tools TI250) and optimized using COMSOL Multiphysics software. I exposed the Pyro-PhDs to 8000 ppm of various organic compounds to explore how the pyroelectric properties of M13 phage respond to the surrounding environment.

4.8.9 Optimization of the temperature variations of infrared heating

To precisely optimize the temperature profile of the pyroelectric phage device, I employed finite element method simulations through COMSOL Multiphysics software. Within the software, I computationally determined the temperature variation in a gold substrate under laser application by constructing a pulse-modulated laser heating model incorporating *Heat transfer in solids physics.*[632] The laser was modeled as a Gaussian beam-type laser, with a radius of 3 mm (actual dimensions: 4 mm x 2 mm). For the heat flux, the *General inward heat flux*, P_g, was defined by equation (21).

$$P_g = A \cdot \left[\frac{E_p}{P_w\left(\frac{\pi}{4}D^2\right)}\right] exp\left[-\left(\frac{(x-x_0)^2}{2\phi^2}\right)\right] \qquad (21)$$

where A is the absorptivity, E_p is the pulse energy, P_w is the pulse width, D is the beam diameter, x_r is the reference point of the laser beam, and ϕ is the standard deviation of the Gaussian laser beam. *Convective heat flux*, q_0, was defined as equation (22).

$$q_0 = h \cdot (T_{ext} - T) \qquad (22)$$

where h is the heat transfer coefficient, T_{ext} is the ambient temperature.

CHAPTER 5: Conclusion and future perspectives

5.1 Concluding remarks

A virus serves as a powerful programmable tool for advancing our understanding of bioelectricity. Using the M13 phage for its simple structure, versatility, and self-assembled nanostructures, I have focused on investigating bioelectrical phenomena at the molecular level under various external stimuli, including friction, mechanical stress, heat, and chemical environments. This thesis demonstrates how genetic modifications of viruses alter structural and electrical properties, thereby introducing practical virus-based bioelectrical applications.

In Chapter 2, the triboelectric phenomenon in the M13 phage is studied. By creating precisely defined structures with varying numbers of negatively charged residues on the protein surface, we investigated the triboelectric effect of the M13 phage using scanning probe microscopy at the molecular level. Computational analysis revealed that genetic engineering of the phage alters the energy levels of the phage, resulting in differences in electron transfer under friction. The proposed phage-based triboelectric devices could generate 76 V of voltage and 5.1 μA of current, powering 30 LED devices. This study offers a promising avenue for sustainable green energy harvesting and a novel methodology for detecting specific viruses in future applications.

In Chapter 3, the piezoelectric property of the M13 phage is demonstrated. This study demonstrates a breakthrough of understanding the piezoelectric capabilities of biomaterials by studying how the surface charge and dipole moment of the material correlates and how they react to various mechanical stimulations. Through computational analysis, the piezoelectric tensor of the phage is defined and the electrical intricacies of the phage and its response to diverse external mechanical stresses are explained. Moreover, the proposed phage-based piezoelectric devices exhibited directional dependency of the piezoelectric effect of the phage, including normal and shear piezoelectricity. This bioengineering approach, encompassing surface charge engineering, genetic modification, and precise polarization control, proves pivotal in optimizing the piezoelectric effect.

In Chapter 4, the pyroelectric characteristics of the M13 phage are described. The molecular-level comprehension of the pyroelectric effect of the phage provides insight into the underlying mechanisms of pyroelectricity in biomaterials. The pyroelectric phenomenon of the phage was characterized using scanning probe microscopy. Furthermore, the molecular mechanism of the pyroelectric effect of the phage was demonstrated through computational analysis and circular dichroism spectroscopy. The results revealed that the coat proteins undergo structural changes upon the application of heat, resulting in alterations in spontaneous polarization and the generation of pyroelectric potential. This discovery suggests potential applications for novel biological pyroelectric modalities in detecting various viral particles and biomaterials.

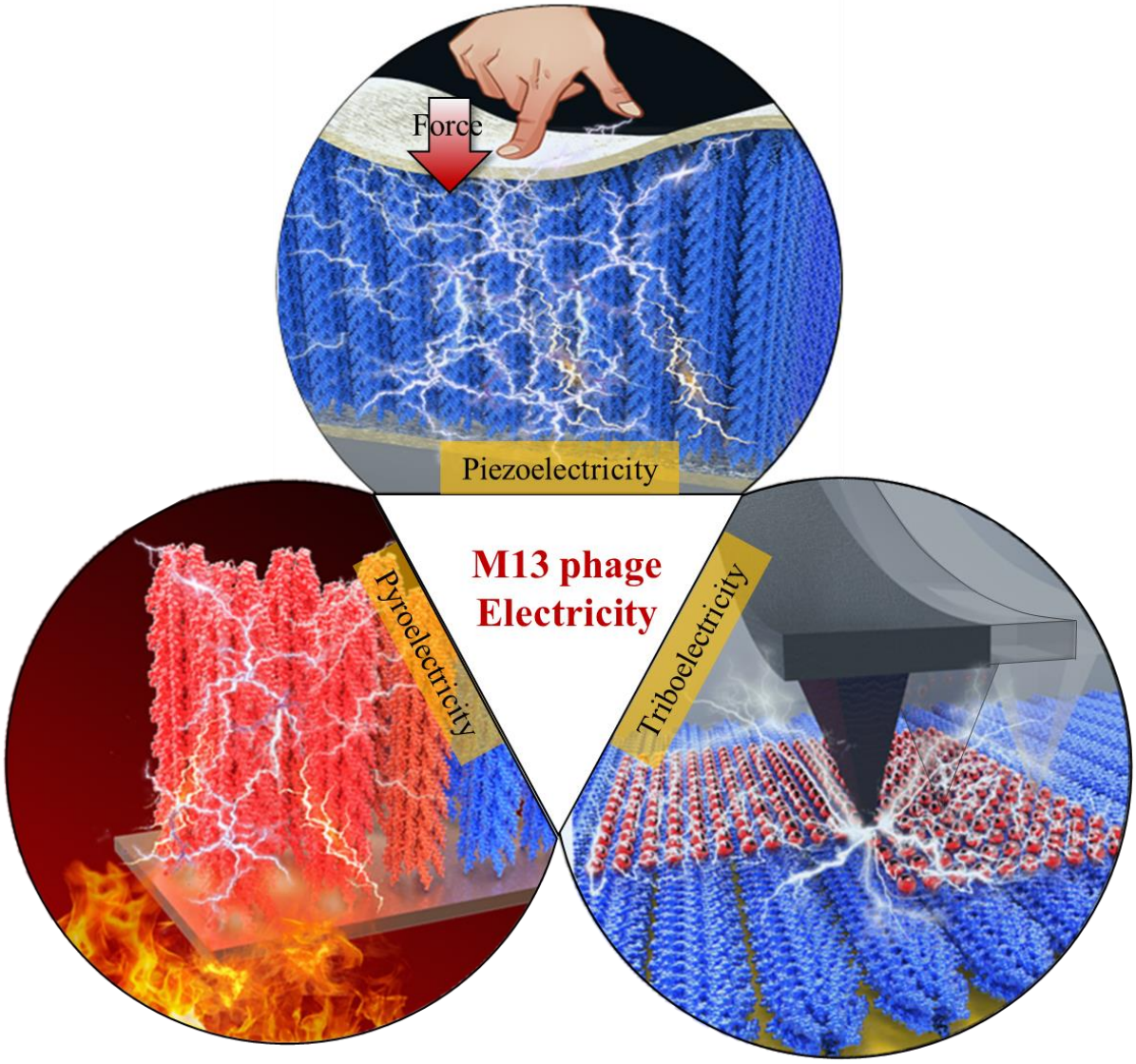

Figure 5-1. Schematic diagram of the different electrical characteristics of the M13 phage in response to different external stimuli: Piezoelectricity (mechanical stress), pyroelectricity (temperature change), and triboelectricity (contact).

5.2 Future perspectives

Building on the extensive exploration of the bioelectrical properties of the M13 phage that unveiled novel avenues in virus-based bioelectrical applications, Chapters 2, 3, and 4 intricately detail the triboelectric, piezoelectric, and pyroelectric characteristics of this versatile viral platform. These chapters collectively demonstrate the potential of the M13 phage in generating sustainable energy and pioneering innovative molecular sensing methodologies. The future perspective, now expanded with Sections 5.2.1, 5.2.2, 5.2.3, and 5.2.4, continues the trajectory of innovation. Section 5.2.1 emphasizes pathways for enhancing the performance

of phage-based triboelectric devices through genetic engineering, chemical modification, and self-assembled nanostructure control. In Section 5.2.2, the focus shifts to optimizing the piezoelectric effect of phage-based devices, addressing challenges in random alignment of phage during self-assembly. Precise control over phage alignment, coupled with advanced deposition and fabrication methods, aims to elevate practical efficacy, particularly in wearable and implantable energy harvesting technologies. Section 5.2.3 explores the responsivity of the pyroelectric characteristics of the M13 phage, aligning with the broader goal of enhancing sensitivity in pyroelectric devices for applications like infrared detection and thermal imaging. The exploration extends to a phage-based pyroelectric molecular sensing system, laying the foundation for potential expansions into protein sensing systems through genome engineering and the expression of specific protein motifs on the M13 phage surface. Lastly, Section 5.2.4 suggests exploring ferroelectricity as a new material property and underscores the importance of controlling dipole moments through genetic engineering for experimental characterization. This discovery could inspire novel applications, drawing parallels with established ferroelectric materials like ferroelectric liquid crystals and exploring concepts from bioelectric memory devices. Collectively, this ongoing research significantly contributes to the evolving field of bioelectricity, establishing a robust foundation for practical applications poised to revolutionize energy harvesting, molecular sensing system, and the study of ferroelectric biomaterials.

5.2.1 Enhancing the performance of phage-based triboelectric devices

The electrical output performance of phage-based triboelectric devices can be further improved through various techniques, including genetic engineering, chemical modification, and self-assembled nanostructure control. Firstly, energy level modification is crucial in the triboelectric effect because it is closely related to electron transfer. Computational analysis in Chapter 2 revealed that the LUMO level of the phage protein decreases with the introduction of glutamates to the phage surface. This demonstrates that genetic engineering of the phage by introducing residues that can significantly lower the LUMO level or by introducing a larger number of glutamates into the phage surface can enhance the triboelectric effect. Next, chemical modification on the phage surface can be effective. It is known that fluorinating the surface of certain materials enhances the triboelectric effect because fluorine is a highly electronegative element, demonstrating its strong tendency to extract electrons. Lastly, enlarging the surface area of the triboelectric layer is significant for the enhancement of the triboelectric effect. M13 phage exhibits various self-assembled nanostructures. Notably, the self-templating phage deposition method has been precisely developed. By depositing phage over a large surface area and controlling the evaporation kinetics and ionic concentration of the phage solution, I expect superior enhancement of the triboelectric performance of phage-based triboelectric devices.

5.2.2 Optimizing the piezoelectric effect of phage-based piezoelectric devices

In the process of self-assembly for the M13 phage, the inherent random alignment

concerning rotational degree of freedom of the phage leads to the simultaneous measurement of various piezoelectric constants in phage-based piezoelectric devices. This simultaneity makes it challenging to differentiate between these integrated piezoelectric constants. For instance, in the horizontal mode of phage-based piezoelectric devices, normal longitudinal modes of d_{11} and d_{22} are randomly mixed, presenting an integrated piezoelectric output. Although I have thoroughly investigated every possible individual piezoelectric constant of the phage using computational methods, it is still necessary to experimentally quantify these constants. Therefore, precise control over phage alignment should be developed. Moreover, limitations in electrode fabrication and phage deposition methods restrict the characterization of all different types of piezoelectric constants. Consequently, the development of appropriate phage deposition and electrode fabrication methods is required. Lastly, it is crucial to not only characterize the inherent normal and shear piezoelectric constants but also to understand the intricate interplay of piezoelectric constants that may manifest during bending or stretching motions, ensuring their efficacy in practical applications. Through a thorough understanding of these complex piezoelectric situations, phage-based piezoelectric devices can be assured of their suitability for practical applications, such as wearable and implantable energy harvesting technologies.

5.2.3 Investigating the responsivity and novel phage-based pyroelectrical applications

Responsivity in the context of pyroelectric devices refers to the ability of the device to generate an electrical response in proportion to changes in temperature or thermal radiation, indicating the effectiveness of the pyroelectric material converts thermal changes into an electrical signal. Higher responsivity is generally desirable in pyroelectric applications, as it suggests that the material is more sensitive to temperature variations. Since phage-based pyroelectric devices can be used for infrared detection, thermal imaging, and other applications where precise measurement of temperature changes is essential, a higher responsivity is desired. Thus, investigating the responsivity of the pyroelectric characteristics of the M13 phage becomes crucial. Furthermore, I have investigated a phage-based pyroelectric molecular sensing system designed to detect polar and toxic molecules using hydrophilic and aromatic interactions. By expressing specific protein motifs on the M13 phage surface through phage genome engineering, the expressed protein motifs have the potential to interact with other protein materials through protein-protein interactions. Leveraging the pyroelectric molecular sensing mechanism, I anticipate that this phage-based pyroelectric sensing system can be expanded to protein sensing systems.

5.2.4 Exploring the ferroelectricity in M13 phage

The non-centrosymmetric structure and the existence of spontaneous polarization of the M13 phage satisfy the requirements to exhibit piezoelectric and pyroelectric properties. We pose a question: Does the M13 phage exhibit ferroelectric properties? Since the M13 phage may demonstrate ferroelectric properties from a crystallographic perspective, I suggest

exploring a new material property—ferroelectricity. This can be an excellent model system to understand the ferroelectric properties of biomaterials in general. To achieve this aim, we must consider the possibility of polarization switching in the phage. The determination of polarization formation in M13 phage is explained in Chapter 3. Phage polarization is primarily determined by the surface charge dipole moment and core dipole moment, which can be manipulated through genetic engineering. If the net dipole moment of the phage is too large, we can expect that polarization switching may be limited and challenging to characterize experimentally. This is because the phage would require substantial energy to significantly deform its physical structure under an external electric field. Therefore, by controlling the magnitude of the surface charge dipole moment and core dipole moment to ensure the phage has a small net dipole moment, I anticipate that it may be applicable for characterizing the ferroelectric property of the phage experimentally. Thus, initially optimizing the magnitude of the dipole moment of the phage through genetic engineering, the ferroelectric properties of the phage can be characterized using scanning probe microscopy or phage-based ferroelectric devices. The discovery of ferroelectricity in the M13 phage could inspire novel applications. Drawing parallels with established ferroelectric materials, such as ferroelectric liquid crystals, and incorporating concepts from bioelectric memory devices inspired by ferroelectric memory might provide insights into potential applications.

References

1 Lee, B. Y. *et al.* Virus-based piezoelectric energy generation. *Nature Nanotechnology* **7**, 351-356 (2012). https://doi.org:10.1038/nnano.2012.69

2 Kim, H. *et al.* M13 Virus Triboelectricity and Energy Harvesting. *Nano Letters* **21**, 6851-6858 (2021). https://doi.org:10.1021/acs.nanolett.1c01881

3 Kim, H. *et al.* Virus-Based Pyroelectricity. *Advanced Materials* **35**, 2305503 (2023). https://doi.org:https://doi.org/10.1002/adma.202305503

4 Lee, J.-H. *et al.* Vertical Self-Assembly of Polarized Phage Nanostructure for Energy Harvesting. *Nano Letters* **19**, 2661-2667 (2019). https://doi.org:10.1021/acs.nanolett.9b00569

5 Kim, T. H. *et al.* Selective and Sensitive TNT Sensors Using Biomimetic Polydiacetylene-Coated CNT-FETs. *ACS Nano* **5**, 2824-2830 (2011). https://doi.org:10.1021/nn103324p

6 Wu, C. H. Electric Fish and the Discovery of Animal Electricity: The mystery of the electric fish motivated research into electricity and was instrumental in the emergence of electrophysiology. *American Scientist* **72**, 598-607 (1984).

7 Piccolino, M. Luigi Galvani and animal electricity: two centuries after the foundation of electrophysiology. *Trends Neurosci* **20**, 443-448 (1997). https://doi.org:10.1016/s0166-2236(97)01101-6

8 Fritzsch, B. Electric organs: History and potential. *Science* **345**, 631-632 (2014). https://doi.org:doi:10.1126/science.345.6197.631-b

9 Dong, L. *et al.* Cardiac energy harvesting and sensing based on piezoelectric and triboelectric designs. *Nano Energy* **76**, 105076 (2020). https://doi.org:https://doi.org/10.1016/j.nanoen.2020.105076

10 Cafarelli, A. *et al.* Piezoelectric Nanomaterials Activated by Ultrasound: The Pathway from Discovery to Future Clinical Adoption. *ACS Nano* **15**, 11066-11086 (2021). https://doi.org:10.1021/acsnano.1c03087

11 Yuan, X. *et al.* Piezoelectricity, Pyroelectricity, and Ferroelectricity in Biomaterials and Biomedical Applications. *Adv. Mater.* **36**, 2308726 (2024). https://doi.org:https://doi.org/10.1002/adma.202308726

12 Kapat, K., Shubhra, Q. T. H., Zhou, M. & Leeuwenburgh, S. Piezoelectric Nano-Biomaterials for Biomedicine and Tissue Regeneration. *Advanced Functional Materials* **30**, 1909045 (2020). https://doi.org:https://doi.org/10.1002/adfm.201909045

13 Khare, D., Basu, B. & Dubey, A. K. Electrical stimulation and piezoelectric biomaterials for bone tissue engineering applications. *Biomaterials* **258**, 120280 (2020). https://doi.org:https://doi.org/10.1016/j.biomaterials.2020.120280

14 Marino, A., Battaglini, M., De Pasquale, D., Degl'Innocenti, A. & Ciofani, G. Ultrasound-Activated Piezoelectric Nanoparticles Inhibit Proliferation of Breast Cancer Cells. *Scientific Reports* **8**, 6257 (2018). https://doi.org:10.1038/s41598-018-24697-1

15 Feiner, R. & Dvir, T. Tissue–electronics interfaces: from implantable devices to engineered tissues. *Nature Reviews Materials* **3**, 17076 (2017). https://doi.org:10.1038/natrevmats.2017.76

16 Kaila, V. R. I. Resolving Chemical Dynamics in Biological Energy Conversion: Long-Range Proton-Coupled Electron Transfer in Respiratory Complex I. *Accounts of Chemical Research* **54**, 4462-4473 (2021).

https://doi.org:10.1021/acs.accounts.1c00524
17 Horiuchi, S. & Tokura, Y. Organic ferroelectrics. *Nat. Mater.* **7**, 357-366 (2008). https://doi.org:10.1038/nmat2137
18 Bennett, J. W. Surveying polar materials in the Inorganic Crystal Structure Database to identify emerging structure types. *Journal of Solid State Chemistry* **281**, 121045 (2020). https://doi.org:https://doi.org/10.1016/j.jssc.2019.121045
19 Smith, M. B. *et al.* Crystal Structure and the Paraelectric-to-Ferroelectric Phase Transition of Nanoscale BaTiO3. *J. Am. Chem. Soc.* **130**, 6955-6963 (2008). https://doi.org:10.1021/ja0758436
20 You, Y.-M. *et al.* An organic-inorganic perovskite ferroelectric with large piezoelectric response. *Science* **357**, 306-309 (2017). https://doi.org:doi:10.1126/science.aai8535
21 Funk, R. H. W. & Scholkmann, F. The significance of bioelectricity on all levels of organization of an organism. Part 1: From the subcellular level to cells. *Progress in Biophysics and Molecular Biology* **177**, 185-201 (2023). https://doi.org:https://doi.org/10.1016/j.pbiomolbio.2022.12.002
22 Li, J. *et al.* Stretchable piezoelectric biocrystal thin films. *Nature Communications* **14**, 6562 (2023). https://doi.org:10.1038/s41467-023-42184-8
23 Huebsch, N. & Mooney, D. J. Inspiration and application in the evolution of biomaterials. *Nature* **462**, 426-432 (2009). https://doi.org:10.1038/nature08601
24 Wang, R., Sui, J. & Wang, X. Natural Piezoelectric Biomaterials: A Biocompatible and Sustainable Building Block for Biomedical Devices. *ACS Nano* **16**, 17708-17728 (2022). https://doi.org:10.1021/acsnano.2c08164
25 Guerin, S. *et al.* Control of piezoelectricity in amino acids by supramolecular packing. *Nature Materials* **17**, 180-186 (2018). https://doi.org:10.1038/nmat5045
26 Guerin, S., Syed, T. A. M. & Thompson, D. Deconstructing collagen piezoelectricity using alanine-hydroxyproline-glycine building blocks. *Nanoscale* **10**, 9653-9663 (2018). https://doi.org:10.1039/C8NR01634H
27 Denning, D. *et al.* Piezoelectric Tensor of Collagen Fibrils Determined at the Nanoscale. *ACS Biomaterials Science & Engineering* **3**, 929-935 (2017). https://doi.org:10.1021/acsbiomaterials.7b00183
28 Zhou, Z., Qian, D. & Minary-Jolandan, M. Molecular Mechanism of Polarization and Piezoelectric Effect in Super-Twisted Collagen. *ACS Biomaterials Science & Engineering* **2**, 929-936 (2016). https://doi.org:10.1021/acsbiomaterials.6b00021
29 Ravi, H. K., Simona, F., Hulliger, J. & Cascella, M. Molecular Origin of Piezo- and Pyroelectric Properties in Collagen Investigated by Molecular Dynamics Simulations. *The Journal of Physical Chemistry B* **116**, 1901-1907 (2012). https://doi.org:10.1021/jp208436j
30 Stapleton, A. *et al.* Pyroelectricity in globular protein lysozyme films. *Journal of Applied Physics* **123** (2018). https://doi.org:10.1063/1.5014029
31 Liu, Y. *et al.* Ferroelectric switching of elastin. *Proceedings of the National Academy of Sciences* **111**, E2780-E2786 (2014). https://doi.org:doi:10.1073/pnas.1402909111
32 Denning, D., Guyonnet, J. & Rodriguez, B. J. Applications of piezoresponse force microscopy in materials research: from inorganic ferroelectrics to biopiezoelectrics and beyond. *International Materials Reviews* **61**, 46-70 (2016). https://doi.org:10.1179/1743280415Y.0000000013
33 Gruverman, A., Alexe, M. & Meier, D. Piezoresponse force microscopy and nanoferroic phenomena. *Nat. Commun.* **10**, 1661 (2019).

https://doi.org:10.1038/s41467-019-09650-8
34 Guckenberger, R. *et al.* A scanning tunneling microscope (STM) for biological applications: design and performance. *Ultramicroscopy* **25**, 111-121 (1988). https://doi.org:10.1016/0304-3991(88)90218-5
35 Stupin, D. D. *et al.* Bioimpedance Spectroscopy: Basics and Applications. *ACS Biomaterials Science & Engineering* **7**, 1962-1986 (2021). https://doi.org:10.1021/acsbiomaterials.0c01570
36 Cho, Y. S. & Gwak, S. J. Novel Sensing Technique for Stem Cells Differentiation Using Dielectric Spectroscopy of Their Proteins. *Sensors (Basel)* **23** (2023). https://doi.org:10.3390/s23052397
37 Willumeit, R. Neutron and X-Ray Techniques for Biological and Biomaterials Studies. *Advanced Engineering Materials* **13**, 747-766 (2011). https://doi.org:https://doi.org/10.1002/adem.201000326
38 Baker, M. J. *et al.* Using Fourier transform IR spectroscopy to analyze biological materials. *Nat. Protoc.* **9**, 1771-1791 (2014). https://doi.org:10.1038/nprot.2014.110
39 Baer, D. R. & Engelhard, M. H. XPS analysis of nanostructured materials and biological surfaces. *Journal of Electron Spectroscopy and Related Phenomena* **178-179**, 415-432 (2010). https://doi.org:https://doi.org/10.1016/j.elspec.2009.09.003
40 Dufrêne, Y. F. *et al.* Imaging modes of atomic force microscopy for application in molecular and cell biology. *Nat. Nanotechnol.* **12**, 295-307 (2017). https://doi.org:10.1038/nnano.2017.45
41 Sinensky, A. K. & Belcher, A. M. Label-free and high-resolution protein/DNA nanoarray analysis using Kelvin probe force microscopy. *Nat. Nanotechnol.* **2**, 653-659 (2007). https://doi.org:10.1038/nnano.2007.293
42 Kang, H. *et al.* Mechanically Robust Silver Nanowires Network for Triboelectric Nanogenerators. *Advanced Functional Materials* **26**, 7717-7724 (2016). https://doi.org:https://doi.org/10.1002/adfm.201603199
43 Cheon, S. *et al.* High-Performance Triboelectric Nanogenerators Based on Electrospun Polyvinylidene Fluoride–Silver Nanowire Composite Nanofibers. *Advanced Functional Materials* **28**, 1703778 (2018). https://doi.org:https://doi.org/10.1002/adfm.201703778
44 Long, Y. *et al.* Moisture-induced autonomous surface potential oscillations for energy harvesting. *Nat. Commun.* **12**, 5287 (2021). https://doi.org:10.1038/s41467-021-25554-y
45 Xu, X. *et al.* Application of molecular dynamics simulation in self-assembled cancer nanomedicine. *Biomaterials Research* **27**, 39 (2023). https://doi.org:10.1186/s40824-023-00386-7
46 Yoon, D. H. E., Weber, C. I., Easson, G. W. D., Broz, K. S. & Tang, S. Y. Rapid determination of internal strains in soft tissues using an experimentally calibrated finite element model derived from magnetic resonance imaging. *Quantitative Imaging in Medicine and Surgery* **10**, 57-65 (2019).
47 Dai, X. & Chen, Y. Computational Biomaterials: Computational Simulations for Biomedicine. *Advanced Materials* **35**, 2204798 (2023). https://doi.org:https://doi.org/10.1002/adma.202204798
48 Hollingsworth, S. A. & Dror, R. O. Molecular Dynamics Simulation for All. *Neuron* **99**, 1129-1143 (2018). https://doi.org:10.1016/j.neuron.2018.08.011
49 Dremin, V., Novikova, I. & Rafailov, E. Simulation of thermal field distribution in

biological tissue and cell culture media irradiated with infrared wavelengths. *Opt. Express* **30**, 23078-23089 (2022). https://doi.org:10.1364/OE.454012

50 Deng, W. *et al.* Computational investigation of ultrasound induced electricity generation via a triboelectric nanogenerator. *Nano Energy* **91**, 106656 (2022). https://doi.org:https://doi.org/10.1016/j.nanoen.2021.106656

51 Chen, C. *et al.* Micro triboelectric ultrasonic device for acoustic energy transfer and signal communication. *Nat. Commun.* **11**, 4143 (2020). https://doi.org:10.1038/s41467-020-17842-w

52 Kim, J. *et al.* High-Performance Piezoelectric, Pyroelectric, and Triboelectric Nanogenerators Based on P(VDF-TrFE) with Controlled Crystallinity and Dipole Alignment. *Advanced Functional Materials* **27**, 1700702 (2017). https://doi.org:https://doi.org/10.1002/adfm.201700702

53 Lee, O.-S., Stupp, S. I. & Schatz, G. C. Atomistic Molecular Dynamics Simulations of Peptide Amphiphile Self-Assembly into Cylindrical Nanofibers. *Journal of the American Chemical Society* **133**, 3677-3683 (2011). https://doi.org:10.1021/ja110966y

54 Lee, O.-S., Cho, V. & Schatz, G. C. Modeling the Self-Assembly of Peptide Amphiphiles into Fibers Using Coarse-Grained Molecular Dynamics. *Nano Letters* **12**, 4907-4913 (2012). https://doi.org:10.1021/nl302487m

55 Zhang, L., Chen, J., He, M. & Su, X. Molecular dynamics simulation-guided toehold mediated strand displacement probe for single-nucleotide variants detection. *Exploration* **2**, 20210265 (2022). https://doi.org:https://doi.org/10.1002/EXP.20210265

56 Sampath, J., Alamdari, S. & Pfaendtner, J. Closing the Gap Between Modeling and Experiments in the Self-Assembly of Biomolecules at Interfaces and in Solution. *Chemistry of Materials* **32**, 8043-8059 (2020). https://doi.org:10.1021/acs.chemmater.0c01891

57 ElMessiery, M. A. Physical basis for piezoelectricity of bone matrix. *IEE Proceedings A (Physical Science, Measurement and Instrumentation, Management and Education, Reviews)* **128**, 336-346 (1981). <https://digital-library.theiet.org/content/journals/10.1049/ip-a-1.1981.0049>.

58 Bera, S. *et al.* Molecular engineering of piezoelectricity in collagen-mimicking peptide assemblies. *Nat Commun* **12**, 2634 (2021). https://doi.org:10.1038/s41467-021-22895-6

59 Bera, S. *et al.* Molecular engineering of piezoelectricity in collagen-mimicking peptide assemblies. *Nature Communications* **12**, 2634 (2021). https://doi.org:10.1038/s41467-021-22895-6

60 Brodland, G. W. How computational models can help unlock biological systems. *Semin Cell Dev Biol* **47-48**, 62-73 (2015). https://doi.org:10.1016/j.semcdb.2015.07.001

61 Pereda, A. E. Electrical synapses and their functional interactions with chemical synapses. *Nature Reviews Neuroscience* **15**, 250-263 (2014). https://doi.org:10.1038/nrn3708

62 Goodwin, G. & McMahon, S. B. The physiological function of different voltage-gated sodium channels in pain. *Nature Reviews Neuroscience* **22**, 263-274 (2021). https://doi.org:10.1038/s41583-021-00444-w

63 Saberi, A., Jabbari, F., Zarrintaj, P., Saeb, M. R. & Mozafari, M. Electrically Conductive Materials: Opportunities and Challenges in Tissue Engineering. *Biomolecules* **9**, 448 (2019).

64 Fersht, A. R. From the first protein structures to our current knowledge of protein

folding: delights and scepticisms. *Nature Reviews Molecular Cell Biology* **9**, 650-654 (2008). https://doi.org:10.1038/nrm2446
65 Chen, H. & Fraser Stoddart, J. From molecular to supramolecular electronics. *Nature Reviews Materials* **6**, 804-828 (2021). https://doi.org:10.1038/s41578-021-00302-2
66 Levental, I. & Lyman, E. Regulation of membrane protein structure and function by their lipid nano-environment. *Nature Reviews Molecular Cell Biology* **24**, 107-122 (2023). https://doi.org:10.1038/s41580-022-00524-4
67 Koons, G. L., Diba, M. & Mikos, A. G. Materials design for bone-tissue engineering. *Nature Reviews Materials* **5**, 584-603 (2020). https://doi.org:10.1038/s41578-020-0204-2
68 Yuk, H., Wu, J. & Zhao, X. Hydrogel interfaces for merging humans and machines. *Nature Reviews Materials* **7**, 935-952 (2022). https://doi.org:10.1038/s41578-022-00483-4
69 Perucca, E. Ein gründliches Experiment über die Kontakttheorie der Triboelektrizität. — Voltaeffekt erster Art und elektrische Doppelschichten beim Kontakt. *Zeitschrift für Physik* **51**, 268-278 (1928). https://doi.org:10.1007/BF01343201
70 Helmholtz, H. Studien über electrische Grenzschichten. *Annalen der Physik* **243**, 337-382 (1879). https://doi.org:https://doi.org/10.1002/andp.18792430702
71 Iversen, P. & Lacks, D. J. A life of its own: The tenuous connection between Thales of Miletus and the study of electrostatic charging. *Journal of Electrostatics* **70**, 309-311 (2012). https://doi.org:https://doi.org/10.1016/j.elstat.2012.03.002
72 Zou, H. *et al.* Quantifying and understanding the triboelectric series of inorganic non-metallic materials. *Nature Communications* **11**, 2093 (2020). https://doi.org:10.1038/s41467-020-15926-1
73 Zou, H. *et al.* Quantifying the triboelectric series. *Nature Communications* **10**, 1427 (2019). https://doi.org:10.1038/s41467-019-09461-x
74 Choi, J. H. *et al.* Development of a triboelectric nanogenerator with enhanced electrical output performance by embedding electrically charged microparticles. *Functional Composites and Structures* **1**, 045005 (2019). https://doi.org:10.1088/2631-6331/ab51b0
75 Ra, Y., Choi, J. H., La, M., Park, S. J. & Choi, D. Development of a highly transparent and flexible touch sensor based on triboelectric effect. *Functional Composites and Structures* **1**, 045001 (2019). https://doi.org:10.1088/2631-6331/ab47ba
76 Davies, D. K. Charge generation on dielectric surfaces. *Journal of Physics D: Applied Physics* **2**, 1533 (1969). https://doi.org:10.1088/0022-3727/2/11/307
77 Wåhlin, A. & Bäckström, G. Sliding electrification of Teflon by metals. *Journal of Applied Physics* **45**, 2058-2064 (2003). https://doi.org:10.1063/1.1663545
78 Kang, H. *et al.* Metal nanowire–polymer matrix hybrid layer for triboelectric nanogenerator. *Nano Energy* **58**, 227-233 (2019). https://doi.org:https://doi.org/10.1016/j.nanoen.2019.01.046
79 Lin, S. *et al.* Electron Transfer in Nanoscale Contact Electrification: Effect of Temperature in the Metal–Dielectric Case. *Advanced Materials* **31**, 1808197 (2019). https://doi.org:https://doi.org/10.1002/adma.201808197
80 Xu, C. *et al.* On the Electron-Transfer Mechanism in the Contact-Electrification Effect. *Advanced Materials* **30**, 1706790 (2018). https://doi.org:https://doi.org/10.1002/adma.201706790
81 Wang, A. C. *et al.* Unraveling Temperature-Dependent Contact Electrification between

Sliding-Mode Triboelectric Pairs. *Advanced Functional Materials* **30**, 1909384 (2020). https://doi.org:https://doi.org/10.1002/adfm.201909384

82 Xu, C. *et al.* Effects of Metal Work Function and Contact Potential Difference on Electron Thermionic Emission in Contact Electrification. *Advanced Functional Materials* **29**, 1903142 (2019). https://doi.org:https://doi.org/10.1002/adfm.201903142

83 Wang, Z. L. & Wang, A. C. On the origin of contact-electrification. *Materials Today* **30**, 34-51 (2019). https://doi.org:https://doi.org/10.1016/j.mattod.2019.05.016

84 Lin, S., Zheng, M., Luo, J. & Wang, Z. L. Effects of Surface Functional Groups on Electron Transfer at Liquid–Solid Interfacial Contact Electrification. *ACS Nano* **14**, 10733-10741 (2020). https://doi.org:10.1021/acsnano.0c06075

85 Li, S. *et al.* Contributions of Different Functional Groups to Contact Electrification of Polymers. *Advanced Materials* **32**, 2001307 (2020). https://doi.org:https://doi.org/10.1002/adma.202001307

86 McCarty, L. S., Winkleman, A. & Whitesides, G. M. Ionic Electrets: Electrostatic Charging of Surfaces by Transferring Mobile Ions upon Contact. *Journal of the American Chemical Society* **129**, 4075-4088 (2007). https://doi.org:10.1021/ja067301e

87 Diaz, A. F., Wollmann, D. & Dreblow, D. Contact electrification: ion transfer to metals and polymers. *Chemistry of Materials* **3**, 997-999 (1991). https://doi.org:10.1021/cm00018a006

88 Wiles, J. A., Fialkowski, M., Radowski, M. R., Whitesides, G. M. & Grzybowski, B. A. Effects of Surface Modification and Moisture on the Rates of Charge Transfer between Metals and Organic Materials. *The Journal of Physical Chemistry B* **108**, 20296-20302 (2004). https://doi.org:10.1021/jp0457904

89 Clarke, D., Whitney, H., Sutton, G. & Robert, D. Detection and Learning of Floral Electric Fields by Bumblebees. *Science* **340**, 66-69 (2013). https://doi.org:doi:10.1126/science.1230883

90 Minasyan, H. A. Erythrocyte and Leukocyte: Two Partners in Bacteria Killing. *International Reviews of Immunology* **33**, 490-497 (2014). https://doi.org:10.3109/08830185.2014.956359

91 Pinto, D. *et al.* Cross-neutralization of SARS-CoV-2 by a human monoclonal SARS-CoV antibody. *Nature* **583**, 290-295 (2020). https://doi.org:10.1038/s41586-020-2349-y

92 Hassanzadeh, K. *et al.* Considerations around the SARS-CoV-2 Spike Protein with Particular Attention to COVID-19 Brain Infection and Neurological Symptoms. *ACS Chemical Neuroscience* **11**, 2361-2369 (2020). https://doi.org:10.1021/acschemneuro.0c00373

93 Zhu, G. *et al.* Triboelectric-Generator-Driven Pulse Electrodeposition for Micropatterning. *Nano Letters* **12**, 4960-4965 (2012). https://doi.org:10.1021/nl302560k

94 Peng, J., Kang, S. D. & Snyder, G. J. Optimization principles and the figure of merit for triboelectric generators. *Science Advances* **3**, eaap8576 (2017). https://doi.org:doi:10.1126/sciadv.aap8576

95 Kwak, S. S. *et al.* Fully Stretchable Textile Triboelectric Nanogenerator with Knitted Fabric Structures. *ACS Nano* **11**, 10733-10741 (2017). https://doi.org:10.1021/acsnano.7b05203

96 Lim, G.-H. *et al.* Fully stretchable and highly durable triboelectric nanogenerators based on gold-nanosheet electrodes for self-powered human-motion detection. *Nano*

Energy **42**, 300-306 (2017). https://doi.org:https://doi.org/10.1016/j.nanoen.2017.11.001

97 Fan, F.-R., Tian, Z.-Q. & Lin Wang, Z. Flexible triboelectric generator. *Nano Energy* **1**, 328-334 (2012). https://doi.org:https://doi.org/10.1016/j.nanoen.2012.01.004

98 Ren, Z. *et al.* Energy Harvesting from Breeze Wind (0.7–6 m s−1) Using Ultra-Stretchable Triboelectric Nanogenerator. *Advanced Energy Materials* **10**, 2001770 (2020). https://doi.org:https://doi.org/10.1002/aenm.202001770

99 Zhang, C. *et al.* Harvesting Wind Energy by a Triboelectric Nanogenerator for an Intelligent High-Speed Train System. *ACS Energy Letters* **6**, 1490-1499 (2021). https://doi.org:10.1021/acsenergylett.1c00368

100 Chen, P. *et al.* Super-Durable, Low-Wear, and High-Performance Fur-Brush Triboelectric Nanogenerator for Wind and Water Energy Harvesting for Smart Agriculture. *Advanced Energy Materials* **11**, 2003066 (2021). https://doi.org:https://doi.org/10.1002/aenm.202003066

101 Ren, Z., Wu, L., Pang, Y., Zhang, W. & Yang, R. Strategies for effectively harvesting wind energy based on triboelectric nanogenerators. *Nano Energy* **100**, 107522 (2022). https://doi.org:https://doi.org/10.1016/j.nanoen.2022.107522

102 Wang, Y. *et al.* Gravity triboelectric nanogenerator for the steady harvesting of natural wind energy. *Nano Energy* **82**, 105740 (2021). https://doi.org:https://doi.org/10.1016/j.nanoen.2020.105740

103 Zou, H.-X. *et al.* A self-regulation strategy for triboelectric nanogenerator and self-powered wind-speed sensor. *Nano Energy* **95**, 106990 (2022). https://doi.org:https://doi.org/10.1016/j.nanoen.2022.106990

104 Liang, X. *et al.* Spherical triboelectric nanogenerator integrated with power management module for harvesting multidirectional water wave energy. *Energy & Environmental Science* **13**, 277-285 (2020). https://doi.org:10.1039/C9EE03258D

105 Xia, K., Fu, J. & Xu, Z. Multiple-Frequency High-Output Triboelectric Nanogenerator Based on a Water Balloon for All-Weather Water Wave Energy Harvesting. *Advanced Energy Materials* **10**, 2000426 (2020). https://doi.org:https://doi.org/10.1002/aenm.202000426

106 Rodrigues, C. *et al.* Emerging triboelectric nanogenerators for ocean wave energy harvesting: state of the art and future perspectives. *Energy & Environmental Science* **13**, 2657-2683 (2020). https://doi.org:10.1039/D0EE01258K

107 Zhang, C. *et al.* Self-Powered Sensor for Quantifying Ocean Surface Water Waves Based on Triboelectric Nanogenerator. *ACS Nano* **14**, 7092-7100 (2020). https://doi.org:10.1021/acsnano.0c01827

108 Zhang, C. *et al.* Active resonance triboelectric nanogenerator for harvesting omnidirectional water-wave energy. *Joule* **5**, 1613-1623 (2021). https://doi.org:https://doi.org/10.1016/j.joule.2021.04.016

109 Liang, X. *et al.* Triboelectric Nanogenerator Network Integrated with Charge Excitation Circuit for Effective Water Wave Energy Harvesting. *Advanced Energy Materials* **10**, 2002123 (2020). https://doi.org:https://doi.org/10.1002/aenm.202002123

110 Seung, W. *et al.* Dual Friction Mode Textile-Based Tire Cord Triboelectric Nanogenerator. *Advanced Functional Materials* **30**, 2002401 (2020). https://doi.org:https://doi.org/10.1002/adfm.202002401

111 Zhu, L. *et al.* A triboelectric nanogenerator sensor based on phononic crystal structures for smart buildings and transportation systems. *Nano Energy* **97**, 107165 (2022).

https://doi.org:https://doi.org/10.1016/j.nanoen.2022.107165
112 Rayegani, A., Matin Nazar, A. & Rashidi, M. Advancements in Triboelectric Nanogenerators (TENGs) for Intelligent Transportation Infrastructure: Enhancing Bridges, Highways, and Tunnels. *Sensors* **23**, 6634 (2023).
113 Zhang, H. *et al.* Single-Electrode-Based Rotating Triboelectric Nanogenerator for Harvesting Energy from Tires. *ACS Nano* **8**, 680-689 (2014). https://doi.org:10.1021/nn4053292
114 Pang, Y. *et al.* Textile-inspired triboelectric nanogenerator as intelligent pavement energy harvester and self-powered skid resistance sensor. *Applied Energy* **348**, 121515 (2023). https://doi.org:https://doi.org/10.1016/j.apenergy.2023.121515
115 Zhang, Q., Barri, K., Kari, S. R., Wang, Z. L. & Alavi, A. H. Multifunctional Triboelectric Nanogenerator-Enabled Structural Elements for Next Generation Civil Infrastructure Monitoring Systems. *Advanced Functional Materials* **31**, 2105825 (2021). https://doi.org:https://doi.org/10.1002/adfm.202105825
116 Huang, K. *et al.* A real-time quantitative acceleration monitoring method based on triboelectric nanogenerator for bridge cable vibration. *Nano Energy* **118**, 108960 (2023). https://doi.org:https://doi.org/10.1016/j.nanoen.2023.108960
117 Pang, Y., Zhu, X., Lee, C. & Liu, S. Triboelectric nanogenerator as next-generation self-powered sensor for cooperative vehicle-infrastructure system. *Nano Energy* **97**, 107219 (2022). https://doi.org:https://doi.org/10.1016/j.nanoen.2022.107219
118 Wang, L., Liu, W., Yan, Z., Wang, F. & Wang, X. Stretchable and Shape-Adaptable Triboelectric Nanogenerator Based on Biocompatible Liquid Electrolyte for Biomechanical Energy Harvesting and Wearable Human–Machine Interaction. *Advanced Functional Materials* **31**, 2007221 (2021). https://doi.org:https://doi.org/10.1002/adfm.202007221
119 Lai, Y.-C., Hsiao, Y.-C., Wu, H.-M. & Wang, Z. L. Waterproof Fabric-Based Multifunctional Triboelectric Nanogenerator for Universally Harvesting Energy from Raindrops, Wind, and Human Motions and as Self-Powered Sensors. *Advanced Science* **6**, 1801883 (2019). https://doi.org:https://doi.org/10.1002/advs.201801883
120 Yuan, W. *et al.* Wearable, Breathable and Waterproof Triboelectric Nanogenerators for Harvesting Human Motion and Raindrop Energy. *Advanced Materials Technologies* **7**, 2101139 (2022). https://doi.org:https://doi.org/10.1002/admt.202101139
121 Shen, S., Xiao, X., Xiao, X. & Chen, J. Wearable triboelectric nanogenerators for heart rate monitoring. *Chemical Communications* **57**, 5871-5879 (2021). https://doi.org:10.1039/D1CC02091A
122 Lin, Z. *et al.* Triboelectric Nanogenerator Enabled Body Sensor Network for Self-Powered Human Heart-Rate Monitoring. *ACS Nano* **11**, 8830-8837 (2017). https://doi.org:10.1021/acsnano.7b02975
123 Su, Y. *et al.* Self-Powered Respiration Monitoring Enabled By a Triboelectric Nanogenerator. *Advanced Materials* **33**, 2101262 (2021). https://doi.org:https://doi.org/10.1002/adma.202101262
124 Lee, D.-M. *et al.* An on-demand bioresorbable neurostimulator. *Nature Communications* **14**, 7315 (2023). https://doi.org:10.1038/s41467-023-42791-5
125 Imani, I. M. *et al.* Ultrasound-Driven On-Demand Transient Triboelectric Nanogenerator for Subcutaneous Antibacterial Activity. *Advanced Science* **10**, 2204801 (2023). https://doi.org:https://doi.org/10.1002/advs.202204801
126 Hinchet, R. *et al.* Transcutaneous ultrasound energy harvesting using capacitive

triboelectric technology. *Science* **365**, 491-494 (2019). https://doi.org:doi:10.1126/science.aan3997
127 Lee, D.-M. *et al.* Ultrasound-mediated triboelectric nanogenerator for powering on-demand transient electronics. *Science Advances* **8**, eabl8423 (2022). https://doi.org:doi:10.1126/sciadv.abl8423
128 Hill, R. M. Characterisation of dielectric loss in solids and liquids. *Nature* **275**, 96-99 (1978). https://doi.org:10.1038/275096a0
129 Zhu, L. & Wang, Q. Novel Ferroelectric Polymers for High Energy Density and Low Loss Dielectrics. *Macromolecules* **45**, 2937-2954 (2012). https://doi.org:10.1021/ma2024057
130 Zhu, L. Exploring Strategies for High Dielectric Constant and Low Loss Polymer Dielectrics. *The Journal of Physical Chemistry Letters* **5**, 3677-3687 (2014). https://doi.org:10.1021/jz501831q
131 Zha, J.-W., Zheng, M.-S., Fan, B.-H. & Dang, Z.-M. Polymer-based dielectrics with high permittivity for electric energy storage: A review. *Nano Energy* **89**, 106438 (2021). https://doi.org:https://doi.org/10.1016/j.nanoen.2021.106438
132 Sun, W., Mao, J., Wang, S., Zhang, L. & Cheng, Y. Review of recent advances of polymer based dielectrics for high-energy storage in electronic power devices from the perspective of target applications. *Frontiers of Chemical Science and Engineering* **15**, 18-34 (2021). https://doi.org:10.1007/s11705-020-1939-4
133 Dissado, L. in *Springer Handbook of Electronic and Photonic Materials* (eds Safa Kasap & Peter Capper) 187-212 (Springer US, 2007).
134 Ieda, M. Dielectric Breakdown Process of Polymers. *IEEE Transactions on Electrical Insulation* **EI-15**, 206-224 (1980). https://doi.org:10.1109/TEI.1980.298314
135 Zhao, L. A formula to calculate solid dielectric breakdown strength based on a model of electron impact ionization and multiplication. *AIP Advances* **10** (2020). https://doi.org:10.1063/1.5110271
136 Wang, C.-Y. *et al.* Dielectric Constant Enhancement and Leakage Current Suppression of Metal–Insulator–Metal Capacitors by Atomic Layer Annealing and the Capping Layer Effect Prepared with a Low Thermal Budget. *ACS Applied Electronic Materials* **5**, 2487-2494 (2023). https://doi.org:10.1021/acsaelm.2c01287
137 Liu, Y., Yao, M. & Yao, X. Excellent leakage current performance and energy storage density achieved in Zr-modified Sr0.925Bi0.05TiO3 thin film. *Materials Letters* **299**, 130083 (2021). https://doi.org:https://doi.org/10.1016/j.matlet.2021.130083
138 Nguyen, M. D., Birkhölzer, Y. A., Houwman, E. P., Koster, G. & Rijnders, G. Enhancing the Energy-Storage Density and Breakdown Strength in PbZrO3/Pb0.9La0.1Zr0.52Ti0.48O3-Derived Antiferroelectric/Relaxor-Ferroelectric Multilayers. *Advanced Energy Materials* **12**, 2200517 (2022). https://doi.org:https://doi.org/10.1002/aenm.202200517
139 Zhang, M. *et al.* High energy storage density and low energy loss achieved by inserting charge traps in all organic dielectric materials. *Journal of Materials Chemistry A* **10**, 16258-16267 (2022). https://doi.org:10.1039/D2TA03884F
140 Jian, G. *et al.* Enhanced dielectric constant and energy density in a BaTiO3/polymer-matrix composite sponge. *Communications Materials* **1**, 91 (2020). https://doi.org:10.1038/s43246-020-00092-0
141 Wu, X., Chen, X., Zhang, Q. M. & Tan, D. Q. Advanced dielectric polymers for energy storage. *Energy Storage Materials* **44**, 29-47 (2022).

https://doi.org:https://doi.org/10.1016/j.ensm.2021.10.010
142 Li, W. *et al.* Electric energy storage properties of poly(vinylidene fluoride). *Applied Physics Letters* **96** (2010). https://doi.org:10.1063/1.3428656
143 Xia, W. & Zhang, Z. PVDF-based dielectric polymers and their applications in electronic materials. *IET Nanodielectrics* **1**, 17-31 (2018). https://doi.org:https://doi.org/10.1049/iet-nde.2018.0001
144 Wei, J. *et al.* Achieving High Dielectric Constant and Low Loss Property in a Dipolar Glass Polymer Containing Strongly Dipolar and Small-Sized Sulfone Groups. *ACS Applied Materials & Interfaces* **7**, 5248-5257 (2015). https://doi.org:10.1021/am508488w
145 Thakur, V. K., Tan, E. J., Lin, M.-F. & Lee, P. S. Poly(vinylidene fluoride)-graft-poly(2-hydroxyethyl methacrylate): a novel material for high energy density capacitors. *Journal of Materials Chemistry* **21**, 3751-3759 (2011). https://doi.org:10.1039/C0JM02408B
146 Gu, L. *et al.* Effects of the Particle Size of $BaTiO_3$ Fillers on Fabrication and Dielectric Properties of $BaTiO_3$/Polymer/Al Films for Capacitor Energy-Storage Application. *Materials (Basel)* **12** (2019). https://doi.org:10.3390/ma12030439
147 Xie, B. *et al.* Enhanced energy density of polymer nanocomposites at a low electric field through aligned BaTiO3 nanowires. *Journal of Materials Chemistry A* **5**, 6070-6078 (2017). https://doi.org:10.1039/C7TA00513J
148 Haleem, N. M. & Rajapakse, A. D. Fault-Type Discrimination in HVDC Transmission Lines Using Rate of Change of Local Currents. *IEEE Transactions on Power Delivery* **35**, 117-129 (2020). https://doi.org:10.1109/TPWRD.2019.2922944
149 Zheng, M.-S. *et al.* Polyurethane induced high breakdown strength and high energy storage density in polyurethane/poly(vinylidene fluoride) composite films. *Applied Physics Letters* **110** (2017). https://doi.org:10.1063/1.4989579
150 Zheng, M.-S. *et al.* Enhanced breakdown strength of poly(vinylidene fluoride) utilizing rubber nanoparticles for energy storage application. *Applied Physics Letters* **109** (2016). https://doi.org:10.1063/1.4961252
151 Mason, W. P. & Baerwald, H. Piezoelectric Crystals and Their Applications to Ultrasonics. *Physics Today* **4**, 23-24 (1951). https://doi.org:10.1063/1.3067231
152 Curie, J. & Curie, P.
153 Maghsoudi Nia, E., Wan Abdullah Zawawi, N. A. & Mahinder Singh, B. S. Design of a pavement using piezoelectric materials. *Materialwissenschaft und Werkstofftechnik* **50**, 320-328 (2019). https://doi.org:https://doi.org/10.1002/mawe.201900002
154 Molinié, P. & Boudia, S. Mastering picocoulombs in the 1890s: The Curies' quartz–electrometer instrumentation, and how it shaped early radioactivity history. *Journal of Electrostatics* **67**, 524-530 (2009). https://doi.org:https://doi.org/10.1016/j.elstat.2009.01.031
155 Dye, D. W. The piezo-electric quartz resonator and its equivalent electrical circuit. *Proceedings of the Physical Society of London* **38**, 399 (1925). https://doi.org:10.1088/1478-7814/38/1/344
156 Trolier-McKinstry, S. in *Piezoelectric and Acoustic Materials for Transducer Applications* (eds Ahmad Safari & E. Koray Akdoğan) 39-56 (Springer US, 2008).
157 de Jong, M., Chen, W., Geerlings, H., Asta, M. & Persson, K. A. A database to enable discovery and design of piezoelectric materials. *Scientific Data* **2**, 150053 (2015). https://doi.org:10.1038/sdata.2015.53

158 Zou, W., Tang, C.-X. & Pan, E. Symmetry types of the piezoelectric tensor and their identification. *Proceedings of the Royal Society A: Mathematical, Physical and Engineering Sciences* **469** (2013).
159 Buroni, J. L. *et al.* Analytical expressions to estimate the effective piezoelectric tensor of a textured polycrystal for any crystal symmetry. *Mechanics of Materials* **151**, 103604 (2020). https://doi.org:https://doi.org/10.1016/j.mechmat.2020.103604
160 T, A. E. H. (1) Lehrbuch der Kristallphysik (mit Ausschluss der Kristalloptik) (2) Leçons de Cristallographie (3) Die Kristallgruppen nebst ihren Beziehungen zu den Raumgittern. *Nature* **86**, 544-546 (1911). https://doi.org:10.1038/086544a0
161 Li, Y., Zhan, Q., Bao, M., Yi, J. & Li, Y. Biomechanical and biological responses of periodontium in orthodontic tooth movement: up-date in a new decade. *International Journal of Oral Science* **13**, 20 (2021). https://doi.org:10.1038/s41368-021-00125-5
162 More, N. & Kapusetti, G. Piezoelectric material - A promising approach for bone and cartilage regeneration. *Med Hypotheses* **108**, 10-16 (2017). https://doi.org:10.1016/j.mehy.2017.07.021
163 Rajabi, A. H., Jaffe, M. & Arinzeh, T. L. Piezoelectric materials for tissue regeneration: A review. *Acta Biomater* **24**, 12-23 (2015). https://doi.org:10.1016/j.actbio.2015.07.010
164 Chen, Z. *et al.* Poling above the Curie temperature driven large enhancement in piezoelectric performance of Mn doped PZT-based piezoceramics. *Nano Energy* **113**, 108546 (2023). https://doi.org:https://doi.org/10.1016/j.nanoen.2023.108546
165 Habib, M. *et al.* Enhancement of Piezoelectricity by Novel Poling Method of the Rare-Earth Modified BiFeO3–BaTiO3 Lead-Free Ceramics. *Advanced Electronic Materials* **9**, 2201210 (2023). https://doi.org:https://doi.org/10.1002/aelm.202201210
166 Kiran, R., Kumar, A., Kumar, R. & Vaish, R. Poling direction driven large enhancement in piezoelectric performance. *Scripta Materialia* **151**, 76-81 (2018). https://doi.org:https://doi.org/10.1016/j.scriptamat.2018.03.029
167 Gao, X. *et al.* The mechanism for the enhanced piezoelectricity in multi-elements doped (K,Na)NbO3 ceramics. *Nature Communications* **12**, 881 (2021). https://doi.org:10.1038/s41467-021-21202-7
168 Yang, J. *et al.* Piezoelectric enhancement of an electrospun AlN-doped P(VDF-TrFE) nanofiber membrane. *Materials Chemistry Frontiers* **5**, 5679-5688 (2021). https://doi.org:10.1039/D1QM00550B
169 Feng, Z., Wang, K., Liu, Y., Han, B. & Yu, D.-G. Piezoelectric Enhancement of Piezoceramic Nanoparticle-Doped PVDF/PCL Core-Sheath Fibers. *Nanomaterials* **13**, 1243 (2023).
170 Wang, B., Li, F. & Chen, L.-Q. Inverse Domain-Size Dependence of Piezoelectricity in Ferroelectric Crystals. *Advanced Materials* **33**, 2105071 (2021). https://doi.org:https://doi.org/10.1002/adma.202105071
171 Ahluwalia, R., Lookman, T., Saxena, A. & Cao, W. Domain-size dependence of piezoelectric properties of ferroelectrics. *Physical Review B* **72**, 014112 (2005). https://doi.org:10.1103/PhysRevB.72.014112
172 Xie, L. *et al.* Controlling the domain size to enhance the piezoelectricity of BiFeO3–BaTiO3via heterovalent doping. *Journal of Materials Chemistry A* **10**, 22540-22550 (2022). https://doi.org:10.1039/D2TA06546K
173 Wang, W., Chen, Z., Zhou, Z., Li, Y. & Liang, R. Enhancing Electromechanical Properties of PZT-Based Piezoelectric Ceramics by High-Temperature Poling for High-Power Applications. *ACS Appl Mater Interfaces* **15**, 15636-15645 (2023).

https://doi.org:10.1021/acsami.2c19802
174 Kvasov, A. *et al.* Piezoelectric enhancement under negative pressure. *Nature Communications* **7**, 12136 (2016). https://doi.org:10.1038/ncomms12136
175 Ren, X. *et al.* Texture technique to achieve enhanced piezoelectric response in BiScO3–PbTiO3 high-temperature piezoelectric ceramics. *Journal of Materials Chemistry C* **11**, 13991-14001 (2023). https://doi.org:10.1039/D3TC02487C
176 Oladapo, B. I., Ismail, S. O., Kayode, J. F. & Ikumapayi, O. M. Piezoelectric effects on bone modeling for enhanced sustainability. *Materials Chemistry and Physics* **305**, 127960 (2023). https://doi.org:https://doi.org/10.1016/j.matchemphys.2023.127960
177 del Castillo, M. & Pérez, N. Machine Learning Identification of Piezoelectric Properties. *Materials* **14**, 2405 (2021).
178 Herzbach, D. & Müser, M. H. Piezoelectric coefficients by molecular dynamics simulations in the constant stress ensemble: A case study of quartz. *Computer Physics Communications* **174**, 17-23 (2006). https://doi.org:https://doi.org/10.1016/j.cpc.2005.07.012
179 Wang, Z. L. & Song, J. Piezoelectric Nanogenerators Based on Zinc Oxide Nanowire Arrays. *Science* **312**, 242-246 (2006). https://doi.org:doi:10.1126/science.1124005
180 Mahapatra, S. D. *et al.* Piezoelectric Materials for Energy Harvesting and Sensing Applications: Roadmap for Future Smart Materials. *Adv Sci (Weinh)* **8**, e2100864 (2021). https://doi.org:10.1002/advs.202100864
181 Covaci, C. & Gontean, A. Piezoelectric Energy Harvesting Solutions: A Review. *Sensors* **20**, 3512 (2020).
182 Li, T. & Lee, P. S. Piezoelectric Energy Harvesting Technology: From Materials, Structures, to Applications. *Small Structures* **3**, 2100128 (2022). https://doi.org:https://doi.org/10.1002/sstr.202100128
183 Tadaki, D. *et al.* Piezoelectric PVDF-based sensors with high pressure sensitivity induced by chemical modification of electrode surfaces. *Sensors and Actuators A: Physical* **316**, 112424 (2020). https://doi.org:https://doi.org/10.1016/j.sna.2020.112424
184 Nguyen, K., Bryant, M., Song, I.-H., You, B. H. & Khaleghian, S. The Application of PVDF-Based Piezoelectric Patches in Energy Harvesting from Tire Deformation. *Sensors* **22**, 9995 (2022).
185 Aabid, A., Hrairi, M., Mohamed Ali, S. J. & Ibrahim, Y. E. Review of Piezoelectric Actuator Applications in Damaged Structures: Challenges and Opportunities. *ACS Omega* **8**, 2844-2860 (2023). https://doi.org:10.1021/acsomega.2c06573
186 Gao, X. *et al.* Piezoelectric Actuators and Motors: Materials, Designs, and Applications. *Advanced Materials Technologies* **5**, 1900716 (2020). https://doi.org:https://doi.org/10.1002/admt.201900716
187 Izadgoshasb, I. Piezoelectric Energy Harvesting towards Self-Powered Internet of Things (IoT) Sensors in Smart Cities. *Sensors (Basel)* **21** (2021). https://doi.org:10.3390/s21248332
188 Xu, C., Song, Y., Han, M. & Zhang, H. Portable and wearable self-powered systems based on emerging energy harvesting technology. *Microsystems & Nanoengineering* **7**, 25 (2021). https://doi.org:10.1038/s41378-021-00248-z
189 Upendra, B., Panigrahi, B., Singh, K. & Sabareesh, G. Recent advancements in piezoelectric energy harvesting for implantable medical devices. *Journal of Intelligent Material Systems and Structures* **0**, 1045389X231200144 https://doi.org:10.1177/1045389x231200144

190 Lu, B. *et al.* Ultra-flexible Piezoelectric Devices Integrated with Heart to Harvest the Biomechanical Energy. *Scientific Reports* **5**, 16065 (2015). https://doi.org:10.1038/srep16065
191 Panda, S. *et al.* Piezoelectric energy harvesting systems for biomedical applications. *Nano Energy* **100**, 107514 (2022). https://doi.org:https://doi.org/10.1016/j.nanoen.2022.107514
192 Hossain, I. Z., Khan, A. & Hossain, G. A Piezoelectric Smart Textile for Energy Harvesting and Wearable Self-Powered Sensors. *Energies* **15**, 5541 (2022).
193 Liu, Y. *et al.* Piezoelectric energy harvesting for self-powered wearable upper limb applications. *Nano Select* **2**, 1459-1479 (2021). https://doi.org:https://doi.org/10.1002/nano.202000242
194 Zhou, H. *et al.* Stretchable piezoelectric energy harvesters and self-powered sensors for wearable and implantable devices. *Biosensors and Bioelectronics* **168**, 112569 (2020). https://doi.org:https://doi.org/10.1016/j.bios.2020.112569
195 Lang, S. B. Pyroelectric Effect in Bone and Tendon. *Nature* **212**, 704-705 (1966). https://doi.org:10.1038/212704a0
196 Focken, C. M. Behaviour of Pyroelectric Crystals. *Nature* **129**, 168-168 (1932). https://doi.org:10.1038/129168a0
197 Newnham, R. E. & Newnham, R. E. in *Properties of Materials: Anisotropy, Symmetry, Structure* 0 (Oxford University Press, 2004).
198 Zhou, Y. *et al.* Giant polarization ripple in transverse pyroelectricity. *Nature Communications* **14**, 426 (2023). https://doi.org:10.1038/s41467-023-35900-x
199 Cuadras, A., Gasulla, M. & Ferrari, V. Thermal energy harvesting through pyroelectricity. *Sensors and Actuators A: Physical* **158**, 132-139 (2010). https://doi.org:https://doi.org/10.1016/j.sna.2009.12.018
200 Yang, Y. *et al.* Flexible Pyroelectric Nanogenerators using a Composite Structure of Lead-Free KNbO3 Nanowires. *Advanced Materials* **24**, 5357-5362 (2012). https://doi.org:https://doi.org/10.1002/adma.201201414
201 Sadhukhan, P. *et al.* Manipulating electron redistribution to achieve electronic pyroelectricity in molecular [FeCo] crystals. *Nature Communications* **12**, 4836 (2021). https://doi.org:10.1038/s41467-021-25041-4
202 Zhao, J. *et al.* Enhanced temperature stability of compensated pyroelectric infrared detector based on Mn:PMN-PT single crystals. *Sensors and Actuators A: Physical* **327**, 112757 (2021). https://doi.org:https://doi.org/10.1016/j.sna.2021.112757
203 Shen, M. *et al.* High pyroelectric response over a broad temperature range in NBT-BZT: SiO2 composites for energy harvesting. *Journal of the European Ceramic Society* **41**, 3379-3386 (2021). https://doi.org:https://doi.org/10.1016/j.jeurceramsoc.2021.01.003
204 Stringfellow, S. B., Gupta, S., Shaw, C., Alcock, J. R. & Whatmore, R. W. Electrical conductivity control in uranium-doped PbZrO3–PbTiO3–Pb(Mg1/3Nb2/3)O3 pyroelectric ceramics. *Journal of the European Ceramic Society* **22**, 573-578 (2002). https://doi.org:https://doi.org/10.1016/S0955-2219(01)00316-8
205 Granzow, T. *et al.* Influence of Ce and Cr doping on the pyroelectric behaviour of Sr0.61Ba0.39Nb2O6. *physica status solidi (a)* **197**, R2-R4 (2003). https://doi.org:https://doi.org/10.1002/pssa.200309002
206 Dishon Ben Ami, S. *et al.* Engineering of Pyroelectric Crystals Decoupled from Piezoelectricity as Illustrated by Doped α-Glycine. *Angewandte Chemie International Edition* **61**, e202213955 (2022). https://doi.org:https://doi.org/10.1002/anie.202213955

207 Raibagkar, L. J. & Bajaj, S. B. Poling effect on the dielectric, pyroelectric and electrical conductivity of ferroelectric ordered–disordered Ba(Ni0.5Nb0.5)O3. *Solid State Ionics* **108**, 105-108 (1998). https://doi.org:https://doi.org/10.1016/S0167-2738(98)00026-5
208 Chen, L. *et al.* Enhancement of pyroelectric catalysis of ferroelectric BaTiO3 crystal: The action mechanism of electric poling. *Ceramics International* **46**, 16763-16769 (2020). https://doi.org:https://doi.org/10.1016/j.ceramint.2020.03.252
209 Kuznetsov, S. A., Paulish, A. G., Navarro-Cía, M. & Arzhannikov, A. V. Selective Pyroelectric Detection of Millimetre Waves Using Ultra-Thin Metasurface Absorbers. *Scientific Reports* **6**, 21079 (2016). https://doi.org:10.1038/srep21079
210 Tian, J. An overview of pyroelectric photodetector: Photoresponse mechanisms and applications. *AIP Advances* **13** (2023). https://doi.org:10.1063/5.0146279
211 Fang, J.-S. *et al.* Path-dependent human identification using a pyroelectric infrared sensor and Fresnel lens arrays. *Opt. Express* **14**, 609-624 (2006). https://doi.org:10.1364/OPEX.14.000609
212 Hu, X. *et al.* Real-time visualized battery health monitoring sensor with piezoelectric/pyroelectric poly (vinylidene fluoride-trifluoroethylene) and thin film transistor array by in-situ poling. *Journal of Power Sources* **467**, 228367 (2020). https://doi.org:https://doi.org/10.1016/j.jpowsour.2020.228367
213 He, J. *et al.* A non-contact flexible pyroelectric sensor for wireless physiological monitoring system. *Science China Information Sciences* **65**, 122402 (2021). https://doi.org:10.1007/s11432-020-3175-6
214 Thakre, A., Kumar, A., Song, H. C., Jeong, D. Y. & Ryu, J. Pyroelectric Energy Conversion and Its Applications-Flexible Energy Harvesters and Sensors. *Sensors (Basel)* **19** (2019). https://doi.org:10.3390/s19092170
215 Black, C. M. *et al.* A pyroelectric thermal imaging system for use in medical diagnosis. *J Biomed Eng* **12**, 281-286 (1990). https://doi.org:10.1016/0141-5425(90)90002-5
216 Black, C. M. *et al.* A pyroelectric thermal imaging system for use in medical diagnosis. *Journal of Biomedical Engineering* **12**, 281-286 (1990). https://doi.org:https://doi.org/10.1016/0141-5425(90)90002-5
217 Lheritier, P. *et al.* Large harvested energy with non-linear pyroelectric modules. *Nature* **609**, 718-721 (2022). https://doi.org:10.1038/s41586-022-05069-2
218 Thakre, A., Kumar, A., Song, H.-C., Jeong, D.-Y. & Ryu, J. Pyroelectric Energy Conversion and Its Applications—Flexible Energy Harvesters and Sensors. *Sensors* **19**, 2170 (2019).
219 Xue, H. *et al.* A wearable pyroelectric nanogenerator and self-powered breathing sensor. *Nano Energy* **38**, 147-154 (2017). https://doi.org:https://doi.org/10.1016/j.nanoen.2017.05.056
220 Ghosh, S. K. & Mandal, D. Envisioned strategy for an early intervention in virus-suspected patients through non-invasive piezo- and pyro-electric-based wearable sensors. *Journal of Materials Chemistry A* **9**, 1887-1909 (2021). https://doi.org:10.1039/D0TA08547B
221 Dawber, M., Rabe, K. M. & Scott, J. F. Physics of thin-film ferroelectric oxides. *Reviews of Modern Physics* **77**, 1083-1130 (2005). https://doi.org:10.1103/RevModPhys.77.1083
222 Scott, J. F. Applications of Modern Ferroelectrics. *Science* **315**, 954-959 (2007). https://doi.org:doi:10.1126/science.1129564
223 Li, W. *et al.* Emergence of ferroelectricity in a nonferroelectric monolayer. *Nature*

Communications **14**, 2757 (2023). https://doi.org:10.1038/s41467-023-38445-1
224 Sharma, P. *et al.* A room-temperature ferroelectric semimetal. *Science Advances* **5**, eaax5080 (2019). https://doi.org:doi:10.1126/sciadv.aax5080
225 Shi, P.-P. *et al.* Symmetry breaking in molecular ferroelectrics. *Chemical Society Reviews* **45**, 3811-3827 (2016). https://doi.org:10.1039/C5CS00308C
226 Boddu, V., Endres, F. & Steinmann, P. Molecular dynamics study of ferroelectric domain nucleation and domain switching dynamics. *Scientific Reports* **7**, 806 (2017). https://doi.org:10.1038/s41598-017-01002-0
227 Palneedi, H., Peddigari, M., Hwang, G.-T., Jeong, D.-Y. & Ryu, J. High-Performance Dielectric Ceramic Films for Energy Storage Capacitors: Progress and Outlook. *Advanced Functional Materials* **28**, 1803665 (2018). https://doi.org:https://doi.org/10.1002/adfm.201803665
228 Fei, Z. *et al.* Ferroelectric switching of a two-dimensional metal. *Nature* **560**, 336-339 (2018). https://doi.org:10.1038/s41586-018-0336-3
229 A century of ferroelectricity. *Nature Materials* **19**, 129-129 (2020). https://doi.org:10.1038/s41563-020-0611-1
230 Kliem, H. & Kuehn, M. Modeling the switching kinetics in ferroelectrics. *Journal of Applied Physics* **110** (2011). https://doi.org:10.1063/1.3660680
231 Lu, H. *et al.* Mechanical writing of ferroelectric polarization. *Science* **336**, 59-61 (2012). https://doi.org:10.1126/science.1218693
232 Zhao, D. *et al.* Depolarization of multidomain ferroelectric materials. *Nature Communications* **10**, 2547 (2019). https://doi.org:10.1038/s41467-019-10530-4
233 El Messiery, M. A., Hastings, G. W. & Rakowski, S. Ferro-electricity of dry cortical bone. *Journal of Biomedical Engineering* **1**, 63-65 (1979). https://doi.org:https://doi.org/10.1016/0141-5425(79)90013-X
234 Boldrini, P. Ferroelectricity in the arterial wall: A new physical component of atherosclerosis. *Journal of Theoretical Biology* **87**, 263-273 (1980). https://doi.org:https://doi.org/10.1016/0022-5193(80)90360-4
235 Liu, Y., Zhang, Y., Chow, M. J., Chen, Q. N. & Li, J. Biological ferroelectricity uncovered in aortic walls by piezoresponse force microscopy. *Phys Rev Lett* **108**, 078103 (2012). https://doi.org:10.1103/PhysRevLett.108.078103
236 Chen, W. *et al.* High-Polarizability Organic Ferroelectric Materials Doping for Enhancing the Built-In Electric Field of Perovskite Solar Cells Realizing Efficiency over 24%. *Advanced Materials* **34**, 2110482 (2022). https://doi.org:https://doi.org/10.1002/adma.202110482
237 Liang, J., Liu, M., Xu, X. & Liu, Z. A valuable strategy to improve ferroelectric performance significantly via metallic ion doping in the lattice nodes of metal–organic frameworks. *Chemical Communications* **57**, 2515-2518 (2021). https://doi.org:10.1039/D0CC08217A
238 Oh, S.-H. V., Hwang, W., Kim, K., Lee, J.-H. & Soon, A. Using Feature-Assisted Machine Learning Algorithms to Boost Polarity in Lead-Free Multicomponent Niobate Alloys for High-Performance Ferroelectrics. *Advanced Science* **9**, 2104569 (2022). https://doi.org:https://doi.org/10.1002/advs.202104569
239 Yun, Y. & Altman, E. I. Using Ferroelectric Poling to Change Adsorption on Oxide Surfaces. *Journal of the American Chemical Society* **129**, 15684-15689 (2007). https://doi.org:10.1021/ja0762644
240 Röhm, H., Leonhard, T., Hoffmann, M. J. & Colsmann, A. Ferroelectric Poling of

Methylammonium Lead Iodide Thin Films. *Advanced Functional Materials* **30**, 1908657 (2020). https://doi.org:https://doi.org/10.1002/adfm.201908657

241 Kim, K. D. *et al.* Ferroelectricity in undoped-HfO2 thin films induced by deposition temperature control during atomic layer deposition. *Journal of Materials Chemistry C* **4**, 6864-6872 (2016). https://doi.org:10.1039/C6TC02003H

242 Liu, J. *et al.* Bidirectional mechanical switching window in ferroelectric thin films predicted by first-principle-based simulations. *npj Computational Materials* **8**, 137 (2022). https://doi.org:10.1038/s41524-022-00829-0

243 Wang, J.-J., Wang, B. & Chen, L.-Q. Understanding, Predicting, and Designing Ferroelectric Domain Structures and Switching Guided by the Phase-Field Method. *Annual Review of Materials Research* **49**, 127-152 (2019). https://doi.org:10.1146/annurev-matsci-070218-121843

244 Dangić, Đ., Fahy, S. & Savić, I. Molecular dynamics simulation of the ferroelectric phase transition in GeTe: Displacive or order-disorder character. *Physical Review B* **106**, 134113 (2022). https://doi.org:10.1103/PhysRevB.106.134113

245 Sarott, M. F., Rossell, M. D., Fiebig, M. & Trassin, M. Multilevel polarization switching in ferroelectric thin films. *Nature Communications* **13**, 3159 (2022). https://doi.org:10.1038/s41467-022-30823-5

246 Sriboriboon, P. *et al.* Deep learning for exploring ultra-thin ferroelectrics with highly improved sensitivity of piezoresponse force microscopy. *npj Computational Materials* **9**, 28 (2023). https://doi.org:10.1038/s41524-023-00982-0

247 Xu, R., Karthik, J., Damodaran, A. R. & Martin, L. W. Stationary domain wall contribution to enhanced ferroelectric susceptibility. *Nature Communications* **5**, 3120 (2014). https://doi.org:10.1038/ncomms4120

248 Bein, B. *et al.* In situ X-ray diffraction and the evolution of polarization during the growth of ferroelectric superlattices. *Nature Communications* **6**, 10136 (2015). https://doi.org:10.1038/ncomms10136

249 Laanait, N., Saenrang, W., Zhou, H., Eom, C. B. & Zhang, Z. Dynamic X-ray diffraction imaging of the ferroelectric response in bismuth ferrite. *Adv Struct Chem Imaging* **3**, 11 (2017). https://doi.org:10.1186/s40679-017-0044-3

250 Chen, W. J. *et al.* Effect of Mechanical Loads on Stability of Nanodomains in Ferroelectric Ultrathin Films: Towards Flexible Erasing of the Non-Volatile Memories. *Scientific Reports* **4**, 5339 (2014). https://doi.org:10.1038/srep05339

251 Xue, F. *et al.* Optoelectronic Ferroelectric Domain-Wall Memories Made from a Single Van Der Waals Ferroelectric. *Advanced Functional Materials* **30**, 2004206 (2020). https://doi.org:https://doi.org/10.1002/adfm.202004206

252 Yao, D. *et al.* Energy-efficient non-volatile ferroelectric based electrostatic doping multilevel optical readout memory. *Opt. Express* **30**, 13572-13582 (2022). https://doi.org:10.1364/OE.456048

253 Anirban, A. Nanoscale laser writing of 3D ferroelectric domains in lithium niobate. *Nature Reviews Physics* **5**, 77-77 (2023). https://doi.org:10.1038/s42254-023-00560-9

254 Kim, J. Y., Choi, M.-J. & Jang, H. W. Ferroelectric field effect transistors: Progress and perspective. *APL Materials* **9** (2021). https://doi.org:10.1063/5.0035515

255 Wang, Z. X. *et al.* Domain memory effect in the organic ferroics. *Nat Commun* **13**, 2379 (2022). https://doi.org:10.1038/s41467-022-30085-1

256 Mao, D. *et al.* Ferroelectric random access memory based on one-transistor–one-capacitor structure for flexible electronics. *Organic Electronics* **14**, 505-510 (2013).

https://doi.org:https://doi.org/10.1016/j.orgel.2012.10.035
257 Wang, D., Hao, S., Dkhil, B., Tian, B. & Duan, C. Ferroelectric materials for neuroinspired computing applications. *Fundamental Research* (2023). https://doi.org:https://doi.org/10.1016/j.fmre.2023.04.013
258 Ishiwara, H. Ferroelectric random access memories. *J Nanosci Nanotechnol* **12**, 7619-7627 (2012). https://doi.org:10.1166/jnn.2012.6651
259 Yeh, C.-P., Lisker, M., Kalkofen, B. & Burte, E. P. Fabrication and investigation of three-dimensional ferroelectric capacitors for the application of FeRAM. *AIP Advances* **6** (2016). https://doi.org:10.1063/1.4945405
260 de Araujo, C. A. P., Solayappan, N., McMillan, L. D., Otsuki, T. & Arita, K. Process Integration of Embedded FeRAMs. *Journal of Electroceramics* **3**, 135-142 (1999). https://doi.org:10.1023/A:1009991026077
261 Aramberri, H., Fedorova, N. S. & Íñiguez, J. Ferroelectric/paraelectric superlattices for energy storage. *Science Advances* **8**, eabn4880 (2022). https://doi.org:doi:10.1126/sciadv.abn4880
262 Shkuratov, S. I. & Lynch, C. S. A review of ferroelectric materials for high power devices. *Journal of Materiomics* **8**, 739-752 (2022). https://doi.org:https://doi.org/10.1016/j.jmat.2022.04.002
263 Íñiguez, J., Zubko, P., Luk'yanchuk, I. & Cano, A. Ferroelectric negative capacitance. *Nature Reviews Materials* **4**, 243-256 (2019). https://doi.org:10.1038/s41578-019-0089-0
264 Wang, Y. *et al.* Bioinspired Amino Acid Based Materials in Bionanotechnology: From Minimalistic Building Blocks and Assembly Mechanism to Applications. *ACS Nano* **18**, 1257-1288 (2024). https://doi.org:10.1021/acsnano.3c08183
265 Min, B. J. A New Energy Ordering and the Dipole Moment of Gas Phase Glycine via Plane-Wave Density Functional Theory Calculations. *Journal of the Korean Physical Society* **72**, 676-680 (2018). https://doi.org:10.3938/jkps.72.676
266 Ramakrishnan, C. & Prasad, N. STUDY OF HYDROGEN BONDS IN AMINO ACIDS AND PEPTIDES*. *International Journal of Protein Research* **3**, 209-231 (1971). https://doi.org:https://doi.org/10.1111/j.1399-3011.1971.tb01714.x
267 Takashima, S. Computation of the dipole moment of protein molecules using protein databases.: Bacteriophage T4 lysozyme and its mutants. *Colloids and Surfaces A: Physicochemical and Engineering Aspects* **148**, 95-106 (1999). https://doi.org:https://doi.org/10.1016/S0927-7757(98)00556-1
268 Millefiori, S., Alparone, A., Millefiori, A. & Vanella, A. Electronic and vibrational polarizabilities of the twenty naturally occurring amino acids. *Biophysical Chemistry* **132**, 139-147 (2008). https://doi.org:https://doi.org/10.1016/j.bpc.2007.11.003
269 Lemanov, V. V. Piezoelectric and pyroelectric properties of protein amino acids as basic materials of Soft State Physics. *Ferroelectrics* **238**, 211-218 (2000). https://doi.org:10.1080/00150190008008786
270 Lemanov, V. V., Popov, S. N. & Pankova, G. A. Piezoelectricity in protein amino acids. *Physics of the Solid State* **53**, 1191-1193 (2011). https://doi.org:10.1134/S1063783411060205
271 Vasilescu, D., Cornillon, R. & Mallet, G. Piezoelectric Resonances in Amino-acids. *Nature* **225**, 635-635 (1970). https://doi.org:10.1038/225635a0
272 Lemanov, V. V., Popov, S. N. & Pankova, G. A. Piezoelectric properties of crystals of some protein aminoacids and their related compounds. *Physics of the Solid State* **44**,

1929-1935 (2002). https://doi.org:10.1134/1.1514783
273 Lemanov, V. V., Popov, S. N. & Pankova, G. A. Protein Amino Acid Crystals: Structure, Symmetry, Physical Properties. *Ferroelectrics* **285**, 207-216 (2003). https://doi.org:10.1080/00150190390206040
274 Pal, A. *et al.* Construction of Triboelectric Series and Chirality Detection of Amino Acids Using Triboelectric Nanogenerator. *Advanced Science* **11**, 2307266 (2024). https://doi.org:https://doi.org/10.1002/advs.202307266
275 Shoulders, M. D. & Raines, R. T. Collagen structure and stability. *Annu Rev Biochem* **78**, 929-958 (2009). https://doi.org:10.1146/annurev.biochem.77.032207.120833
276 Trębacz, H. & Barzycka, A. Mechanical Properties and Functions of Elastin: An Overview. *Biomolecules* **13** (2023). https://doi.org:10.3390/biom13030574
277 Liu, Y., Shao, Z. & Vollrath, F. Relationships between supercontraction and mechanical properties of spider silk. *Nature Materials* **4**, 901-905 (2005). https://doi.org:10.1038/nmat1534
278 Rodríguez, J. S. *et al.* Structural and Optoelectronic Properties of the α-, β-, and γ-Glycine Polymorphs and the Glycine Dihydrate Crystal: A DFT Study. *Crystal Growth & Design* **19**, 5204-5217 (2019). https://doi.org:10.1021/acs.cgd.9b00593
279 Srinivasan, K. Crystal growth of α and γ glycine polymorphs and their polymorphic phase transformations. *Journal of Crystal Growth* **311**, 156-162 (2008). https://doi.org:https://doi.org/10.1016/j.jcrysgro.2008.10.084
280 Sankar, S., Manikandan, M. R., Gopal Ram, S. D., Mahalingam, T. & Ravi, G. Gel growth of α and γ glycine and their characterization. *Journal of Crystal Growth* **312**, 2729-2733 (2010). https://doi.org:https://doi.org/10.1016/j.jcrysgro.2010.04.051
281 Albrecht, G. & Corey, R. B. The Crystal Structure of Glycine. *Journal of the American Chemical Society* **61**, 1087-1103 (1939). https://doi.org:10.1021/ja01874a028
282 Igarashi, K., Sasaki, Y., Azuma, M., Noda, H. & Ooshima, H. Control of Polymorphs on the Crystallization of Glycine Using a WWDJ Batch Crystallizer. *Engineering in Life Sciences* **3**, 159-163 (2003). https://doi.org:https://doi.org/10.1002/elsc.200390021
283 Perlovich, G. L., Hansen, L. K. & Bauer-Brandl, A. The Polymorphism of Glycine. Thermochemical and structural aspects. *Journal of Thermal Analysis and Calorimetry* **66**, 699-715 (2001). https://doi.org:10.1023/A:1013179702730
284 Bystrov, V. S. *et al.* Bioferroelectricity in Nanostructured Glycine and Thymine: Molecular Modeling and Ferroelectric Properties at the Nanoscale. *Ferroelectrics* **475**, 107-126 (2015). https://doi.org:10.1080/00150193.2015.995574
285 Zhang, Z. *et al.* Active self-assembly of piezoelectric biomolecular films via synergistic nanoconfinement and in-situ poling. *Nature Communications* **14**, 4094 (2023). https://doi.org:10.1038/s41467-023-39692-y
286 Heredia, A. *et al.* Nanoscale Ferroelectricity in Crystalline γ-Glycine. *Advanced Functional Materials* **22**, 2996-3003 (2012). https://doi.org:https://doi.org/10.1002/adfm.201103011
287 Tylczyński, Z. & Busz, P. Low-temperature phase transition in γ-glycine single crystal. Pyroelectric, piezoelectric, dielectric and elastic properties. *Materials Chemistry and Physics* **183**, 254-262 (2016). https://doi.org:https://doi.org/10.1016/j.matchemphys.2016.08.025
288 Hu, P. *et al.* Bioferroelectric Properties of Glycine Crystals. *The Journal of Physical Chemistry Letters* **10**, 1319-1324 (2019). https://doi.org:10.1021/acs.jpclett.8b03837
289 Zhu, C. *et al.* Characterizing hydrophobicity of amino acid side chains in a protein

environment via measuring contact angle of a water nanodroplet on planar peptide network. *Proceedings of the National Academy of Sciences* **113**, 12946-12951 (2016). https://doi.org:doi:10.1073/pnas.1616138113

290 Tulip, P. R. & Clark, S. J. Structural and electronic properties of L-amino acids. *Physical Review B* **71**, 195117 (2005). https://doi.org:10.1103/PhysRevB.71.195117

291 Tylczyński, Z., Sterczyńska, A. & Wiesner, M. Temperature dependences of piezoelectric, elastic and dielectric constants of L-alanine crystal. *Journal of Physics: Condensed Matter* **23**, 355901 (2011). https://doi.org:10.1088/0953-8984/23/35/355901

292 Yuan, H. *et al.* Rational Design of Biological Crystals with Enhanced Physical Properties by Hydrogen Bonding Interactions. *Research* **6**, 0046 (2023). https://doi.org:doi:10.34133/research.0046

293 Donnell, J. O. *et al.* Piezoelectricity in the proteinogenic amino acid L-leucine: A novel piezoactive bioelectret. *IEEE Transactions on Dielectrics and Electrical Insulation* **27**, 1465-1468 (2020). https://doi.org:10.1109/TDEI.2020.008908

294 Cheng, Y. *et al.* Boosting the Piezoelectric Sensitivity of Amino Acid Crystals by Mechanical Annealing for the Engineering of Fully Degradable Force Sensors. *Advanced Science* **10**, 2207269 (2023). https://doi.org:https://doi.org/10.1002/advs.202207269

295 Ji, W. *et al.* Rigid Tightly Packed Amino Acid Crystals as Functional Supramolecular Materials. *ACS Nano* **13**, 14477-14485 (2019). https://doi.org:10.1021/acsnano.9b08217

296 Guerin, S., Tofail, S. A. M. & Thompson, D. Longitudinal Piezoelectricity in Orthorhombic Amino Acid Crystal Films. *Crystal Growth & Design* **18**, 4844-4848 (2018). https://doi.org:10.1021/acs.cgd.8b00835

297 Kumar, R. & Bera, S. Recent approaches in development of bio-based artificial piezoelectric constructs for biomedical applications. *Giant* **17**, 100214 (2024). https://doi.org:https://doi.org/10.1016/j.giant.2023.100214

298 Mandal, I., Paul, S. & Venkatramani, R. Optical backbone-sidechain charge transfer transitions in proteins sensitive to secondary structure and modifications. *Faraday Discussions* **207**, 115-135 (2018). https://doi.org:10.1039/C7FD00203C

299 Yarmarkin, V. K., Shulman, S. G. & Lemanov, V. V. Pyroelectric Properties of Novel Protein Amino Acid-based Single Crystals. *Ferroelectrics* **348**, 118-123 (2007). https://doi.org:10.1080/00150190701196260

300 Mishuk, E., Weissbuch, I., Lahav, M. & Lubomirsky, I. Pyroelectricity in Nonpolar Directions in Crystals: Enantiomeric Disorder and Surface Wetting in Racemic α-Amino-Acids. *Crystal Growth & Design* **14**, 3839-3848 (2014). https://doi.org:10.1021/cg5003644

301 Yuan, H. *et al.* The engineering of molecular packing in amino acid crystals for the enhanced triboelectric effect. *Nano Energy* **110**, 108375 (2023). https://doi.org:https://doi.org/10.1016/j.nanoen.2023.108375

302 Ashok Kumar, R., Ezhil Vizhi, R., Vijayan, N. & Rajan Babu, D. Structural, dielectric and piezoelectric properties of nonlinear optical γ-glycine single crystals. *Physica B: Condensed Matter* **406**, 2594-2600 (2011). https://doi.org:https://doi.org/10.1016/j.physb.2011.04.001

303 Lemanov, V. V. Piezoelectric and pyroelectric properties of protein amino acids as basic materials of soft state physics. *Ferroelectrics* **238**, 775-782 (2000).

304 Guerin, S. Ab-Initio Predictions of the Energy Harvesting Performance of L-Arginine and L-Valine Single Crystals. *Frontiers in Mechanical Engineering-Switzerland* **7** (2021). https://doi.org:10.3389/fmech.2021.738446
305 Yuan, H. *et al.* Modified Stranski–Krastanov Growth of Amino Acid Arrays toward Piezoelectric Energy Harvesting. *ACS Applied Materials & Interfaces* **14**, 46304-46312 (2022). https://doi.org:10.1021/acsami.2c13399
306 O'Donnell, J. *et al.* Atomistic-Benchmarking towards a protocol development for rapid quantitative metrology of piezoelectric biomolecular materials. *Applied Materials Today* **21**, 100818 (2020). https://doi.org:https://doi.org/10.1016/j.apmt.2020.100818
307 Guerin, S. *et al.* Racemic Amino Acid Piezoelectric Transducer. *Physical Review Letters* **122**, 047701 (2019). https://doi.org:10.1103/PhysRevLett.122.047701
308 Shen, Y. *et al.* From Protein Building Blocks to Functional Materials. *ACS Nano* **15**, 5819-5837 (2021). https://doi.org:10.1021/acsnano.0c08510
309 Chen, J. & Zou, X. Self-assemble peptide biomaterials and their biomedical applications. *Bioactive Materials* **4**, 120-131 (2019). https://doi.org:https://doi.org/10.1016/j.bioactmat.2019.01.002
310 Zhang, S. Fabrication of novel biomaterials through molecular self-assembly. *Nature Biotechnology* **21**, 1171-1178 (2003). https://doi.org:10.1038/nbt874
311 Tao, K., Makam, P., Aizen, R. & Gazit, E. Self-assembling peptide semiconductors. *Science* **358**, eaam9756 (2017). https://doi.org:doi:10.1126/science.aam9756
312 Yuan, H. *et al.* Piezoelectric Peptide and Metabolite Materials. *Research (Wash D C)* **2019**, 9025939 (2019). https://doi.org:10.34133/2019/9025939
313 Kelly, C. M. *et al.* Conformational dynamics and aggregation behavior of piezoelectric diphenylalanine peptides in an external electric field. *Biophysical Chemistry* **196**, 16-24 (2015). https://doi.org:https://doi.org/10.1016/j.bpc.2014.08.009
314 Bera, S. *et al.* Rigid helical-like assemblies from a self-aggregating tripeptide. *Nat. Mater.* **18**, 503-509 (2019). https://doi.org:10.1038/s41563-019-0343-2
315 Yan, X., Zhu, P. & Li, J. Self-assembly and application of diphenylalanine-based nanostructures. *Chemical Society Reviews* **39**, 1877-1890 (2010). https://doi.org:10.1039/B915765B
316 Kholkin, A., Amdursky, N., Bdikin, I., Gazit, E. & Rosenman, G. Strong piezoelectricity in bioinspired peptide nanotubes. *ACS nano* **4**, 610-614 (2010). https://doi.org:10.1021/nn901327v
317 Heredia, A. *et al.* Temperature-driven phase transformation in self-assembled diphenylalanine peptide nanotubes. *Journal of Physics D: Applied Physics* **43**, 462001 (2010). https://doi.org:10.1088/0022-3727/43/46/462001
318 Reches, M. & Gazit, E. Casting metal nanowires within discrete self-assembled peptide nanotubes. *Science* **300**, 625-627 (2003). https://doi.org:10.1126/science.1082387
319 Amdursky, N. *et al.* Structural Transition in Peptide Nanotubes. *Biomacromolecules* **12**, 1349-1354 (2011). https://doi.org:10.1021/bm200117w
320 Görbitz, C. H. Nanotube Formation by Hydrophobic Dipeptides. *Chemistry – A European Journal* **7**, 5153-5159 (2001). https://doi.org:https://doi.org/10.1002/1521-3765(20011203)7:23<5153::AID-CHEM5153>3.0.CO;2-N
321 Gazit, E. A possible role for pi-stacking in the self-assembly of amyloid fibrils. *Faseb j* **16**, 77-83 (2002). https://doi.org:10.1096/fj.01-0442hyp
322 Vasilev, S. *et al.* Piezoelectric properties of diphenylalanine microtubes prepared from the solution. *Journal of Physics and Chemistry of Solids* **93**, 68-72 (2016).

https://doi.org:https://doi.org/10.1016/j.jpcs.2016.02.002
323 Nguyen, V., Zhu, R., Jenkins, K. & Yang, R. Self-assembly of diphenylalanine peptide with controlled polarization for power generation. *Nature Communications* **7**, 13566 (2016). https://doi.org:10.1038/ncomms13566
324 Su, Y. *et al.* Electric Field-Assisted Self-Assembly of Diphenylalanine Peptides for High-Performance Energy Conversion. *ACS Materials Letters* **5**, 2317-2323 (2023). https://doi.org:10.1021/acsmaterialslett.3c00664
325 Lee, J.-H. *et al.* Diphenylalanine Peptide Nanotube Energy Harvesters. *ACS Nano* **12**, 8138-8144 (2018). https://doi.org:10.1021/acsnano.8b03118
326 Park, H. *et al.* Self-assembly of unidirectionally polarized piezoelectric peptide nanotubes using environmentally friendly solvents. *Applied Surface Science* **618**, 156588 (2023). https://doi.org:https://doi.org/10.1016/j.apsusc.2023.156588
327 Tao, Z. *et al.* Diphenylalanine-based degradable piezoelectric nanogenerators enabled by polylactic acid polymer-assisted transfer. *Nano Energy* **88**, 106229 (2021). https://doi.org:https://doi.org/10.1016/j.nanoen.2021.106229
328 Jenkins, K., Kelly, S., Nguyen, V., Wu, Y. & Yang, R. Piezoelectric diphenylalanine peptide for greatly improved flexible nanogenerators. *Nano Energy* **51**, 317-323 (2018). https://doi.org:https://doi.org/10.1016/j.nanoen.2018.06.061
329 Bosne, E. D. *et al.* Piezoelectric resonators based on self-assembled diphenylalanine microtubes. *Applied Physics Letters* **102** (2013). https://doi.org:10.1063/1.4793417
330 Esin, A. *et al.* Pyroelectric effect and polarization instability in self-assembled diphenylalanine microtubes. *Applied Physics Letters* **109** (2016). https://doi.org:10.1063/1.4962652
331 Bdikin, I. *et al.* Polarization switching and patterning in self-assembled peptide tubular structures. *Journal of Applied Physics* **111** (2012). https://doi.org:10.1063/1.3699202
332 Bdikin, I. *et al.* Evidence of ferroelectricity and phase transition in pressed diphenylalanine peptide nanotubes. *Applied Physics Letters* **100** (2012). https://doi.org:10.1063/1.3676417
333 Bystrov, V. S. *et al.* BioFerroelectricity: Diphenylalanine Peptide Nanotubes Computational Modeling and Ferroelectric Properties at the Nanoscale. *Ferroelectrics* **440**, 3-24 (2012). https://doi.org:10.1080/00150193.2012.741923
334 Adler-Abramovich, L. *et al.* Self-assembled arrays of peptide nanotubes by vapour deposition. *Nature Nanotechnology* **4**, 849-854 (2009). https://doi.org:10.1038/nnano.2009.298
335 Jeon, J. & Shell, M. S. Self-Assembly of Cyclo-diphenylalanine Peptides in Vacuum. *The Journal of Physical Chemistry B* **118**, 6644-6652 (2014). https://doi.org:10.1021/jp501503x
336 Park, I. W. *et al.* Vertically aligned cyclo-phenylalanine peptide nanowire-based high-performance triboelectric energy generator. *Nano Energy* **57**, 737-745 (2019). https://doi.org:https://doi.org/10.1016/j.nanoen.2019.01.008
337 Liu, D. *et al.* Performance enhanced triboelectric nanogenerator by taking advantage of water in humid environments. *Nano Energy* **88**, 106303 (2021). https://doi.org:https://doi.org/10.1016/j.nanoen.2021.106303
338 Chang, T.-H. *et al.* Protein-based contact electrification and its uses for mechanical energy harvesting and humidity detecting. *Nano Energy* **21**, 238-246 (2016). https://doi.org:https://doi.org/10.1016/j.nanoen.2016.01.017
339 Wang, N., Zheng, Y., Feng, Y., Zhou, F. & Wang, D. Biofilm material based triboelectric

nanogenerator with high output performance in 95% humidity environment. *Nano Energy* **77**, 105088 (2020). https://doi.org:https://doi.org/10.1016/j.nanoen.2020.105088

340 Slabov, V. *et al.* Triboelectric Generator Based on Oriented Self-Assembled Peptide Microbelts. *Nanomaterials (Basel)* **12** (2022). https://doi.org:10.3390/nano12223955

341 Tayeb-Fligelman, E. *et al.* The cytotoxic Staphylococcus aureus PSMα3 reveals a cross-α amyloid-like fibril. *Science* **355**, 831-833 (2017). https://doi.org:10.1126/science.aaf4901

342 Nguyen, V., Jenkins, K. & Yang, R. Epitaxial growth of vertically aligned piezoelectric diphenylalanine peptide microrods with uniform polarization. *Nano Energy* **17**, 323-329 (2015). https://doi.org:https://doi.org/10.1016/j.nanoen.2015.08.020

343 Kim, Y. *et al.* Control of the Biodegradability of Piezoelectric Peptide Nanotubes Integrated with Hydrophobic Porphyrin. *ACS Applied Materials & Interfaces* **14**, 38778-38785 (2022). https://doi.org:10.1021/acsami.2c09751

344 Huggins, M. L. The Structure of Fibrous Proteins. *Chem. Rev.* **32**, 195-218 (1943). https://doi.org:10.1021/cr60102a002

345 van Raaij, M. J. & Mitraki, A. in *Proteins in Solution and at Interfaces* 219-232 (2013).

346 Ottani, V., Martini, D., Franchi, M., Ruggeri, A. & Raspanti, M. Hierarchical structures in fibrillar collagens. *Micron* **33**, 587-596 (2002). https://doi.org:https://doi.org/10.1016/S0968-4328(02)00033-1

347 Gautieri, A., Vesentini, S., Redaelli, A. & Buehler, M. J. Hierarchical Structure and Nanomechanics of Collagen Microfibrils from the Atomistic Scale Up. *Nano Letters* **11**, 757-766 (2011). https://doi.org:10.1021/nl103943u

348 Liu, X., Zheng, C., Luo, X., Wang, X. & Jiang, H. Recent advances of collagen-based biomaterials: Multi-hierarchical structure, modification and biomedical applications. *Materials Science and Engineering: C* **99**, 1509-1522 (2019). https://doi.org:https://doi.org/10.1016/j.msec.2019.02.070

349 Ramachandran, G. N. & Kartha, G. Structure of Collagen. *Nature* **176**, 593-595 (1955). https://doi.org:10.1038/176593a0

350 Brodsky, B. & Ramshaw, J. A. The collagen triple-helix structure. *Matrix Biol* **15**, 545-554 (1997). https://doi.org:10.1016/s0945-053x(97)90030-5

351 Brodsky, B. & Persikov, A. V. Molecular structure of the collagen triple helix. *Adv Protein Chem* **70**, 301-339 (2005). https://doi.org:10.1016/s0065-3233(05)70009-7

352 Minary-Jolandan, M. & Yu, M. F. Nanoscale characterization of isolated individual type I collagen fibrils: polarization and piezoelectricity. *Nanotechnology* **20**, 085706 (2009). https://doi.org:10.1088/0957-4484/20/8/085706

353 Kramer, R. Z., Bella, J., Mayville, P., Brodsky, B. & Berman, H. M. Sequence dependent conformational variations of collagen triple-helical structure. *Nature Structural Biology* **6**, 454-457 (1999). https://doi.org:10.1038/8259

354 Orgel, J. P., Irving, T. C., Miller, A. & Wess, T. J. Microfibrillar structure of type I collagen in situ. *Proc Natl Acad Sci U S A* **103**, 9001-9005 (2006). https://doi.org:10.1073/pnas.0502718103

355 Hulmes, D. J. S. & Miller, A. Quasi-hexagonal molecular packing in collagen fibrils. *Nature* **282**, 878-880 (1979). https://doi.org:10.1038/282878a0

356 Vivekananthan, V. *et al.* Biocompatible Collagen Nanofibrils: An Approach for Sustainable Energy Harvesting and Battery-Free Humidity Sensor Applications. *ACS*

Applied Materials & Interfaces **10**, 18650-18656 (2018). https://doi.org:10.1021/acsami.8b02915

357 Guzzi Plepis, A. M. D., Goissis, G. & Das-Gupta, D. K. Dielectric and pyroelectric characterization of anionic and native collagen. *Polymer Engineering & Science* **36**, 2932-2938 (1996). https://doi.org:https://doi.org/10.1002/pen.10694

358 Acosta, K. L., Srivastava, S., Wilkie, W. K. & Inman, D. J. Primary and secondary pyroelectric effects in macro-fiber composites. *Composites Part B: Engineering* **177**, 107275 (2019). https://doi.org:https://doi.org/10.1016/j.compositesb.2019.107275

359 Li, L. *et al.* Electrospun hydrolyzed collagen from tanned leather shavings for bio-triboelectric nanogenerators. *Materials Advances* **3**, 5080-5086 (2022). https://doi.org:10.1039/D2MA00457G

360 Kim, J., Koo, B.-K. & Knoblich, J. A. Human organoids: model systems for human biology and medicine. *Nature Reviews Molecular Cell Biology* **21**, 571-584 (2020). https://doi.org:10.1038/s41580-020-0259-3

361 Ben Amar, M., Nassoy, P. & LeGoff, L. Physics of growing biological tissues: the complex cross-talk between cell activity, growth and resistance. *Philos Trans A Math Phys Eng Sci* **377**, 20180070 (2019). https://doi.org:10.1098/rsta.2018.0070

362 Bandzerewicz, A. & Gadomska-Gajadhur, A. Into the Tissues: Extracellular Matrix and Its Artificial Substitutes: Cell Signalling Mechanisms. *Cells* **11** (2022). https://doi.org:10.3390/cells11050914

363 Hu, M., Ling, Z. & Ren, X. Extracellular matrix dynamics: tracking in biological systems and their implications. *Journal of Biological Engineering* **16**, 13 (2022). https://doi.org:10.1186/s13036-022-00292-x

364 Yeo, J. *et al.* Multiscale modeling of keratin, collagen, elastin and related human diseases: Perspectives from atomistic to coarse-grained molecular dynamics simulations. *Extreme Mech Lett* **20**, 112-124 (2018). https://doi.org:10.1016/j.eml.2018.01.009

365 Trębacz, H. & Barzycka, A. Mechanical Properties and Functions of Elastin: An Overview. *Biomolecules* **13**, 574 (2023).

366 Coenen, A. M. J., Bernaerts, K. V., Harings, J. A. W., Jockenhoevel, S. & Ghazanfari, S. Elastic materials for tissue engineering applications: Natural, synthetic, and hybrid polymers. *Acta Biomaterialia* **79**, 60-82 (2018). https://doi.org:https://doi.org/10.1016/j.actbio.2018.08.027

367 Mohammed, B., Bialkowski, K., Abbosh, A., Mills, P. C. & Bradley, A. P. Closed-form equation to estimate the dielectric properties of biological tissues as a function of age. *Bioelectromagnetics* **38**, 474-481 (2017). https://doi.org:https://doi.org/10.1002/bem.22054

368 Kim, D. *et al.* Biomolecular Piezoelectric Materials: From Amino Acids to Living Tissues. *Adv. Mater.* **32**, 1906989 (2020). https://doi.org:https://doi.org/10.1002/adma.201906989

369 Tofail, S. A. M. Pyroelectricity in Biological Materials and Biomaterials: A Five Decades Long Journey. *Ferroelectrics* **472**, 11-18 (2014). https://doi.org:10.1080/00150193.2014.964101

370 Bystrov, V. S., Seyedhosseini, E., Kopyl, S., Bdikin, I. K. & Kholkin, A. L. Piezoelectricity and ferroelectricity in biomaterials: Molecular modeling and piezoresponse force microscopy measurements. *J. Appl. Phys.* **116** (2014). https://doi.org:10.1063/1.4891443

371 Sun, Y., Zeng, K. & Li, T. Piezo-/ferroelectric phenomena in biomaterials: A brief review of recent progress and perspectives. *Science China Physics, Mechanics & Astronomy* **63**, 278701 (2020). https://doi.org:10.1007/s11433-019-1500-y
372 Fukada, E. & Yasuda, I. On the Piezoelectric Effect of Bone. *Journal of the Physical Society of Japan* **12**, 1158-1162 (1957). https://doi.org:10.1143/JPSJ.12.1158
373 Marino, A. A. & Gross, B. D. Piezoelectricity in cementum, dentine and bone. *Arch Oral Biol* **34**, 507-509 (1989). https://doi.org:10.1016/0003-9969(89)90087-3
374 Fukada, E. & Yasuda, I. Piezoelectric Effects in Collagen. *Japanese Journal of Applied Physics* **3**, 117 (1964). https://doi.org:10.1143/JJAP.3.117
375 Barbosa, F., Ferreira, F. C. & Silva, J. C. Piezoelectric Electrospun Fibrous Scaffolds for Bone, Articular Cartilage and Osteochondral Tissue Engineering. *Int J Mol Sci* **23** (2022). https://doi.org:10.3390/ijms23062907
376 Fukada, E. & Hara, K. Piezoelectric Effect in Blood Vessel Walls. *Journal of the Physical Society of Japan* **26**, 777-780 (1969). https://doi.org:10.1143/JPSJ.26.777
377 Ghosh, S. *et al.* Piezoelectric response of scleral collagen. *J Biomed Mater Res* **39**, 453-457 (1998). https://doi.org:10.1002/(sici)1097-4636(19980305)39:3<453::aid-jbm15>3.0.co;2-b
378 Athenstaedt, H., Claussen, H. & Schaper, D. Epidermis of Human Skin: Pyroelectric and Piezoelectric Sensor Layer. *Science* **216**, 1018-1020 (1982). https://doi.org:doi:10.1126/science.6177041
379 Lang, S. B., Marino, A. A., Berkovic, G., Fowler, M. & Abreo, K. D. Piezoelectricity in the human pineal gland. *Bioelectrochemistry and Bioenergetics* **41**, 191-195 (1996). https://doi.org:https://doi.org/10.1016/S0302-4598(96)05147-1
380 Marino, A. A., Becker, R. O. & Soderholm, S. C. Origin of the piezoelectric effect in bone. *Calcif Tissue Res* **8**, 177-180 (1971). https://doi.org:10.1007/bf02010135
381 Halperin, C. *et al.* Piezoelectric Effect in Human Bones Studied in Nanometer Scale. *Nano Letters* **4**, 1253-1256 (2004). https://doi.org:10.1021/nl049453i
382 Hastings, G. W. & Mahmud, F. A. Electrical effects in bone. *J Biomed Eng* **10**, 515-521 (1988). https://doi.org:10.1016/0141-5425(88)90109-4
383 Tandon, B., Blaker, J. J. & Cartmell, S. H. Piezoelectric materials as stimulatory biomedical materials and scaffolds for bone repair. *Acta Biomater* **73**, 1-20 (2018). https://doi.org:10.1016/j.actbio.2018.04.026
384 Ashrafi, M., Alonso-Rasgado, T., Baguneid, M. & Bayat, A. The efficacy of electrical stimulation in experimentally induced cutaneous wounds in animals. *Vet Dermatol* **27**, 235-e257 (2016). https://doi.org:10.1111/vde.12328
385 Rajabi, A. H., Jaffe, M. & Arinzeh, T. L. Piezoelectric materials for tissue regeneration: A review. *Acta Biomaterialia* **24**, 12-23 (2015). https://doi.org:https://doi.org/10.1016/j.actbio.2015.07.010
386 Lang, S. B. PYROELECTRIC EFFECT IN BONE AND TENDON. *Nature* **212**, 705-& (1966).
387 Athenstaedt, H. Permanent Longitudinal Electric Polarization and Pyroelectric Behaviour of Collagenous Structures and Nervous Tissue in Man and other Vertebrates. *Nature* **228**, 830-834 (1970). https://doi.org:10.1038/228830a0
388 Roetschi, H. New type of loop tracer for ferroelectrics. *Journal of Scientific Instruments* **39**, 152 (1962). https://doi.org:10.1088/0950-7671/39/4/304
389 Hastings, G. W., ElMessiery, M. A. & Rakowski, S. Mechano-electrical properties of bone. *Biomaterials* **2**, 225-233 (1981). https://doi.org:10.1016/0142-9612(81)90062-4

390 Liu, X. Y. *et al.* Strong correlation between early stage atherosclerosis and electromechanical coupling of aorta. *Nanoscale* **8**, 6975-6980 (2016). https://doi.org:10.1039/c5nr07398g
391 Liu, Y. *et al.* Glucose suppresses biological ferroelectricity in aortic elastin. *Phys Rev Lett* **110**, 168101 (2013). https://doi.org:10.1103/PhysRevLett.110.168101
392 Liyanage, L. *et al.* Multimodal Structural Analysis of the Human Aorta: From Valve to Bifurcation. *European Journal of Vascular and Endovascular Surgery* **63**, 721-730 (2022). https://doi.org:https://doi.org/10.1016/j.ejvs.2022.02.005
393 Marino, A. A. & Becker, R. O. Piezoelectricity in hydrated frozen bone and tendon. *Nature* **253**, 627-628 (1975). https://doi.org:10.1038/253627a0
394 Lenz, T. *et al.* Ferroelectricity and piezoelectricity in soft biological tissue: Porcine aortic walls revisited. *Applied Physics Letters* **111** (2017). https://doi.org:10.1063/1.4998228
395 Li, F., Jin, L., Xu, Z. & Zhang, S. Electrostrictive effect in ferroelectrics: An alternative approach to improve piezoelectricity. *Applied Physics Reviews* **1** (2014). https://doi.org:10.1063/1.4861260
396 Newnham, R. E., Sundar, V., Yimnirun, R., Su, J. & Zhang, Q. M. Electrostriction: Nonlinear Electromechanical Coupling in Solid Dielectrics. *The Journal of Physical Chemistry B* **101**, 10141-10150 (1997). https://doi.org:10.1021/jp971522c
397 Scott, J. F. Ferroelectrics go bananas. *Journal of Physics: Condensed Matter* **20**, 021001 (2008). https://doi.org:10.1088/0953-8984/20/02/021001
398 Reyes-Gasga, J. *et al.* Detection of the piezoelectricity effect in nanocrystals from human teeth. *Journal of Physics and Chemistry of Solids* **136**, 109140 (2020). https://doi.org:https://doi.org/10.1016/j.jpcs.2019.109140
399 Kalinin, S. V., Rodriguez, B. J., Jesse, S., Thundat, T. & Gruverman, A. Electromechanical imaging of biological systems with sub-10nm resolution. *Applied Physics Letters* **87** (2005). https://doi.org:10.1063/1.2006984
400 Athenstaedt, H. Pyroelectric and piezoelectric behaviour of human dental hard tissues. *Archives of Oral Biology* **16**, 495-501 (1971). https://doi.org:https://doi.org/10.1016/0003-9969(71)90194-4
401 Denning, D. *et al.* Piezoelectricity in collagen type II fibrils measured by scanning probe microscopy. *Journal of Applied Physics* **116** (2014). https://doi.org:10.1063/1.4891400
402 Góes, J. C., Figueiró, S. D., de Paiva, J. A. C. & Sombra, A. S. B. Piezoelectric and Dielectric Properties of Collagen Films. *physica status solidi (a)* **176**, 1077-1083 (1999). https://doi.org:https://doi.org/10.1002/(SICI)1521-396X(199912)176:2<1077::AID-PSSA1077>3.0.CO;2-F
403 Jiang, P. *et al.* Electromechanical Coupling of Murine Lung Tissues Probed by Piezoresponse Force Microscopy. *ACS Biomaterials Science & Engineering* **3**, 1827-1835 (2017). https://doi.org:10.1021/acsbiomaterials.7b00107
404 Rossi, D. D., Domenici, C. & Pastacaldi, P. Piezoelectric Properties of Dry Human Skin. *IEEE Transactions on Electrical Insulation* **EI-21**, 511-517 (1986). https://doi.org:10.1109/TEI.1986.349102
405 Ghosh, S. K., Park, J., Na, S., Kim, M. P. & Ko, H. A Fully Biodegradable Ferroelectric Skin Sensor from Edible Porcine Skin Gelatine. *Advanced Science* **8**, 2005010 (2021). https://doi.org:https://doi.org/10.1002/advs.202005010
406 Fukada, E. History and recent progress in piezoelectric polymers. *IEEE Transactions*

on Ultrasonics, Ferroelectrics, and Frequency Control **47**, 1277-1290 (2000). https://doi.org:10.1109/58.883516

407 Sarkar, L., Yelagala, B. P., Singh, S. G. & Vanjari, S. R. K. Electrodeposition as a facile way for the preparation of piezoelectric ultrathin silk film–based flexible nanogenerators. *International Journal of Energy Research* **46**, 3443-3457 (2022). https://doi.org:https://doi.org/10.1002/er.7393

408 Karan, S. K. *et al.* Nature driven spider silk as high energy conversion efficient bio-piezoelectric nanogenerator. *Nano Energy* **49**, 655-666 (2018). https://doi.org:https://doi.org/10.1016/j.nanoen.2018.05.014

409 Yucel, T., Cebe, P. & Kaplan, D. L. Structural Origins of Silk Piezoelectricity. *Advanced Functional Materials* **21**, 779-785 (2011). https://doi.org:https://doi.org/10.1002/adfm.201002077

410 Kim, H.-J. *et al.* Silk Nanofiber-Networked Bio-Triboelectric Generator: Silk Bio-TEG. *Advanced Energy Materials* **6**, 1502329 (2016). https://doi.org:https://doi.org/10.1002/aenm.201502329

411 Stapleton, A. *et al.* Converse piezoelectricity and ferroelectricity in crystals of lysozyme protein revealed by piezoresponse force microscopy. *Ferroelectrics* **525**, 135-145 (2018). https://doi.org:10.1080/00150193.2018.1432825

412 Stapleton, A. *et al.* Pyroelectricity in globular protein lysozyme films. *J. Appl. Phys.* **123**, 5 (2018). https://doi.org:10.1063/1.5014029

413 Loebenstein, G. Native Protein, an Immunizing Agent against Virus Infection. *Nature* **185**, 122-123 (1960). https://doi.org:10.1038/185122a0

414 Lytras, S., Xia, W., Hughes, J., Jiang, X. & Robertson, D. L. The animal origin of SARS-CoV-2. *Science* **373**, 968-970 (2021). https://doi.org:doi:10.1126/science.abh0117

415 Sampath, S. *et al.* Pandemics Throughout the History. *Cureus* **13**, e18136 (2021). https://doi.org:10.7759/cureus.18136

416 Radiom, M. *et al.* Mechanical tuning of virus-like particles. *Journal of Colloid and Interface Science* **634**, 963-971 (2023). https://doi.org:https://doi.org/10.1016/j.jcis.2022.12.090

417 Chan, V. S. Use of genetically modified viruses and genetically engineered virus-vector vaccines: environmental effects. *J Toxicol Environ Health A* **69**, 1971-1977 (2006). https://doi.org:10.1080/15287390600751405

418 Zandi, R., Reguera, D., Bruinsma, R. F., Gelbart, W. M. & Rudnick, J. Origin of icosahedral symmetry in viruses. *Proceedings of the National Academy of Sciences* **101**, 15556-15560 (2004). https://doi.org:doi:10.1073/pnas.0405844101

419 Horne, R. W. & Wildy, P. Symmetry in virus architecture. *Virology* **15**, 348-373 (1961). https://doi.org:https://doi.org/10.1016/0042-6822(61)90366-X

420 Chaudhari, H. V., Inamdar, M. M. & Kondabagil, K. Scaling relation between genome length and particle size of viruses provides insights into viral life history. *iScience* **24**, 102452 (2021). https://doi.org:https://doi.org/10.1016/j.isci.2021.102452

421 Cao, C. *et al.* The architecture of the SARS-CoV-2 RNA genome inside virion. *Nature Communications* **12**, 3917 (2021). https://doi.org:10.1038/s41467-021-22785-x

422 Dadonaite, B. *et al.* The structure of the influenza A virus genome. *Nature Microbiology* **4**, 1781-1789 (2019). https://doi.org:10.1038/s41564-019-0513-7

423 Jia, Q. & Xiang, Y. Cryo-EM structure of a bacteriophage M13 mini variant. *Nature Communications* **14**, 5421 (2023). https://doi.org:10.1038/s41467-023-41151-7

424 Butler, P. J. Self-assembly of tobacco mosaic virus: the role of an intermediate aggregate in generating both specificity and speed. *Philos Trans R Soc Lond B Biol Sci* **354**, 537-550 (1999). https://doi.org:10.1098/rstb.1999.0405
425 Calder, L. J., Wasilewski, S., Berriman, J. A. & Rosenthal, P. B. Structural organization of a filamentous influenza A virus. *Proceedings of the National Academy of Sciences* **107**, 10685-10690 (2010). https://doi.org:doi:10.1073/pnas.1002123107
426 Speir, J. A., Munshi, S., Wang, G., Baker, T. S. & Johnson, J. E. Structures of the native and swollen forms of cowpea chlorotic mottle virus determined by X-ray crystallography and cryo-electron microscopy. *Structure* **3**, 63-78 (1995). https://doi.org:10.1016/s0969-2126(01)00135-6
427 Gallardo, J., Pérez-Illana, M., Martín-González, N. & San Martín, C. Adenovirus Structure: What Is New? *Int J Mol Sci* **22** (2021). https://doi.org:10.3390/ijms22105240
428 Connolly, S. A., Jardetzky, T. S. & Longnecker, R. The structural basis of herpesvirus entry. *Nat Rev Microbiol* **19**, 110-121 (2021). https://doi.org:10.1038/s41579-020-00448-w
429 Schoeman, D. & Fielding, B. C. Coronavirus envelope protein: current knowledge. *Virol J* **16**, 69 (2019). https://doi.org:10.1186/s12985-019-1182-0
430 Chai, J. *et al.* Structural basis for SARS-CoV-2 envelope protein recognition of human cell junction protein PALS1. *Nature Communications* **12**, 3433 (2021). https://doi.org:10.1038/s41467-021-23533-x
431 Klenk, H.-D., Rott, R. & Becht, H. On the structure of the influenza virus envelope. *Virology* **47**, 579-591 (1972). https://doi.org:https://doi.org/10.1016/0042-6822(72)90547-8
432 Zolla-Pazner, S. & Cardozo, T. Structure–function relationships of HIV-1 envelope sequence-variable regions refocus vaccine design. *Nature Reviews Immunology* **10**, 527-535 (2010). https://doi.org:10.1038/nri2801
433 Zhu, P. *et al.* Distribution and three-dimensional structure of AIDS virus envelope spikes. *Nature* **441**, 847-852 (2006). https://doi.org:10.1038/nature04817
434 Dai, L. *et al.* Structures of the Zika Virus Envelope Protein and Its Complex with a Flavivirus Broadly Protective Antibody. *Cell Host Microbe* **19**, 696-704 (2016). https://doi.org:10.1016/j.chom.2016.04.013
435 Tan, T. Y. *et al.* Capsid protein structure in Zika virus reveals the flavivirus assembly process. *Nature Communications* **11**, 895 (2020). https://doi.org:10.1038/s41467-020-14647-9
436 Cuervo, A. *et al.* Structures of T7 bacteriophage portal and tail suggest a viral DNA retention and ejection mechanism. *Nature Communications* **10**, 3746 (2019). https://doi.org:10.1038/s41467-019-11705-9
437 Su, H.-P. *et al.* The 1.51-Å structure of the poxvirus L1 protein, a target of potent neutralizing antibodies. *Proceedings of the National Academy of Sciences* **102**, 4240-4245 (2005). https://doi.org:doi:10.1073/pnas.0501103102
438 Fondong, V. N. Geminivirus protein structure and function. *Mol Plant Pathol* **14**, 635-649 (2013). https://doi.org:10.1111/mpp.12032
439 Hesketh, E. L. *et al.* The 3.3 Å structure of a plant geminivirus using cryo-EM. *Nature Communications* **9**, 2369 (2018). https://doi.org:10.1038/s41467-018-04793-6
440 Jiang, W. & Tang, L. Atomic cryo-EM structures of viruses. *Curr Opin Struct Biol* **46**, 122-129 (2017). https://doi.org:10.1016/j.sbi.2017.07.002
441 Klein, S. *et al.* SARS-CoV-2 structure and replication characterized by in situ cryo-

electron tomography. *Nature Communications* **11**, 5885 (2020). https://doi.org:10.1038/s41467-020-19619-7

442 Ortega-Esteban, Á. *et al.* Cryo-electron Microscopy Structure, Assembly, and Mechanics Show Morphogenesis and Evolution of Human Picobirnavirus. *J Virol* **94** (2020). https://doi.org:10.1128/jvi.01542-20

443 MacCuspie, R. I., Nuraje, N., Lee, S. Y., Runge, A. & Matsui, H. Comparison of electrical properties of viruses studied by AC capacitance scanning probe microscopy. *J Am Chem Soc* **130**, 887-891 (2008). https://doi.org:10.1021/ja075244z

444 Passaretti, P., Sun, Y., Dafforn, T. R. & Oppenheimer, P. G. Determination and characterisation of the surface charge properties of the bacteriophage M13 to assist bio-nanoengineering. *RSC Advances* **10**, 25385-25392 (2020). https://doi.org:10.1039/D0RA04086J

445 Fantini, J., Azzaz, F., Chahinian, H. & Yahi, N. Electrostatic Surface Potential as a Key Parameter in Virus Transmission and Evolution: How to Manage Future Virus Pandemics in the Post-COVID-19 Era. *Viruses* **15** (2023). https://doi.org:10.3390/v15020284

446 Fedorov, V. *et al.* Electrostatic Map of the SARS-CoV-2 Virion Specifies Binding Sites of the Antiviral Cationic Photosensitizer. *Int J Mol Sci* **23** (2022). https://doi.org:10.3390/ijms23137304

447 Philippe, N., Shukla, A., Abergel, C. & Bisio, H. Genetic manipulation of giant viruses and their host, Acanthamoeba castellanii. *Nature Protocols* (2023). https://doi.org:10.1038/s41596-023-00910-y

448 Mateu, M. G. Virus engineering: functionalization and stabilization. *Protein Engineering, Design and Selection* **24**, 53-63 (2010). https://doi.org:10.1093/protein/gzq069

449 Kim, D. Y. *et al.* Enhancement of protein expression by alphavirus replicons by designing self-replicating subgenomic RNAs. *Proceedings of the National Academy of Sciences* **111**, 10708-10713 (2014). https://doi.org:doi:10.1073/pnas.1408677111

450 Varanda, C., Félix, M. D. R., Campos, M. D. & Materatski, P. An Overview of the Application of Viruses to Biotechnology. *Viruses* **13** (2021). https://doi.org:10.3390/v13102073

451 Lico, C., Chen, Q. & Santi, L. Viral vectors for production of recombinant proteins in plants. *Journal of Cellular Physiology* **216**, 366-377 (2008). https://doi.org:https://doi.org/10.1002/jcp.21423

452 Wu, Y., Liu, G. & Carstens, E. B. Replication, integration, and packaging of plasmid DNA following cotransfection with baculovirus viral DNA. *J Virol* **73**, 5473-5480 (1999). https://doi.org:10.1128/jvi.73.7.5473-5480.1999

453 Dovrolis, N. *et al.* ZWA: Viral genome assembly and characterization hindrances from virus-host chimeric reads; a refining approach. *PLoS Comput Biol* **17**, e1009304 (2021). https://doi.org:10.1371/journal.pcbi.1009304

454 Thi Nhu Thao, T. *et al.* Rapid reconstruction of SARS-CoV-2 using a synthetic genomics platform. *Nature* **582**, 561-565 (2020). https://doi.org:10.1038/s41586-020-2294-9

455 Rosano, G. L., Morales, E. S. & Ceccarelli, E. A. New tools for recombinant protein production in Escherichia coli: A 5-year update. *Protein Science* **28**, 1412-1422 (2019). https://doi.org:https://doi.org/10.1002/pro.3668

456 Chen, X. & Gonçalves, M. A. Engineered Viruses as Genome Editing Devices. *Mol*

Ther **24**, 447-457 (2016). https://doi.org:10.1038/mt.2015.164
457 Zhu, J. *et al.* Design of bacteriophage T4-based artificial viral vectors for human genome remodeling. *Nature Communications* **14**, 2928 (2023). https://doi.org:10.1038/s41467-023-38364-1
458 van Aken, J. & Hammond, E. Genetic engineering and biological weapons. New technologies, desires and threats from biological research. *EMBO Rep* **4 Spec No**, S57-60 (2003). https://doi.org:10.1038/sj.embor.embor860
459 Giese, B. The viral era: New biotechnologies give humans an unprecedented control over Nature and require appropriate safeguards. *EMBO Rep* **22**, e53229 (2021). https://doi.org:10.15252/embr.202153229
460 Smith, G. P. & Petrenko, V. A. Phage Display. *Chemical Reviews* **97**, 391-410 (1997). https://doi.org:10.1021/cr960065d
461 Lee, J. H. *et al.* Production of tunable nanomaterials using hierarchically assembled bacteriophages. *Nature Protocols* **12**, 1999-2013 (2017). https://doi.org:10.1038/nprot.2017.085
462 Chung, W.-J. *et al.* Biomimetic self-templating supramolecular structures. *Nature* **478**, 364-368 (2011). https://doi.org:10.1038/nature10513
463 Wang, R. *et al.* M13 phage: a versatile building block for a highly specific analysis platform. *Analytical and Bioanalytical Chemistry* **415**, 3927-3944 (2023). https://doi.org:10.1007/s00216-023-04606-w
464 Kim, W.-G. *et al.* Experimental and numerical evaluation of a genetically engineered M13 bacteriophage with high sensitivity and selectivity for 2,4,6-trinitrotoluene. *Organic & Biomolecular Chemistry* **17**, 5666-5670 (2019). https://doi.org:10.1039/C8OB03075H
465 Jaworski, J. W., Raorane, D., Huh, J. H., Majumdar, A. & Lee, S. W. Evolutionary screening of biomimetic coatings for selective detection of explosives. *Langmuir* **24**, 4938-4943 (2008). https://doi.org:10.1021/la7035289
466 Heo, K. *et al.* Transient self-templating assembly of M13 bacteriophage for enhanced biopiezoelectric devices. *Nano Energy* **56**, 716-723 (2019). https://doi.org:https://doi.org/10.1016/j.nanoen.2018.11.084
467 Oh, D. *et al.* M13 Virus-Directed Synthesis of Nanostructured Metal Oxides for Lithium–Oxygen Batteries. *Nano Letters* **14**, 4837-4845 (2014). https://doi.org:10.1021/nl502078m
468 Lee, Y. J. *et al.* Fabricating Genetically Engineered High-Power Lithium-Ion Batteries Using Multiple Virus Genes. *Science* **324**, 1051-1055 (2009). https://doi.org:doi:10.1126/science.1171541
469 Nam, K. T. *et al.* Virus-Enabled Synthesis and Assembly of Nanowires for Lithium Ion Battery Electrodes. *Science* **312**, 885-888 (2006). https://doi.org:doi:10.1126/science.1122716
470 Oh, D. *et al.* Graphene Sheets Stabilized on Genetically Engineered M13 Viral Templates as Conducting Frameworks for Hybrid Energy-Storage Materials. *Small* **8**, 1006-1011 (2012). https://doi.org:https://doi.org/10.1002/smll.201102036
471 Lee, Y. M. *et al.* Highly Interconnected Porous Electrodes for Dye-Sensitized Solar Cells Using Viruses as a Sacrificial Template. *Advanced Functional Materials* **21**, 1160-1167 (2011). https://doi.org:https://doi.org/10.1002/adfm.201001774
472 Dang, X. *et al.* Virus-templated self-assembled single-walled carbon nanotubes for highly efficient electron collection in photovoltaic devices. *Nature Nanotechnology* **6**,

377-384 (2011). https://doi.org:10.1038/nnano.2011.50
473 Lin, H.-S. *et al.* Denatured M13 Bacteriophage-Templated Perovskite Solar Cells Exhibiting High Efficiency. *Advanced Science* **7**, 2000782 (2020). https://doi.org:https://doi.org/10.1002/advs.202000782
474 Han, J. *et al.* Genetic Manipulation of M13 Bacteriophage for Enhancing the Efficiency of Virus-Inoculated Perovskite Solar Cells with a Certified Efficiency of 22.3%. *Advanced Energy Materials* **11**, 2101221 (2021). https://doi.org:https://doi.org/10.1002/aenm.202101221
475 Plank, J. M. *et al.* Bifunctional M13 Bacteriophage Nanospheroids for the Synthesis of Hybrid Noncentrosymmetric Nanoparticles. *ACS Applied Nano Materials* **3**, 10668-10677 (2020). https://doi.org:10.1021/acsanm.0c01876
476 Janczuk-Richter, M., Marinović, I., Niedziółka-Jönsson, J. & Szot-Karpińska, K. Recent applications of bacteriophage-based electrodes: A mini-review. *Electrochemistry Communications* **99**, 11-15 (2019). https://doi.org:https://doi.org/10.1016/j.elecom.2018.12.011
477 Kim, I., Moon, J. S. & Oh, J. W. Recent advances in M13 bacteriophage-based optical sensing applications. *Nano Converg* **3**, 27 (2016). https://doi.org:10.1186/s40580-016-0087-5
478 Chang, C. *et al.* Engineered M13 phage as a novel therapeutic bionanomaterial for clinical applications: From tissue regeneration to cancer therapy. *Mater Today Bio* **20**, 100612 (2023). https://doi.org:10.1016/j.mtbio.2023.100612
479 Park, I. W. *et al.* Recent Developments and Prospects of M13- Bacteriophage Based Piezoelectric Energy Harvesting Devices. *Nanomaterials (Basel)* **10** (2020). https://doi.org:10.3390/nano10010093
480 Lee, Y. *et al.* Virus-templated Au and Au–Pt core–shell nanowires and their electrocatalytic activities for fuel cell applications. *Energy & Environmental Science* **5**, 8328-8334 (2012). https://doi.org:10.1039/C2EE21156D
481 Blaik, R. A., Lan, E., Huang, Y. & Dunn, B. Gold-Coated M13 Bacteriophage as a Template for Glucose Oxidase Biofuel Cells with Direct Electron Transfer. *ACS Nano* **10**, 324-332 (2016). https://doi.org:10.1021/acsnano.5b04580
482 Jin, H.-E. & Lee, S.-W. in *Virus-Derived Nanoparticles for Advanced Technologies: Methods and Protocols* (eds Christina Wege & George P. Lomonossoff) 487-502 (Springer New York, 2018).
483 Luque, D. & Castón, J. R. Cryo-electron microscopy for the study of virus assembly. *Nature Chemical Biology* **16**, 231-239 (2020). https://doi.org:10.1038/s41589-020-0477-1
484 Yang, S. H., Chung, W.-J., McFarland, S. & Lee, S.-W. Assembly of Bacteriophage into Functional Materials. *The Chemical Record* **13**, 43-59 (2013). https://doi.org:https://doi.org/10.1002/tcr.201200012
485 Passaretti, P., Khan, I., Dafforn, T. R. & Goldberg Oppenheimer, P. Improvements in the production of purified M13 bacteriophage bio-nanoparticle. *Scientific Reports* **10**, 18538 (2020). https://doi.org:10.1038/s41598-020-75205-3
486 Oh, J.-W. *et al.* Biomimetic virus-based colourimetric sensors. *Nature Communications* **5**, 3043 (2014). https://doi.org:10.1038/ncomms4043
487 Lee, J. H. *et al.* Phage-Based Structural Color Sensors and Their Pattern Recognition Sensing System. *ACS Nano* **11**, 3632-3641 (2017). https://doi.org:10.1021/acsnano.6b07942

488 Moon, J. S. *et al.* M13 Bacteriophage-Based Self-Assembly Structures and Their Functional Capabilities. *Mini Rev Org Chem* **12**, 271-281 (2015). https://doi.org:10.2174/1570193x1203150429105418
489 Kadiri, V. M. *et al.* Genetically Modified M13 Bacteriophage Nanonets for Enzyme Catalysis and Recovery. *Catalysts* **9**, 723 (2019).
490 Tian, L. *et al.* Self-assembling nanofibrous bacteriophage microgels as sprayable antimicrobials targeting multidrug-resistant bacteria. *Nature Communications* **13**, 7158 (2022). https://doi.org:10.1038/s41467-022-34803-7
491 Chung, W. J., Lee, D. Y. & Yoo, S. Y. Chemical modulation of M13 bacteriophage and its functional opportunities for nanomedicine. *Int J Nanomedicine* **9**, 5825-5836 (2014). https://doi.org:10.2147/ijn.S73883
492 Li, J., Liu, Y., Zhang, Y., Cai, H. L. & Xiong, R. G. Molecular ferroelectrics: where electronics meet biology. *Phys Chem Chem Phys* **15**, 20786-20796 (2013). https://doi.org:10.1039/c3cp52501e
493 Saini, M., Singh, Y., Arora, P., Arora, V. & Jain, K. Implant biomaterials: A comprehensive review. *World J Clin Cases* **3**, 52-57 (2015). https://doi.org:10.12998/wjcc.v3.i1.52
494 Liu, H., Ge, J., Ma, E. & Yang, L. in *Biomaterials in Translational Medicine* (eds Lei Yang, Sarit B. Bhaduri, & Thomas J. Webster) 213-255 (Academic Press, 2019).
495 Gonçalves, I. M. *et al.* Recent trends of biomaterials and biosensors for organ-on-chip platforms. *Bioprinting* **26**, e00202 (2022). https://doi.org:https://doi.org/10.1016/j.bprint.2022.e00202
496 Shin, D. M., Hong, S. W. & Hwang, Y. H. Recent Advances in Organic Piezoelectric Biomaterials for Energy and Biomedical Applications. *Nanomaterials (Basel)* **10** (2020). https://doi.org:10.3390/nano10010123
497 Song, K. Y. *et al.* Recent progress on nature-derived biomaterials for eco-friendly triboelectric nanogenerators. *EcoMat* **5**, e12357 (2023). https://doi.org:https://doi.org/10.1002/eom2.12357
498 Slabov, V., Kopyl, S., Soares dos Santos, M. P. & Kholkin, A. L. Natural and Eco-Friendly Materials for Triboelectric Energy Harvesting. *Nano-Micro Letters* **12**, 42 (2020). https://doi.org:10.1007/s40820-020-0373-y
499 Lemanov, V. V. in *Piezoelectric Materials: Advances in Science, Technology and Applications* (eds Carmen Galassi, Maria Dinescu, Kenji Uchino, & Michael Sayer) 1-9 (Springer Netherlands, 2000).
500 Zhen, Z., Zheng, Y., Ge, Z., Lai, C. & Xi, T. Biological effect and molecular mechanism study of biomaterials based on proteomic research. *Journal of Materials Science & Technology* **33**, 607-615 (2017). https://doi.org:https://doi.org/10.1016/j.jmst.2017.01.001
501 Xie, W. *et al.* Static and Dynamic: Evolving Biomaterial Mechanical Properties to Control Cellular Mechanotransduction. *Advanced Science* **10**, 2204594 (2023). https://doi.org:https://doi.org/10.1002/advs.202204594
502 Williams-Noonan, B. J., Kamboukos, A., Todorova, N. & Yarovsky, I. Self-assembling peptide biomaterials: Insights from spontaneous and enhanced sampling molecular dynamics simulations. *Chemical Physics Reviews* **4** (2023). https://doi.org:10.1063/5.0142302
503 Yuan, X. *et al.* Piezoelectricity, Pyroelectricity, and Ferroelectricity in Biomaterials and Biomedical Applications. *Advanced Materials* **n/a**, 2308726

https://doi.org:https://doi.org/10.1002/adma.202308726
504 Wang, W., Li, J., Liu, H. & Ge, S. Advancing Versatile Ferroelectric Materials Toward Biomedical Applications. *Adv Sci (Weinh)* **8**, 2003074 (2020). https://doi.org:10.1002/advs.202003074
505 Tofail, S. A. M. Ferroelectricity in biological building blocks: Slipping on a banana peel? *Journal of Advanced Dielectrics* **13**, 2341004 (2023). https://doi.org:10.1142/s2010135x23410047
506 Wang, Z., Chen, R., Yang, S., Li, S. & Gao, Z. Design and application of stimuli-responsive DNA hydrogels: A review. *Materials Today Bio* **16**, 100430 (2022). https://doi.org:https://doi.org/10.1016/j.mtbio.2022.100430
507 Kolpashchikov, D. M. Evolution of Hybridization Probes to DNA Machines and Robots. *Accounts of Chemical Research* **52**, 1949-1956 (2019). https://doi.org:10.1021/acs.accounts.9b00098
508 Wu, Y., Ali, S. & White, R. J. Electrocatalytic Mechanism for Improving Sensitivity and Specificity of Electrochemical Nucleic Acid-Based Sensors with Covalent Redox Tags—Part I. *ACS Sensors* **5**, 3833-3841 (2020). https://doi.org:10.1021/acssensors.0c02362
509 Umeki, Y., Saito, M., Takahashi, Y., Takakura, Y. & Nishikawa, M. Retardation of Antigen Release from DNA Hydrogel Using Cholesterol-Modified DNA for Increased Antigen-Specific Immune Response. *Advanced Healthcare Materials* **6**, 1700355 (2017). https://doi.org:https://doi.org/10.1002/adhm.201700355
510 Bao, G. Protein Mechanics: A New Frontier in Biomechanics. *Exp Mech* **49**, 153-164 (2009). https://doi.org:10.1007/s11340-008-9154-0
511 Wang, E., Desai, M. S. & Lee, S.-W. Light-Controlled Graphene-Elastin Composite Hydrogel Actuators. *Nano Letters* **13**, 2826-2830 (2013). https://doi.org:10.1021/nl401088b
512 Bo, X. *et al.* High power-output and highly stretchable protein-based biomechanical energy harvester. *Chemical Engineering Journal* **451**, 138714 (2023). https://doi.org:https://doi.org/10.1016/j.cej.2022.138714
513 Bassett, C. A. & Becker, R. O. Generation of electric potentials by bone in response to mechanical stress. *Science* **137**, 1063-1064 (1962). https://doi.org:10.1126/science.137.3535.1063
514 Poillot, P., Le Maitre, C. L. & Huyghe, J. M. The strain-generated electrical potential in cartilaginous tissues: a role for piezoelectricity. *Biophys Rev* **13**, 91-100 (2021). https://doi.org:10.1007/s12551-021-00779-9
515 Krassowska, W. & Filev, P. D. Modeling electroporation in a single cell. *Biophys J* **92**, 404-417 (2007). https://doi.org:10.1529/biophysj.106.094235
516 Tsong, T. Y. Electroporation of cell membranes. *Biophys J* **60**, 297-306 (1991). https://doi.org:10.1016/s0006-3495(91)82054-9
517 George, L. F. & Bates, E. A. Mechanisms Underlying Influence of Bioelectricity in Development. *Front Cell Dev Biol* **10**, 772230 (2022). https://doi.org:10.3389/fcell.2022.772230
518 Riol, A., Cervera, J., Levin, M. & Mafe, S. Cell Systems Bioelectricity: How Different Intercellular Gap Junctions Could Regionalize a Multicellular Aggregate. *Cancers* **13**, 5300 (2021).
519 Bioelectric Fields at the Beginnings of Life. *Bioelectricity* **4**, 237-247 (2022). https://doi.org:10.1089/bioe.2022.0012

520 Nadezhdin, K. D. *et al.* Structural mechanism of heat-induced opening of a temperature-sensitive TRP channel. *Nat Struct Mol Biol* **28**, 564-572 (2021). https://doi.org:10.1038/s41594-021-00615-4
521 Catacuzzeno, L. *et al.* Energy harvesting from a bio cell. *Nano Energy* **56**, 823-827 (2019). https://doi.org:https://doi.org/10.1016/j.nanoen.2018.12.023
522 Afroz, A. S., Romano, D., Inglese, F. & Stefanini, C. Towards Bio-Hybrid Energy Harvesting in the Real-World: Pushing the Boundaries of Technologies and Strategies Using Bio-Electrochemical and Bio-Mechanical Processes. *Applied Sciences* **11**, 2220 (2021).
523 Dagdeviren, C., Li, Z. & Wang, Z. L. Energy Harvesting from the Animal/Human Body for Self-Powered Electronics. *Annual Review of Biomedical Engineering* **19**, 85-108 (2017). https://doi.org:10.1146/annurev-bioeng-071516-044517
524 Clementi, G. *et al.* in *2022 21st International Conference on Micro and Nanotechnology for Power Generation and Energy Conversion Applications (PowerMEMS)*. 79-81.
525 Liu, L., Guo, X., Liu, W. & Lee, C. Recent Progress in the Energy Harvesting Technology-From Self-Powered Sensors to Self-Sustained IoT, and New Applications. *Nanomaterials (Basel)* **11** (2021). https://doi.org:10.3390/nano11112975
526 Giner-Casares, J. J., Henriksen-Lacey, M., Coronado-Puchau, M. & Liz-Marzán, L. M. Inorganic nanoparticles for biomedicine: where materials scientists meet medical research. *Materials Today* **19**, 19-28 (2016). https://doi.org:https://doi.org/10.1016/j.mattod.2015.07.004
527 Fattahi, P., Yang, G., Kim, G. & Abidian, M. R. A review of organic and inorganic biomaterials for neural interfaces. *Adv Mater* **26**, 1846-1885 (2014). https://doi.org:10.1002/adma.201304496
528 Hennig, A. *et al.* Scope and Limitations of Surface Functional Group Quantification Methods: Exploratory Study with Poly(acrylic acid)-Grafted Micro- and Nanoparticles. *Journal of the American Chemical Society* **134**, 8268-8276 (2012). https://doi.org:10.1021/ja302649g
529 Hegde, V. I., Aykol, M., Kirklin, S. & Wolverton, C. The phase stability network of all inorganic materials. *Sci Adv* **6**, eaay5606 (2020). https://doi.org:10.1126/sciadv.aay5606
530 Kim, S. J. *et al.* A Surface Chemical Reaction in Organic–Inorganic Materials Using a New Chemical Evaporation System. *Chemistry of Materials* **27**, 4546-4551 (2015). https://doi.org:10.1021/acs.chemmater.5b00377
531 Dong, K., Peng, X. & Wang, Z. L. Fiber/Fabric-Based Piezoelectric and Triboelectric Nanogenerators for Flexible/Stretchable and Wearable Electronics and Artificial Intelligence. *Advanced Materials* **32**, 1902549 (2020). https://doi.org:https://doi.org/10.1002/adma.201902549
532 Peng, X. *et al.* A breathable, biodegradable, antibacterial, and self-powered electronic skin based on all-nanofiber triboelectric nanogenerators. *Science Advances* **6**, eaba9624 (2020). https://doi.org:doi:10.1126/sciadv.aba9624
533 Wang, J., Wang, H., Thakor, N. V. & Lee, C. Self-Powered Direct Muscle Stimulation Using a Triboelectric Nanogenerator (TENG) Integrated with a Flexible Multiple-Channel Intramuscular Electrode. *ACS Nano* **13**, 3589-3599 (2019). https://doi.org:10.1021/acsnano.9b00140
534 Shi, Q. *et al.* Progress in wearable electronics/photonics—Moving toward the era of

artificial intelligence and internet of things. *InfoMat* **2**, 1131-1162 (2020). https://doi.org:https://doi.org/10.1002/inf2.12122
535 He, T., Guo, X. & Lee, C. Flourishing energy harvesters for future body sensor network: from single to multiple energy sources. *iScience* **24**, 101934 (2021). https://doi.org:https://doi.org/10.1016/j.isci.2020.101934
536 Dong, B. *et al.* Technology evolution from self-powered sensors to AIoT enabled smart homes. *Nano Energy* **79**, 105414 (2021). https://doi.org:https://doi.org/10.1016/j.nanoen.2020.105414
537 Zhu, M., Yi, Z., Yang, B. & Lee, C. Making use of nanoenergy from human – Nanogenerator and self-powered sensor enabled sustainable wireless IoT sensory systems. *Nano Today* **36**, 101016 (2021). https://doi.org:https://doi.org/10.1016/j.nantod.2020.101016
538 Plante, J. A. *et al.* Spike mutation D614G alters SARS-CoV-2 fitness. *Nature* **592**, 116-121 (2021). https://doi.org:10.1038/s41586-020-2895-3
539 McLellan, J. S. *et al.* Structure of HIV-1 gp120 V1/V2 domain with broadly neutralizing antibody PG9. *Nature* **480**, 336-343 (2011). https://doi.org:10.1038/nature10696
540 Lacks, D. J. & Shinbrot, T. Long-standing and unresolved issues in triboelectric charging. *Nature Reviews Chemistry* **3**, 465-476 (2019). https://doi.org:10.1038/s41570-019-0115-1
541 Dogic, Z. & Fraden, S. Smectic Phase in a Colloidal Suspension of Semiflexible Virus Particles. *Physical Review Letters* **78**, 2417-2420 (1997). https://doi.org:10.1103/PhysRevLett.78.2417
542 Hemminga, M. A. *et al.* Viruses: incredible nanomachines. New advances with filamentous phages. *European Biophysics Journal* **39**, 541-550 (2010). https://doi.org:10.1007/s00249-009-0523-0
543 Zimmermann, K., Hagedorn, H., Heuck, C. C., Hinrichsen, M. & Ludwig, H. The ionic properties of the filamentous bacteriophages Pf1 and fd. *Journal of Biological Chemistry* **261**, 1653-1655 (1986). https://doi.org:https://doi.org/10.1016/S0021-9258(17)35990-2
544 Lowell, J. & Rose-Innes, A. C. Contact electrification. *Advances in Physics* **29**, 947-1023 (1980). https://doi.org:10.1080/00018738000101466
545 Zhou, Y. S. *et al.* In Situ Quantitative Study of Nanoscale Triboelectrification and Patterning. *Nano Letters* **13**, 2771-2776 (2013). https://doi.org:10.1021/nl401006x
546 Kim, S. *et al.* Rewritable ghost floating gates by tunnelling triboelectrification for two-dimensional electronics. *Nature Communications* **8**, 15891 (2017). https://doi.org:10.1038/ncomms15891
547 Melitz, W., Shen, J., Kummel, A. C. & Lee, S. Kelvin probe force microscopy and its application. *Surface Science Reports* **66**, 1-27 (2011). https://doi.org:https://doi.org/10.1016/j.surfrep.2010.10.001
548 Nonnenmacher, M., O'Boyle, M. P. & Wickramasinghe, H. K. Kelvin probe force microscopy. *Applied Physics Letters* **58**, 2921-2923 (1991). https://doi.org:10.1063/1.105227
549 Knorr, N., Rosselli, S. & Nelles, G. Surface-potential decay of biased-probe contact-charged amorphous polymer films. *Journal of Applied Physics* **107** (2010). https://doi.org:10.1063/1.3309763
550 Lee, J.-H. *et al.* Control of Skin Potential by Triboelectrification with Ferroelectric Polymers. *Advanced Materials* **27**, 5553-5558 (2015).

https://doi.org:https://doi.org/10.1002/adma.201502463
551 Bannwarth, C., Ehlert, S. & Grimme, S. GFN2-xTB—An Accurate and Broadly Parametrized Self-Consistent Tight-Binding Quantum Chemical Method with Multipole Electrostatics and Density-Dependent Dispersion Contributions. *Journal of Chemical Theory and Computation* **15**, 1652-1671 (2019). https://doi.org:10.1021/acs.jctc.8b01176
552 Zhu, M. *et al.* Self-Powered and Self-Functional Cotton Sock Using Piezoelectric and Triboelectric Hybrid Mechanism for Healthcare and Sports Monitoring. *ACS Nano* **13**, 1940-1952 (2019). https://doi.org:10.1021/acsnano.8b08329
553 Fernandez-Yague, M. A. *et al.* A Self-Powered Piezo-Bioelectric Device Regulates Tendon Repair-Associated Signaling Pathways through Modulation of Mechanosensitive Ion Channels. *Advanced Materials* **33**, 2008788 (2021). https://doi.org:https://doi.org/10.1002/adma.202008788
554 Pui, T.-S. *et al.* Non-invasive Detection of Cellular Bioelectricity Based on Carbon Nanotube Devices for High-Throughput Drug Screening. *Advanced Materials* **22**, 3199-3203 (2010). https://doi.org:https://doi.org/10.1002/adma.201000548
555 Wang, W. *et al.* Bioinspired Nanosucker Array for Enhancing Bioelectricity Generation in Microbial Fuel Cells. *Advanced Materials* **28**, 270-275 (2016). https://doi.org:https://doi.org/10.1002/adma.201503609
556 Kim, Y. J. *et al.* Photosynthetic Nanomaterial Hybrids for Bioelectricity and Renewable Energy Systems. *Advanced Materials* **33**, 2005919 (2021). https://doi.org:https://doi.org/10.1002/adma.202005919
557 Balu, R., Dutta, N. K., Dutta, A. K. & Choudhury, N. R. Resilin-mimetics as a smart biomaterial platform for biomedical applications. *Nature Communications* **12**, 149 (2021). https://doi.org:10.1038/s41467-020-20375-x
558 Chorsi, M. T. *et al.* Piezoelectric Biomaterials for Sensors and Actuators. *Advanced Materials* **31**, 1802084 (2019). https://doi.org:https://doi.org/10.1002/adma.201802084
559 Yuan, X. *et al.* Piezoelectricity, Pyroelectricity, and Ferroelectricity in Biomaterials and Biomedical Applications. *Advanced Materials* **n/a**, 2308726 (2023). https://doi.org:https://doi.org/10.1002/adma.202308726
560 Chae, I., Jeong, C. K., Ounaies, Z. & Kim, S. H. Review on Electromechanical Coupling Properties of Biomaterials. *ACS Appl Bio Mater* **1**, 936-953 (2018). https://doi.org:10.1021/acsabm.8b00309
561 Huang, T. *et al.* "Self-Matched" Tribo/Piezoelectric Nanogenerators Using Vapor-Induced Phase-Separated Poly(vinylidene fluoride) and Recombinant Spider Silk. *Adv Mater* **32**, e1907336 (2020). https://doi.org:10.1002/adma.201907336
562 Pan, C.-T. *et al.* Energy Harvesters Incorporating Silk from the Taiwan-Native Spider Nephila pilipes. *ACS Applied Energy Materials* **1**, 5627-5635 (2018). https://doi.org:10.1021/acsaem.8b01169
563 Jiang, C. *et al.* Engineering squandered plant protein into eco-friendly triboelectric films for highly efficient energy harvesting. *Nano Energy* **101**, 107589 (2022). https://doi.org:https://doi.org/10.1016/j.nanoen.2022.107589
564 Jiang, C. *et al.* Plant-protein-enabled biodegradable triboelectric nanogenerator for sustainable agriculture. *Fundamental Research* **2**, 974-984 (2022). https://doi.org:https://doi.org/10.1016/j.fmre.2021.09.010
565 Han, W. M. *et al.* Microstructural heterogeneity directs micromechanics and mechanobiology in native and engineered fibrocartilage. *Nature Materials* **15**, 477-484

(2016). https://doi.org:10.1038/nmat4520
566 Sarikaya, M., Tamerler, C., Jen, A. K. Y., Schulten, K. & Baneyx, F. Molecular biomimetics: nanotechnology through biology. *Nature Materials* **2**, 577-585 (2003). https://doi.org:10.1038/nmat964
567 Yarger, J. L., Cherry, B. R. & van der Vaart, A. Uncovering the structure–function relationship in spider silk. *Nature Reviews Materials* **3**, 18008 (2018). https://doi.org:10.1038/natrevmats.2018.8
568 Moorthy, H., Datta, L. P. & Govindaraju, T. Molecular Architectonics-guided Design of Biomaterials. *Chemistry – An Asian Journal* **16**, 423-442 (2021). https://doi.org:https://doi.org/10.1002/asia.202001445
569 Kingon, A. I. & Srinivasan, S. Lead zirconate titanate thin films directly on copper electrodes for ferroelectric, dielectric and piezoelectric applications. *Nature Materials* **4**, 233-237 (2005). https://doi.org:10.1038/nmat1334
570 Dagdeviren, C. *et al.* Conformal piezoelectric systems for clinical and experimental characterization of soft tissue biomechanics. *Nature Materials* **14**, 728-736 (2015). https://doi.org:10.1038/nmat4289
571 Saito, Y. *et al.* Lead-free piezoceramics. *Nature* **432**, 84-87 (2004). https://doi.org:10.1038/nature03028
572 Valencia, S. *et al.* Interface-induced room-temperature multiferroicity in BaTiO3. *Nature Materials* **10**, 753-758 (2011). https://doi.org:10.1038/nmat3098
573 Zhao, C. *et al.* Practical High Piezoelectricity in Barium Titanate Ceramics Utilizing Multiphase Convergence with Broad Structural Flexibility. *Journal of the American Chemical Society* **140**, 15252-15260 (2018). https://doi.org:10.1021/jacs.8b07844
574 Kobiakov, I. B. Elastic, piezoelectric and dielectric properties of ZnO and CdS single crystals in a wide range of temperatures. *Solid State Communications* **35**, 305-310 (1980). https://doi.org:https://doi.org/10.1016/0038-1098(80)90502-5
575 Su, Y. *et al.* High-performance piezoelectric composites via β phase programming. *Nature Communications* **13**, 4867 (2022). https://doi.org:10.1038/s41467-022-32518-3
576 Yan, Y., Zhou, J. E., Maurya, D., Wang, Y. U. & Priya, S. Giant piezoelectric voltage coefficient in grain-oriented modified PbTiO3 material. *Nature Communications* **7**, 13089 (2016). https://doi.org:10.1038/ncomms13089
577 Gu, L. *et al.* Enhancing the current density of a piezoelectric nanogenerator using a three-dimensional intercalation electrode. *Nature Communications* **11**, 1030 (2020). https://doi.org:10.1038/s41467-020-14846-4
578 Li, C.-E. & Zhou, J.-G. PNC-3 modified lead metaniobate piezoelectric ceramics. *Ferroelectrics* **154**, 353-356 (1994). https://doi.org:10.1080/00150199408017312
579 Sahu, K. R., Chakraborty, K. R. & De, U. Crystallographic phases in PbNb2O6 and Piezoelectricity. *Materials Today: Proceedings* **11**, 869-874 (2019). https://doi.org:https://doi.org/10.1016/j.matpr.2019.03.058
580 Gao, X. *et al.* Giant Piezoelectric Coefficients in Relaxor Piezoelectric Ceramic PNN-PZT for Vibration Energy Harvesting. *Advanced Functional Materials* **28**, 1706895 (2018). https://doi.org:https://doi.org/10.1002/adfm.201706895
581 Li, P. *et al.* Ultrahigh Piezoelectric Properties in Textured (K,Na)NbO3-Based Lead-Free Ceramics. *Advanced Materials* **30**, 1705171 (2018). https://doi.org:https://doi.org/10.1002/adma.201705171
582 Thomann, H. Piezoelectric Ceramics. *Advanced Materials* **2**, 458-463 (1990). https://doi.org:https://doi.org/10.1002/adma.19900021004

583 Twiney, R. C. Novel piezoelectric materials. *Advanced Materials* **4**, 819-822 (1992). https://doi.org:https://doi.org/10.1002/adma.19920041213
584 Leng, H. *et al.* Design and development of high-power piezoelectric ceramics through integration of crystallographic texturing and acceptor-doping. *Acta Materialia* **206**, 116610 (2021). https://doi.org:https://doi.org/10.1016/j.actamat.2020.116610
585 Go, S.-H. *et al.* Effect of the Crystal Structure on the Piezoelectricity of [001]-Textured (Na, K)(Nb, Sb)O3-SrZrO3-(Bi, Ag)ZrO3 Lead-Free Piezoelectric Thick Film. *Actuators* **12**, 66 (2023).
586 Chen, C. *et al.* Structural Design Optimization of Physical Vapor Transport Furnace for Aluminum Nitride Crystal Growth via Modeling and Simulation. *Industrial & Engineering Chemistry Research* **62**, 17287-17296 (2023). https://doi.org:10.1021/acs.iecr.3c01207
587 Chen, K., Zhu, Y., Liu, Z. & Xue, D. State of the Art in Crystallization of LiNbO(3) and Their Applications. *Molecules* **26** (2021). https://doi.org:10.3390/molecules26227044
588 Baasandorj, L. & Chen, Z. Recent Developments on Relaxor-PbTiO3 Ferroelectric Crystals. *Crystals* **12**, 56 (2022).
589 Dani, S. S., Tripathy, A., Alluri, N. R., Balasubramaniam, S. & Ramadoss, A. A critical review: the impact of electrical poling on the longitudinal piezoelectric strain coefficient. *Materials Advances* **3**, 8886-8921 (2022). https://doi.org:10.1039/D2MA00559J
590 Chen, Z. *et al.* High-performance and high-thermally stable PSN-PZT piezoelectric ceramics achieved by high-temperature poling. *Journal of Materials Science & Technology* **116**, 238-245 (2022). https://doi.org:https://doi.org/10.1016/j.jmst.2021.09.022
591 Liu, Y. & Wang, L. A robust-based configuration design method of piezoelectric materials for mechanical load identification considering structural vibration suppression. *Computer Methods in Applied Mechanics and Engineering* **410**, 115998 (2023). https://doi.org:https://doi.org/10.1016/j.cma.2023.115998
592 Mojena-Medina, D. *et al.* Design, Implementation, and Validation of a Piezoelectric Device to Study the Effects of Dynamic Mechanical Stimulation on Cell Proliferation, Migration and Morphology. *Sensors (Basel)* **20** (2020). https://doi.org:10.3390/s20072155
593 Bannister, F. A. Crystallography in Modern Science: Crystallography in Physics. *Nature* **167**, 965-968 (1951). https://doi.org:10.1038/167965a0
594 Martineau, C. NMR crystallography: Applications to inorganic materials. *Solid State Nucl Magn Reson* **63-64**, 1-12 (2014). https://doi.org:10.1016/j.ssnmr.2014.07.001
595 Hojo, J. & Inada, M. in *Materials Chemistry of Ceramics* (ed Junichi Hojo) 1-22 (Springer Singapore, 2019).
596 Takashima, S. & Yamaoka, K. The electric dipole moment of DNA-binding HU protein calculated by the use of an NMR database. *Biophys Chem* **80**, 153-163 (1999). https://doi.org:10.1016/s0301-4622(99)00072-1
597 Takashima, S. The structure and dipole moment of globular proteins in solution and crystalline states: use of NMR and X-ray databases for the numerical calculation of dipole moment. *Biopolymers* **58**, 398-409 (2001). https://doi.org:10.1002/1097-0282(20010405)58:4<398::Aid-bip1016>3.0.Co;2-9
598 Cruz-Valeriano, E. *et al.* Dielectric constant measurement using atomic force microscopy of dielectric films: a system theory approach. *Applied Physics A* **124**, 667

(2018). https://doi.org:10.1007/s00339-018-2093-4
599 Gramse, G., Casuso, I., Toset, J., Fumagalli, L. & Gomila, G. Quantitative dielectric constant measurement of thin films by DC electrostatic force microscopy. *Nanotechnology* **20**, 395702 (2009). https://doi.org:10.1088/0957-4484/20/39/395702
600 Fumagalli, L., Esteban-Ferrer, D., Cuervo, A., Carrascosa, J. L. & Gomila, G. Label-free identification of single dielectric nanoparticles and viruses with ultraweak polarization forces. *Nature Materials* **11**, 808-816 (2012). https://doi.org:10.1038/nmat3369
601 Liu, J., Gaikwad, R., Hande, A., Das, S. & Thundat, T. Mapping and Quantifying Surface Charges on Clay Nanoparticles. *Langmuir* **31**, 10469-10476 (2015). https://doi.org:10.1021/acs.langmuir.5b02859
602 Goswami, A. *et al.* Mapping the surface potential, charge density and adhesion of cellulose nanocrystals using advanced scanning probe microscopy. *Carbohydrate Polymers* **246**, 116393 (2020). https://doi.org:https://doi.org/10.1016/j.carbpol.2020.116393
603 Schaadt, D. M., Yu, E. T., Sankar, S. & Berkowitz, A. E. Charge storage in Co nanoclusters embedded in SiO2 by scanning force microscopy. *Applied Physics Letters* **74**, 472-474 (1999). https://doi.org:10.1063/1.123039
604 Pallen, M. J. & Wren, B. W. Bacterial pathogenomics. *Nature* **449**, 835-842 (2007). https://doi.org:10.1038/nature06248
605 Dimitrov, D. S. Virus entry: molecular mechanisms and biomedical applications. *Nature Reviews Microbiology* **2**, 109-122 (2004). https://doi.org:10.1038/nrmicro817
606 Lee, S.-W., Mao, C., Flynn, C. E. & Belcher, A. M. Ordering of Quantum Dots Using Genetically Engineered Viruses. *Science* **296**, 892-895 (2002). https://doi.org:doi:10.1126/science.1068054
607 Kim, W.-G. *et al.* Biomimetic self-templating optical structures fabricated by genetically engineered M13 bacteriophage. *Biosensors and Bioelectronics* **85**, 853-859 (2016). https://doi.org:https://doi.org/10.1016/j.bios.2016.05.099
608 Merzlyak, A., Indrakanti, S. & Lee, S.-W. Genetically Engineered Nanofiber-Like Viruses For Tissue Regenerating Materials. *Nano Letters* **9**, 846-852 (2009). https://doi.org:10.1021/nl8036728
609 Oh, J. W. & Han, D. W. Virus-Based Nanomaterials and Nanostructures. *Nanomaterials (Basel)* **10** (2020). https://doi.org:10.3390/nano10030567
610 Pandya, S. *et al.* Pyroelectric energy conversion with large energy and power density in relaxor ferroelectric thin films. *Nature Materials* **17**, 432-438 (2018). https://doi.org:10.1038/s41563-018-0059-8
611 Pandya, S. *et al.* Understanding the Role of Ferroelastic Domains on the Pyroelectric and Electrocaloric Effects in Ferroelectric Thin Films. *Advanced Materials* **31**, 1803312 (2019). https://doi.org:https://doi.org/10.1002/adma.201803312
612 Song, K., Zhao, R., Wang, Z. L. & Yang, Y. Conjuncted Pyro-Piezoelectric Effect for Self-Powered Simultaneous Temperature and Pressure Sensing. *Advanced Materials* **31**, 1902831 (2019). https://doi.org:https://doi.org/10.1002/adma.201902831
613 Yang, M.-M. *et al.* Piezoelectric and pyroelectric effects induced by interface polar symmetry. *Nature* **584**, 377-381 (2020). https://doi.org:10.1038/s41586-020-2602-4
614 Tayi, A. S., Kaeser, A., Matsumoto, M., Aida, T. & Stupp, S. I. Supramolecular ferroelectrics. *Nature Chemistry* **7**, 281-294 (2015). https://doi.org:10.1038/nchem.2206

615 Zhang, D., Wu, H., Bowen, C. R. & Yang, Y. Recent Advances in Pyroelectric Materials and Applications. *Small* **17**, 2103960 (2021). https://doi.org:https://doi.org/10.1002/smll.202103960
616 Meirzadeh, E. *et al.* Origin and structure of polar domains in doped molecular crystals. *Nature Communications* **7**, 13351 (2016). https://doi.org:10.1038/ncomms13351
617 Meirzadeh, E., Dishon, S., Lubomirsky, I. & Ehre, D. Surface Pyroelectricity and Piezoelectricity of Centrosymmetric Crystals. *Israel Journal of Chemistry* **61**, 750-757 (2021). https://doi.org:https://doi.org/10.1002/ijch.202100050
618 Athenstaedt, H. Pyroelectric sensors of organisms. *Ferroelectrics* **11**, 365-369 (1976). https://doi.org:10.1080/00150197608236582
619 Groten, J., Zirkl, M., Jakopic, G., Leitner, A. & Stadlober, B. Pyroelectric scanning probe microscopy: A method for local measurement of the pyroelectric effect in ferroelectric thin films. *Physical Review B* **82**, 054112 (2010). https://doi.org:10.1103/PhysRevB.82.054112
620 Tofail, S. A. M., Baldisserri, C., Haverty, D., McMonagle, J. B. & Erhart, J. Pyroelectric surface charge in hydroxyapatite ceramics. *Journal of Applied Physics* **106** (2009). https://doi.org:10.1063/1.3262628
621 Lang, S. B. *et al.* Pyroelectric, piezoelectric, and photoeffects in hydroxyapatite thin films on silicon. *Applied Physics Letters* **98** (2011). https://doi.org:10.1063/1.3571294
622 Athenstaedt, H. Pyroelectric properties of wheat. *Ferroelectrics* **14**, 753-759 (1976). https://doi.org:10.1080/00150197608237794
623 Maity, K., Mondal, A. & Saha, M. C. Cellulose Nanocrystal-Based All-3D-Printed Pyro-Piezoelectric Nanogenerator for Hybrid Energy Harvesting and Self-Powered Cardiorespiratory Monitoring toward the Human–Machine Interface. *ACS Applied Materials & Interfaces* **15**, 13956-13970 (2023). https://doi.org:10.1021/acsami.2c21680
624 Simhony, M. & Athenstaedt, H. Measurement of the pyroelectric coefficient and permittivity on Rhododendron and Encephalartos leaves and on the insect Periplaneta americana. *Biophysical Journal* **29**, 331-337 (1980). https://doi.org:https://doi.org/10.1016/S0006-3495(80)85136-8
625 Burgener, M. *et al.* Polar Nature of Biomimetic Fluorapatite/Gelatin Composites: A Comparison of Bipolar Objects and the Polar State of Natural Tissue. *Biomacromolecules* **16**, 2814-2819 (2015). https://doi.org:10.1021/acs.biomac.5b00770
626 Athenstaedt, H. Pyroelectric and piezoelectric behaviour of human dental hard tissues. *Arch Oral Biol* **16**, 495-501 (1971). https://doi.org:10.1016/0003-9969(71)90194-4
627 Marino, A. A. & Gross, B. D. Piezoelectricity in cementum, dentine and bone. *Archives of Oral Biology* **34**, 507-509 (1989). https://doi.org:https://doi.org/10.1016/0003-9969(89)90087-3
628 Lang, S. B. & Athenstaedt, H. Anomalous pyroelectric behavior in the leaves of the palm-like plant encephalartos villosus. *Ferroelectrics* **17**, 511-519 (1977). https://doi.org:10.1080/00150197808236775
629 Miles, A. J. & Wallace, B. A. Circular dichroism spectroscopy of membrane proteins. *Chemical Society Reviews* **45**, 4859-4872 (2016). https://doi.org:10.1039/C5CS00084J
630 Miles, A. J. & Wallace, B. A. CDtoolX, a downloadable software package for processing and analyses of circular dichroism spectroscopic data. *Protein Sci* **27**, 1717-1722 (2018). https://doi.org:10.1002/pro.3474

631 Rai, V. N., Srivastava, A. K., Mukherjee, C. & Deb, S. K. Surface enhanced absorption and transmission from dye coated gold nanoparticles in thin films. *Appl Opt* **51**, 2606-2615 (2012). https://doi.org:10.1364/ao.51.002606

632 Vora, H. D., Santhanakrishnan, S., Harimkar, S. P., Boetcher, S. K. S. & Dahotre, N. B. One-dimensional multipulse laser machining of structural alumina: evolution of surface topography. *The International Journal of Advanced Manufacturing Technology* **68**, 69-83 (2013). https://doi.org:10.1007/s00170-012-4709-8

Appendix

A.1 Calculation of the coordinates of positive and negative charges

```
#!/bin/bash
# Author: David Small, Molecular Graphics and Computation Facility
# usage: charge_centers_from_mae file.mae
# file.mae must contain (force-field) partial charges
#	one way to get this is to use desmond system builder, then export that entry as mae
# the script uses the r_m_charge1 column from file.mae, because that's what compute_dipole_charged.py uses
m_atom_line=$(grep -n 'm_atom\[' $1 | awk '{ split($1,arr,":"); print arr[1]; }')
tail -n +$m_atom_line $1 | awk 'BEGIN {
  readData = 0;
  n_charge = 0.0; p_charge = 0.0;
  for (i=1; i<=6; i++) nr[i] = 0.0;
}
{
  if (readData)
  {
    if ($1 == ":::") exit;
    else
    {
		n=split($0,arr,"\"");
		count = 1;
		for (i = 1; i <= n; i++)
		{
			if ((i % 2) == 0)
			{
```

```
                    lineCols[count] = "";
                    count++;
                }
                else
                {
                    nn = split(arr[i], arrarr, " ");
                    for (ii = 1; ii <= nn; ii++)
                    {
                        lineCols[count] = arrarr[ii];
                        count++;
                    }
                }
            }
            # print count;
        chg = lineCols[qcol];
        if (chg > 0.0)
        {
            p_charge += chg;
            j = 3;
        }
        else
        {
            n_charge += chg;
              j = 0;
        }
        for (i=1; i<4; i++) nr[j+i] += chg * lineCols[rcol[i]];
    }
}
else
```

```
  {
    if ($1 == "r_m_x_coord") rcol[1] = NR-1;
    if ($1 == "r_m_y_coord") rcol[2] = NR-1;
    if ($1 == "r_m_z_coord") rcol[3] = NR-1;
    if ($1 == "r_m_charge1") qcol = NR-1;
    if ($1 == ":::") readData = 1;
  }
}
END {
  for (i=1; i<=3; i++)
  {
    if (n_charge < 0.0) nr[i] /= n_charge;
    if (p_charge > 0.0) nr[i+3] /= p_charge;
  }
  print "Total negative charge:",n_charge;
  print "Center of negative charge:",nr[1],nr[2],nr[3];
  print "Total positive charge:",p_charge;
  print "Center of positive charge:",nr[4],nr[5],nr[6];
}'
```

A.2 Deformation of a M13 phage model

```
# Author: David Small, Molecular Graphics and Computation Facility
import sys
from schrodinger.structure import StructureReader
st = list(StructureReader(sys.argv[1]))[0]
# print(st.property["r_pdb_PDB_CRYST1_alpha"])
from schrodinger.application.matsci.nano import xtal
# xtal.trans_cart_to_frac_from_vecs(coords, a_vec, b_vec, c_vec, rec=False)
```

```
# xtal.trans_frac_to_cart_from_vecs(coords, a_vec, b_vec, c_vec, rec=False)
# xtal.get_lattice_vectors(a_param, b_param, c_param, alpha_param, beta_param, gamma_param)
a_vec = [st.property["r_chorus_box_ax"], st.property["r_chorus_box_ay"], st.property["r_chorus_box_az"]]
b_vec = [st.property["r_chorus_box_bx"], st.property["r_chorus_box_by"], st.property["r_chorus_box_bz"]]
c_vec = [st.property["r_chorus_box_cx"], st.property["r_chorus_box_cy"], st.property["r_chorus_box_cz"]]
f_coords = xtal.trans_cart_to_frac_from_vecs(st.getXYZ(), a_vec, b_vec, c_vec)
print(f_coords)
new_lattice_constants = [float(gta) for gta in sys.argv[2:8]]
new_a, new_b, new_c = xtal.get_lattice_vectors(*new_lattice_constants)
new_xyz_coords = xtal.trans_frac_to_cart_from_vecs(f_coords, new_a, new_b, new_c)
prefixes = ["r_pdb_PDB_CRYST1", "s_pdb_PDB_CRYST1", "i_pdb_PDB_CRYST1", "r_chorus_box"]
for key in st.property:
    if any(key.startswith(sta) for sta in prefixes):
        del st.property[key]
st.property["r_chorus_box_ax"] = new_a[0]
st.property["r_chorus_box_ay"] = new_a[1]
st.property["r_chorus_box_az"] = new_a[2]
st.property["r_chorus_box_bx"] = new_b[0]
st.property["r_chorus_box_by"] = new_b[1]
st.property["r_chorus_box_bz"] = new_b[2]
st.property["r_chorus_box_cx"] = new_c[0]
st.property["r_chorus_box_cy"] = new_c[1]
st.property["r_chorus_box_cz"] = new_c[2]
```

```
st.property["r_pdb_PDB_CRYST1_a"] = new_lattice_constants[0]
st.property["r_pdb_PDB_CRYST1_b"] = new_lattice_constants[1]
st.property["r_pdb_PDB_CRYST1_c"] = new_lattice_constants[2]
st.property["r_pdb_PDB_CRYST1_alpha"] = new_lattice_constants[3]
st.property["r_pdb_PDB_CRYST1_beta"] = new_lattice_constants[4]
st.property["r_pdb_PDB_CRYST1_gamma"] = new_lattice_constants[5]
st.setXYZ(new_xyz_coords)
st.write("deformed_structure.mae")
```

A.3 Temperature controller in Kelvin probe force microscopy measurements

```
# Author: Seung-Wuk Lee
#include <SPI.h>
#include <Wire.h>
#include <Adafruit_GFX.h>
#include <Adafruit_SSD1306.h>
#include <PIDController.h>
// Max6675 thermosensor was not used: instead thermister with 100k ohn register read thorugh A0
// Define Rotary Encoder Pins
#define CLK_PIN 2
#define DATA_PIN 3
#define SW_PIN 4
// Mosfet Pin
#define mosfet_pin 11
// Serial Enable
#define __DEBUG__
#define SCREEN_WIDTH 128 // OLED display width, in pixels
#define SCREEN_HEIGHT 64 // OLED display height, in pixels
```

```
#define OLED_RESET        -1 // Reset pin # (or -1 if sharing Arduino reset pin)
/*In this section we have defined the gain values for the
  * proportional, integral, and derivative controller I have set
  * the gain values with the help of trial and error methods.
*/
#define __Kp 30 // Proportional constant
#define __Ki 0.7 // Integral Constant
#define __Kd 200 // Derivative Constant
int clockPin; // Placeholder por pin status used by the rotary encoder
int clockPinState; // Placeholder por pin status used by the rotary encoder
int set_temperature = 25; // This set_temperature value will increas or decreas if when the rotarty encoder is turned
float temperature_value_c = 0.0; // stores temperature value
long debounce = 0; // Debounce delay
int encoder_btn_count = 0; // used to check encoder button press
/*
MAX6675 thermocouple(thermoCLK, thermoCS, thermoDO); // Create an instance for the MAX6675 Sensor Called "thermocouple"
*/
Adafruit_SSD1306 display(SCREEN_WIDTH, SCREEN_HEIGHT, &Wire, OLED_RESET);// Create an instance for the SSD1306 128X64 OLED "display"
PIDController pid; // Create an instance of the PID controller class, called "pid"
////////////////////// add all necessary parameter    ////////////
int led_pin = 6;              //PWM output pin
const int VOL_PIN = 0;    // voltage input pin
//float set_temp =40;
int ThermistorPin = 1;
float Vo;
```

```
float V1;
float R1 = 10000;
float logR2, R2, T;
float c1 = 1.009249522e-03, c2 = 2.378405444e-04, c3 = 2.019202697e-07;
int value;
float volt;
float average;
float average_1;
float pyro_coeff;
int i;
int j;
//define time
//unsigned long time;
int sec = 0;
int Min = 0;
int Hour = 0;
int m_sec = 0;
float FT=0;
float CT=0;
// Voltage reading
float V2;
float V3;
float R3 = 100000;
float R4 = 10000;
//////////////////////// ////////////
void setup() {
#ifdef __DEBUG__
```

```
    Serial.begin(9600);
  #endif
    pinMode(mosfet_pin, OUTPUT); // MOSFET output PIN
    pinMode(CLK_PIN, INPUT); // Encoer Clock Pin
    pinMode(DATA_PIN, INPUT); //Encoder Data Pin
    pinMode(SW_PIN, INPUT_PULLUP);// Encoder SW Pin
    pid.begin();                  // initialize the PID instance
    pid.setpoint(150);        // The "goal" the PID controller tries to "reach"
    pid.tune(__Kp, __Ki,__Kd);        // Tune the PID, arguments: kP, kI, kD
    pid.limit(0, 255);        // Limit the PID output between 0 and 255, this is important
to get rid of integral windup!
    if (!display.begin(SSD1306_SWITCHCAPVCC, 0x3C)) {
  #ifdef __DEBUG__
      Serial.println(F("SSD1306 allocation failed"));
  #endif
      for (;;); // Don't proceed, loop forever
    }
    //
    display.setRotation(2); //Rotate the Display
    display.display(); //Show initial display buffer contents on the screen -- the library
initializes this with an Adafruit splash screen.
    display.clearDisplay(); // Cleear the Display
    display.setTextSize(2); // Set text Size
    display.setTextColor(WHITE); // set LCD Colour
    display.setCursor(30, 0); // Set Cursor Position
    display.println("Lee Lab"); // Print the this Text
    display.setCursor(0, 20);    // Set Cursor Position
    display.println("Temperatur"); // Print the this Text
```

```
    display.setCursor(22, 40); // Set Cursor Position
    display.println("Control"); // Print the this Text
    display.display(); // Update the Display
    delay(2000); // Delay of 200 ms
  }
  void set_temp()
  {
    if (encoder_btn_count == 2) // check if the button is pressed twice and its in temperature set mode.
    {
      display.clearDisplay(); // clear the display
      display.setTextSize(2); // Set text Size
      display.setCursor(16, 0); // set the diplay cursor
      display.print("Set Temp."); // Print Set Temp. on the display
      display.setCursor(45, 25); // set the cursor
      display.print(set_temperature);// print the set temperature value on the display
      display.display(); // Update the Display
    }
  }
  void read_encoder() // In this function we read the encoder data and increment the counter if its rotaing clockwise and decrement the counter if its rotating counter clockwis
  {
    clockPin = digitalRead(CLK_PIN); // we read the clock pin of the rotary encoder
    if (clockPin != clockPinState    && clockPin == 1) { // if this condition is true then the encoder is rotaing counter clockwise and we decremetn the counter
      if (digitalRead(DATA_PIN) != clockPin) set_temperature = set_temperature - 3; // decrmetn the counter.
      else    set_temperature = set_temperature + 1; // Encoder is rotating CW so increment
```

```
        if (set_temperature < 1 )set_temperature = 1; // if the counter value is less than 1
the set it back to 1
        if (set_temperature > 150 ) set_temperature = 150; //if the counter value is grater
than 150 then set it back to 150
    #ifdef __DEBUG__
        Serial.println(set_temperature); // print the set temperature value on the serial
monitor window
    #endif
      }
      clockPinState = clockPin; // Remember last CLK_PIN state
      if ( digitalRead(SW_PIN) == LOW)      //If we detect LOW signal, button is pressed
      {
        if ( millis() - debounce > 80) { //debounce delay
          encoder_btn_count++; // Increment the values
          if (encoder_btn_count > 2) encoder_btn_count = 1;
    #ifdef __DEBUG__
          Serial.println(encoder_btn_count);
    #endif
        }
        debounce = millis(); // update the time variable
      }
    }
    void loop()
    {
      Vo = analogRead(ThermistorPin);    // thermister reading
      V1 = analogRead(0);        // voltage reading after amplification
    float samples;
    float NUMSAMPLES= 5 ;
```

```
  // take N samples in a row, with a slight delay
  for (int i = 0; i < NUMSAMPLES; i++) samples += Vo;
    Vo = samples/NUMSAMPLES;
    delay(1);
float samples_1;
float NUMSAMPLES_1= 5 ;
  // take N samples in a row, with a slight delay
  for (int i = 0; i < NUMSAMPLES_1; i++) samples_1 += Vo;
    V1 = samples_1/NUMSAMPLES_1;
    delay(1);
  R2 = R1 * (1023.0 / (float)Vo - 1.0);
  logR2 = log(R2);
  T = (1.0 / (c1 + c2*logR2 + c3*logR2*logR2*logR2));
  T = T - 273.15;
  FT = (T * 9.0)/ 5.0 + 32.0;// Farhenheit temp
  CT=(FT-32)/1.8;                    // Celcius temp
float vPow = 5.0;
   float V2 = (V1 * vPow) / 1024.0;
   float V3 = V2 / (R4 / (R3 + R4));
  Serial.print("Temperature: ");
  Serial.print(CT);
  Serial.print(" C");
  Serial.print("; ");
  Serial.print("Voltage: ");
  Serial.print(V3);
  Serial.print("mV");
  Serial.print("; ");
```

read_encoder(); //Call The Read Encoder Function

set_temp(); // Call the Set Temperature Function

if (encoder_btn_count == 1) // check if the button is pressed and its in Free Running Mode -- in this mode the arduino continiously updates the screen and adjusts the PWM output according to the temperature.

{

// temperature_value_c = thermocouple.readCelsius(); // Read the Temperature using the readCelsius methode from MAX6675 Library.

temperature_value_c = CT; // Read the Temperature using the readCelsius methode from MAX6675 Library.

int output = pid.compute(temperature_value_c); // Let the PID compute the value, returns the optimal output

analogWrite(mosfet_pin, output); // Write the output to the output pin

pid.setpoint(set_temperature); // Use the setpoint methode of the PID library to

display.clearDisplay(); // Clear the display

display.setTextSize(2); // Set text Size

display.setCursor(16, 0); // Set the Display Cursor

display.print("Cur Temp."); //Print to the Display

display.setCursor(45, 25);// Set the Display Cursor

//

display.print(CT); // Print the Temperature value to the display in celcius

// display.print(temperature_value_c); // Print the Temperature value to the display in celcius

display.display(); // Update the Display

#ifdef __DEBUG__

// Serial.print(temperature_value_c); // Print the Temperature value in *C on serial monitor

// Serial.print(" "); // Print an Empty Space

Serial.print("; feedback output : "); // Print the Calculate Output value in the

serial monitor.

```
        Serial.println(output); // Print the Calculate Output value in the serial monitor.
    #endif
        delay(200); // Wait 200ms to update the OLED dispaly.
      }
    }
```

A.4 Information of graphic figures

The graphic figures in this dissertation were constructed by Han Kim using Powerpoint, Pymol, Maestro, Chemdraw, Rhinoceros 3D, and KeyShot software. Particularly, several components were purchased: Escherichia coli in Figure 1-21 was purchased from Pngtree, the oscilloscope in Figure 4-23 was purchased from TURBOSQUID, and the electric spark, fire, and finger in Figure 5-1 were purchased from Pngtree.